UNIVERSITY OF CALIFORNIA SAN DIEGO

Characterization and Understanding of Microstructure Transformation in Li-Ion Battery Recycling and Fast-Charging

A Dissertation submitted in partial satisfaction of the requirements
for the degree Doctor of Philosophy

in

Materials Science and Engineering

by

Hongpeng Gao

Committee in charge:

Professor Zheng Chen, Chair
Professor Ping Liu, Co-Chair
Professor Jian Luo
Professor Shyue Ping Ong
Professor Yu Qiao

2025

The dissertation of Hongpeng Gao is approved, and it is acceptable in quality and form for publication on microfilm and electronically.

University of California San Diego

2025

DEDICATION

This dissertation is dedicated to my supervisor, parents, family and friends.

TABLE OF CONTENTS

LIST OF FIGURES

LIST OF TABLES

ACKNOWLEDGEMENTS

First and foremost, I would like to express my deepest gratitude to my advisor, **Professor Zheng Chen**, for his unwavering support, guidance, and encouragement throughout my research journey. His continuous generosity in sharing knowledge, time, and resources has been invaluable to my academic and professional growth. Even when my ideas seemed challenging or required significant investments of time, effort, and funding, he always placed his trust in me and provided insightful suggestions. I still vividly remember writing my first manuscript— I cannot begin to fathom the countless nights and immense patience he devoted to refining my work and shaping my research. I am truly fortunate to have him as my advisor, and I deeply appreciate his mentorship, which has been instrumental in shaping my future career.

I am also sincerely grateful to my collaborators, **Dr. Yan Chen** and **Dr. Ke An** from Oak Ridge National Laboratory (ORNL), and **Dr. Johanna Nelson Weker** from Stanford Linear Accelerator Center (SLAC), for their invaluable guidance, expertise, and support. Their instructions and the opportunities they provided have been instrumental in my research, and I am truly appreciative of their contributions.

Additionally, I would like to extend my sincere appreciation to my committee members: **Professor Ping Liu, Professor Jian Luo, Professor Shyue Ping Ong, and Professor Yu Qiao**, for their valuable time, insightful feedback, and encouragement.

Beyond academia, I owe immense gratitude to my parents, **Baodong Gao and Aifeng Du**, for their unconditional love and selfless sacrifices. Their unwavering support has been my greatest source of strength, especially during the most challenging times. Without them, I could not have overcome the difficulties darkest time in my life.

I would also like to express my heartfelt thanks to my girlfriend, **Luqi Zhang**, for her support, love, and companionship. She has shown me her enthusiasm and the true essence of life, providing endless encouragement and joy through every step of this journey.

Lastly, I would like to extend my deepest appreciation to my co-authors and labmates at the **Sustainable Materials Energy Lab (SMEL)**. Their invaluable support, collaboration, and friendship have made my research experience truly enriching.

Chapter 2, in full, is a reprint of the material "Efficient Direct Recycling of Degraded $LiMn_2O_4$ Cathodes by One-Step Hydrothermal Relithiation" as it appears in ACS applied materials & interfaces Hongpeng Gao, Qizhang Yan, Panpan Xu, Haodong Liu, Mingqian Li, Ping Liu, Jian Luo, Zheng Chen, 2020. The dissertation author was the primary investigator and author of this paper.

Chapter 3, in full, is a reprint of the material "Understanding and Controlling Structural Defects and Disordering in $LiNi_{0.5}Mn_{1.5}O_4$ Cathodes for Direct Recycling" as it appears in ACS nano Hongpeng Gao, Bing Han, Duc Tran, Luqi Zhang, Zishuo Zhao, Yu-ting Chen, Wei Tang, Mingjie Xu, Junlin Wu, Xiaolu Yu, Varun Gupta, Maura Appleberry, Haodong Liu, Yijie Yin, Weiliang Yao, Mingqian Li, Weikang Li, Linqin Mu, Ying Shirley Meng, Zheng Chen, 2024. The dissertation author was the primary investigator and author of this paper.

Chapter 4, in full, is a reprint of the material "Direct Upcycling of Spent $LiNi_{0.33}Co_{0.33}Mn_{0.33}O_2$ Cathodes to Nickle-Rich NCMs Using Lean Precursors: from Polycrystals to Single-Crystals" as it appears in ACS Energy Letters Hongpeng Gao, Qizhang Yan, Duc Tran, Xiaolu Yu, Haodong Liu, Mingqian Li, Weikang Li, Junlin Wu, Wei Tang, Varun Gupta, Jian Luo, Zheng Chen, 2023. The dissertation author was the primary investigator and author of this paper.

Chapter 5, in full, is a reprint of the material “Enhanced Electrolyte Transport and Kinetics Mitigate Graphite Exfoliation and Li Plating in Fast-Charging Li-Ion Batteries” as it appears in Advanced Energy Materials Hongpeng Gao, Qizhang Yan, John Holoubek, Yijie Yin, Wurigumula Bao, Haodong Liu, Artem Baskin, Mingqian Li, Guorui Cai, Weikang Li, Duc Tran, Ping Liu, Jian Luo, Ying Shirley Meng, Zheng Chen, 2023. The dissertation author was the primary investigator and author of this paper.

VITA

2016 Bachelor of Science in Materials Science and Engineering, Tsinghua University, China

2018 Master of Science in Materials Science and Engineering, Stanford University, USA

2025 Doctor of Philosophy in Materials Science and Engineering, University of California San Diego, USA

PUBLICATIONS
(from 2019)

1. Zhang, Y.; Tang, W.; **Gao, H.**; Li, M.; Wan, H.; Kong, X.; Liu, X.; Chen, G.; Chen, Z. Monolithic Layered Silicon Composed of a Crystalline–Amorphous Network for Sustainable Lithium-Ion Battery Anodes. ACS nano 2024.

2. Yu, X.; Yu, S.; Lin, J.; Gupta, V.; **Gao, H.**; Li, W.; Appleberry, M.; Liu, P.; Chen, Z. Multifunctional Scavenger Boosts Cathode Interfacial Stability with Reduced Water Footprint for Direct Recycling of Spent Lithium‐Ion Batteries. Advanced Materials 2024, 36 (41), 2408463.

3. Xu, P.; Guo, X.; Jiao, B.; Chen, J.; Zhang, M.; Liu, H.; Yu, X.; Appleberry, M.; Yang, Z.; **Gao, H.** Proton-exchange induced reactivity in layered oxides for lithium-ion batteries. Nature Communications 2024, 15 (1), 9842.

4. **Gao, H.**; Han, B.; Tran, D.; Zhang, L.; Zhao, Z.; Chen, Y.-t.; Tang, W.; Xu, M.; Wu, J.; Yu, X. Understanding and Controlling Structural Defects and Disordering in LiNi0. 5Mn1. 5O4 Cathodes for Direct Recycling. ACS nano 2024, 18 (44), 30737-30748.

5. Cai, G.; **Gao, H.**; Li, M.; Gupta, V.; Holoubek, J.; Pascal, T. A.; Liu, P.; Chen, Z. Partially Ion‐Paired Solvation Structure Design for Lithium‐Sulfur Batteries under Extreme Operating Conditions. Angewandte Chemie International Edition 2024, 63 (5), e202316786.

6. Xu, P.; Tan, D. H. S.; Jiao, B.; **Gao, H.**; Yu, X.; Chen, Z. A materials perspective on direct recycling of lithium‐ion batteries: principles, challenges and opportunities. Advanced Functional Materials 2023, 33 (14), 2213168.

7. Xia, D.; **Gao, H.**; Li, M.; Holoubek, J.; Yan, Q.; Yin, Y.; Xu, P.; Chen, Z. Enabling rechargeable Li‐MnO2 batteries using ether electrolytes. SmartMat 2023, 4 (5), e1208.

8. Holoubek, J.; Yu, K.; Wu, J.; Wang, S.; Li, M.; **Gao, H.**; Hui, Z.; Hyun, G.; Yin, Y.; Mu, A. U. Toward a quantitative interfacial description of solvation for Li metal battery operation under

extreme conditions. Proceedings of the National Academy of Sciences 2023, 120 (41), e2310714120.

9. Gupta, V.; Yu, X.; **Gao, H.**; Brooks, C.; Li, W.; Chen, Z. Scalable direct recycling of cathode black mass from spent lithium‐ion batteries. Advanced Energy Materials 2023, 13 (6), 2203093.

10. **Gao, H.**; Yan, Q.; Tran, D.; Yu, X.; Liu, H.; Li, M.; Li, W.; Wu, J.; Tang, W.; Gupta, V. Upcycling of spent LiNi0. 33Co0. 33Mn0. 33O2 to single-crystal Ni-rich cathodes using lean precursors. ACS Energy Letters 2023, 8 (10), 4136-4144.

11. **Gao, H**.; Yan, Q.; Holoubek, J.; Yin, Y.; Bao, W.; Liu, H.; Baskin, A.; Li, M.; Cai, G.; Li, W. Enhanced Electrolyte Transport and Kinetics Mitigate Graphite Exfoliation and Li Plating in Fast‐Charging Li‐Ion Batteries. Advanced Energy Materials 2023, 13 (5), 2202906.

12. Yu, X.; Yu, S.; Yang, Z.; **Gao, H.**; Xu, P.; Cai, G.; Rose, S.; Brooks, C.; Liu, P.; Chen, Z. Achieving low-temperature hydrothermal relithiation by redox mediation for direct recycling of spent lithium-ion battery cathodes. Energy Storage Materials 2022, 51, 54-62.

13. Yu, X.; Li, W.; Gupta, V.; **Gao, H.**; Tran, D.; Sarwar, S.; Chen, Z. Current Challenges in Efficient Lithium‐Ion Batteries’ Recycling: A Perspective. Global Challenges 2022, 6 (12), 2200099.

14. Xu, P.; Tan, D. H. S.; **Gao, H.**; Rose, S.; Chen, Z. Recycling of Li-Ion Batteries for Electric Vehicles. 2022.

15. Li, M.; Cai, G.; Holoubek, J.; Yu, K.; Liu, H.; Sarwar, S.; Yan, Q.; **Gao, H.**; Zhang, D.; Zhou, H. Hierarchically structured metal carbides as conductive fillers in thermo‐responsive polymer nanocomposites for battery safety. Nano Energy 2022, 103, 107726.

16. Holoubek, J.; Kim, K.; Yin, Y.; Wu, Z.; Liu, H.; Li, M.; Chen, A.; **Gao, H.**; Cai, G.; Pascal, T. A. Electrolyte design implications of ion-pairing in low-temperature Li metal batteries. Energy & Environmental Science 2022, 15 (4), 1647-1658.

17. **Gao, H.**; Tran, D.; Chen, Z. Seeking direct cathode regeneration for more efficient lithium-ion battery recycling. Current Opinion in Electrochemistry 2022, 31, 100875.

18. Cai, G.; Holoubek, J.; Li, M.; **Gao, H.**; Yin, Y.; Yu, S.; Liu, H.; Pascal, T. A.; Liu, P.; Chen, Z. Solvent selection criteria for temperature-resilient lithium–sulfur batteries. Proceedings of the National Academy of Sciences 2022, 119 (28), e2200392119.

19. Xu, P.; Yang, Z.; Yu, X.; Holoubek, J.; **Gao, H.**; Li, M.; Cai, G.; Bloom, I.; Liu, H.; Chen, Y. Design and optimization of the direct recycling of spent Li-ion battery cathode materials. ACS Sustainable Chemistry & Engineering 2021, 9 (12), 4543-4553.

20. Xia, D.; Yang, J.; Li, M.; **Gao, H.**; Gong, F. Hybridized cobalt/manganese vanadates as high-performance anodes in lithium ion battery. Materials Letters 2021, 283, 128782.

21. Xia, D.; **Gao, H.**; Li, M.; Gong, F.; Li, M. Transition metal vanadates electrodes in lithium-ion batteries: a holistic review. Energy Storage Materials 2021, 35, 169-191.

22. Wang, D.; Yan, Q.; Li, M.; **Gao, H.**; Tian, J.; Shan, Z.; Wang, N.; Luo, J.; Zhou, M.; Chen, Z. Boosting the cycling stability of Ni-rich layered oxide cathode by dry coating of ultrastable Li 3 V 2 (PO 4) 3 nanoparticles. Nanoscale 2021, 13 (5), 2811-2819.

23. Rose, S.; Xu, P.; **Gao, H.**; Li, M.; Yu, X.; Chen, Z. Boosting the Recycling Efficiency of Spent Lithium‐Ion Battery Cathodes Using a Green Reductant. Advanced Energy and Sustainability Research 2021, 2 (8), 2100040.

24. Zhang, Y.; Zhang, R.; Chen, S.; **Gao, H.**; Li, M.; Song, X.; Xin, H. L.; Chen, Z. Diatomite‐Derived Hierarchical Porous Crystalline‐AmorphousNetwork for High‐Performance and Sustainable Si Anodes. Advanced Functional Materials 2020, 30 (50), 2005956.

25. Zhang, Y.; Song, X.; Zhang, P.; **Gao, H.**; Ou, C.; Kong, X. Production of activated carbons from four wastes via one-step activation and their applications in Pb2+ adsorption: insight of ash content. Chemosphere 2020, 245, 125587.

26. Xu, P.; Dai, Q.; **Gao, H.**; Liu, H.; Zhang, M.; Li, M.; Chen, Y.; An, K.; Meng, Y. S.; Liu, P. Efficient direct recycling of lithium-ion battery cathodes by targeted healing. Joule 2020, 4 (12), 2609-2626.

27. Markey, B.; Zhang, M.; Robb, I.; Xu, P.; **Gao, H.**; Zhang, D.; Holoubek, J.; Xia, D.; Zhao, Y.; Guo, J. Effective upcycling of graphite anode: healing and doping enabled direct regeneration. Journal of The Electrochemical Society 2020, 167 (16), 160511.

28. Li, M.; Shi, Y.; **Gao, H.**; Chen, Z. Bio‐Inspired Nanospiky Metal Particles Enable Thin, Flexible, and Thermo‐Responsive Polymer Nanocomposites for Thermal Regulation. Advanced Functional Materials 2020, 30 (23), 1910328.

29. Kong, X.; **Gao, H.**; Song, X.; Deng, Y.; Zhang, Y. Adsorption of phenol on porous carbon from Toona sinensis leaves and its mechanism. Chemical Physics Letters 2020, 739, 137046.

30. **Gao, H.**; Yan, Q.; Xu, P.; Liu, H.; Li, M.; Liu, P.; Luo, J.; Chen, Z. Efficient direct recycling of degraded LiMn2O4 cathodes by one-step hydrothermal relithiation. ACS Applied Materials & Interfaces 2020, 12 (46), 51546-51554.

31. Chang, Q.; Zhang, P.; Mostaghimi, A. H. B.; Zhao, X.; Denny, S. R.; Lee, J. H.; **Gao, H.**; Zhang, Y.; Xin, H. L.; Siahrostami, S. Promoting H2O2 production via 2-electron oxygen reduction by coordinating partially oxidized Pd with defect carbon. Nature Communications 2020, 11 (1), 2178.

32. Zhang, Y.; **Gao, H.**; Song, X.; Kong, X.; Xu, H. Preparation of Hierarchical Porous Carbon from Wheat Bran for Free‐Standing Electrode of High Areal Capacitance Supercapacitor. ChemElectroChem 2019, 6 (21), 5486-5491.

33. Ma, Z.; Wan, H.; Wang, W.; Zhang, X.; Uno, T.; Yang, Q.; Yue, J.; **Gao, H.**; Zhong, Y.; Tian, Y. A theranostic agent for cancer therapy and imaging in the second near-infrared window. Nano Research 2019, 12, 273-279.

ABSTRACT OF THE DISSERTATION

Characterization and Understanding of Microstructure Transformation in Li-Ion Battery Recycling and Fast-Charging

by

Hongpeng Gao

Doctor of Philosophy in Materials Science and Engineering

University of California San Diego, 2025

Professor Zheng Chen, Chair
Professor Ping Liu, Co-Chair

The transition to a low-carbon economy relies heavily on lithium-ion batteries (LIBs), which power electric vehicles (EVs), consumer electronics, and renewable energy storage. Despite significant advancements in LIBs, sustainable end-of-life management and efficient recycling methods are critical for reducing environmental impact and resource consumption. A direct

recycling method using hydrothermal treatment in a Li-containing solution has successfully regenerated degraded lithium manganese oxide (LMO) cathodes, restoring their high capacity and long cycling stability while minimizing the environmental footprint compared to traditional pyrometallurgical and hydrometallurgical processes. However, discrepancies among cathode chemistries present challenges, particularly in high-voltage spinel-type materials such as $LiNi_{0.5}Mn_{1.5}O_4$, where structural instabilities, defect formation, and Li/Mn disordering contribute to sluggish Li+ transport and irreversible capacity loss. A defect engineering strategy inducing twin boundaries and preferred grain orientation has been employed to enhance Li^+ diffusion and cycling stability.

Another strategy is upcycling cathode materials into high end cathodes beyond its virgin performance. Here, we report an efficient upcycling method, converting spent polycrystalline $LiNi_{0.33}Co_{0.33}Mn_{0.33}O_2$ (NCM111) up to single-crystal $LiNi_{0.8}Co_{0.1}Mn_{0.1}O_2$ (NCM811) with lean input of precursors. Systematical investigation of the microstructure evolution in the upcycling process revealed an Ostwald ripening phenomenon during particle transformation. Optimizing sintering temperature and reaction time results in single-crystal particles showing uniform Ni element distribution and valence state, clean surface, and tunable sizes.

Despite these advances in recycling and upcycling, LIBs still suffer from performance limitations under extreme fast-charging (XFC) conditions. Charging at high-rate leads to lithium plating, unfavorable solid electrolyte interphase (SEI) formation, and solvent co-intercalation, ultimately degrading cycle life. These failure modes primarily stem from the inadequacies of conventional electrolytes; however, using an ester-based electrolyte has significantly improved capacity retention. Addressing both sustainable battery recycling and performance degradation

under XFC is crucial for advancing next-generation LIBs, ensuring long-term efficiency, and promoting a circular economy for energy storage solutions.

Overall, this thesis explores the aforementioned strategies, providing fundamental insights and guidance for the rational design of highly efficient recycling and upcycling methodology and innovative electrolytes. By bridging sustainability with performance optimization, this work paves the way for more durable, efficient, and environmentally responsible energy storage solutions.

Chapter 1 Introduction

1.1 Background

The transition to a low-carbon economy relies heavily on lithium-ion batteries (LIBs), which power electric vehicles (EVs), consumer electronics, and renewable energy storage. LIBs are essential for reducing global greenhouse gas (GHG) emissions, as transportation and energy storage sectors account for nearly 60% of global CO_2 emissions. As countries push for electrification mandates, such as the European Union's 2035 ban on internal combustion engine (ICE) vehicle sales. The demand for LIBs is expected to quadruple by 2030, reaching a projected 4.7 TWh in global battery production.

However, despite their environmental benefits, LIBs face two critical challenges that must be addressed to ensure long-term sustainability and scalability:

1. Sustainability Challenges: Resource Scarcity & End-of-Life Management
2. Performance Challenges: Enabling Fast Charging Without Degradation

1.2 The Sustainability Challenge: Resource Constraints & Battery Recycling

An expeditious growth in the demand for lithium-ion batteries (LIBs) in the consumer electronics and electric vehicles (EVs) industries has raised significant concerns in the materials and environmental sustainability with spent LIBs[1, 2]. Despite the advantages in reduction of carbon dioxide emission and fossil fuel's dependance associated with increasing LIB deployment, the spent LIBs, containing metal elements (Li, Co, Ni, Mn) and flammable organic electrolytes, are extremely harmful to the environment under improper disposal or treatments[3]. It is urgent to create effective waste management strategy for end-of-life (EOL) LIBs, which can not only treat the environment hazards but also efficiently recycle the valuable materials.

Today's industry technologies for recycling LIBs are pyrometallurgy and hydrometallurgy, inheriting from recycling the Ni-MH batteries[4, 5]. However, these technologies mainly focus on the recovery of the most expensive element (*e.g.*, Co and Ni) contained in cathode[6, 7]. As the EV market shifts toward low-Co or even Co-free LIBs, the conventional recycling strategies would become less attractive for future LIB recycling since the reduced economic return is no longer able to compensate the high processing cost[2]. Moreover, their process associated with destructing materials into the elemental forms and resynthesis require significant energy inputs and lead to secondary pollution concerns[8]. Since the spent LIBs from EVs often retain 70-80% of their original capacity, a non-destructive technology, so called "direct recycling", emerges as a more promising alternative[9]. A typical direct recycling process is capable of rejuvenating both spent cathodes and anodes while avoiding the leaching and smelting process in conventional methods. Neither intensive energy nor extensive chemicals are required in the direct recycling process, which significantly reduces the energy input and the processing cost[10, 11].

Recent studies demonstrated that the direct recycling can effectively recycle both Co-free and Co-containing cathodes[12-15]. However, there is yet to be a single universal protocol for direct recycling. Since different cathodes experience distinct degradation mechanisms in the state-of-art LIBs, the direct recycling process parameters will be unique for a specific battery chemistry. A common step in direct recycling is the re-lithiation process to recover the cathodes within its reusable chemical formulas[16]. Although solid-state sintering by mixing Li salt with degraded cathode is the simplest way for direct recycling, it is challenging to precisely determine the amount of supplementary Li source for mixed waste stream with spent LIBs at a wide range of state of health (SOH). Recent efforts in direct recycling have been largely devoted into designing novel self-saturation methods to replenish sufficient Li ions into the cathode crystal structures for

composition recovery, which will be followed by thermal treatment to achieve a desired crystal structure. Both steps are essential for regenerating spent electrode materials with the same performance as the pristine ones.

A universal direct recycling protocol is not yet developed for all kinds of cathodes, as the degradation mechanisms and healing conditions are different. The multiplicity of battery chemistries is one key barrier for direct recycling because single-cathode input is preferred to recover high-quality cathode powder. Battery technologies are evolving at a rapid pace while the recycling techniques are insufficient to meet the requirements of the market[17]. However, reaching single material chemistry requires laborious sorting or by acid leaching regeneration methods for the separation at elemental level[18]. Both inevitably increase the overall recycling cost and period. To minimized the labor-intensive sorting process, the concept of Battery Identity Global Passport (BIGP) could significantly ease the pain and be materialized through a digital chip comprising information that identifies the battery at the cradle (manufacturers) and at the gate (recyclers)[19]. This concept could manage the global battery flow and jeopardize the chances to recycle Li-ion batteries in responsible and profitable ways. In this thesis (Chapter 2-4), multiple direct-recycling and upcycling methods have been proposed to achieve sustainability in spinel type and layer structure cathodes in lithium-ion batteries.

1.3 The Performance Challenge: Fast Charging and Battery Degradation

While sustainability is a crucial consideration, LIBs must also deliver improved performance metrics to meet the demands of modern energy storage applications. The widespread integration of lithium-ion battery (LIB)-powered electric vehicles (EVs) is a crucial milestone in transitioning to a future driven by sustainable energy sources. While significant advancements in LIB energy density have extended EV driving ranges, battery charging times still fall short compared to the quick refueling of gasoline-powered vehicles. To bridge this gap, the U.S.

Department of Energy has set an ambitious extreme fast-charging (XFC) target, aiming to reduce charging times to 15 minutes or less without compromising energy density or battery cycle life. Achieving and surpassing this goal requires a thorough understanding and optimization of various kinetic limitations in high-energy LIBs. Fundamentally, these limitations include Li+ diffusion within electrode materials, Li+ migration through the solid-electrolyte interphase (SEI), Li+ diffusion through the electrolyte, and charge transfer at the electrode interface.

Although extensive research has focused on enhancing battery electrode material performance at high charge rates (4C and above), maintaining both adequate energy density and cycle stability alongside rapid charging remains a formidable challenge. While alternative electrode materials have been developed to support high-rate cycling, none offer energy densities comparable to graphite anodes and transition-metal oxide cathodes. However, retaining electrode materials and loadings necessary for EV-level energy density often results in significant trade-offs in cyclability and safety under high-rate cycling conditions. Cathode materials, in particular, suffer from diminished capacity retention at high charging rates due to sluggish kinetics in micron-scale particles, which imposes excessive strain on the electrode composite. Previous studies have shown that despite significant structural and surface modifications caused by high degrees of Li^+ depletion, the capacity losses in NMC cathodes are relatively recoverable. Consequently, the anode is widely regarded as the limiting factor for energy retention and cycle life.

Specifically, the close proximity of the LiC_6 redox potential to the Li/Li^+ reference potential makes lithium metal plating a significant concern. This issue can lead to rapid cell failure and severe safety hazards due to internal short circuits caused by dendritic growth. To address these challenges, researchers have explored various electrode design strategies, including patterned graphite anode architectures and increasing active surface area by modifying graphite or

incorporating high-surface-area carbons into the composite. While these approaches show promise, they typically create additional void space within the electrodes, necessitating higher electrolyte loading, which in turn reduces overall energy density at scale. Although the rational design of charging protocols is another essential approach, fast storage kinetics remains a fundamental requirement. While several strategies exist for optimizing electrode performance, many interfacial phenomena at the electrode/electrolyte interface remain to be fully understood and addressed.

In this thesis (Chapter 5), I investigated the rate-induced anode failure in $LiNi_{0.6}Mn_{0.2}Co_{0.2}$ (NMC 622) || graphite full pouch cells using conventional carbonate electrolytes under extreme fast-charging (XFC) conditions. Our findings provide clear evidence that graphite anodes in these cells undergo significant capacity degradation, primarily due to lithium loss through Li plating, the dislocation of isolated graphite, and exfoliation-driven interstitial SEI formation—resulting from insufficient charge-transfer kinetics. To address these challenges, a key advancement in fast-charging electrolytes has been proposed, aimed at enhancing ionic conductivity and increasing the Li^+ transference number in ester-based electrolyte systems. This improvement has the potential to transform high-rate cycling performance in lithium-ion batteries.

Chapter 2 Direct Recycling of Spent Spinel Cathodes

2.1 Introduction

Among the state-of-art energy storage technologies, lithium-ion batteries (LIBs) have dominating applications in portable electronics, electric vehicles (EVs), and stationary energy storage [20, 21]. The LIB industry has experienced a revolutionary development in the last decade with remarkable performance improvements, satisfying many key performance requirements such as high energy density, high power density, good cycling stability[22]. The global market of LIB expands dramatically as result of the significant growth in EV market recent years, representing more than 180 GWh of worldwide LIB sales in 2018. Considering the limited service life for EVs applications (8 calendar years) and the environmental impact of inappropriate battery disposal, there is an urgent need to develop efficient and sustainable methods for recycling/regenerating the materials out of spent LIBs[9, 23].

The state-of-the-art approaches in LIB recycling industry are mainly based on hydrometallurgical and pyrometallurgical processes[24, 25]. Both methods involve energy-intensive or caustic processes such as sintering, acid leaching and chemical precipitation, which are unavoidably associated with heavy CO_2 emission and other waste generation[26, 27]. These methods can be viable in processing Co-containing LIBs since the value of Co product (e.g., CoSO4) may compensate for the high operation cost. However, for many other LIBs, such as LiMn2O4 (LMO) batteries, the low intrinsic value of their elemental components (e.g., Mn) poses huge challenges for recycling via traditional ways[28] . Nevertheless, such low-cost batteries offer unique properties for many applications. For example, LMO is an appealing cathode material due to its high thermal stability and low cost. These features make it attractive for low-cost EVs and large-scale energy storage.

On the other hand, direct regeneration without destructive high-temperature smelting and acid leaching process is attracting considerable attentions, as it can potentially provide a cost-reduction and environment-benign solution for recycling useful materials from spent batteries. Various methodologies have been demonstrated for direct regeneration of layered oxide cathode, such as $LiCoO_2$ (LCO) and $LiNi_xCo_yMn_zO_2$ (or NCM, x+y+z=1). These include electrochemical treatment[16], hydrothermal relithiation[29], Ionothermal lithiation[30], molten salt relithiation[31] and solid-state sintering[32] approaches. For example, Yang et al have recently demonstrated a direct regeneration method of NCM, with the first discharge capacity of 158 mAh/g and the retention of 77.8% after 100 cycles at 1C via combining hydrothermal treatment and short-annealing process[13]. Tao et al successful regenerated spent NCM via a cost-effective Li halide as Li source in ionic liquids with the advantages of low vapor pressures[30]. Jianlin et al provide a promising improvement on treating the spent NCM by water process avoiding the spam on N-methyl-2-pyrrolidone (NMP)[33]. In spite of successful demonstrations on direct regeneration of LIBs containing high-value transition elements (e.g. Co, Ni), only a few studies have been done on regenerating cathodes with low cost such as LMO [34, 35]. The direct recycling by extraction valuable element via supercritical carbon dioxide (CO_2) has been demonstrated to be costly and not worthy in the case of LMO batteries[36].

By leveraging the knowledge established in developing various synthesis methods for spinel cathode materials[37-39], in this work, we demonstrated an one-step direct regeneration method to effectively recycle spent LMO cathodes, which showed successful reconstruction of stoichiometric composition and restored crystallinity from severely degraded LMO cathode materials with different state of health (SOH). Specifically, we used a hydrothermal treatment with dilute lithium hydroxide (LiOH) solution to simultaneously relithiate degraded LMO particles and

heal the microstructure defects. **Figure 2-1** illustrates the relithiation process highlighting the migration of lithiation inside the spinel structure along (110) direction during hydrothermal process. The reasons for capacity fading have been investigated in the last decade, which are mainly ascribed to Li loss[40], Mn migration[41] and John-Tell distortion[42, 43]. By tuning the operation conditions, the composition and structure evolution of LMO during the regeneration process was systematically investigated via various physicochemical characterizations. The study on the kinetic mechanism combined with neutron diffraction indicates that the lithium loss and lattice distortion can be fully recovered to the original levels of the pristine materials. This work provides a new direction towards cost-effective and environment-friendly battery recycling to potentially address the sustainability issues related to LIBs.

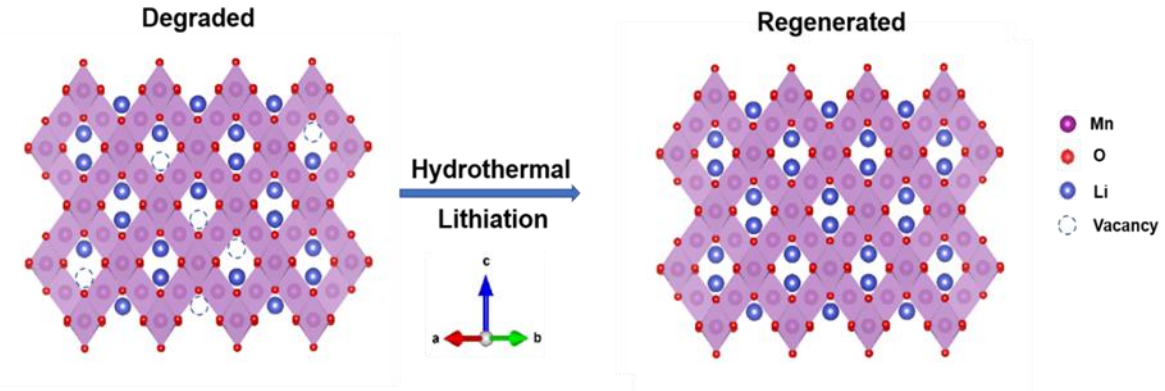

Figure 2-1 Illustration of the hydrothermal lithiation process in which Li^+ is re-dosed to the Li-deficient sites to recover its desired stoichiometry.

2.2 Efficient Direct Recycling of Degraded $LiMn_2O_4$ Cathodes by One-Step Hydrothermal Relithiation

2.2.1. Experimental

2.2.1.1 Commercial pouch cell assembly

Dry pouch cells (500 mAh) made with lithium manganese oxide (LMO) as cathode active materials and graphite as anode active materials were directly supplied from Guangdong Canrd New Energy Technology Co., Ltd, China. The electrolyte was battery grade lithium hexafluorophosphate ($LiFP_6$) solution in ethylene carbonate (EC) and dimethyl carbonate (DEC) purchased from Sigma-Aldrich, with the composition of 1.0 M $LiPF_6$ in EC/DEC=50/50 (v/v) (LP40). The dry pouch cells were filled by 1 mL of electrolyte and sealed by the vacuum sealer machine (MTI Corp.) inside the glove box. After 24 h standing time, the pouch cells were activated in the voltage window of 3-4.3V by C/10 (50 mA) (1C =148 mA/g) under constant current - constant voltage (CC-CV) cycling with the cut-off current at C/20 (25 mA). The activated pouch cells were cycled between 3.0-4.3V at 1.5 C (750 mA) for 40 cycles, then 0.5C (250 mA) for other 160 cycles.

2.2.1.2 Homemade single-layer pouch cell assembly

Single-layer LMO-graphite pouch cells were also built in our lab to investigate the lithium distribution in the cycled cells. The pristine LMO powders (MTI Corp.) were mixed with polyvinylidene fluoride (PVDF, KYNAR 2800) and carbon black (Super P65) in N-Methyl-2-pyrrolidone (NMP, Sigma-Aldrich, anhydrous, 99.5%) at a mass ratio of 8: 1: 1 to form homogeneous slurries. The slurries were casted by a doctor blade and then dried under vacuum at room temperature for 2 h followed by drying at 80 °C for 6 h. After rolling, the cathodes were cut into 4.4 cm*5.7 cm with a mass loading of 6.8 mg/cm^2. The pre-baked graphite (Graphite & Carbon Products, G80) was mixed with PVDF and Super P65 in NMP at a mass ratio of 90:5:5. The slurries were casted by a doctor blade and then dried under vacuum at 80 °C for 6 h. After rolling, the anodes were then cut into 4.5 cm*5.8 cm with a mass loading of 3.7 mg/cm^2. After matching the electrodes under controlled N/P ratio (1.1-1.15), single layer pouch cells were

assembled with a tri-layer membrane (Celgard 2320) as the separator and 500 ul of LP40 as the electrolyte. All the home-made pouch cells were activated in the voltage window of 3-4.3V at C/10 under CCCV cycling with the cut-off current of C/20. The cells were cycled between 3.0-4.3V at C/2 under CCCV with the cut-off current C/5 for 200 cycles.

2.2.1.3 Cathode materials harvesting

All the pouch cells were discharged to 2.8V before disassembly. The cathode strips were harvested from both the commercial and home-made pouch cells, by thoroughly rinsing with dimethyl carbonate (DMC) and then soaked in NMP for 6h under 50 °C. The active materials, binder and carbon black were removed from the aluminum substrates by sonification and scrapping. After centrifuging the NMP suspension at 3500 rpm for 5 min, active materials were precipitated. The precipitation was washed several times by NMP. Then the active materials were collected and dried under vacuum at 80 °C overnight for regeneration.

2.2.1.4 Regeneration of cathode materials

For the hydrothermal treatment, 0.25g of cycled LMO materials were added into a 100 ml of Teflon-lined autoclave filled with 80 ml of lithium hydroxide (LiOH) solution with different concentrations. The autoclaves were consistently heated at 180 °C for different periods of time. After cooling down naturally till room temperature, the treated powders were washed by deionized water for at least 5 times till PH ~7, and then dried under vacuum at 80 ^{o}C overnight.

2.2.1.5 Characterization

The compositions of cycled/regenerated LMO cathode materials were measured by an Inductively-coupled plasma quadrupole mass spectrometer (ICP-MS, Thermo Scientific™, iCAP™

RQ model). Their crystal structures were examined by X-ray powder diffraction (XRD) employing a Bruker D2 Phaser (Cu Kα radiation, λ=1.5406 Å) from scanning rate of 0.58 deg/min.

Time-of-flight (TOF) powder neutron diffraction was measured at the VULCAN instrument at the Spallation Neutron Sources (SNS), Oak Ridge National Laboratory (ORNL)[44]. The diffraction pattern was measured at the detector banks at $2\theta = \pm 90°$, equipped 5 mm receiving collimators. Neutron powder diffraction patterns were collected in the high intensity mode ($\Delta d/d$ ~0.45%) for a duration of 2 h under the nominal 1.4 MW SNS operation, and then processed using VDRIVE software[45]. Rietveld refinement against the neutron diffraction was performed using General Structure Analysis System (GSAS) software with EXPGUI interface[46, 47].

The morphology of the pristine, cycled and regenerated LMO powder was observed by Ultra High Resolution Scanning Electron Microscope (UHR SEM, FEI XL30). The particle size distribution is analyzed with Nano Measurer software. The microstructures of the regenerated LMO powder were further confirmed by high resolution transmission electron microscopic (HR-TEM) images which were collected on JEOL-2800 at 200 kV with a Gatan OneView Camera (25 fps, full 4K resolution). The detailed structure information was measured by DigitalMicrograph (DM). X-ray photoelectron spectroscopic (XPS) measurement was conducted with an AXIS Supra by Kratos Analytical with Al Ka anode source working at 15 kV and 10^{-8} Torr chamber pressure. The spectra data were processed by CasaXPS software. All spectra were calibrated with the hydrocarbon C 1s peak at 284.6 eV. The XPS depth profile analysis was carried out with a gas cluster ion source (GCIS) using focused energetic Ar ion beam.

Note for XPS analysis

During the photoemission process, an energy coupling interaction between unpaired electrons in the valence shell and unpaired electrons within the core level occurs following the

excitation of core level electrons[48, 49]. The result of this multiple splitting for manganese is that Mn 2p spectra taken from a single chemical species contain multiple peaks over a broad energy range (~6eV).

2.2.1.6 Analysis of lithium distribution in cycled pouch cells

After cycling at 0.5C under CCCV with a cut-off current of 0.1C for 200 cycles, the home-made pouch cells were disassembled in glove box. 10 µl of electrolyte has been collected by a pipette and diluted into 10 ml of DMC. The anodes were rinsed by DMC for 2 h and then soaked in 1M HCl for 3 days. The cathode active materials were collected by the same method as harvesting commercial pouch cells described above. The compositions of electrolyte, anode electrodes and cathode electrodes were measured by ICP-MS.

2.2.1.7 Electrochemical characterization.

The active materials were mixed with PVDF, and Super P65 in NMP at a mass ratio of 8:1:1. Then the formed slurries were cast on an aluminum foil using a doctor blade and dried in vacuum at 80 °C for 6 h. The LMO cathodes were cut and compressed by rolling. The areal mass loading of LMO electrodes for coil cells are around 10 mg/cm2. Coin cells were assembled with a Li metal disc (thickness 1.1 mm) as the counter electrode, LP40 as the electrolyte, and a tri-layer membrane (Celgard 2320) as the separator. Galvanostatic charge-discharge was carried out using a Neware battery testing system in the potential range of 3.0-4.3 V at 0.5C for 200 cycles after C/10 in the initial cycle and 0.3C in the following two cycles.

2.2.1.8 Economic and environmental analysis

The EverBatt model, a closed-loop battery recycling model developed at Argonne National Laboratory[50], was used to conduct techno-economic and life-cycle analysis of pyrometallurgical,

hydrometallurgical, and direct cathode recycling processes. The analysis was focused on the total energy consumptions and GHG emissions of the three recycling methods. Moreover, the cost and revenue of the three recycling methods were modeled as well.

2.2.1.8.1 Evaluation of the life-cycle total energy use and greenhouse gas (GHG) emissions in recycling

Pyrometallurgical (**Figure 2-2**) and hydrometallurgical (**Figure 2-3)** recycling processes were included as battery end-of-life management options. Note that the entire process is built for the mixture of different kinds of batteries, especially the steps focusing on Ni and Co recovery (e.g., leaching, solvent extraction, precipitation). In the current recycling industry, pyrometallurgical and hydrometallurgical recyclers do not sort batteries before processing. As a result, spent batteries will end up going through the same recycling process regardless of cathode chemistry, applying in LMO recycling study.

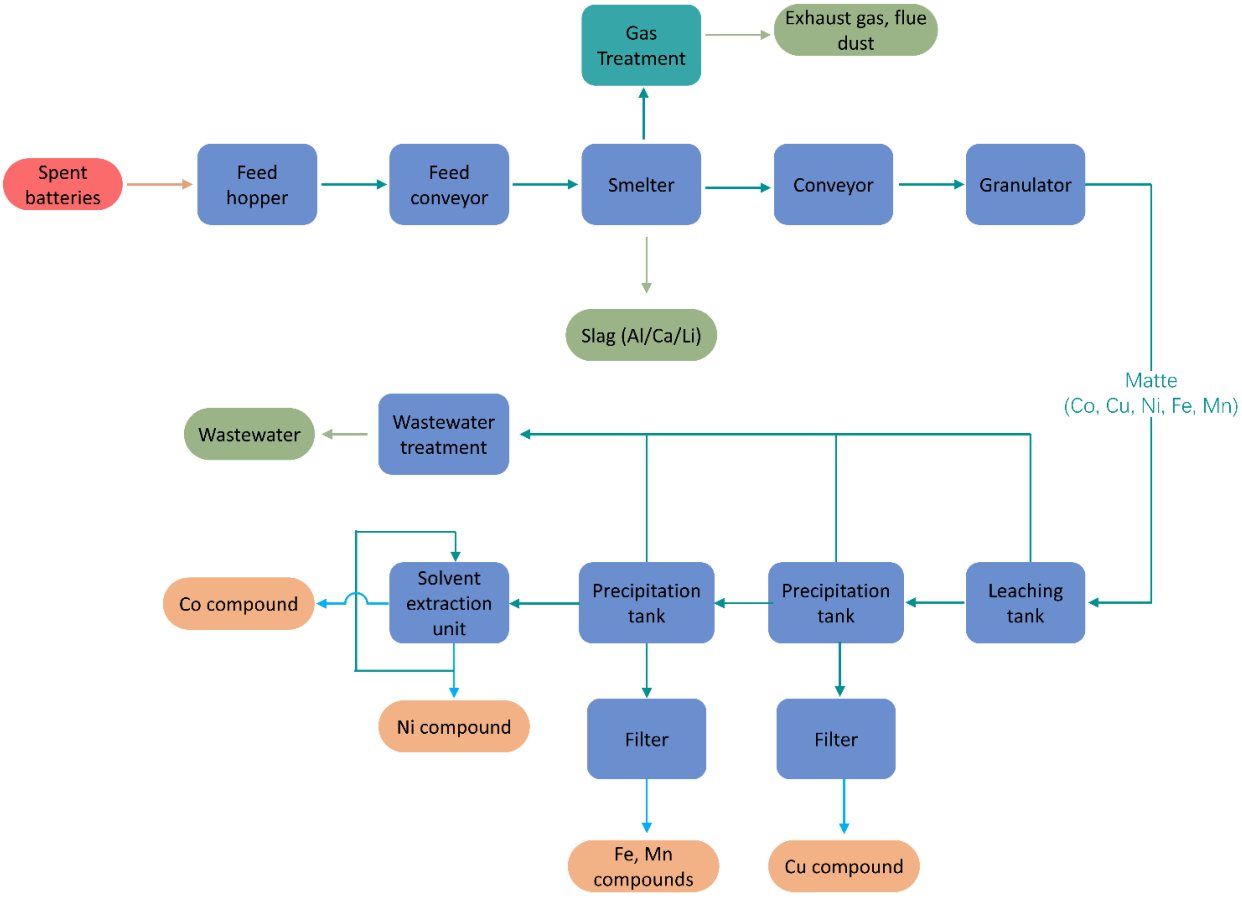

Figure 2-2 Follow diagram of a generic pyrometallurgical recycling process.

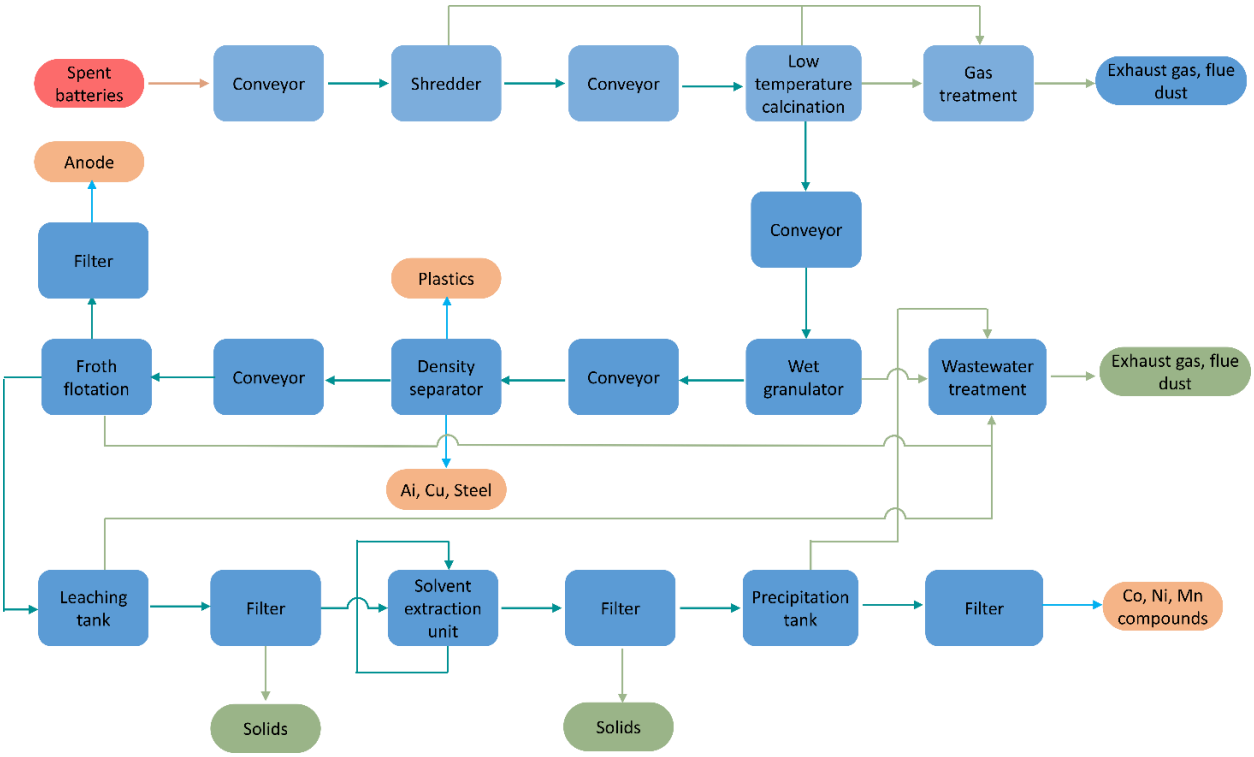

Figure 2-3 Flow diagram of a generic hydrometallurgical recycling process.

The generic direct recycling process in EverBatt was modified in this study to reflect the changes in the process design, as depicted in **Figure 2-4**. In the direct recycling process, batteries are discharged, dissembled, and shredded. After that, the materials undergo a series of physical separation processes to separate out scrap metals, plastics, anode powder and cathode powder. After separation, the harvested cathode materials are sent to aqueous relithiation to refunctionalize cathode powder.

The three recycling plants, featuring pyrometallurgical, hydrometallurgical, and direct recycling processes, respectively, are assumed to be based on processing capacity of 10,000 metric tons per year in the U.S.

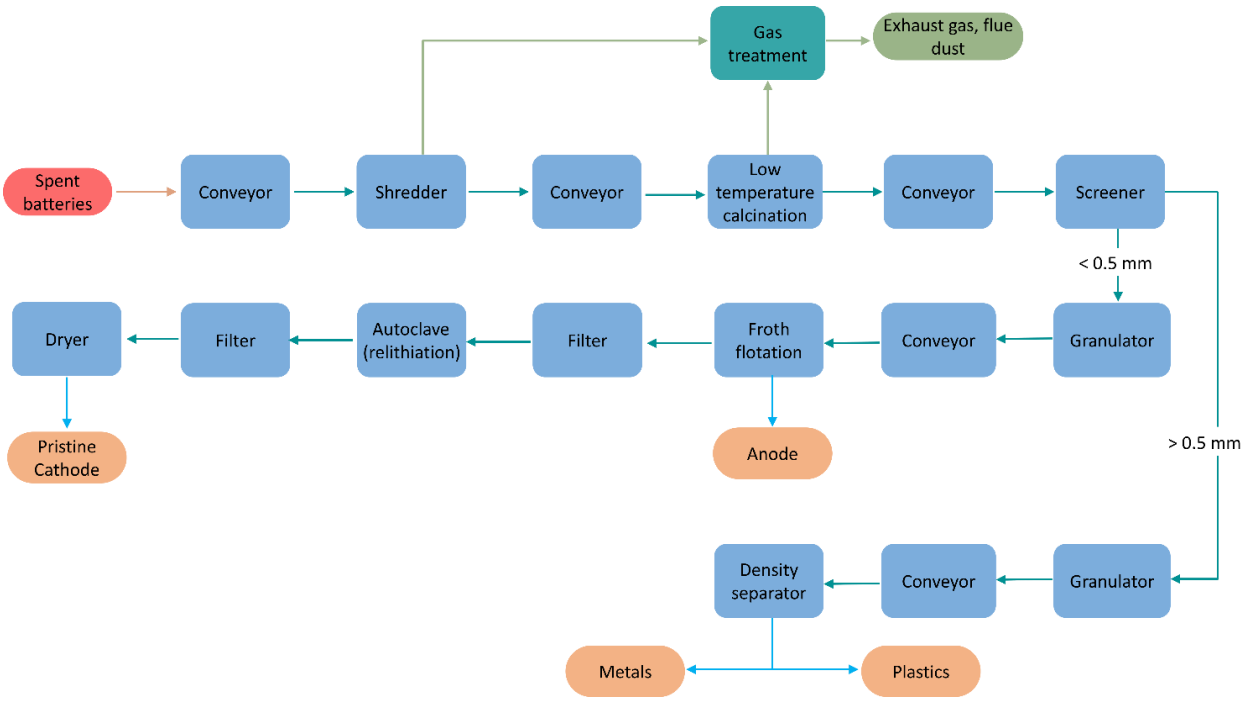

Figure 2-4 Flow diagram of a generic direct recycling process.

The modeling of life-cycle total energy and GHG emissions is based on the materials and energy flows through the recycling process, as discussed below.

Materials input

The materials requirements for the three recycling technologies are summarized in **Table 2-1**. The materials requirements for the generic pyrometallurgical and hydrometallurgical processes are obtained from EverBatt, and are reproduced here for the readers' understanding. The materials requirements for the direct recycling process are obtained based on our lab process. Life cycle analysis accounts for the environmental impacts of all the materials consumed in the process(es) by capturing the environmental impacts associated with their upstream production.

Table 2-1 Materials requirements (kg) to recycle 1 kg of spent batteries through different recycling technologies.

	Pyrometallurgy	Hydrometallurgy	Direct recycling
Ammonium Hydroxide	NA	0.03	NA
Hydrochloric Acid	0.21	0.01	NA
Hydrogen Peroxide	0.06	0.37	NA
Sodium Hydroxide	NA	0.56	NA
Limestone	0.30	NA	NA
Sand	0.15	NA	NA
Sulfuric Acid	NA	1.08	NA
Soda Ash	NA	0.02	NA
Lithium Hydroxide	NA	NA	0.028

Energy input

To calculate the life-cycle environmental impacts attributable to all types of energy consumed in the process(es), life cycle analysis considers the environmental impacts associated with upstream fuel production and electricity generation, as well as those associated with on-site fuel combustion (e.g., diesel/natural gas combustion). The energy requirements to recycle 1 kg of spent batteries through different recycling technologies are summarized in **Table 2-2**. Again, the purchased energy consumptions for the generic pyrometallurgical and hydrometallurgical processes are obtained from EverBatt, while that for the direct recycling process is estimated from engineering calculations based on our lab process.

Table 2-2 Energy requirements (MJ) to recycle 1 kg of spent battery through different recycling technologies.

	Pyrometallurgy	Hydrometallurgy	Direct recycling
Diesel	0.6	0.6	0.6
Natural gas	NA	2.5	0
Electricity	4.68	0.13	0.57

Process emissions

In the life cycle analysis, we also accounted for environmental impacts associated with process emissions that are not due to fuel combustion. For the three recycling processes, process emissions include those from material combustion and thermal decomposition. The former arises from burning off materials during the recycling processes, including graphite, carbon black, electrolyte, plastics, and the binder material in the pyrometallurgical process, and electrolyte and the binder material in the hydrometallurgical and direct recycling processes. The latter arises from the decomposition of Li_2CO_3 during the relithiation step of the direct recycling process. As the pyrometallurgical process involves burning off various battery constituents, it leads to much higher emissions than those from the other two recycling methods. The detailed modeling results are listed in **Table 2-3**. The total energy use and GHG emissions are plotted as column chart shown in result and discussion. Total energy use is the cumulative energy use pertaining to the process, including fossil energy use and renewable energy use. Fossil energy use can be further broken down to that of coal, natural gas, and petroleum. GHG emissions are calculated based on 100-year global warming potentials from the fifth assessment report of the Intergovernmental Panel on Climate Change[51].

Table 2-3 Life-cycle environmental impacts of different recycling methods.

	Pyrometallurgy	Hydrometallurgy	Direct recycling
Total energy use in MJ per kg cell recycled			
Total Energy	16.765	30.664	3.906
Fossil fuels	13.424	28.373	0.880
Coal	2.643	5.866	2.062
Natural gas	9.865	20.601	0.965
Petroleum	0.916	1.906	3.906
Total Emissions in g per kg cell recycled			
VOC	0.149	0.380	0.090
CO	0.590	1.177	0.325
NO_x	1.078	2.437	0.751
PM10	0.096	0.210	0.071
PM2.5	0.059	0.142	0.058
SOx	0.869	23.786	0.266
BC	0.017	0.028	0.021
OC	0.015	0.043	0.017
CH_4	2.137	4.640	0.592
N_2O	0.015	0.037	0.006
CO_2	1,915	2,120	519
CO_2 (w/ C in VOC & CO)	1,916	2,123	520
GHGs	1,984	2,272	0.090

2.2.1.8.2 Cost and revenue analysis of different recycling processes

The specific cost parameters chosen for the recycling plant are summarized in **Table 2-4**.

Table 2-4 Manufacturing cost details for different recycling processes per year (10,000 tons of spent batteries).

	Pyro	Hydrometallurgy	Direct recycling
I. Manufacturing Cost, $/year	$ 29,356,789	$ 21,038,124	$ 7,484,478
A. Direct Product Costs	$ 10,131,784	$ 10,431,528	$ 3,904,987
Raw Materials	$ 1,239,000	$ 5,792,956	$ 365,375
Operating labor	$ 2,157,714	$ 1,316,571	$ 1,115,429
Direct supervisory and clerical labor	$ 323,657	$ 197,486	$ 167,314
Utilities	$ 1,415,640	$ 319,886	$ 1,128,943
Maintenance and Repairs	$ 3,860,400	$ 2,113,456	$ 883,812
Operating supplies	$ 579,060	$ 317,018	$ 132,572
Laboratory charges	$ 215,771	$ 131,657	$ 111,543
Patents and royalties	$ 340,540	$ 242,497	NA
B. Fixed Charges	$ 16,054,120	$ 8,792,840	$ 3,579,491
Depreciation	$ 7,548,015	$ 4,128,851	$ 1,725,984
Local taxes	$ 3,088,320	$ 1,690,765	$ 707,050
Insurance	$ 772,080	$ 422,691	$ 176,762
Rent	$ 356,371	$ 202,249	$ 85,883
Financing (interest)	$ 4,289,334	$ 2,348,284	$ 883,812
C. Plant Overhead Costs	$ 3,170,886	$ 1,813,756	NA
II. General Expenses, $/year	$ 4,697,205	$ 3,211,596	NA
A. Administrative costs	$ 951,266	$ 544,127	NA
B. Distribution and selling costs	$ 2,043,240	$ 1,454,983	NA
C. R&D costs	$ 1,702,700	1,212,486	NA
III. Total Product Cost $/year=Manufacturing Cost+General Expenses	$ 34,053,995	$ 24,249,721	$ 7,484,478

The revenue calculation was based on the sales of recycled materials. The prices are obtained from EverBatt and listed in **Table 2-5**. The recycled yield of components is assumed to be 90%. "~" means the material cannot be accessible in the specific recycling. The weight

percentage of Cu, Al, graphite and LMO in a cell is 15.0%, 7.8%, 14.1% and 40.8%, respectively. Combining with the cost obtained from **Table 2-4**, the achieved profit is calculated and shown in result and discussion.

Table 2-5 Value of recycled materials ($/kg)

	Pyrometallurgy	**Hydrometallurgy**	**Direct recycling**
Cu	$6.6	$6.6	$6.6
Al	NA	$1.3	$1.3
Graphite	NA	$0.28	$0.28
$LiMn_2O_4$	NA	NA	$7.00
Mn in product	NA	$1.43	NA
MnO_2	NA	$1.00	NA
$MnSO_4$	NA	$2.13	NA

2.2.2 Results and discussions

Both commercial and home-made pouch cells were used for the demonstration of our direct recycling approach. The details for assembling different pouch cells were described in the experimental section (Supporting Information). All the pouch cells were cycled in the voltage window of 3.0-4.3V until more than 20% capacity degradation was obtained (**Figure 2-5**). The LMO cathode materials were collected and purified by a typical procedure developed in our previous work[32]. The obtained cathode particles with composition and structure degradation were subject to the hydrothermal treatment (denoted as "HT") under different conditions. The regenerated cathode particles were carefully characterized and made into new cells to evaluate the electrochemical performance.

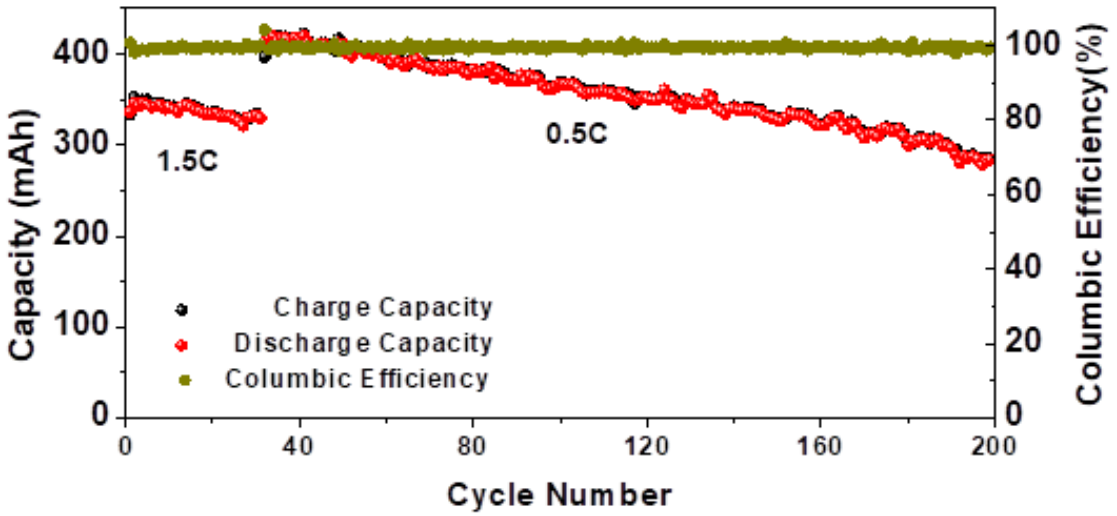

Figure 2-5 Cycling performance of LMO commercial pouch cell. The cell was cycled in a voltage range of 3-4.5 V. The capacity degradation was 25% after 200 cycles.

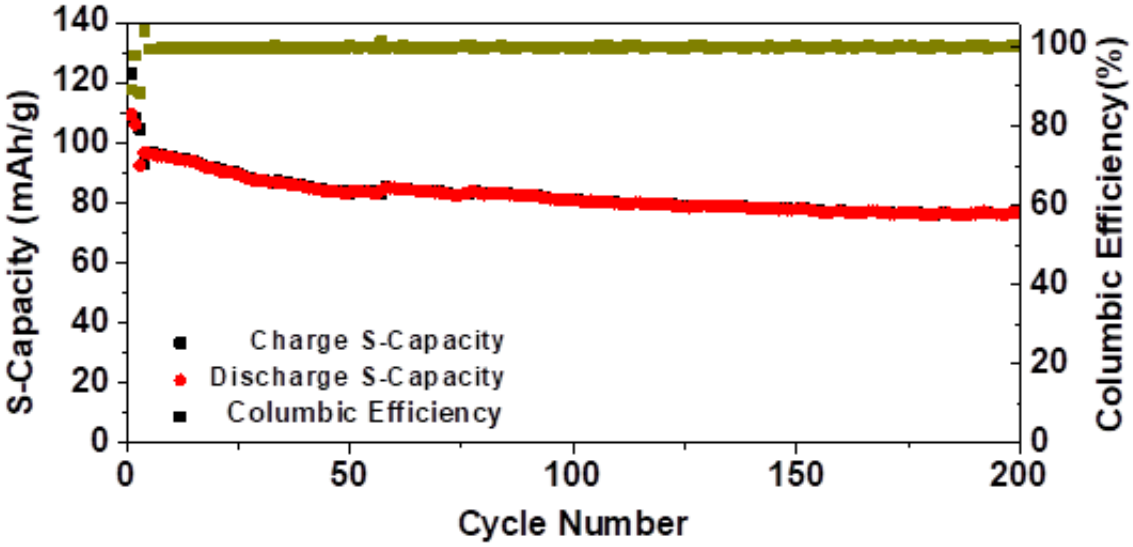

Figure 2-6 Cycling performance of LMO home-made pouch cell. The cell was cycled in a voltage range of 3-4.5 V at 0.5C. The capacity degradation was 20 % after 200 cycles.

We first analyzed the cell components to identify the sources of capacity degradation associated with composition changes. For more quantitative analysis, home-made LMO/graphite single layer pouch cells with controlled cathode mass were used to investigate the Li distribution in degraded cells under room temperature. After 200 cycles in a voltage range of 3.0-4.3 V at 0.5C,

20% capacity fading appeared in our home-made pouch cells (**Figure 2-6**). The causes of capacity loss of the full cell are complicated, including the SEI formation on anode surface, lattice distortion caused by John-Tell effect[43], Mn (II) dissolution induced by Mn(III) disproportion[52, 53]. To identify the Li distribution, the graphite and LMO electrodes from cycled LMO pouch cell were immersed in diethyl carbonate (DEC) solution separately to wash out the residual electrolyte. Then the anode and cathode active materials were scratched off their current collectors and soaked the into hydrochloric acid to extract metal elements. A complete analysis was conducted to investigate the distribution of Li coming from the cathode side. **Figure 2-7** shows that 82.6% of Li was retained inside the degraded spinel cathode particles, 13.5% of Li in anode where the consumption of Li was likely associated with the formation of thick SEI during long-term cycling[54]. Interestingly, 0.8mM Mn was detected in 1M $LiPF_6$ EC/DEC electrolyte. In William's work, the same level concentration of Mn was detected after the LMO powders were exposed to electrolyte. Although the appreciable Mn dissolution may cause the structure degradation, the overall loss of Li dominates the capacity fading compared with the tiny loss of Mn in cathodes[55]. Thus, compensation of the Li loss is a critical step to fix the degradation issues of LMO cathode for regeneration. The compositions of cycled and regenerated LMO cathode materials were measured by an inductively coupled plasma quadrupole mass spectrometer (ICP-MS). Note that the imperfect stoichiometry from the composition of commercial LMO particle are often designed for the extension of cycle life and the oxygen defects are caused by their high temperature sintering process[56]. The cycling data of commercial pouch cells shows that the capacity loss was more than 20% after 200 cycles under room temperature. Composition data in **Table 2-6** shows that the cathode material had 13% of Li loss compared with the pristine LMO even though the cells were discharged at cut-off voltage at 3.0 V.

Table 2-6 Lattice parameters and ICP results of the pristine, cycled, and regenerated LMO particles. The LMO sample regenerated in 0.02, 0.1 and 0.2M of LiOH for 12h was named as 0.02M HT-LMO, 0.1M HT-LMO and 0.2M HT-LMO, respectively.

Sample	a/Å	R_{wp}/%	R_p/%	Composit ion
Pristine LMO	8.2275(2)	3.93	2.05	$Li_{1.058}Mn_{1.951}O_{3.932}$
Cycled LMO	8.1930(4)	3.53	1.90	$Li_{0.885}Mn_{1.943}O_{3.942}$
0.02M HT-LMO	8.2218(3)	3.51	3.00	$Li_{1.033}Mn_{1.945}O_{3.939}$
0.1M HT-LMO	8.2272(2)	3.39	2.63	$Li_{1.060}Mn_{1.942}O_{3.944}$
0.2M HT-LMO	8.2274(3)	2.76	1.65	$Li_{1.067}Mn_{1.933}O_{3.944}$

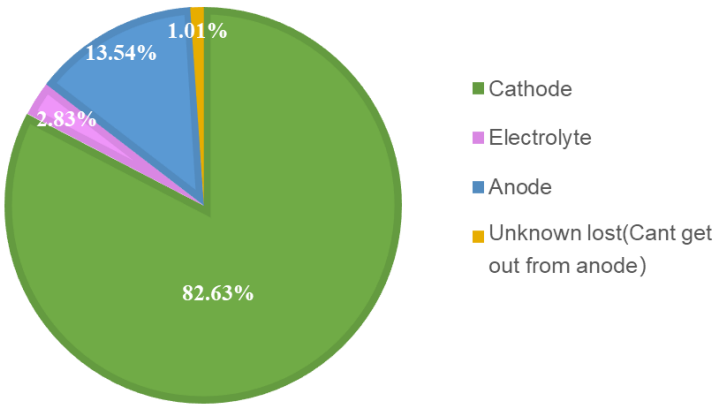

Figure 2-7 Lithium distribution of LMO home-made pouch cell. The capacity degradation was 20 % after 200 cycles.

To design an optimal regeneration process, we first investigated the relithiation kinetics during the hydrothermal treatment process in 0.1M LiOH at 180°C. **Table 2-7** and **Figure 2-8a** reveal that the Li composition can reach to the pristine level (e.g., 1.06 Li per Mn) after being treated for 6h. Further extending the treatment time up to 12h does not cause continuous increase of Li concentration in the solid LMO particles, which was confirmed by the refinement XRD (**Figure 2-8b-d**). In addition, cell cycling performance (**Figure 2-9**) indicates that 12h treatment

sample has been regenerated to the commercial reusable LMO cathode (to be discussed subsequently), which maintains high crystallinity and pure single phase.

Table 2-7 XRD refinement and ICP results of regenerated LMO particle after different hydrothermal time.

Sample	a/Å	Rwp%	Rp%	Composition
0.1M HT 3h LMO	8.2096	2.22	1.59	$Li_{1.009}Mn_{1.942}O_{3.936}$
0.1M HT 6h LMO	8.2268	5.51	3.37	$Li_{1.057}Mn_{1.942}O_{3.934}$
0.1M HT 12h LMO	8.2272	3.39	2.63	$Li_{1.060}Mn_{1.942}O_{3.945}$

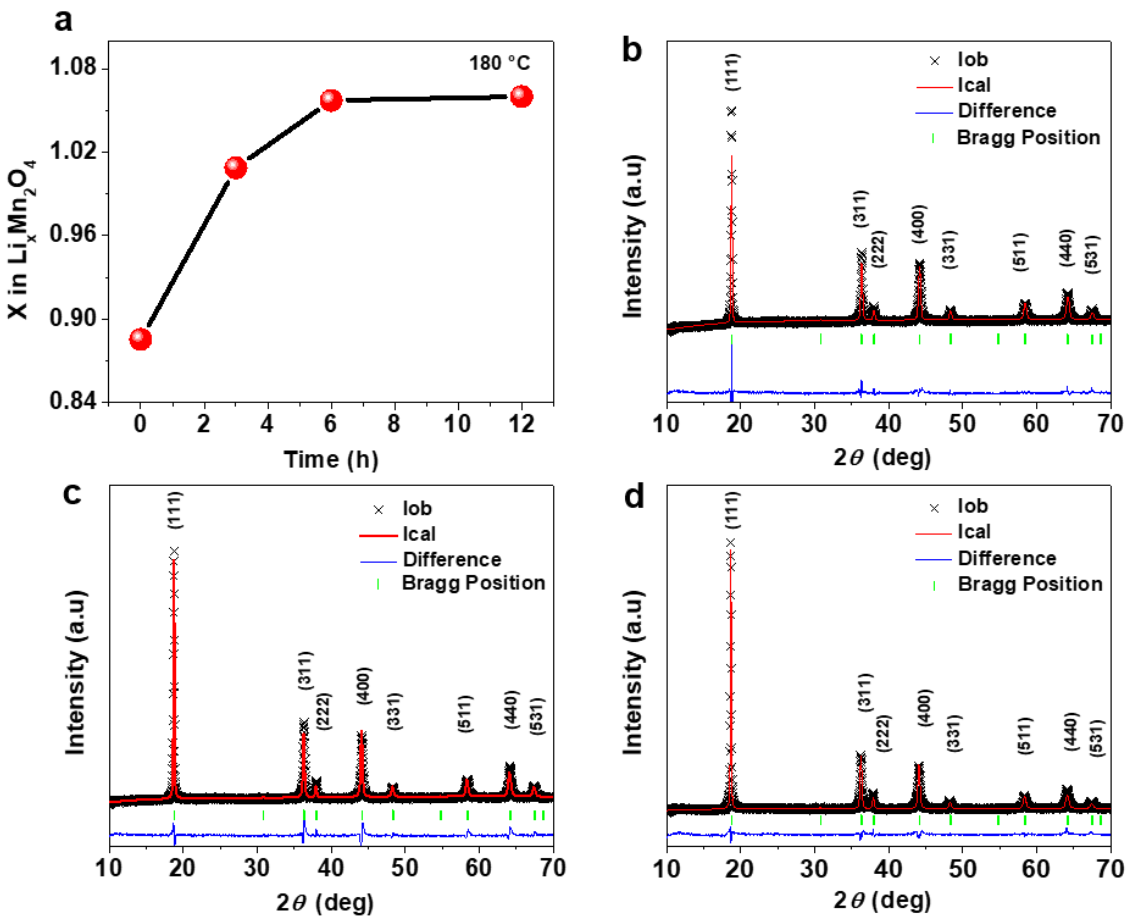

Figure 2-8 (a) Lithiation kinetics of degraded LIB cathode particles during hydrothermal treatment. The LMO sample regenerated in 0.1M of LiOH was named as HT-3h-LMO, HT-6h-LMO and HT-12h-LMO, respectively. Refinement XRD pattern of regenerated LMO particles. (b) HT-3h LMO (c) HT-6h LMO (d) HT-12h LMO.

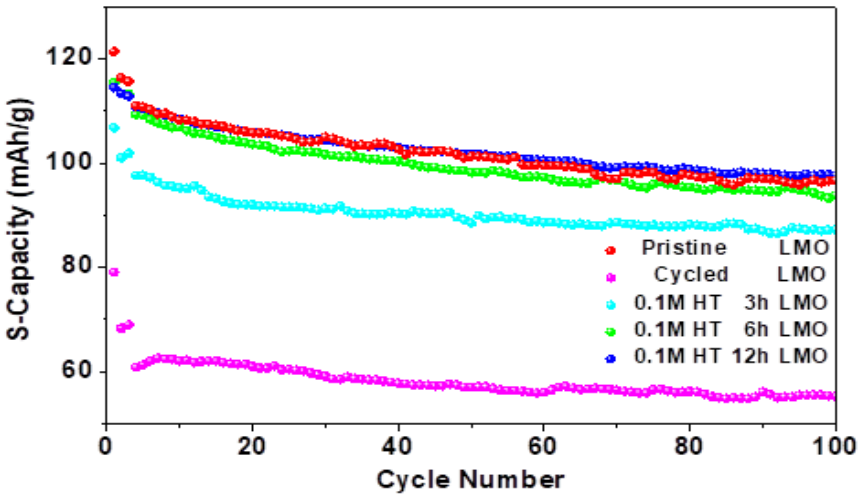

Figure 2-9 Cycling performance of pristine, non-treated and regenerated LMO samples at 0.5C. The regeneration was conducted by hydrothermal treatment at 180 °C in 0.1M LiOH solution for different periods of time.

Concentration of Li^+ in the hydrothermal solution is also an important parameter determining the relithiation behavior. With the concentration of LiOH solution changed from 0.02M to 0.2M, the degraded LMO particles can be fully recovered to reach the desired stoichiometry (~1.0 Li per Mn) at 180°C for 12h. As shown in **Table 2-6**, the composition of the regenerated LMO is sensitive to the concentration of the LiOH solution. When the LiOH concentration reached 0.4M, more Li^+ can be inserted into the lattice forming lithium-rich Li_2MnO_3 phase, as shown in **Figure 2-10a** with the increased intensity of impurity peaks at 18.8, 37.0 and 44.8 degree (marked by star). These peaks are in perfect match with (001), (130) and (131) peaks of the C2/*m* layered phase of Li_2MnO_3 [57, 58].

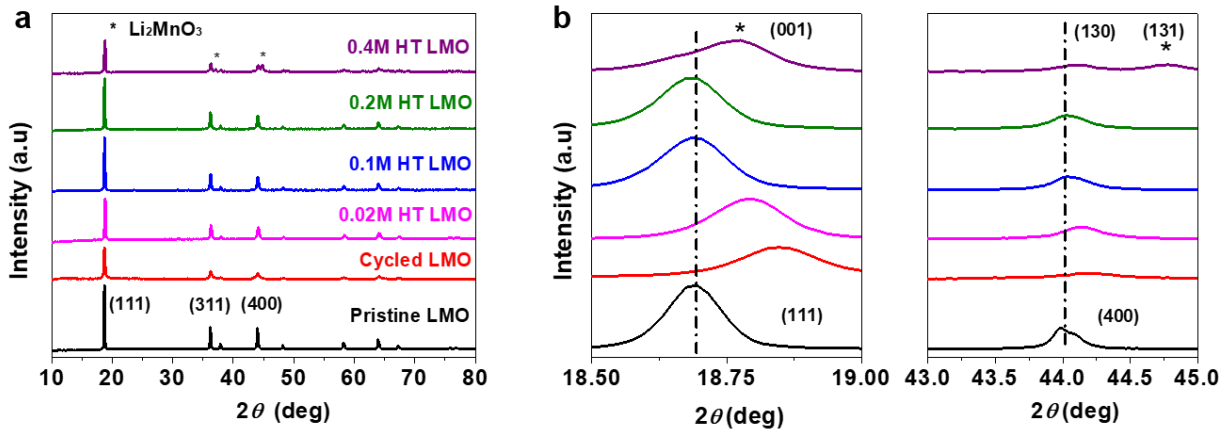

Figure 2-10 XRD patterns of pristine, cycled, and regenerated (a) LMO particles by hydrothermal treatment under 0.02M, 0.1M, 0.2M and 0.4M LiOH solution; (b) enlargement of the regions in the range of 18.5-19.0° and 43-45 °.

It is also critical to further investigate the evolution of the crystal structure of degraded LMO during the hydrothermal reaction. X-ray diffraction (XRD) patterns of cycled, pristine and regenerated LMO are shown in **Figure2- 10**. The standard pattern of spinel phase with $Fd\bar{3}m$ space group was validated in all samples[59]. Although no additional impurity peaks exist, the peaks became broader and less intense in cycled LMO compared to pristine LMO. A shift of the major (111) spinel peaks to higher angles can also be clearly found in **Figure 2-10b**, corresponding to the lattice parameter shrinkage from 8.23 Å to 8.19 Å. It indicates that, although the spinel structure was retained, the more Li^+ removed from their tetrahedral sites, the more decrease of unit-cell dimension are observed[60]. Thus, it is reasonable that the extent of Li^+ loss can be reflected on the right shift of (111) peaks which allows us to validate the effectiveness of our regeneration method. For example, after hydrothermal treatment in 0.1M LiOH for 12h, the (111) peak shifts back to lower angles and with intensity recovered to the pristine level. These results suggest the successful reconstruction of the crystal structure and high crystallinity of the regenerated LMO product.

Rietveld refinement was performed on all the XRD patterns using the General Structure Analysis System (GSAS) software (**Figure 2-11**). Both R_B (Bragg factor) and R_{wp} (weighted profile *R*-factor) are less than 5% which indicates the reliability of the refinement results. The lattice parameters of all the samples are compared in **Table 2-6.** The results further validate that not only the Li loss is compensated but also the structure can be repaired after simple hydrothermal treatment. For the purpose of demonstration, hydrothermal relithiation with 0.1M of LiOH at 180 ℃ for 12 h was selected to treat the degraded LMO cathode particles for the next step.

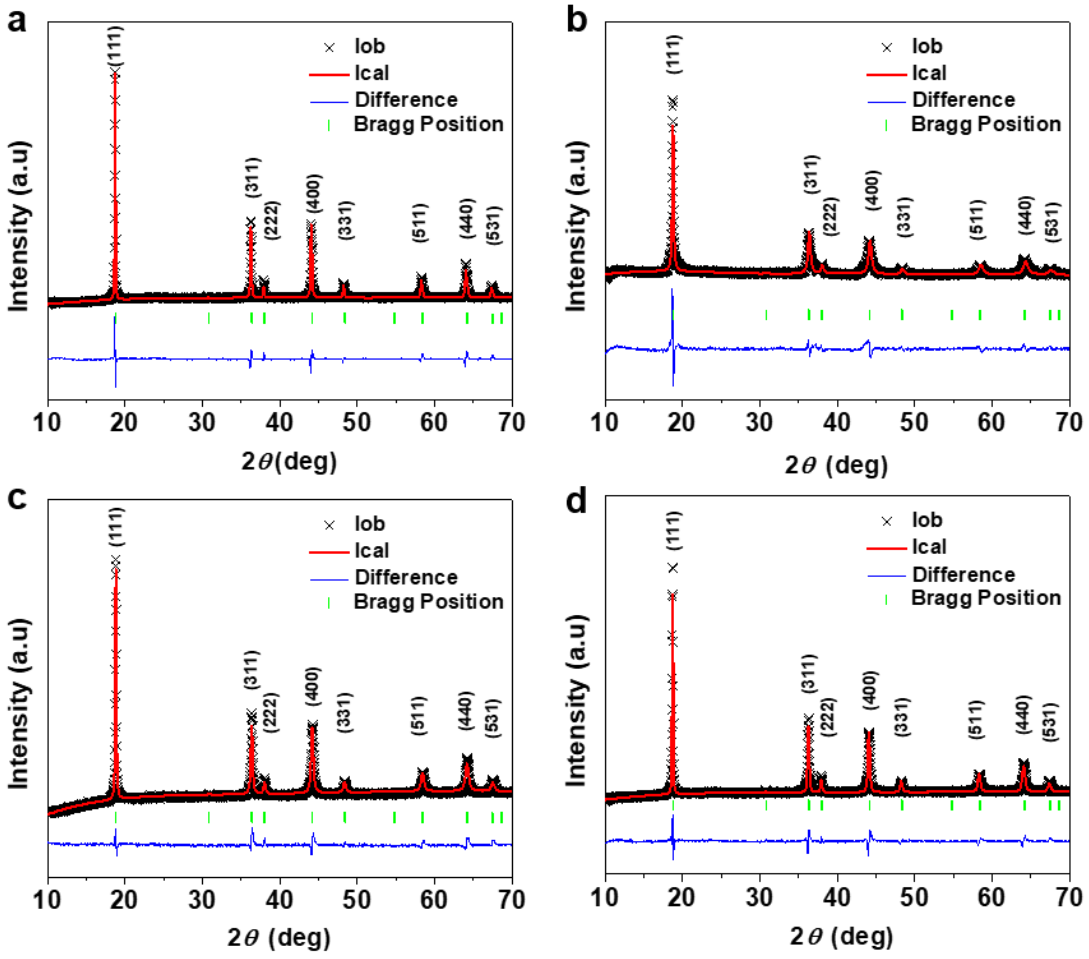

Figure 2-11 Refinement XRD pattern of pristine, cycled and regenerated LMO particles: (a) Pristine LMO (b) Cycled LMO (c) 0.02M HT 12h LMO (d) 0.2M HT 12h LMO.

To further quantify the occupancy of Li sites inside the lattice, neutron diffraction measurement was conducted on the pristine, cycled, and regenerated LMO from 0.1M of LiOH **(Figure 2-12**). As we expected, it evidently indicates that Li, Mn and O are located on the 8a (tetrahedral), 16d (octahedral), and 32e Wyckoff sites, respectively[61, 62]. The Rietveld refinement results are listed in **Table 2-8.** The average Mn oxidation state increased from 3.52 to 3.60 during the long-term cycling because the Li vacancies appear inside the spinel lattice. After hydrothermal treatment, the average Mn oxidation state decreased back to 3.54 and the lattice parameter of face-centered cubic (FCC) conventional unit cell increased from 8.1955(2) Å to 8.2280(3) Å due to the complement of Li into the vacancies. The decrease of Mn-O bond length in cycled LMO is ascribed to the reduction of Mn radius, whereas the radius of Mn^{4+} (0.530 Å) is smaller than that of Mn^{3+} ion (0.645 Å)[63]. After regeneration, the bond length was resumed to the pristine value. In addition, the changes of the composition were also consistent with the structure parameters (**Table 2-8**), which further confirms that the degraded LMO cathode was successfully regenerated in 0.1M LiOH solution.

Table 2-8 Neutron diffraction refinement results of pristine, cycled, and regenerated

Sample	a/Å	Mn-O bond	Oxide	Composition
Pristine LMO	8.2307(2	1.954	+3.52	$Li_{1.058}Mn_{1.942}O_{3.944}$
Cycled LMO	8.1955(2	1.943	+3.60	$Li_{0.896}Mn_{1.942}O_{3.944}$
0.1M HTLMO	8.2280(3	1.953	+3.54	$Li_{1.066}Mn_{1.934}O_{3.952}$

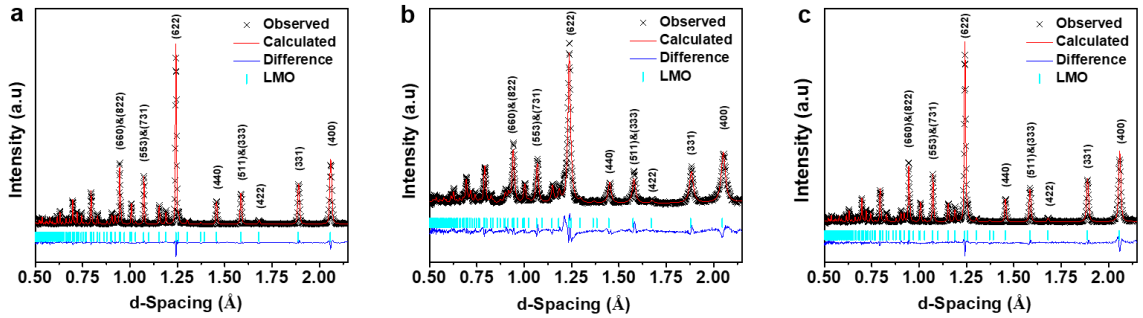

Figure 2-12 Rietveld refinement results of neutron diffraction patterns of (a) pristine, (b) cycled, and (c) regenerated LMO particles from 0.1M of LiOH.

The scanning electron microscopic (SEM) images and size distribution of the pristine, cycled and regenerated LMO particles are displayed in **Figure 2-13**. All the particles have the similar morphology and sizes of about 1.2 μm. After long term cycling, the average size of LMO particle increased due to the aggregation issue. After hydrothermal treatment, the spent LMO particles become more uniform and maintain a narrow distribution. To obtain more insights in the microstructure, the regenerated cathode materials were carefully examined by high-resolution transmission electron microscope (HRTEM) (**Figure 2-14a-b)**. The interplanar spacings of regenerated LMO were measured to be 0.48 nm and 0.25 nm, which corresponds to the orientation of (111) and (311) atom plane found in typical LMO, respectively [49, 64, 65]. The fast Fourier transform (FFT) patterns are indexed to the diffraction of the <011> and <010> zone axes [66]. Thus, the HRTEM images also confirm the reconstruction of the spinel structure in the regenerated LMO. Additional HRTEM images of cycled LMO particles in the surface and bulk regions are shown in **Figure 2-15**.

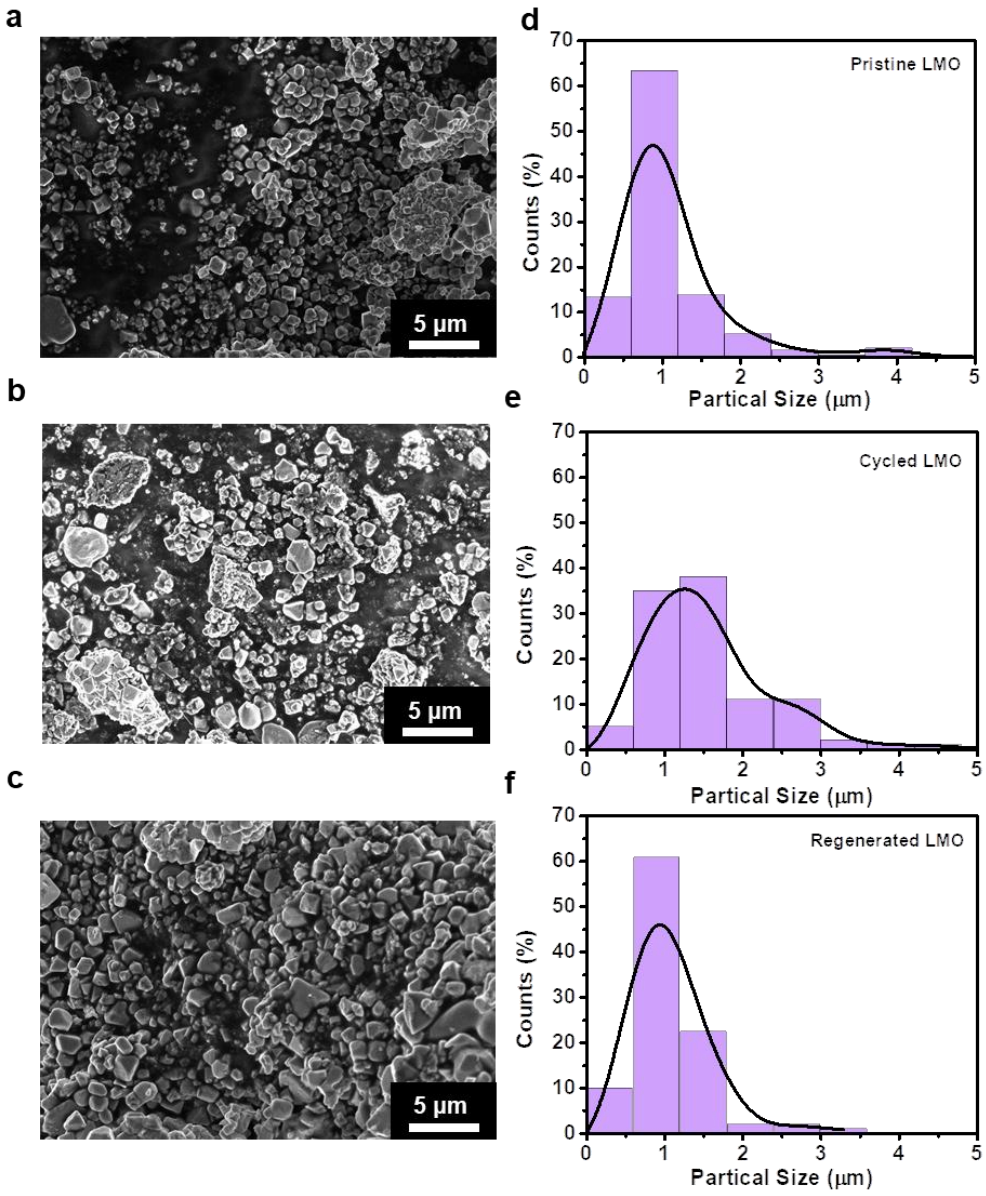

Figure 2-13 SEM images of the (a) pristine, (b) cycled and (c) regenerated LMO particles and size distribution of the (d) pristine, (e) cycled and (f) regenerated LMO particles.

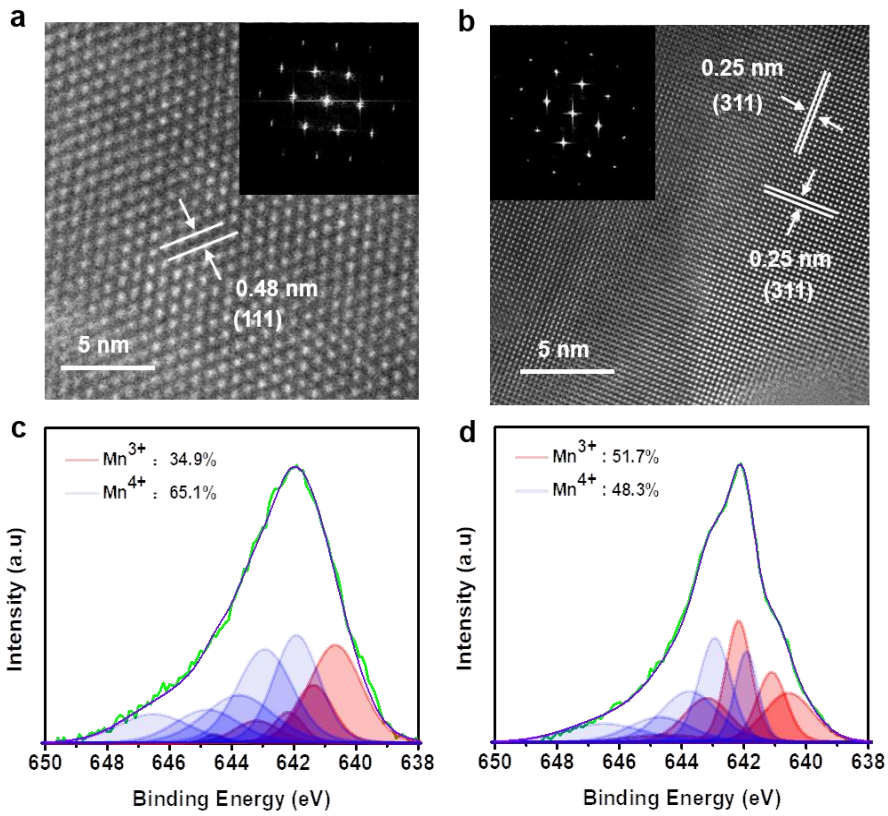

Figure 2-14 (a) HRTEM images and FFT patterns of regenerated LMO particles in the bulk region and (b) surface region. (c) XPS spectra of cycled LMO and (d) regenerated LMO particles.

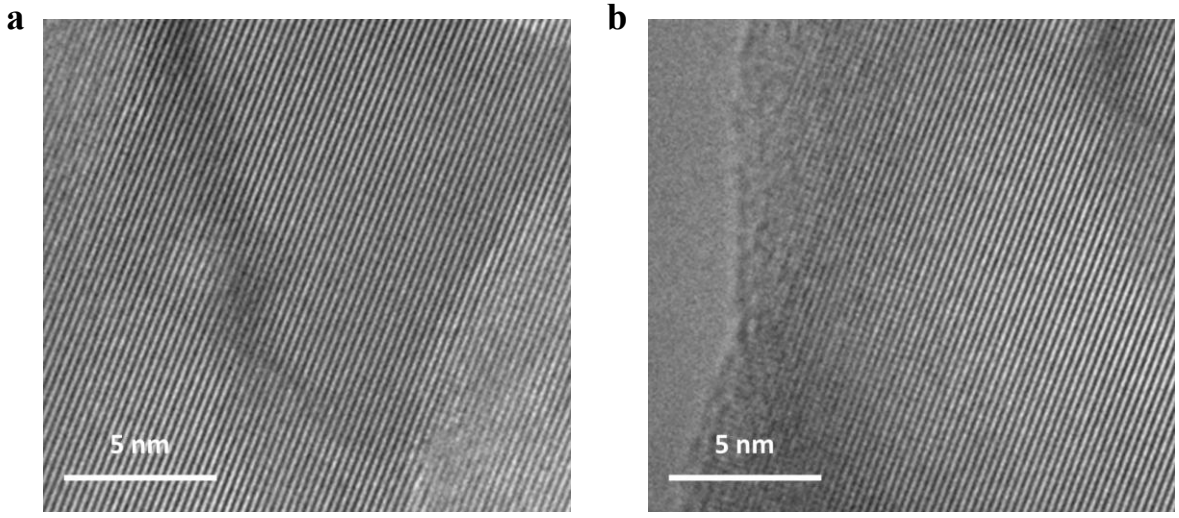

Figure 2-15 HRTEM images of cycled LMO particles in the surface and bulk regions.

X-ray photoelectron spectroscopic (XPS) measurement was performed on cycled and regenerated LMO to investigate the changes of the valence status **(Figure 2-14c-d**). Peak fitting was conducted on the Mn $2p_{3/2}$ spectrum to provide detailed distribution of the valence information of Mn in both samples (**Table. 2-9&2-10**) [67, 68]. **Figure 2-14c** shows a board shoulder in the region of high bonding energy, which can be ascribed to the high Mn^{4+} composition. **Figure 2-14d** shows a clear shoulder in low bonding energy region indicating the Mn^{3+} contribution. Quantitative analysis reveals that 51.7% and 48.3% of Mn can be assigned to Mn^{3+} Mn^{4+}, respectively, in the regenerated cathode, which is in good agreement with the valence distribution of Mn in typical LMO. By comparison, 34.9% Mn^{3+} and 65.1% Mn^{4+} were found in cycled cathode. The increase of the average valence state of Mn can be attributed to the Li loss inside lattice. Therefore, the more dominant contribution of Mn^{4+} in the cycled cathodes and its disappearance in regenerated cathodes further support that the Li-deficient spinel phases formed after cycling was recovered into well-defined, less defective structure after regeneration.

To evaluate the electrochemical performance of the pristine, cycled and regenerated LMO samples, galvanostatic charge/discharge test was conducted in a voltage range of 3.0-4.3 V. To compare the different electrochemical performance achieved with LMO regenerated in LiOH solution with different concentrations, differential capacity plots (dQ/dV) at the first cycle at 0.1C were also acquired (**Figure 2-16a**). Unlike the broad peak of 0.02M regenerated sample, the LMO regenerated in 0.1M of LiOH displayed sharp intrinsic reduction peaks at 4.16 V and 4.03 V (labeled as R_1 and R_2) and oxidation peaks at 4.11 V and 3.97 V (labeled as O_1 and O_2), which can be ascribed to the two-step mechanism of the electrochemical Li^+ intercalation and extraction from tetrahedral sites in spinel structure[69, 70]. The peak separations between charge and discharge scan

are 57 mV and 61 mV, respectively, which is good indication of high reversibility of the electrochemical reaction, with small polarization and favorable reaction kinetics[71].

Table 2-9 Mn(2p3/2) peak parameters for Mn in regenerated LMO particles.

Peak	**BE (eV)**	**Component Percent (%)**	**Total Percent (%)**
Mn^{3+}	640.55	11.08	
Mn^{3+}	641.10	9.68	
Mn^{3+}	642.16	14.52	51.7
Mn^{3+}	643.18	9.50	
Mn^{3+}	644.55	2.56	
Mn^{4+}	641.9	9.65	
Mn^{4+}	642.92	15.53	
Mn^{4+}	643.75	13.44	48.3
Mn^{4+}	644.70	7.20	
Mn^{4+}	646.50	6.85	

Table 2-10 Mn(2p3/2) peak parameters for Mn in cycled LMO particles.

Peak	**BE (eV)**	**Component Percent (%)**	**Total Percent (%)**
Mn^{3+}	640.65	18.96	
Mn^{3+}	641.35	8.23	
Mn^{3+}	642.16	3.36	34.9
Mn^{3+}	643.18	3.67	
Mn^{3+}	644.55	0.67	
Mn^{4+}	641.9	18.26	
Mn^{4+}	642.92	19.13	
Mn^{4+}	643.75	12.1	65.1
Mn^{4+}	644.78	7.92	
Mn^{4+}	646.50	7.70	

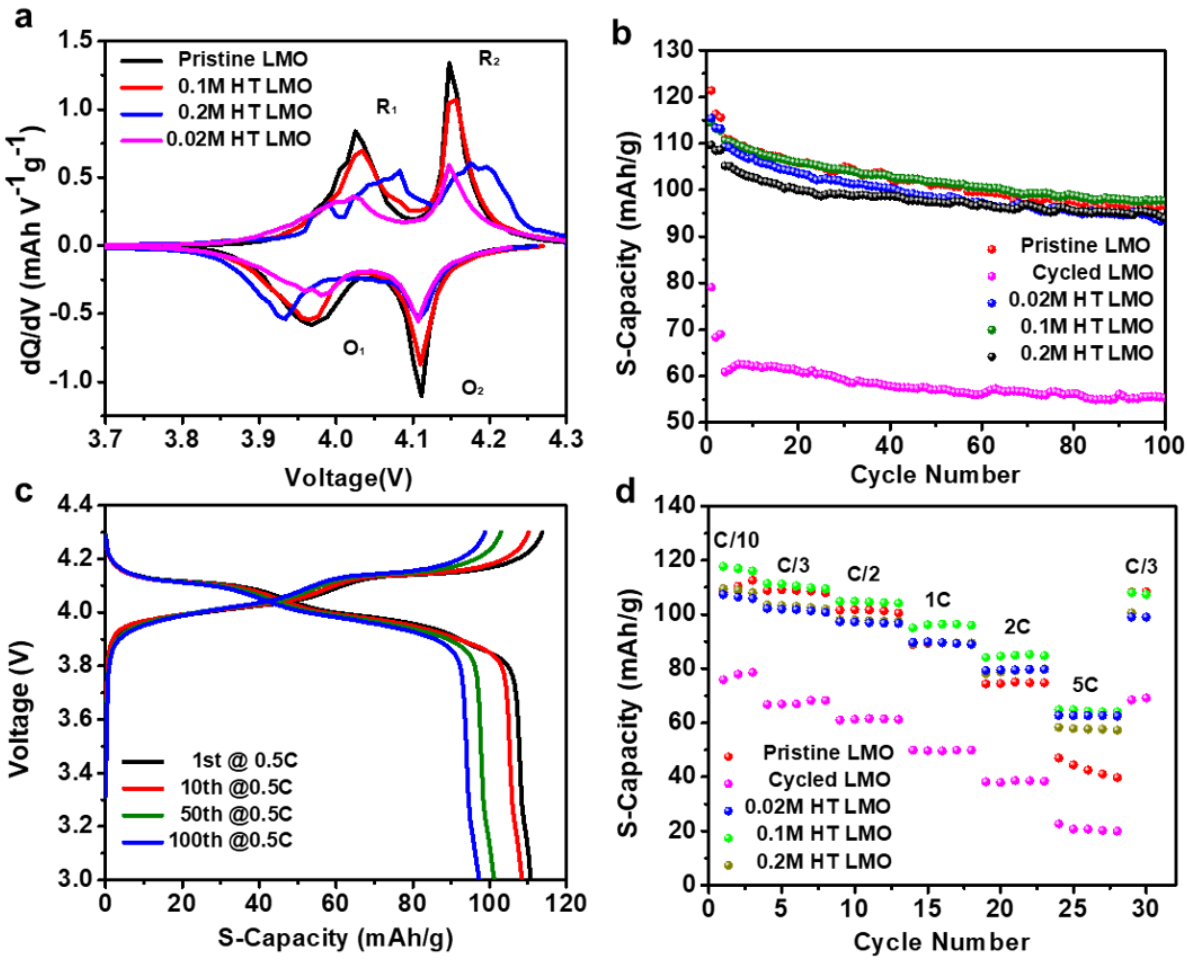

Figure 2-16 (a) dQ/dV plots of pristine and regenerated LMO samples at 0.1C. (b) Cycling performance of pristine, non-treated and regenerated LMO samples at 0.5C; (c) Charge/discharged curve of LMO regenerated in 0.1M of LiOH at the 1st, 10th, 50th and 100th cycle at 0.5C. (d) Rate performance of different LMO samples. HT-LMO: hydrothermal treatment at 180 °C for 12 h in LiOH solution with different concentrations.

For LMO regenerated from 0.2 M of LiOH, two tiny split peaks were obtained instead of only one reduction peak (R_1), indicating the unexpected side reaction at the initial activation cycle. It also caused a relatively lower initial columbic efficiency (82%) compared with 90% of LMO obtained in 0.1M LiOH. Furthermore, the larger peak separation suggests more severe polarization and poorer reversibility.

As shown in **Figure 2-16b**, the pristine LMO cathode showed a discharge capacity of 112 mAh/g at the first cycle at 0.5C (1C = 148 mAh/g) and 97 mAh/g after 100 cycles, corresponding

to a capacity retention of 86.6%. The cycled LMO cathode (harvested from spent cells without any treatment) showed a discharge capacity of only 61 mAh/g at first cycle at 0.5C and 55 mAh/g after 100 cycles, which is expected again due to the Li^+ loss and irreversible lattice distortion. By hydrothermal treatment at 180 ^oC for 12 h, the electrochemical properties were fully recovered: a discharge capacity of 109, 111 and 105 mAh/g at the first cycle at 0.5C and 94, 98 and 94 mAh/g after 100 cycles were obtained by LMO treated in 0.02, 0.1 and 0.2M LiOH, respectively. In addition, the cycling stability of LMO was also recovered. For example, with the hydrothermal treatment in 0.1M LiOH solution, the cycling stability of regenerated LMO was fully recovered to 88% capacity retention after 100 cycles, which was slightly improved even compared with the pristine LMO. Interestingly, both LMO samples obtained in 0.02M and 0.2M LiOH showed slightly lower initial capacity compared with the sample regenerated in 0.1M LiOH solution. That can be ascribed to the remaining Li deficiencies in 0.02M HT LMO and phase impurity in 0.2M HT LMO samples, which is consistent with the structure information described earlier.

In addition, compared with cycled LMO and LMO regenerated in 0.1M of LiOH, the sharp peak indicates that the well-defined spinel structure with remarkable electrochemistry activity and high crystallinity was obtained by 0.1M HT treatment. Two distinguished plateaus in the charge/discharge curves at 1^{st}, 10^{th}, 50^{th} and 100^{th} cycles are shown in **Figure 2-16c**, corresponding to two sharp peaks in differential capacity plots (**Figure 2-16a**), indicating the good cycling and crystalline stability[72]. The rate performance of the pristine, cycled and regenerated LMO cathodes materials is shown in **Figure 2-16d.** The 0.1M HT LMO showed an improved capacity at high rates compared with pristine LMO particles. For example, the 0.1M HT LMO electrode delivered a specific capacity of, 95, 84 and 65 mAh/g at 1, 2, and 5C(1C = 1.48 mAh/cm^2) respectively, in contrast to 89, 74, and 47 mAh/g for the pristine LMO. It indicates that hydrothermal treatment

can eliminate the lattice defects and enhance the lithium diffusion kinetics inside the cycled and commercial particles[73].

Considering that spent LMO cells may have different SOHs, we also examined our regeneration approach using cells with a much higher degree of degradation. For example, a cell with 60% of capacity fading was obtained by cycling in a voltage range of 3.0-4.3V for 500 cycles. Using the same regeneration protocol developed above, LMO cathode with Li deficiency of up to 40% was fully recovered to the desired stoichiometry, which was supported by the compositions of cycled and regenerated LMO particles as shown in **Table 2-11**. In addition, the undesired Li deficient phases were also converted back to the original spinel phase with the efficient relithiation process. Similar to the other samples, the electrochemical performance was also resumed to the same level of pristine LMO cathodes (**Figure 2-17**). The successful demonstration of direct regeneration of heavily degraded LMO cathode strongly suggests that our developed method can be applied to different cases of spent LMO cells.

Table 2-11 Composition of heavily decayed and regenerated LMO particles.

Sample	**Composition**
Cycled LMO	$Li_{0.641}Mn_{1.929}O_{3.944}$
Pristine LMO	$Li_{1.058}Mn_{1.951}O_{3.936}$
0.1M LMO HT	$Li_{1.050}Mn_{1.942}O_{3.945}$

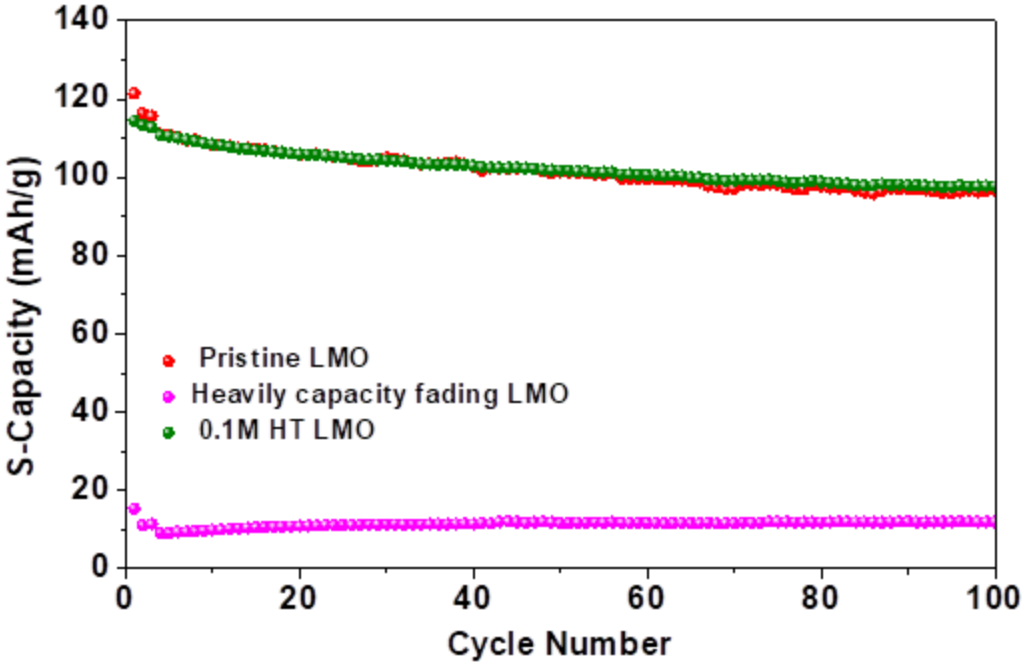

Figure 2-17 Cycling performance of pristine, heavily decayed (60% original capacity loss) and regenerated LMO samples at 0.5C. The regeneration was conducted by hydrothermal treatment at 180 °C in 0.1M LiOH solution for 12h.

Compared with traditional pyrometallurgical recycling and hydrometallurgical recycling, our direct regeneration method for closed-loop LMO recycling shows potential economic and environmental benefits, which were analyzed by the EverBatt model developed by Argonne National Laboratory[50] (see detailed methods in Supporting Information).

In this model, by assuming 10,000 tons of spent LMO batteries annual processing capacity, the life-cycle analysis of the three different recycling methods was performed in terms of energy consumption, greenhouse gas (GHG) emission, operation cost and overall profit. The flow chart for each recycling process was mentioned in **Figure 2-2-4**. In the pyrometallurgical process, the high-temperature smelting process not only consumes a large amount of energy but also generates exhaust gas. The following gas treatment process is necessary but expensive[6, 74]. In the hydrometallurgical process, most of the energy use comes from the upstream production of the

strong acid/base/ consumed for leaching and precipitation treatment. **Figure 2-18a** shows that a total energy consumption of 18.5 and 30.7 MJ per kg of spent cells is required in pyrometallurgical and hydrometallurgical process, respectively. By comparison, the total energy consumption for direct recycling is only 4.1 MJ per kg of spent cells. Consistently, high GHG emission values generated from burning fuels in both pyro- and hydrometallurgical processes (**Figure 2-18b**). In comparison, our direct regeneration process only accounts for around 20% of the GHG emission caused in the two traditional methods.

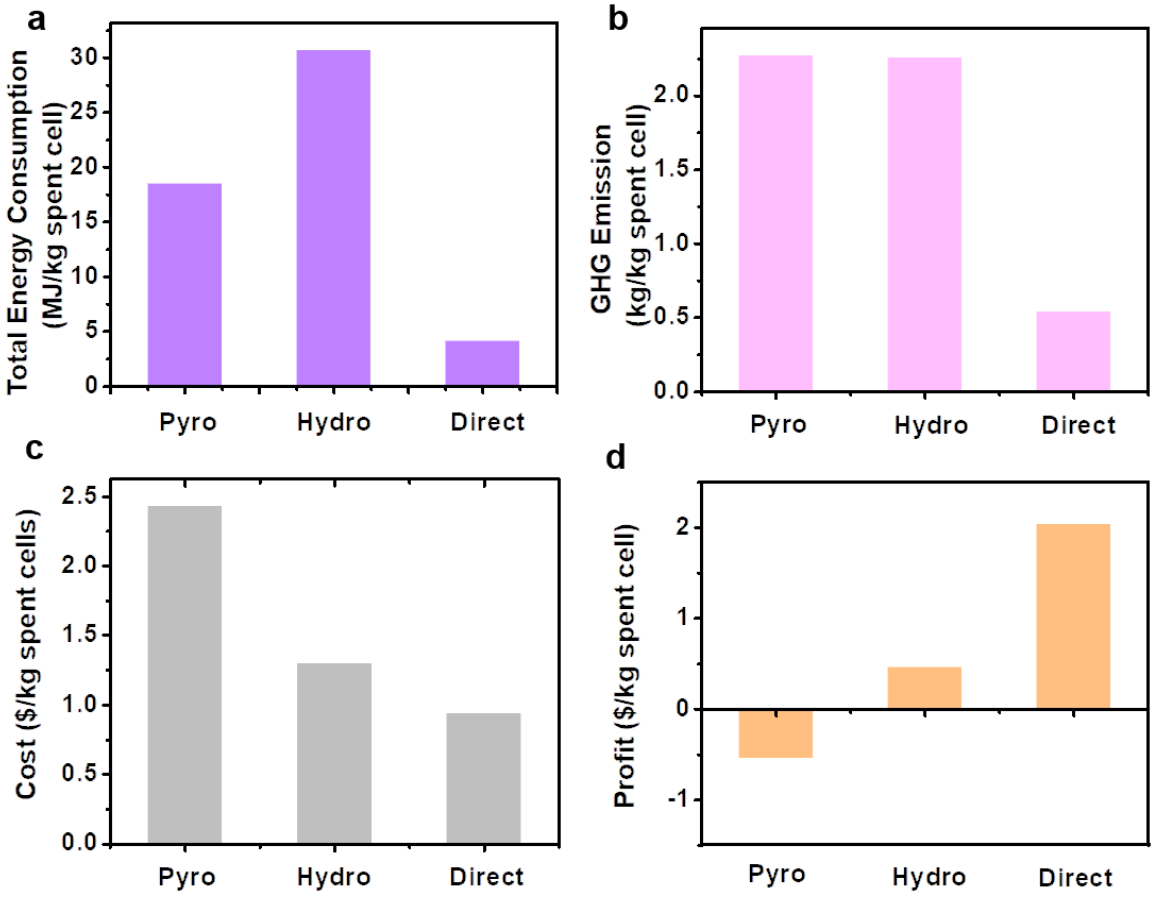

Figure 2-18 Life-cycle analysis based on EverBatt model. (a) Total energy consumption and (b) GHG emissions per kg of recycled cells from pyrometallurgical, hydrometallurgical and direct recycling, respectively. (c) Recycling cost and (d) profit per kg of spent LMO batteries obtained from pyrometallurgical, hydrometallurgical and direct recycling, respectively.

The cost and profit were also modeled and the results are compared in **Figure 2-18c and d**. Compared with LCO and NCM cathodes, LMO has not been recycled on an industrial scale due to the low profit (or even economic loss)[75]. The total cost of pyrometallurgical, hydrometallurgical, and direct recycling of LMO batteries was estimated to be $2.43, $1.3 and $0.94 per kg of spent battery cells processed, respectively. It is worth to be mentioned that the only hydrometallurgical method collecting manganese as manganese sulfate and manganese dioxide, while high-quality LMO cathode powder is obtained in the direct regeneration method. Since the current market value of LMO ($7.00/kg) is much higher than that of Mn in product ($1.43/kg), an economic benefit with a potential profit of $2.03 per kg of spent cells can be obtained in the direct recycling process. In comparison, the expected profit in pyrometallurgical method is calculated negatively. As the result of the significant reductions in total energy use, GHG emissions and processing cost, as well as the potential increase of overall profit, the non-destructive, one-step aqueous direct regeneration method may be a preferable option for closed-loop LIB recycling. While the EverBatt model might have oversimplified the actual processing steps in the LIB recycling, we believe the side-by-side comparison among the three recycling approaches can provide valuable guidance to select and improve the next-generation LIB recycling strategies.

2.2.3 Conclusion

In summary, we have successfully demonstrated complete regeneration of degraded LMO cathodes with different SOHs using a simple direct recycling approach. Particularly, the perfect reconstruction of desired stoichiometry and phase purity enabled by the one-step hydrothermal treatment in dilute Li-containing solutions provides the regenerated LMO particles with high capacity, long cycling stability and high rate performance, on par with commercial pristine LMO materials. The understanding on the mechanism of the hydrothermal relithiation process provides

a potential solution for sustainable and closed-loop re-manufacturing of energy materials. The life-cycle analysis further suggests that our work represents a simple yet efficient approach to re-functionalize high-performance LMO cathodes, with distinct environmental and economic advantages over traditional pyrometallurgical and hydrometallurgical methods. Continuous improvement of the direct recycling method towards automated electrode separation and process intensification will pave the way for its practical application.

2.2.4 Acknowledgements

Chapter 2, in full, is a reprint of the material "Efficient Direct Recycling of Degraded $LiMn_2O_4$ Cathodes by One-Step Hydrothermal Relithiation" as it appears in ACS applied materials & interfaces Hongpeng Gao, Qizhang Yan, Panpan Xu, Haodong Liu, Mingqian Li, Ping Liu, Jian Luo, Zheng Chen, 2020. The dissertation author was the primary investigator and author of this paper.

Chapter 3 Understanding and Controlling Structural Defects and Disordering in Spinel Cathode for Direct Recycling

3.1 Introduction

The widespread adoption of electric vehicles (EVs) using lithium-ion batteries (LIBs) is a vital step in moving towards a sustainable energy and carbon neutrality future[76]. There is a growing demand for high power and energy densities in LIBs to increase the driving range of EVs[77]. As the most valuable part, the cathode material constitutes more than 40% of both cost and weight ratios when considering all components in LIBs [5]. Current efforts in both research and commercialization related to cathode materials primarily center on three categories: lithium metal oxides with a layered structure, such as lithium nickel cobalt manganese oxide ($LiNi_xCo_yMn_zO_2$, where $x + y + z = 1$, referred to as NCM), lithium iron phosphate ($LiFePO_4$, known as LFP) with an olivine structure, and lithium manganese oxides ($LiMn_2O_4$, LMO) with a spinel structure[78]. Layered lithium metal oxides offer high energy densities, but their widespread causes concern with expensive and environmentally harmful cobalt elements, especially when considering the broader adoption of electric vehicles[79]. Cobalt-free cathodes, such as LFP and LMO, provide relatively lower energy density (< 500 Wh/kg at the material level), which might fall short of the requirements for long-range electric vehicles[80]. Cobalt-free, lithium- and manganese-rich layered oxide materials have also garnered significant attention due to their impressive energy density, but there remain challenges related to their limited phase reversibility during cycling, primarily due to issues originating from stoichiometric oxygen loss[81].

$LiNi_{0.5}Mn_{1.5}O_4$ (LNMO), a derivative from LMO through nickel substitution, presents an appealing substitute. Ni substitution enhances the operating voltage of the parent LMO cathode from 4V to ~4.8V (vs. Li/Li^+) consequently increasing theoretical energy density from 480 to 620 Wh/Kg, leveling with the NCM cathodes[82]. Nonetheless, the LNMO still encounters some

obstacles, such as inferior electronic conductivity[83], fast capacity degradation[84] and issues with the current carbonate electrolyte system stemming from its high operating voltage[85]. Though there is a deep history in literature on efforts to mitigate the Jahn-Teller distortion and disproportion reaction of Mn^{3+}, avoiding such complex cross-talking phenomenon remains an immense challenge[86, 87]. One effective approach is the control of Mn^{3+} content to safeguard the surface against deteriorating acidic reactions from liquid electrolytes[88]. Thus far, researchers have primarily concentrated on modifying the surface through techniques such as elemental doping, interfacial adjustments[89], and electrolyte engineering[90] to improve the aforementioned drawbacks thereby improving the cycling stability and rate performance. On the other hand, by understanding LNMO degradation mechanisms, defect engineering can be applied to regulate Mn^{3+} content and enhance the electrochemical performance [91].

Despite decades of research that have unveiled the degradation mechanism of LNMO cathodes, there has been limited investigation into the healing or repairing of these cathodes. As a cobalt-free, low-cost cathode, traditional hydrometallurgical and pyrometallurgical processes, characterized by intensive energy consumption, chemical cost and waste generation, are not suitable for remunerative LNMO recycling[92]. The emerging direct recycling technology, started with a relithiation step to produce rejuvenated cathode active materials, has gained increasing attention due to its minimal energy consumption and maximum profitability when recycling materials like NCM[93, 94], LFP[55], LMO[95], and $LiNi_{0.88}Co_{0.095}Al_{0.025}O_2$ (NCA)[96]. Among various relithiation methods (such as solid-sintering[97], molten salt[98], ionothermal[30], and redox mediation[99]), hydrothermal treatment[94] stands out as the most versatile process, demonstrating self-saturation in various structures (spinel[95], olivine[100], and layered structure[101]). With its high effectiveness, low

cost and potential scalability, hydrothermal relithiation treatment is a suitable approach for investigating the rejuvenation mechanism of LNMO.

Understanding the structural evolution of spinel-type cathodes through the direct recycling process is crucial for advancing next-generation battery recycling. As cathode materials undergo resynthesis and experience regrowth of grains during the recycling process, the introduction of cation disordering, anti-sites, and dislocations gives rise to distinctive electrochemical properties. Previous studies have demonstrated that the elaboration of defects can bring about a transformative effect on the performance of spinel-type cathodes[102]. Consequently, identification of a systematic structural repairing mechanism for such cathodes becomes imperative for comprehending the electrochemical properties related to its structure and fully revitalizing its performance. Despite the existence of various strategies for recycling optimization, many phenomena associated with cathode direct recycling still await complete discovery and resolution.

Herein, we provide a thorough analysis of the healing mechanism of spent LNMO cathodes, encompassing relithiation and structure reconstruction. We present clear evidence of Li/Mn disordering layers induced during an aqueous relithiation process, resulting in significant capacity loss and insufficient reversible capacity. To address these issues, we systematically rectify these failures through careful design of post-annealing conditions. By introducing abundant twin boundaries and preferred grain orientations in spinel lattice structures, we successfully rejuvenate the electrochemical activity of degraded LNMO cathodes. Notably, the resulting regenerated LNMO demonstrates a significant enhancement in its rate performance without sacrificing energy density, retaining 97.4% capacity after 100 cycles at C/3, comparable to the pristine LNMO. This effective direct recycling method, employing defect engineering, not only reveals the healing

mechanism in spinel structures but also provides insights for designing synthetic strategies of next-generation sustainable LIBs.

3.2 Understanding and Controlling Structural Defects and Disordering in $LiNi_{0.5}Mn_{1.5}O_4$

3.2.1 Experimental

3.2.1.1 Materials

The pristine LNMO particle were obtained from Haldor Topsoe corporation, Denmark. The spent LNMO cathode were harvested from multilayer LNMO/Graphite pouch cell (>3Ah) cycled between 2.8-4.8V at 0.33 C for more than 350 cycles. The standards for TEM-EELS, Mn_2O_3 and MnO_2 were purchased from Sigma-Aldrich.

3.2.1.2 Cathode harvesting

All the pouch cells were discharged to 2.8V before disassembly. The cathode strips were harvested by thoroughly rinsing with dimethyl carbonate (DMC) and then soaked in NMP for 6h under 50 °C. The active materials, binder and carbon black were removed from the aluminum substrates by sonification and scrapping. Active materials were precipitated after centrifuging at 3500 rpm for 5 min. The precipitated active materials were then repeatedly washed several times in NMP by dispersion and centrifugation. Then the active materials were collected and dried under vacuum at 80 °C overnight for regeneration.

3.2.1.3 Regeneration of cathode materials

The collected S-LNMO particles underwent relithiation via a hydrothermal treatment. Specifically, 0.25g of S-LNMO was placed into a 100 ml Teflon-lined autoclave containing 80 ml of lithium hydroxide (LiOH) solution at various concentrations. The autoclaves were heated at

180°C for 6 hours. After naturally cooling to room temperature, the treated powders were washed at least five times with deionized water until the pH was approximately 7, then dried under vacuum at 80°C overnight. The samples treated in 0.1M, 1M, and 4M LiOH solutions are referred to as "L-LNMO-1," "L-LNMO-2," and "L-LNMO-3," respectively.

Based on ICP measurements, L-LNMO-2, with the correct stoichiometry, was selected for further treatment. L-LNMO was then annealed at different temperatures for 4 hours, with a ramping rate of 5°C/min under a 1 L/min oxygen flow. The annealed samples at 650°C, 750°C, 850°C, and 950°C are labeled as 'R-LNMO-1', 'R-LNMO-2', 'R-LNMO-3', and 'R-LNMO-4,' respectively. Among these, R-LNMO-3 exhibited the best electrochemical performance under optimal regeneration conditions.

3.2.1.3 Materials characterization

The chemical composition of LNMO powders was evaluated by inductively coupled plasma mass spectrometry (ICP–MS, Thermo Scientific, iCAP RQ model). Their crystal structures were examined by X-ray powder diffraction (XRD) employing a Bruker D2 Phaser (Cu Kα radiation, λ=1.5406 Å). The morphology of the LNMO powders was observed by FEI Apreo LoVac scanning electron microscope (SEM) with X-Max 80 EDS detector.

Time-of-flight (TOF) powder neutron diffraction was measured at the VULCAN instrument at the Spallation Neutron Sources (SNS), Oak Ridge National Laboratory (ORNL). The diffraction pattern was measured at the detector banks at $2\theta = \pm 90°$, equipped with 5 mm receiving collimators. Neutron powder diffraction patterns were collected in the high-intensity mode ($\Delta d/d \sim 0.45\%$) for a duration of 2 h under the nominal 1.4 MW SNS operation and then processed using VDRIVE software. Rietveld refinement against the neutron diffraction was performed using General Structure Analysis System (GSAS) software with the EXPGUI interface.

X-ray photoelectron spectroscopic (XPS) measurement was conducted with an AXIS Supra by Kratos Analytical with an Al Ka anode source working at 15 kV and 10-8 Torr chamber pressure. The spectra data were processed by CasaXPS software. All spectra were calibrated with the hydrocarbon C 1s peak at 284.6 eV. Aberration corrected scanning transmission electron microscopy (AC-STEM) was conducted using a JEOL JEM-ARM 300F at 300 kV.

TEM-EELS characterizations were performed using a ThermoFisher Talos 200X TEM electron microscope system operating at an accelerating voltage of 200 kV. The system was equipped with a Schottky X-ray FEG field emission electron gun, a Gatan Continuum (1069) EELS spectrometer, a STEM model, 4 in-column SDD Super-X detectors, and a Ceta camera. Additionally, the TALOS microscope was outfitted with a high-resolution Gatan imaging filter (Gatan Continuum 1069) for EELS mapping, with a probe current of approximately 140 pA for EELS maps.

Soft X-ray absorption spectroscopy (soft XAS) was performed at Beamline 8-2 of the Stanford Synchrotron Radiation Lightsource (SSRL). Data acquisition occurred under ultrahigh vacuum conditions (10^{-9} Torr) at room temperature, with an energy resolution of approximately 0.2 eV and a beam spot size of about 1 mm². Samples were mounted on an aluminum sample holder inside an argon-filled glovebox and securely sealed during transfer. The soft XAS data were analyzed using Pymca, normalized to a range of [0,1].

Spectroscopic transmission X-ray microscopy (TXM) was performed at the 6-2c beamline at the Stanford Synchrotron Radiation Light source (SSRL). 8.95 keV X-rays were utilized to characterize the particle morphology. The LNMO particles were placed in a quartz tube and sealed with epoxy in an Ar-filled glovebox. The tomography data were taken over an angular range of 180°. The field of view of each tile was 16 μm, consisting of 1024 × 1024 pixels, with a pixel size

of 28.7 nm. The images were then processed in the TXM-Wizard software suite, with reference correction, energy average, image alignment, and 2D X-ray Absorption Near-Edge Structure (2D XANES) analysis. The edge energy maps saved by TXM-Wizard were exported into 64-bit .raw files using MATLAB for visualization.

The cross-section microstructures of LNMO particles were characterized by a Helios G4 PFIB UXe DualBeam plasma focused ion beam / scanning electron microscope (P-FIB / SEM) with a xenon source and electron backscatter diffraction (EBSD) detector. Sample milling was conducted at 30 kV with a 2.5 µA current. Afterwards, a lower current (500 and 60 nA) was used to polish the cross-section. Electron imaging was conducted at 5 kV and 4 nA beam conditions.

3.2.1.4 Electrochemical testing

The electrochemical performance was evaluated by fabricating CR2032 half coin-cells assembled in an Ar-filled glovebox kept at <0.1 ppm O_2 and <0.1 ppm H_2O. The cathode electrode was prepared by casting the slurry composed of cathode powder, conductive agent (Super P65) and polyvinylidene fluoride (PVDF) with a mass ratio of 8:1:1 in N-methyl-2-pyrrolidone (NMP) solvent on an Al foil. After drying at 120 ^{o}C for 12 h in a vacuum oven, it was punched and calendared. Coin cells were then made inside that glovebox with the prepared cathode (mass loading of ~ 4.5 mg), Li metal as the anode, and LP57 (1.2M LiPF6 in EC/EMC=3:7) as the electrolyte. Galvanostatic charge-discharge was carried out using a Neware battery testing system in the potential range of 3.0-4.85 V at different rates for certain cycles after C/10 in the first 3 activation cycles. EIS tests of LNMO/Li coin cell with different SOCs were performed on a Biologic VSP-300 potentiostat with a 10 mV perturbation in the frequency range of 1 MHz to 100 mHz. The fitting of the EIS data has been conducted via Z-view software. DRT was analyzed via MATLAB based DRT calculation code developed by T.H. Wan et al[103]. The direct current internal resistance (DCIR) experiment was performed by charging and discharging the cell at

constant current (0.1 C-rate) to different state-of-charge (SOC) (20%, 40%, 60% and 80%) after 2 formation cycles. Thereafter, the process of applying a pulse current charge for 30 s, rest for 10 min, pulse current discharge for 30 s, and rest for 10 min was repeated. The pulse current was applied in the following order: 0.5 C-, 1 C-, and 2 C-rate. Three cells were tested in parallel to account for variability and to generate the error bars. All the C-rates for the electrochemical tests were based on the practical capacity of 135mAh /g.

3.2.2 Results and discussions

Compositional and structural restoration of the spent LNMO cathodes

Defect engineering has shown effectiveness in tuning the electrochemical performance of spinel cathodes by regulating the oxygen deficiency[104-106], transition metal ordering[107, 108] and crystallographic properties[109, 110]. Additionally, the mechanism of compositional repairment in spent LMO cathodes has been well elucidated in our previous work.[95] In this work, we successfully rejuvenated the spent LNMO cathode with abundant defects by hydrothermal treatment and optimized annealing conditions. The structural evolution of the LNMO cathodes is illustrated in **Figure 3-1**. Briefly, the spent LNMO cathodes (named as "S-LNMO") are harvested from multilayer LNMO/graphite pouch cell (>3Ah) by the method reported in our previous work[111]. The obtained spent cathode particles with both compositional and structure degradation are subjected to hydrothermal treatment (denoted as "L-LNMO") under different conditions for relithiation purpose. Following a short annealing process at optimized temperature, the regenerated LNMO particles (denoted as "R-LNMO") are obtained, featuring a presence of twinning defects with substantial enhancement of Li^+ diffusion.

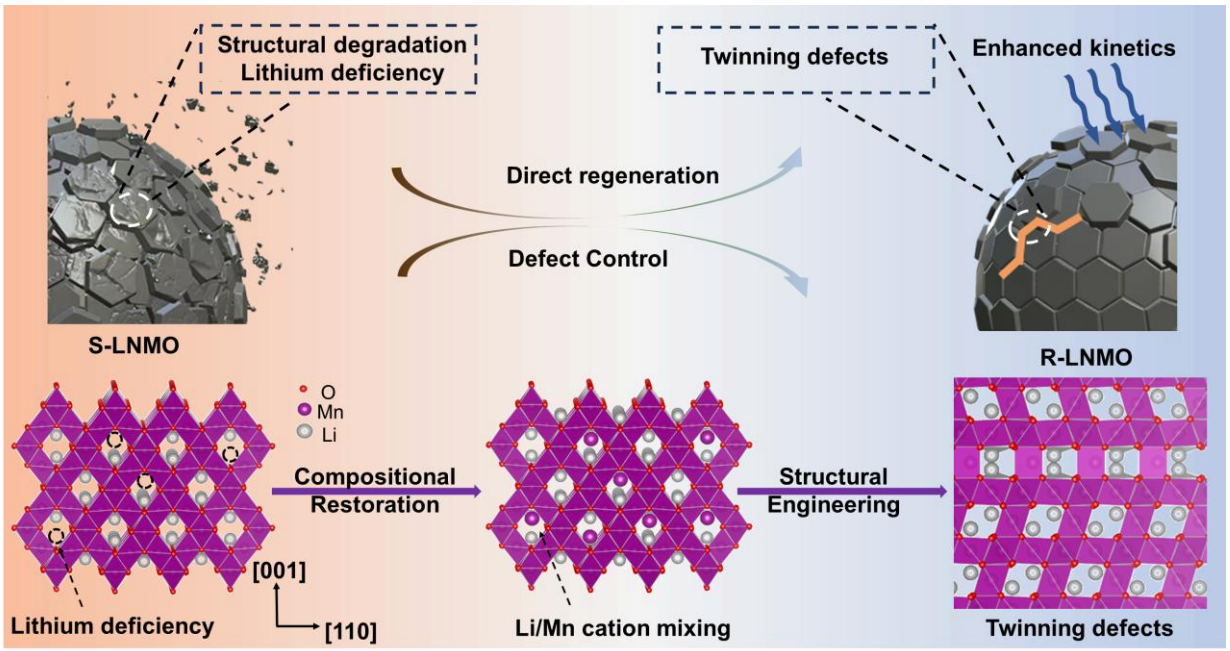

Figure 3-1 Schematic illustration of the direct regeneration of LNMO cathodes with defect control.

A hydrothermal treatment in LiOH solution is applied to spent LNMO particles to compensate for the lithium loss in spent LNMO powders. Following an optimal short annealing step, the regenerated LNMO particles are obtained with induced defects, e.g., twin boundaries and preferred lattice orientation, resulting distinctive Li+ diffusion kinetics.

The lithiation mechanism for restoring the composition of the spent LNMO was elucidated by inductively coupled plasma quadrupole mass spectrometry (ICP-MS) measurements of S-LNMO and samples subjected to lithiation treatment with varying concentrations of LiOH (**Figure 3-2**). Note that the 30% lithium deficiency was observed after 300 cycles in a voltage range of 2.8-4.8 V at 0.33C in the multilayer LNMO/graphite pouch cells **(Figure 3-3)**. An ideal composition ($Li_{1.020}Ni_{0.460}Mn_{1.540}O_4$) can be achieved, which is comparable to the pristine level ($Li_{1.001}Ni_{0.453}Mn_{1.524}O_4$) by optimized re-lithiation kinetic control in hydrothermal treatment with 1M LiOH solution (**Table 3-1**). After the short-term annealing step under designed temperature, the R-LNMO has no significant variation in terms of composition compared with that in L-LNMO.

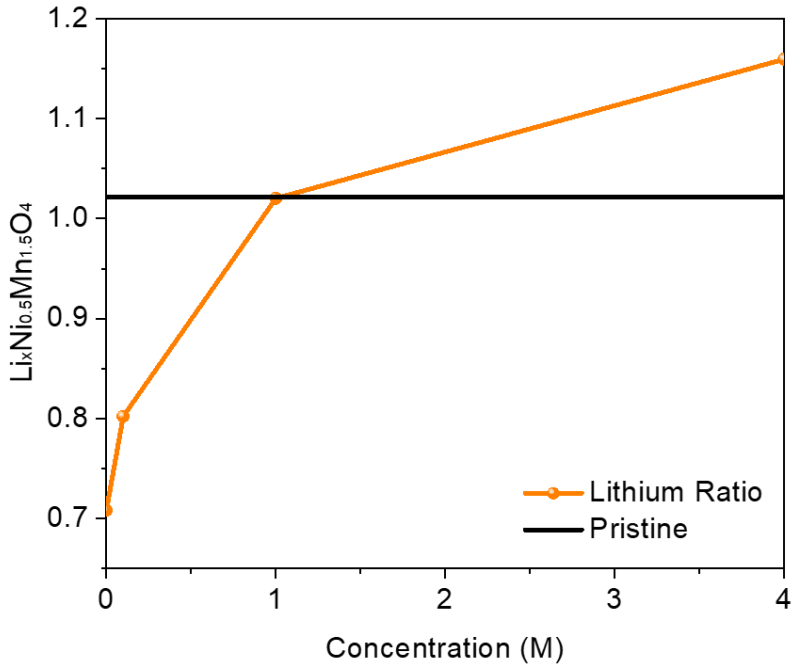

Figure 3-2 The compositional evolution of the S-LNMO particles during the relithiation process. The ICP results of L-LNMO particles collected from hydrothermal treatment in various concentration of LiOH solution.

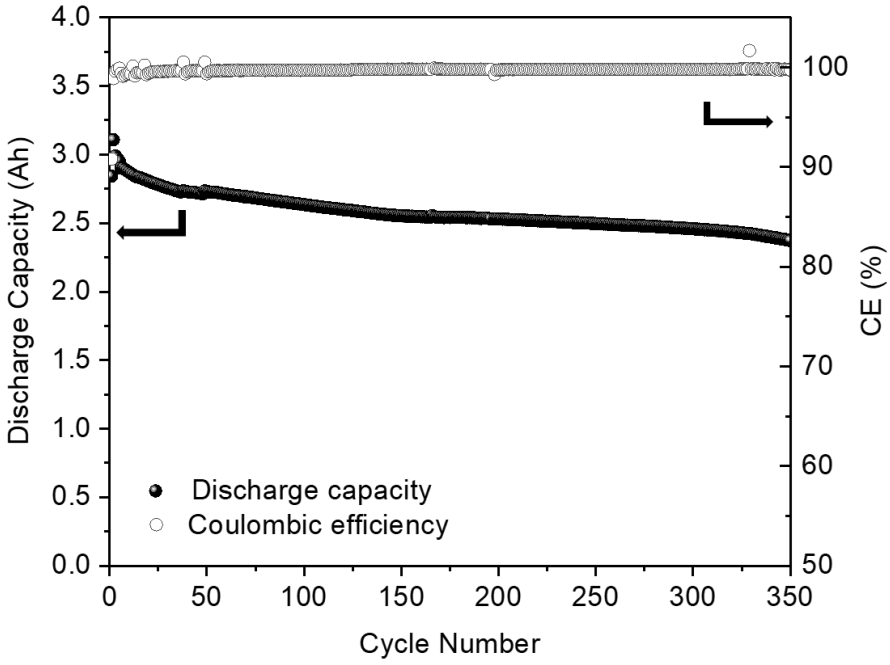

Figure 3-3 The electrochemical performance of spent LNMO cells. Cycling performance of multilayer LNMO pouch cells for recycling.

Table 3-1 Compositional analysis of LNMO particles of interest. ICP results of P-LNMO, S-LNMO, L-LNMO and R-LNMO.

Sample	**Li**	**Ni**	**Mn**
P-LNMO	1.001	0.453	1.524
S-LNMO	0.705	0.460	1.540
L-LNMO	1.008	0.477	1.524
R-LNMO	1.002	0.460	1.540

Scanning electron microscope (SEM) images have been examined to demonstrate the efficacy of our regeneration method. **Figure 3-4a-c** and **Figure 3-5** display the of S-LNMO, L-LNMO, R-LNMO and P-LNMO under optimized conditions. These images reveal that the S-LNMO particles did experience some cracking issue during extended cycling. Following an effective regeneration process, the morphology of R-LNMO was successfully restored to its pristine level. This suggests a resolution of the cracking problem by crystal regrowth during the annealing process. From the neutron diffraction patterns (**Figure 3-4d-f** and **Figure 6)**, the peak positions in all samples are well matched with the standard pattern of a $Fd\bar{3}m$ space group[112]. Additionally, Rietveld refinement was carried out on all neutron diffraction patterns using the GSAS software with EXPGUI as the graphical user interface (**Table 3-2**). The unit cell lattice parameter in S-LNMO decreases from 8.179 Å to 8.147 Å (compared to P-LNMO), due to a 30% loss of lithium. This shrinkage indicates a low packing fraction caused by the reduced number of atoms and the sizes difference of cations (Ni^{2+} = 69 pm, Ni^{3+}= 53 pm, and Ni^{4+} = 48 pm)[113, 114]. After the lithiation process, an enlarged lattice parameter has been observed, despite the sample having a similar stoichiometry to the pristine material, suggesting the presence of Li/transition metal (Li/TM) disordering which contributes to the loose packing of the unit cell. The hydrothermally treated sample exhibits significant Li/TM mixing in 8a sites (2.89%) compared to

P-LNMO (0.56%). In contrast, R-LNMO achieves lattice parameter shrinkage through a short annealing step. This process facilitates cation diffusion and heals oxygen deficiencies, especially at high temperatures in a pure oxygen atmosphere[107, 115].

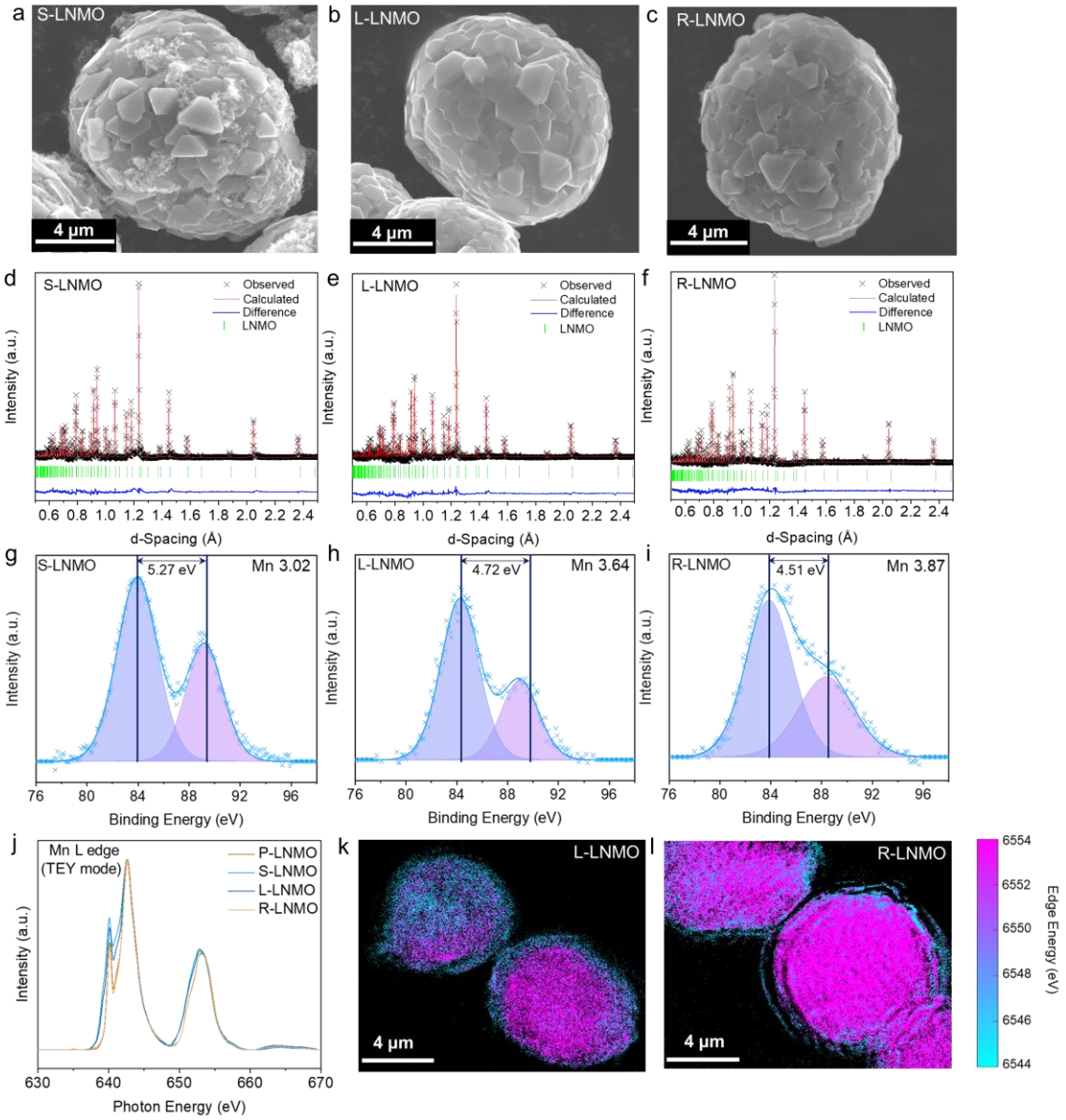

Figure 3-4 The phase identification and structural dynamics during the regeneration process. The SEM images of (a) S-LNMO, (b) L-LNMO and (c) R-LNMO. The Rietveld refinement neutron diffraction patterns of (d) S-LNMO, (e) L-LNMO and (f) R-LNMO. The Mn 3s XPS spectra of (g) S-LNMO, (h) L-LNMO and (i) R-LNMO. (j) Mn L-edge soft XAS spectra of the LNMO particles of interest. The 2D XANES mapping images of Mn in (k) L-LNMO and (l) R-LNMO.

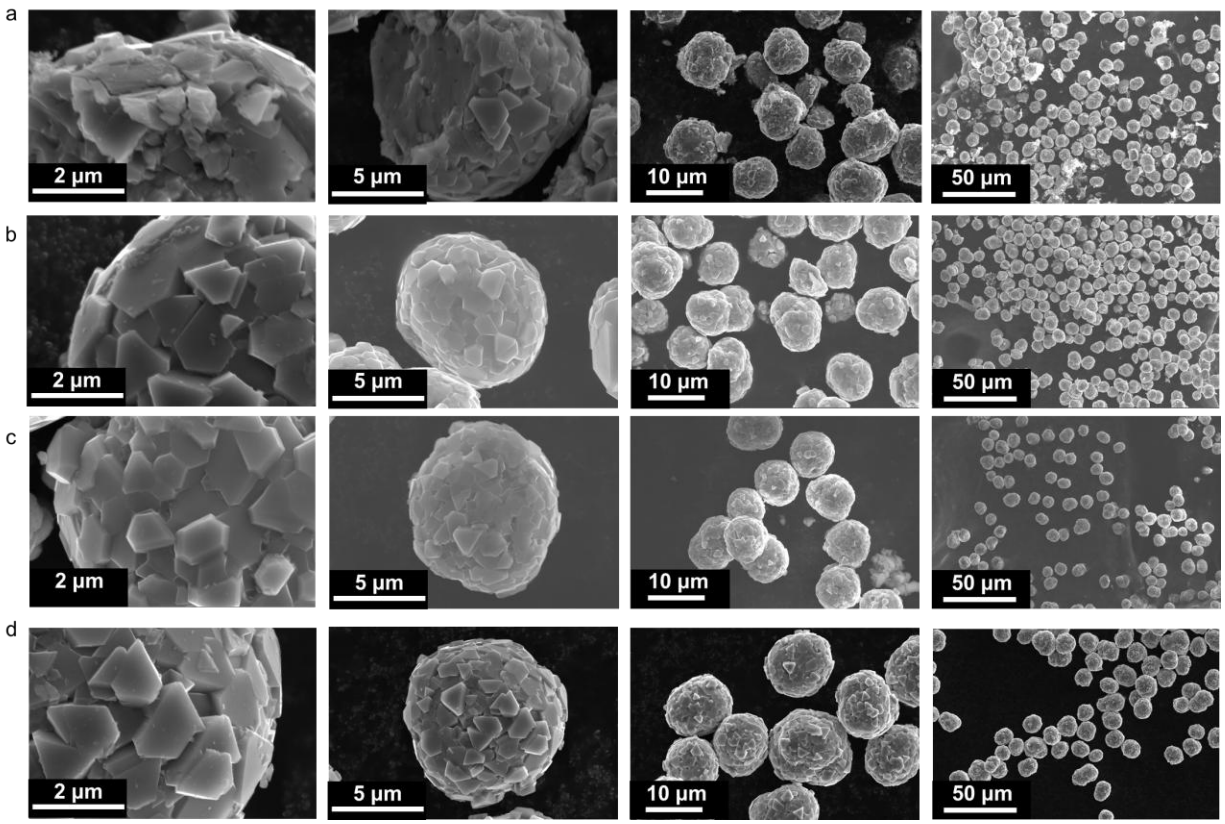

Figure 3-5 The morphology of the LNMO particles of interest. The SEM images of (a) S-LNMO, (b) L-LNMO, (c) R-LNMO and (d) P-LNMO.

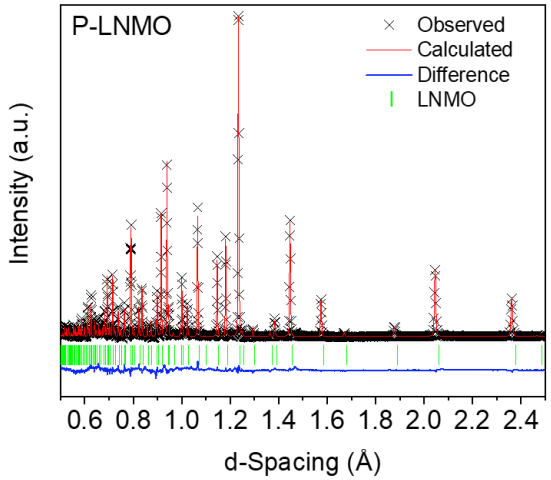

Figure 3-6 The bulk structure analysis of LNMO particles of interest. The Rietveld refinement neutron diffraction pattern of pristine LNMO.

Table 3-2 Investigation of Li/Mn disordering in LNMO particles of interest. The Rietveld refinement results of neutron diffraction in P-LNMO, S-LNMO, L-LNMO and R-LNMO.

Sample	Lattice Parameter/ Å	8a occupancy (Li: Mn)	wR_p/%	R_p/%
P-LNMO	8.1793	0.56	4.17	3.10
S-LNMO	8.1470	1.53	3.21	2.33
L-LNMO	8.1872	2.89	4.76	3.55
R-LNMO	8.1710	0.47	3.58	2.79

X-ray photoelectron spectroscopy (XPS) was conducted on the treated LNMO particles to verify the valence changes in transition metals. The Mn 3s spectra, as depicted in **Figure 3-4g-i**, were fitted to illustrate the evolution of the average oxidation state (AOS) of Mn. This analysis involved assessing the difference in binding energy between peaks (ΔE) and using the equation[116] AOS = 8.956 − 1.126 ΔE to approximate the average Mn oxidation state. As shown in **Figure 3-7**, a significant amount of Ni^{3+} exists in S-LNMO. Despite ~30% lithium loss in spent materials, the Mn valence in S-LNMO drops from +3.76 to +3.02 due to the high AOS of Ni. The elevated Mn valence is observed following relithiation treatment in LiOH solutions of varying concentrations. The AOS of Mn increased from +3.02 to +3.10, +3.64 and +3.41 after relithiation in 0.1M, 1M and 4M LiOH solutions (referred to as "L-LNMO-1", "L-LNMO-2" and "L-LNMO-3", respectively) (**Figure 3-8**). Although Ni^{3+} remains dominant on the L-LNMO surface after relithiation(**Figure 3-7**), the increase in Mn valence is attributed to repaired oxygen vacancies in the LNMO particles. **Figure 3-9** illustrates a notable growth of a side peak at ~531 eV, reflecting the mitigation of oxygen defects after relithiation treatment[104]. Additionally, these oxygen vacancies are reduced to pristine levels following the annealing step under oxygen flow. As indicated by a reduction of Mn valence in L-LNMO-3, the spinel structure became unstable,

entering an overlithiated status during hydrothermal treatment with LiOH concentrations exceeding 1M. The impurity phase can be identified as Li_2MnO_3 based on the XRD pattern of the L-LNMO-3 (**Figure 3-10**), This phenomenon has also been reported in $LiMn_2O_4$ regeneration by hydrothermal reaction[95]. However, followed by a short annealing step, the Mn and Ni valence was successfully restored to the pristine level in R-LNMO. This outcome is corroborated by Raman spectra in **Figure 3-11**, in which two characteristic Ni-O stretching bands at 390 and 491 $cm^{-1}$are detected, representing the E_g and F_{2g}^2 vibrational modes in the spinel structure. Additionally, a Mn-O symmetric stretching vibration is observed at 630 cm^{-1}, confirming the A_{1g} vibration in the MnO_6 octahedra[117]. A small peak at 546 cm^{-1} related to the F_{2g}^1 vibrational mode is observed as well, indicating that the as-prepared LNMO samples can be indexed to the *Fd3m* space group (disordered spinel with high symmetry)[87]. Notably, the overlithiated sample (L-LNMO-3) displays an indistinct F_{2g}^1 peak, suggesting a compromised symmetry in the spinel structure. Furthermore, the L-LNMO samples exhibit a broad A_{1g} peak, indicative of multiple vibration modes in MnO_6 octahedra due to the mixture of Mn valence status. In contrast, R-LNMO demonstrates a significant improvement in the sharpness of the A_{1g} peak. This enhancement underscores the crucial role played by the annealing step in reconstructing the well-defined lattice structure, signifying its importance in reversing the adverse effects caused by the overlithiated status during hydrothermal treatment.

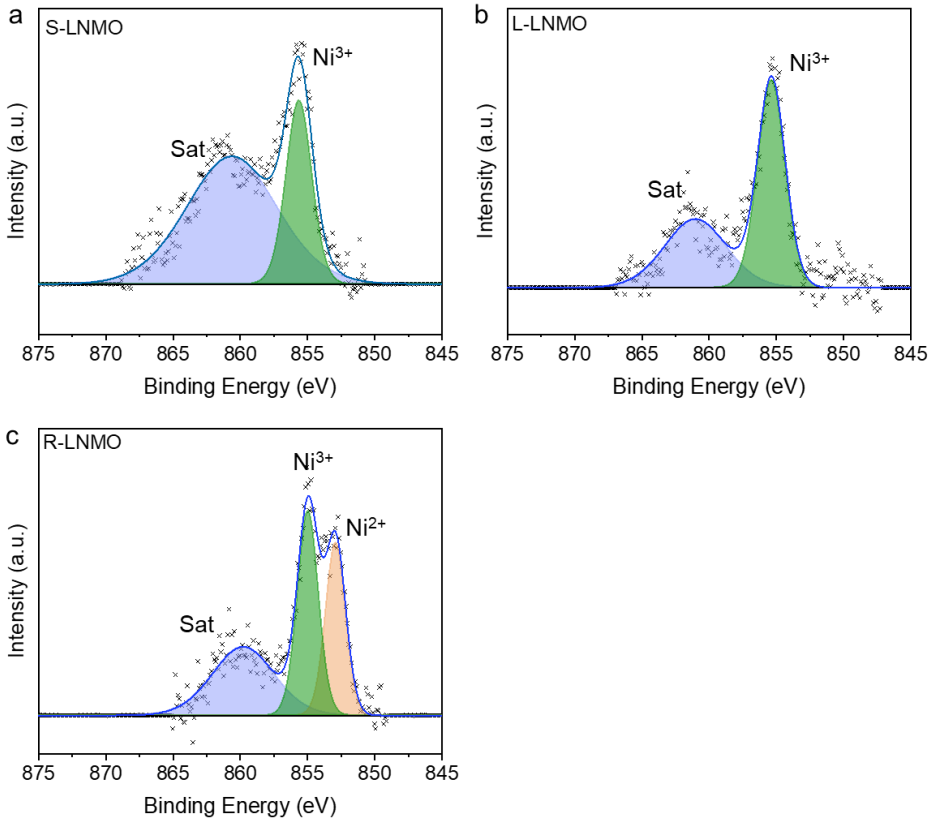

Figure 3-7 The elemental valence analysis of LNMO particles of interest. The Ni $2p_{3/2}$ XPS spectra of (a) S-LNMO, (b) L-LNMO, and (c) R-LNMO.

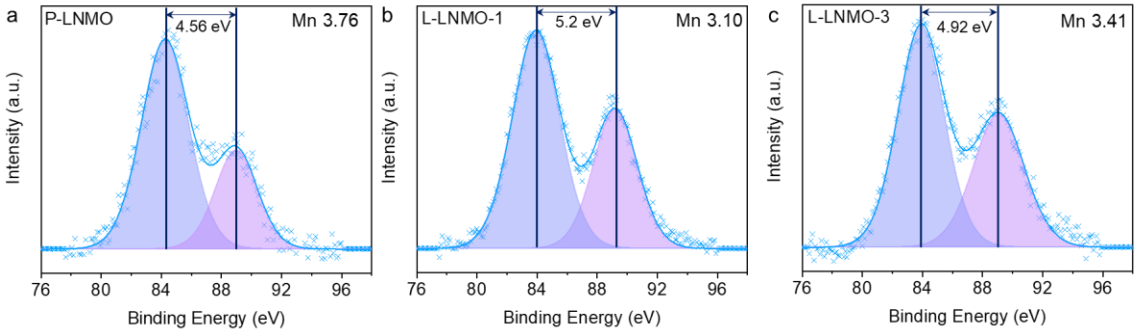

Figure 3-8 The elemental valence analysis of LNMO particles of interest. The Mn 3s XPS spectra of (a) P-LNMO, (b) L-LNMO-1, and (c) L-LNMO-3.

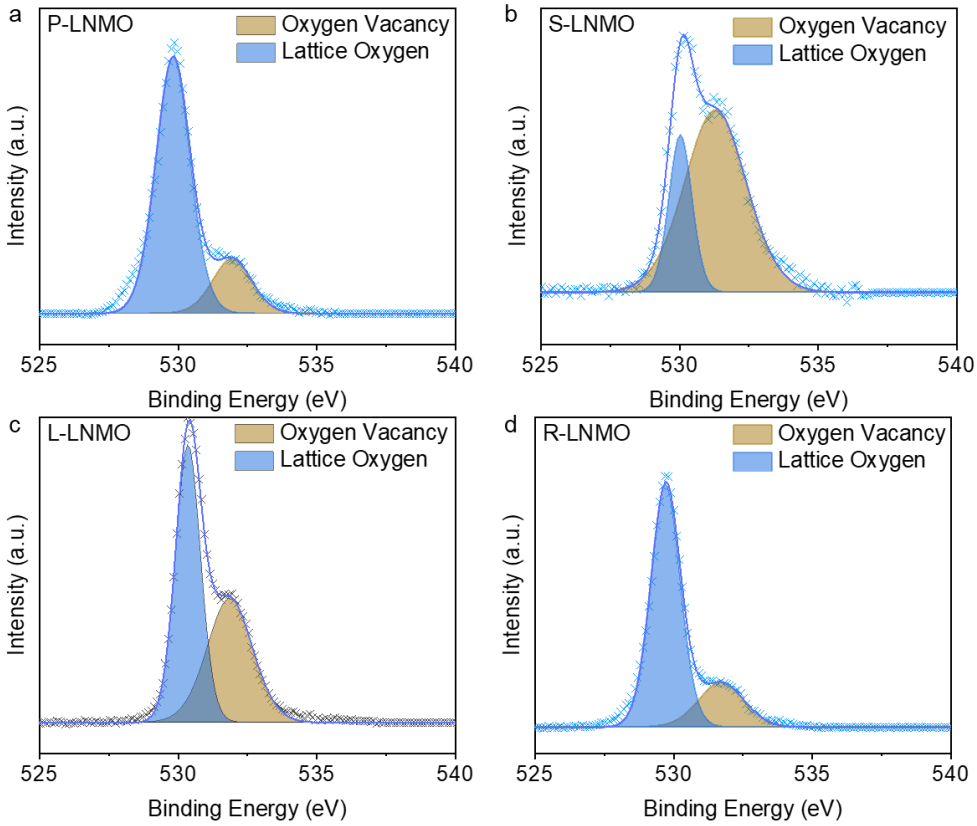

Figure 3-9 The elemental valence analysis of LNMO particles of interest. The O 1s XPS spectra of (a) P-LNMO, (b)S-LNMO, (c) L-LNMO, and (d) R-LNMO.

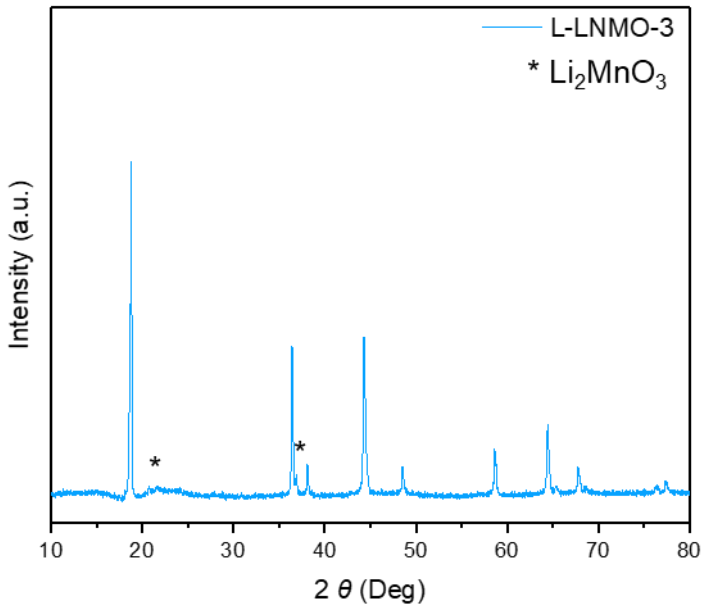

Figure 3-10 The phase determination of the overlithiated LNMO particles. The XRD pattern of the L-LNMO-3.

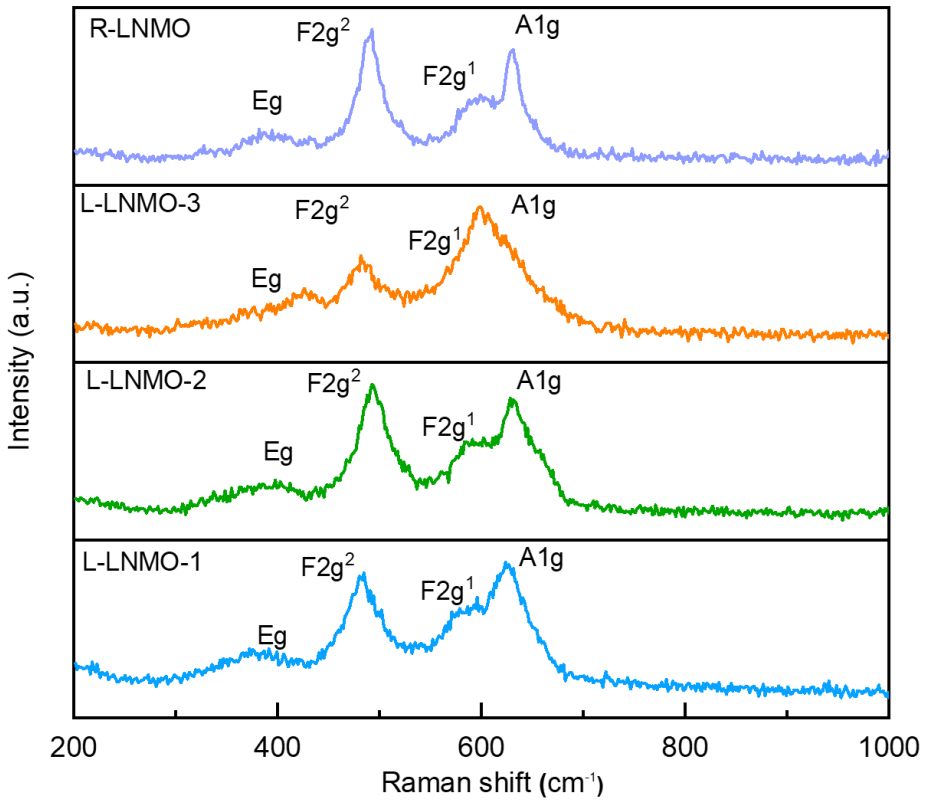

Figure 3-11 The structural analysis and bond information of LNMO particles of interest. Raman spectra of (a) R-LNMO, (b)L-LNMO-1, (c) L-LNMO-2 and (d)L-LNMO-3.

Via soft X-ray absorption spectroscopy (XAS), we compared the surface Mn states of the LNMO particles, delving deeper into the valence distribution of transition metals during the regeneration process. All the LNMO particles exhibit a characteristic of Mn (IV), shown in **Figure. 3-4j**. The presence of side peak around 640 eV indicates the lower valence of Mn at the surface in S-LNMO and L-LNMO[118]. The fluorescence-yield (FY) mode has a probing depth of 50 nm. The comparison of the TEY and FY mode demonstrates the abundance of Mn (III) in L-LNMO, which could be eliminated by following regeneration process (**Figure 3-12**). Furthermore, 2D X-ray Absorption Near-Edge Structure (XANES) mapping with a resolution of 28.7 nm per pixel was conducted to provide a detailed investigation into the edge energy distribution of Mn, revealing elemental restoration. As depicted in **Figure 3-4k**, the 2D XANES mapping shows a lower near-edge energy of Mn near the surface of the L-LNMO particles, confirming previous findings

obtained through surface-sensitive technologies such as XPS and Raman spectroscopy. Following the annealing step, the near-edge energy of Mn shifts to higher energy level with good uniformity (**Figure 3-4l**). Despite the stoichiometric composition obtained through this effective recycling method, a more detailed examination of structure evolution in LNMO particles is necessary to fully understand the influence of defect controlling on performance.

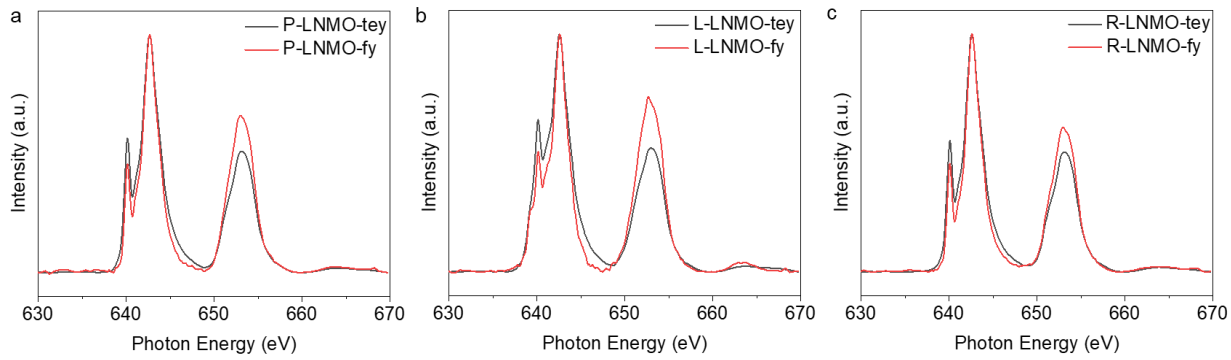

Figure 3-12 Mn L-edge soft XAS spectra of the LNMO particles of interest. Comparison of the Tey and Fy mode of Mn L-edge in P-LNMO, L-LNMO and R-LNMO.

Identification and mitigation of Li/Mn disordering

To comprehend the remaining issue of samples obtained from hydrothermal treatment (without annealing) with the stoichiometric composition, a detailed structural analysis was undertaken through neutron diffraction. As mentioned earlier, this analysis provides insights into atomic occupancy, with Li^+ typically occupying tetrahedral 8a sites and Mn/Ni ions occupying octahedral 16d sites in a typical face-centered cubic $Fd\bar{3}m$ structure. Moreover, the refinement results reveal significant site occupancies of Mn ions at the 8a sites in L-LNMO particles, causing a significant Li/Mn cation mixing (2.89%). In contrast, only 0.56% and 0.47 % Li/Mn mixing are observed in P-LNMO and R-LNMO samples (**Table 3-2**). This substantial Li/Mn cation disordering aligns with the result of structural failure discussed earlier.

The atomic arrangement of L-LNMO particles was examined using high-angle annular dark field scanning transmission electron microscopy (HAADF-STEM) to investigate the presence of Li/Mn disordering on the surface. As STEM images reflect the Z-contrast of materials, **Figure 3-13a** demonstrates a well-defined spinel structure in the bulk area (Region II), with the positions of transition metals (16d sites) resolved atomically along the [110] zone axis. In **Figures 3-13b-c**, a significant reorganization of the atomic arrangement and lattice structure distortion is evident in the surface region (Region I). Additionally, the Fast Fourier Transform (FFT) image in Figures **3-13d-e** displays duplicated bright dots with an ellipse shape (marked by a white circle), indicating lattice distortion and phase impurity in the surface area of L-LNMO. Note that lithium (8a sites) and oxygen (32e sites) are not visible in the Z-contrast STEM image due to their low atomic masses. Upon close observation of the images, the corresponding line profiles illustrate the atomic arrangement intuitively in four selected unit cells near the surface. **Figure 3-13f** reveals a notable intensity at the Li position, indicating the occupancy of the transition metal ion in 8a sites near the surface of L-LNMO, while a well-defined spinel-type lattice is shown in bulk area (**Figure 3-13g**). To eliminate the Li/Mn disordering, an annealing treatment is applied to reconstruct the lattice structure. As shown in **Figure 3-13h**, a uniform feature is revealed in R-LNMO particles from bulk to surface. No lattice distortion or cation disordering exists in enlarged images (**Figure 3-13i-j**). Moreover, the FFT images (**Figure 3-13k-l**) and line profiles (**Figure 3-13m-n**) illustrate the effectiveness of the reconstruction via the annealing step.

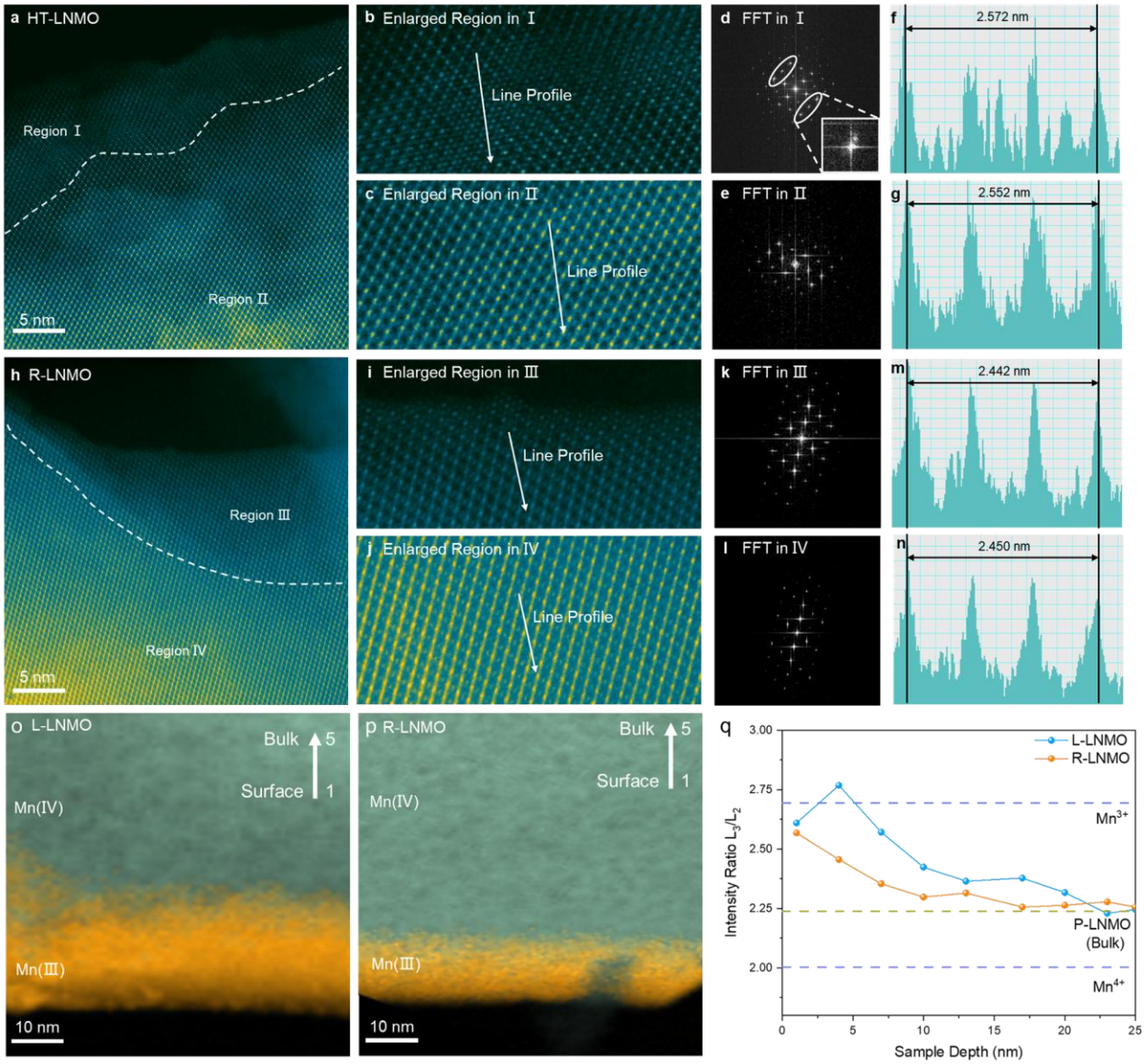

Figure 3-13 The observation of Li/Mn disordering and microstructure change in treated LNMO particles. (a) HRTEM image, (b, c) enlarged figures, (d, e) fast Fourier transform (FFT) images and (f, g) line profiles in b and c of L-LNMO. (h) HRTEM image, (i, j) enlarged figures, (k, l) fast Fourier transform (FFT) images and (m, n) line profiles in i and j of R-LNMO. (o, p) The HAADF-STEM-EELS mapping images and (q) spatially resolved intensity ratio of L3/L2 peak from surface to bulk of L-LNMO and R-LNMO.

A combination of HAADF-STEM and Electron Energy Loss Spectroscopy (EELS) was employed to gain further insights into Li/Mn structural defects. The HAADF-STEM images provide spatial information correlated with the recorded spectrum. As a fingerprint for the

oxidation state of Mn, an EELS mapping combined with L_3/L_2 peak ratio analysis is applied to P-LNMO, L-LNMO, and R-LNMO, using pure Mn_2O_3 and MnO_2 as references. The resulting mapping, as shown in **Figure 3-13o**, reveals a thicker low-valence layer of Mn near the surface in L-LNMO. In contrast, **Figure 3-13p** illustrates that the Mn valence mapping of R-LNMO shows a similar thickness compared with the P-LNMO materials (**Figure 3-14**), indicating the attainment of a stable structure with desired valence of Mn. The L_3/L_2 peak ratio of Mn extracted in EELS spectra, spanning from the surface to the bulk, is illustrated in **Figure 3-13q**. Notably, the increase in the peak ratio of Mn L_3/L_2 from bulk to surface suggests a reduction of bulk Mn^{4+} to Mn^{3+} on the surface of L-LMNO particles[119] On the other hand, the R-LNMO illustrates a thinner Mn transition zone and a similar ratio as the bulk signal of P-LNMO. Therefore, a short annealing step has successfully reconstructed the well-defined spinel lattice, reversing the adverse effects caused by Li/Mn disordering during lithiation treatment.

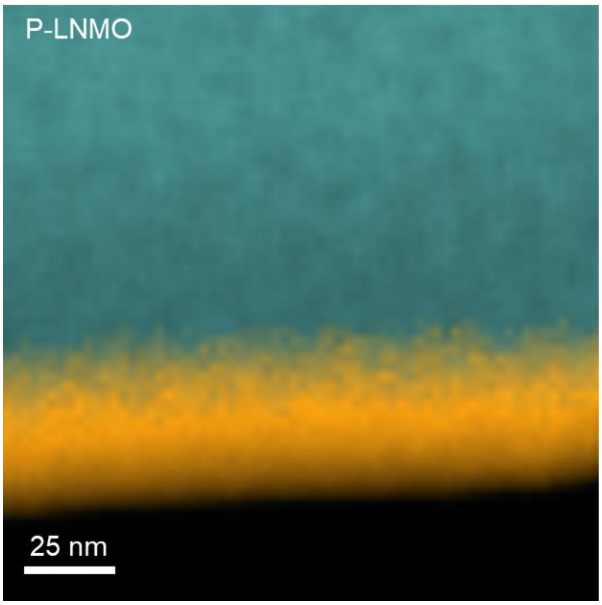

Figure 3-14 The spatial valence inhomogeneities of LNMO particles of interest. The STEM-EELS mappings of Mn L edge energy from P-LNMO.

Electrochemical Response of treated LNMO particles

The electrochemical performance of different LNMO cathodes was further assessed through half cells within the potential range of 3.0 V to 4.85 V (vs Li/Li^+). The performance of S-LNMO as collected was found to have a discharge capacity less than 60% compared to that of P-LNMO (**Figure 3-15**). As depicted in **Figure 3-16a**, the treated LNMO contains a portion of Mn^{3+}, which is oxidized to the Mn^{4+} state at the beginning of charging, resulting in a voltage plateau at around 4.1 V (vs Li/Li^+). With increased LiOH concentration during hydrothermal treatment, the plateau around 4.1 V contributes more charge capacity in the initial formation cycle. However, this irreversible capacity, stemming from excess Mn^{3+} oxidation generated by overlithiation during hydrothermal treatment, is entirely lost in the subsequent discharge cycle. Thus, despite having a sufficient amount of lithium in the lattice, the electrochemical performance cannot be fully recovered only through hydrothermal treatment.

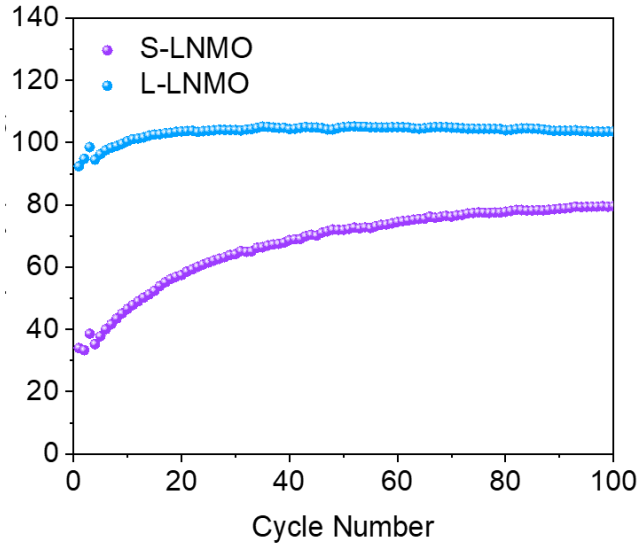

Figure 3-15 The electrochemical performance of spent LNMO particles. The cycling performance of S-LNMO and L-LNMO particles at C/3.

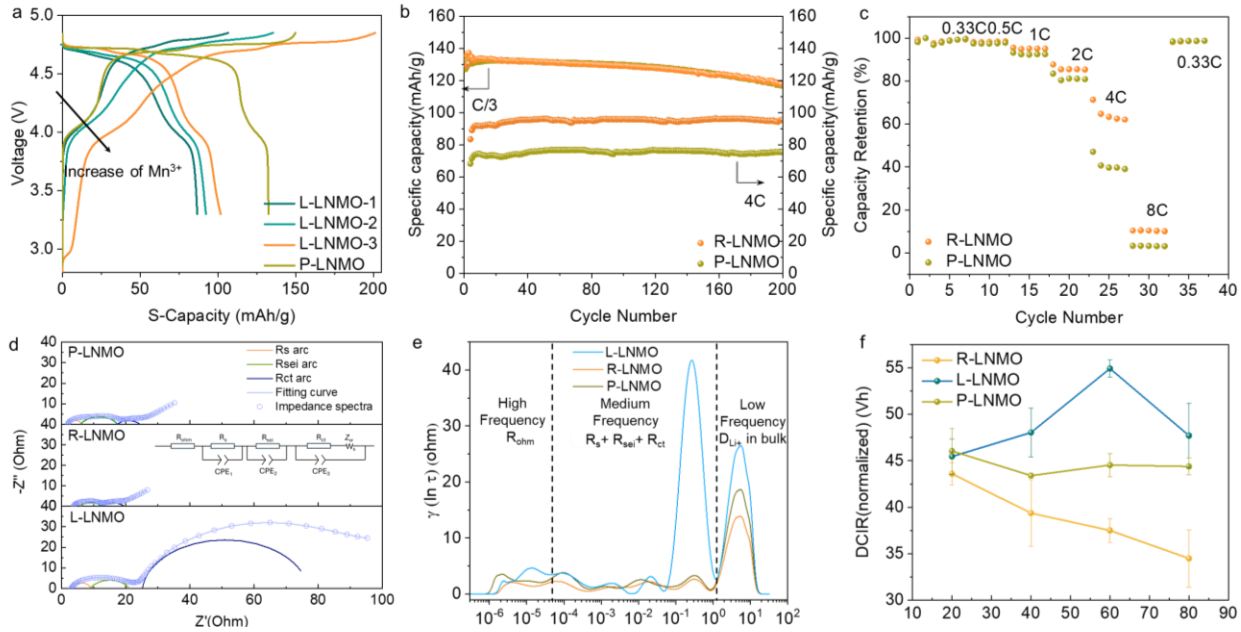

Figure 3-16 The electrochemical properties evaluation of different LNMO samples. (a) Voltage profile of P-LNMO and L-LNMO particles in different relithiation conditions. (b) Cycling performance of S-LNMO, P-LNMO and R-LNMO at C/3 and 4C. (c) Rate performance of P-LNMO and R-LNMO. (d) EIS fitting and (e) DRT analysis of P-LNMO, L-LNMO and R-LNMO at 100% SOC. (f) DCIR result of P-LNMO, L-LNMO and R-LNMO at different SOC.

We implemented a systematic investigation on the annealing process to optimize the electrochemical performance of R-LNMO. Avoiding the oxygen deficiency during the regeneration, an oxygen atmosphere was chosen to heal the defects of the remaining low-valence Mn^{3+} after hydrothermal treatment. Varying degrees of cation ordering in R-LNMO cathodes are obtained in different temperatures after 4h annealing under 650 °C, 750°C, 850°C and 950°C (referred as 'R-LNMO-1', 'R-LNMO-2', 'R-LNMO-3' and 'R-LNMO-4'). As depicted in **Figure 3-17**, the Mn^{3+} plateau tends to diminish after annealing in an oxygen atmosphere at all temperatures. R-LNMO-1 and R-LNMO-2 exhibit a higher degree of cation ordering than R-LNMO-3, likely due to the proximity to the phase transition temperature of ordered/disordered LNMO. A more detailed analysis using dQ/dV versus V plots reveals two peaks around 4.7 V (**Figure 3-18)**, indicating the two-step oxidation or reduction for the Ni^{2+}/Ni^{4+} redox couple. The

separation between these peaks reflects the disordered/ordered phases, with a narrower separation indicating a higher degree of cation ordering[120]. In **Figure 3-19**, a worse cycling stability is observed in R-LNMO-2 and R-LNMO-1, attributed to their high degree of cation ordering, which leads to poor electronic conductivity in ordered LNMO cathodes[121]. The proportion of ordered and disordered phases in the sintered samples was further analyzed qualitatively using Raman spectroscopy (**Figure 3-20**). Among the sintered LNMO samples, R-LNMO-2, sintered at 750°C, exhibited the most distinct Eg vibrational mode around 400 cm^{-1}, indicating the most ordered structure. This resulted in the worst cycling stability and the narrowest dQ/dV peak splitting. With optimized temperature, R-LNMO demonstrated a cycling performance similar to the pristine sample, retaining 97.4% capacity after 100 cycles and 87.96% after 200 cycles at a C/3 rate (**Figure 3-16b**). Additionally, **Figure 3-16c** highlights the superior rate performance of R-LNMO compared to the pristine sample. Notably, R-LNMO maintained stable cyclability at a 4C rate, delivering 92.6 mAh/g, in contrast to 73.7 mAh/g in the pristine sample. However, as shown in **Figure 3-21**, the enhanced rate performance was diminished when higher annealing temperatures were applied in R-LNMO-4. Therefore, this distinctive electrochemical performance is attained by effectively adjusting the Mn^{3+} content through an optimized annealing process.

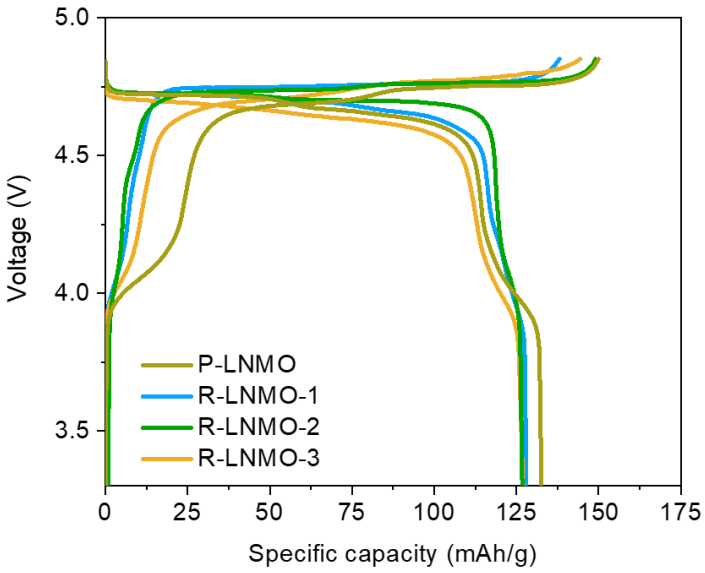

Figure 3-17 The electrochemical performance of annealed LNMO particles of interest. The voltage profile of P-LNMO and R-LNMO particles in different temperatures.

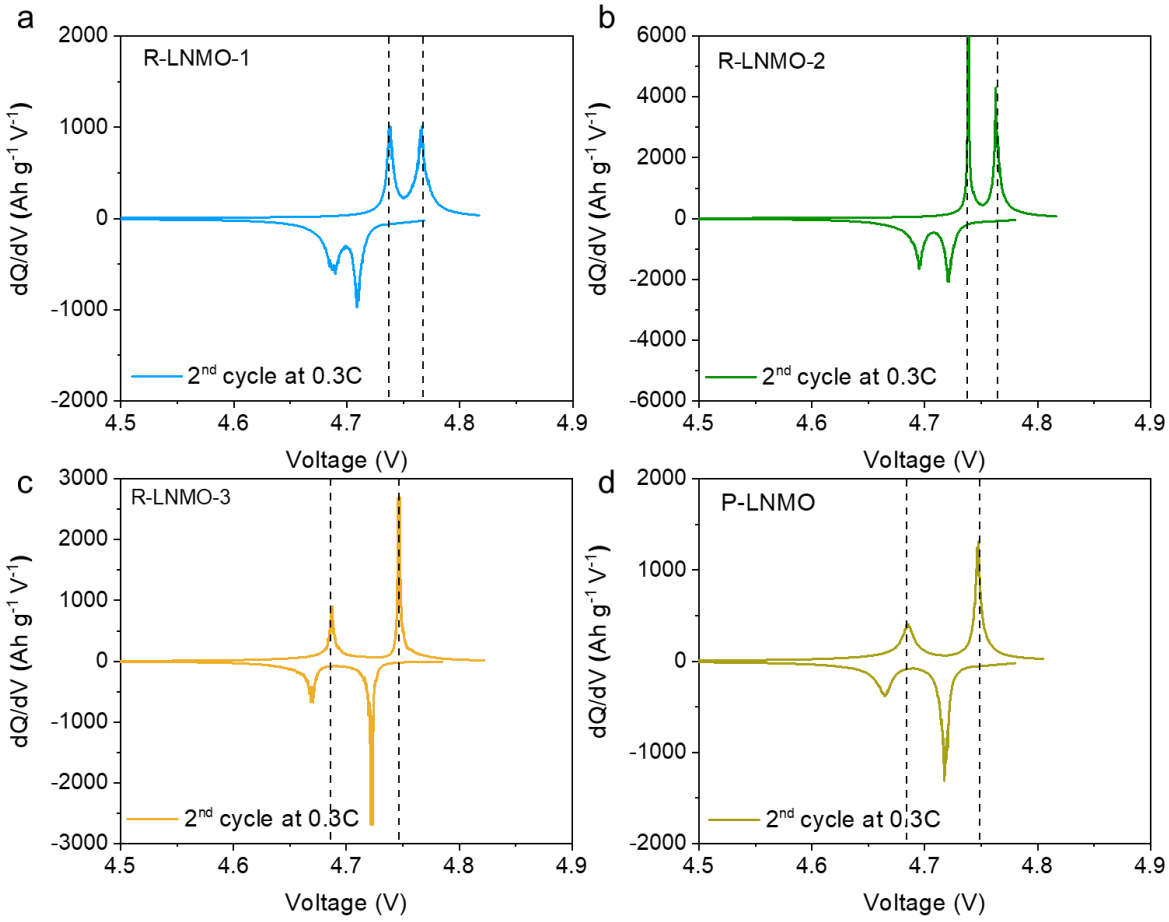

Figure 3-18 The electrochemical performance of annealed LNMO particles of interest. The dQ/dV plots of (a) R-LNMO-1, (b) R-LNMO-2, (c) R-LNMO-3 and P-LNMO.

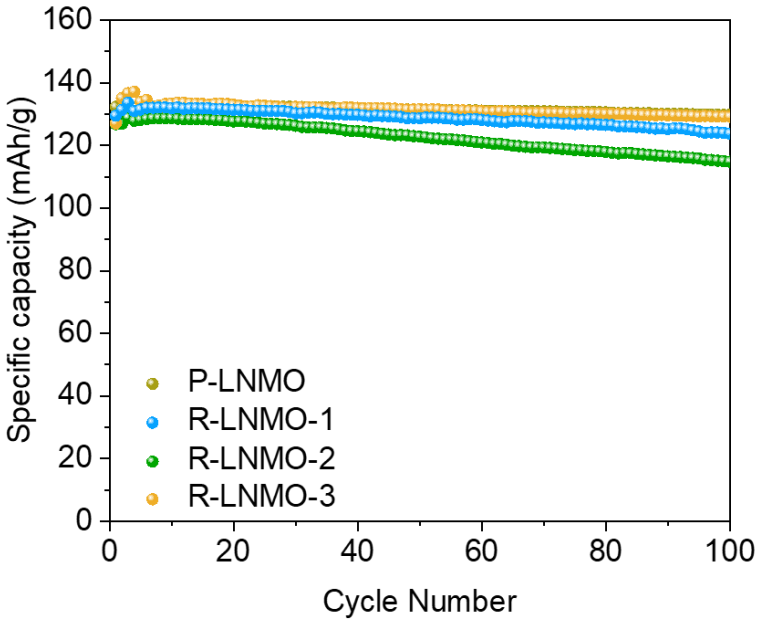

Figure 3-19 The electrochemical performance of annealed LNMO particles of interest. The cycling performance of P-LNMO and R-LNMO particles in different temperatures.

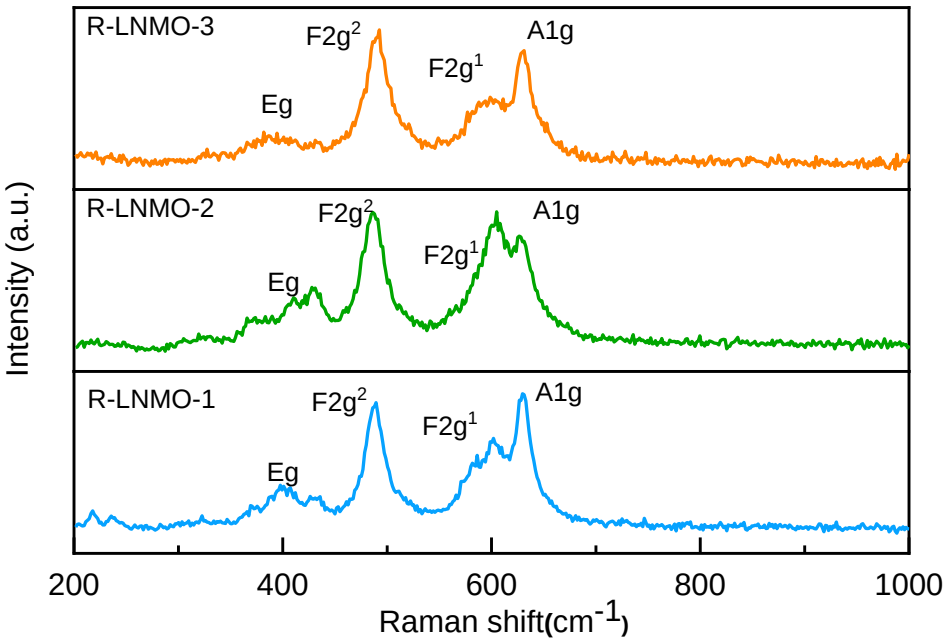

Figure 3-20 The structural analysis and bond information of sintered LNMO particles of interest. Raman spectra of (a) R-LNMO-1, (b)R-LNMO-2, and (c)R-LNMO-3.

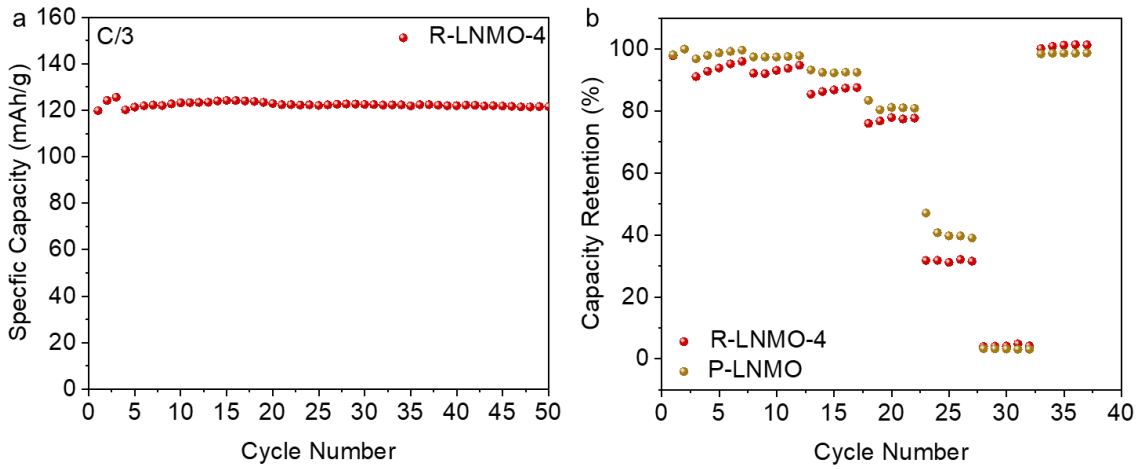

Figure 3-21 The electrochemical performance of R-LNMO-4. (a) Cycling and performance of R-LNMO-4 at C/3. (b) Rate performance of P-LNMO and R-LNMO-4.

A comprehensive electrochemical analysis has been carried out to further understand the divergence in kinetic dynamics. We conducted an electrochemical impedance spectroscopy (EIS) analysis with the distributions of relaxation times (DRT) calculation and direct current internal resistance (DCIR) to unveil the improvement in Li^+ kinetics in regenerated LNMO cathodes. EIS measurements were performed under different states of charge (SOC) during the charging process, as shown in **Figure 3-22**. The observed three semi-circles correspond to the resistance of the contact interface (R_s), solid-electrolyte interface (R_{sei}), and charge transfer (R_{ct}) from high to low frequency. Consistent with the enhanced high-rate performance, smaller Rct value (7.41 Ohm) was observed in R-LNMO compared to it (12.86 Ohm) in P-LNMO (**Table 3-3**). On the other hand, the enlarged Rct value (51.59 Ohm) in L-LNMO (**Figure 3-16d** and **3-16e**) indicates that the hydrothermal-treated sample exhibits significantly increased resistance, due to the abundance of mentioned lattice defects. Nevertheless, at both 60% SOC and 100% SOC, R-LNMO demonstrates the lowest resistance compared to P-LNMO, indicating faster kinetics in the bulk and interface (**Figure 3-23**).

The DCIR was measured at different SOC and normalized by the capacity of individual cells. These values represent the average from repeated tests in three cells after different current pulses at 0.5C, 1C, and 2C (see details in methods).The R_{DCIR} value comprises R_i (series resistance), R_{ct} (charge transfer resistance), and R_{diff} (diffusion resistance)[122]. Given that the morphology and electrode-electrolyte interface of R-LNMO are identical to the pristine sample, the variation in determined R_{DCIR} can be considered to represent the difference in Li^+ diffusivity among samples. As depicted in **Figure 3-16f**, the highest DCIR value was detected in L-LNMO, owing to the impedance by its imperfect cation mixing. Intuitively, the lower R_{DCIR} across the entire SOC range indicates that R-LNMO has rapid lithium-ion diffusion kinetics compared to the pristine sample. Although such a variation in Li^+ diffusion resulting from defect engineering is valuable, understanding the structural properties required for this improvement is vital for future progress.

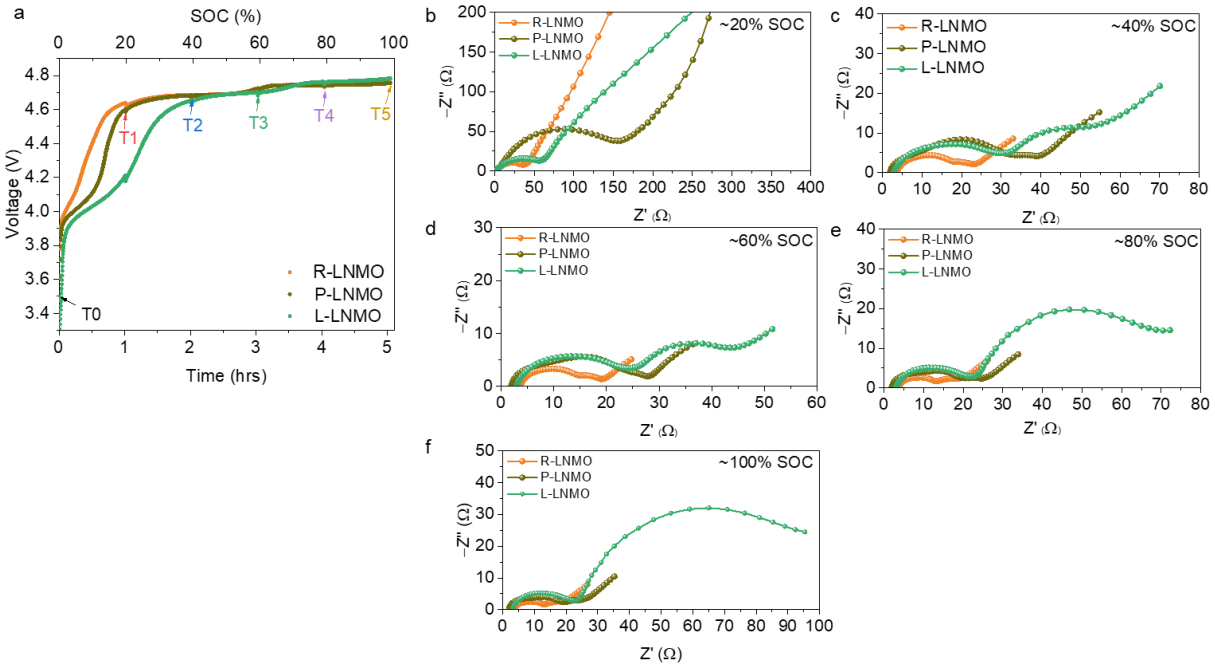

Figure 3-22 The interfacial impedance analysis in LNMO particles of interest. The Electrochemical impedance spectroscopy (EIS) analysis of R-LNMO, L-LNMO and P-LNMO at different SOC.

Table 3-3 The interfacial impedance analysis in LNMO particles of interest. The EIS fitting result of LNMO particles at 100 SOC and 60 SOC.

100 SOC

Sample	Rs	Rsei	Rct
P-LNMO	3.536	10.78	12.86
L-LNMO	6.084	12.03	51.59
R-LNMO	2.424	5.809	7.41

60 SOC

Sample	Rs	Rsei	Rct
P-LNMO	3.895	12.71	5.559
L-LNMO	5.563	14.0	17.88
R-LNMO	2.512	6.166	5.468

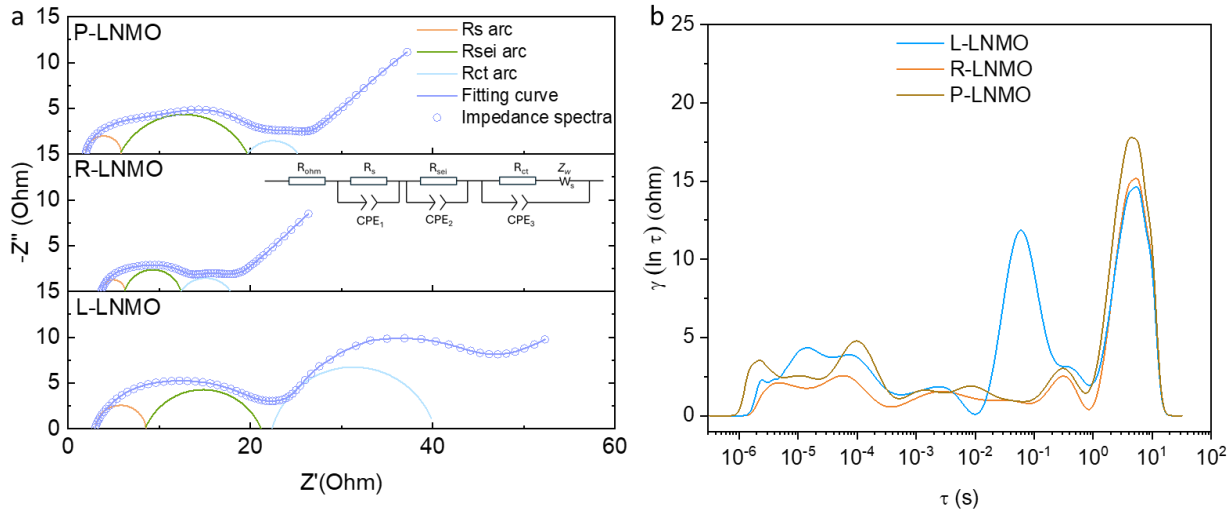

Figure 3-23 The interfacial impedance analysis in LNMO particles of interest. The EIS fitting and DRT analysis of R-LNMO, L-LNMO and P-LNMO at 60% SOC.

The DCIR was measured at different SOC and normalized by the capacity of individual cells. These values represent the average from repeated tests in three cells after different current pulses at 0.5C, 1C, and 2C (see details in methods).The R_{DCIR} value comprises R_i (series resistance), R_{ct} (charge transfer resistance), and R_{diff} (diffusion resistance)[122]. Given that the morphology and electrode-electrolyte interface of R-LNMO are identical to the pristine sample, the variation in determined R_{DCIR} can be considered to represent the difference in Li^+ diffusivity among samples. As depicted in **Figure 3-16f**, the highest DCIR value was detected in L-LNMO, owing to the impedance by its imperfect cation mixing. Intuitively, the lower R_{DCIR} across the entire SOC range indicates that R-LNMO has rapid lithium-ion diffusion kinetics compared to the pristine sample. Although such a variation in Li^+ diffusion resulting from defect engineering is valuable, understanding the structural properties required for this improvement is vital for future progress.

Li+ diffusion Dominated by Induced Defects

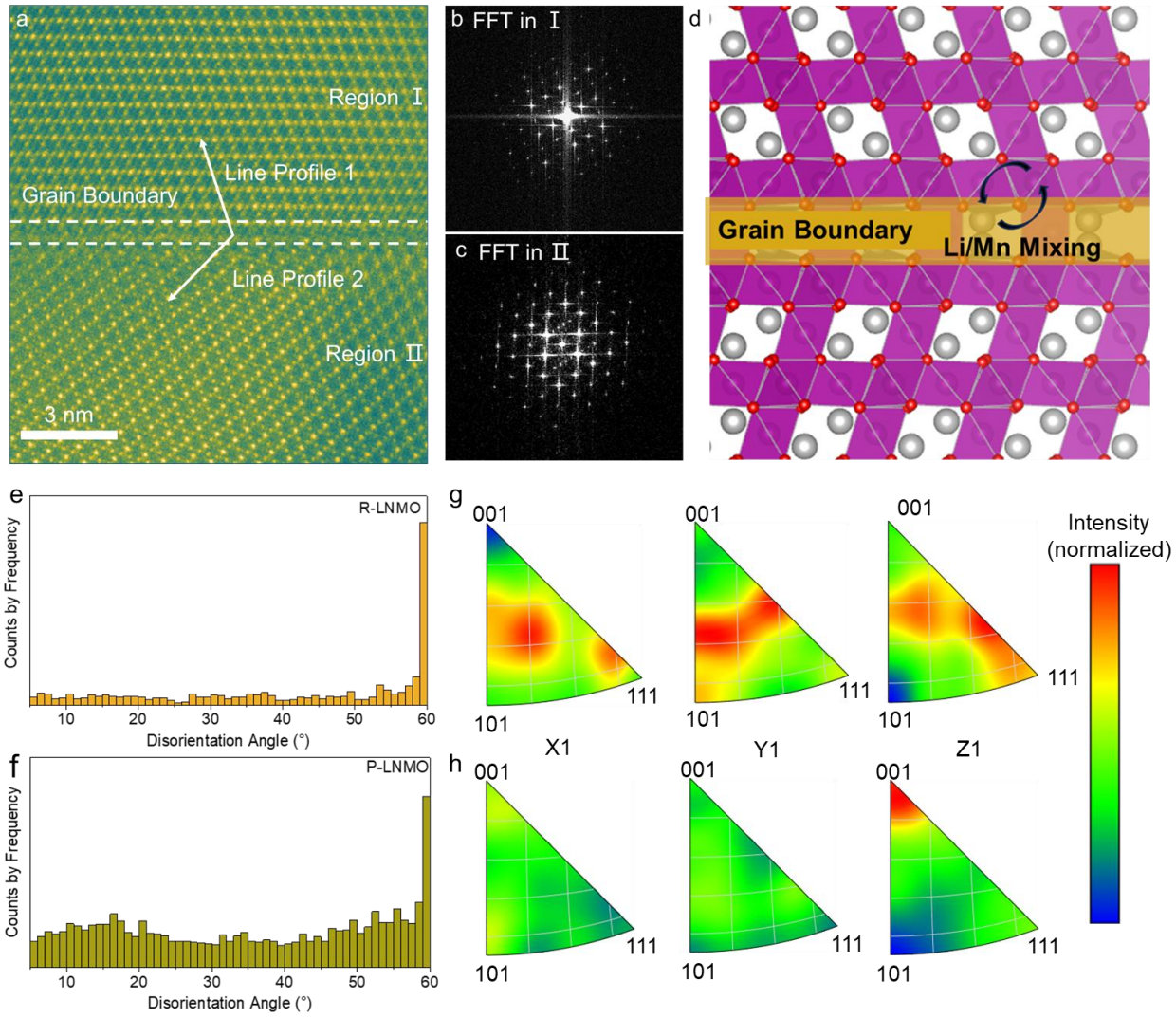

Figure 3-24 Evidence of twining defects and preferred grain orientations in regenerated cathodes. (a) HAADF-STEM images of the grain boundary in R-LNMO particle. (b, c) Fast Fourier transform (FFT) images of regions in a. (d) Structure schematic of twining grain boundary (Li, Mn, and O). (e, f) The disorientation angle distribution in R-LNMO and P-LNMO. (g, h) The inverse pole figures (IPF) in x, y, z directions in R-LNMO and P-LNMO. The color bar refers to the intensity of IPF pole figure.

To gain a more precise understanding of the underlying structure and electrochemical behavior of regenerated LNMO particles at an atomic level, we conducted further characterization using spherical aberration-corrected STEM measurements. Upon revisiting the microstructure of R-LNMO (**Figure 3-24a**), a prominent feature emerged in the lattice-twinning structures

accompanied by a substantial number of twin boundaries. The asymmetrical twinning structure in R-LNMO reveals that the upper and lower variants are connected via an operation of reflection and an additional shift along the {111} mirror plane[91]. Consequently, the {111} planes become staggered, crossing the twin boundary (highlighted by white lines). In **Figure 3-24b-c**, the FFT images of two regions demonstrate the different orientations of the bulk across the twinning feature. In **Figure 3-25**, two-line profiles extracted from the twinning structures demonstrate that the intensities of Mn atoms located at the twin boundaries are weaker than those in the bulk region (indicated by blue dashed lines as a guide). This observation implies that lithium will occupy the Mn sites at twinning boundaries rather than the surface region in regenerated LNMO, resulting in the decreased intensity of these columns (**Figure 3-24d**). This insight underscores the accommodation of Li/Mn disordering and the presence of twin boundary defects in regenerated LNMO, which is considered as a key reason of enhanced inter-granular Li^+ diffusion.

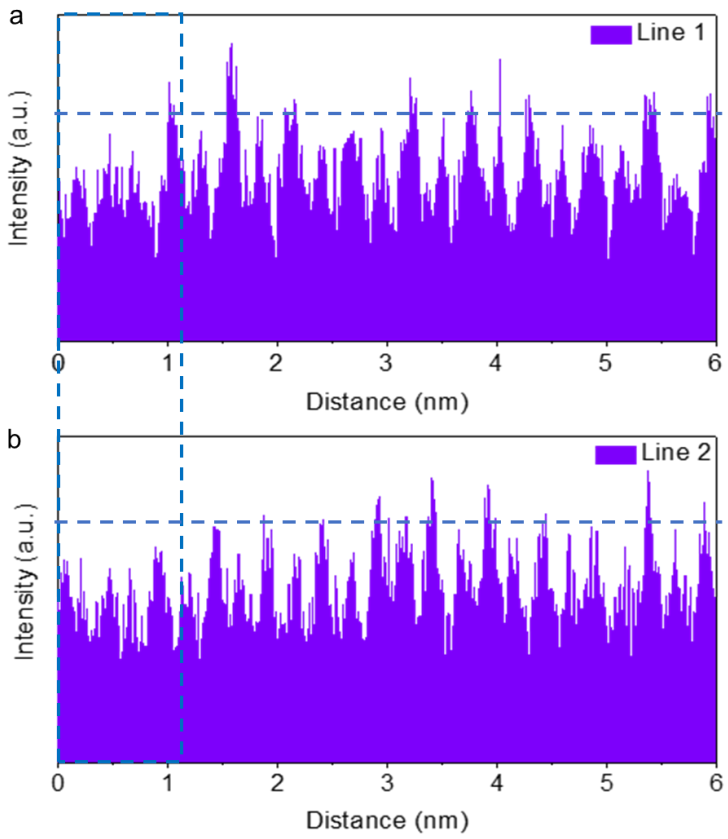

Figure 3-25 The microstructure of twinning defects. Linear profile of the atomic contrast curve of Line 1 and Line 2 in **Figure. 3-24a**.

To further elucidate the structural merits in regenerated cathodes, we conducted an electron backscatter diffraction (EBSD) experiment to statistically analyze the crystallographic features. To quantify grain orientation and morphologies across the entire cross-section of the LNMO particles, the EBSD test was performed following a milling process by Plasma Focused Ion Beam (PFIB). The selected cleanup area for both samples is depicted in **Figure 3-26**. In the context of a cubic crystal, applying possible symmetries, the misorientation between two adjacent grains can be reduced to the disorientation angle ranging from 0^{o}–62.80^{o}[123]. Notably, **Figure 3-24e** illustrates a distinct peak present in the regenerated cathode at around 60 ^{o}, corresponding to the twin $\sum 3/<111>$ boundaries[124]. In comparison, the pristine LNMO exhibits a more random grain

disorientation at lower angles (**Figure 3-24f**). Li^+ diffuses from one tetrahedral site to an adjacent one through an octahedral vacancy surrounded by six Mn ions at the octahedral site, forming a channel perpendicular to the {111} surface[91]. The energy barrier for this channel is primarily influenced by the surrounding six Mn ions. Notably, the energy barrier for Li^+ diffusion along the twin boundary is lower than in the bulk region in spinel type structure[91]. This observation is consistent with the electrochemical behavior of R-LNMO-4, as the diminished twin boundaries after high-temperature annealing lead to altered diffusion properties. Thus, the induced twin boundaries contribute to the divergence in Li^+ diffusion in regenerated LNMO samples.

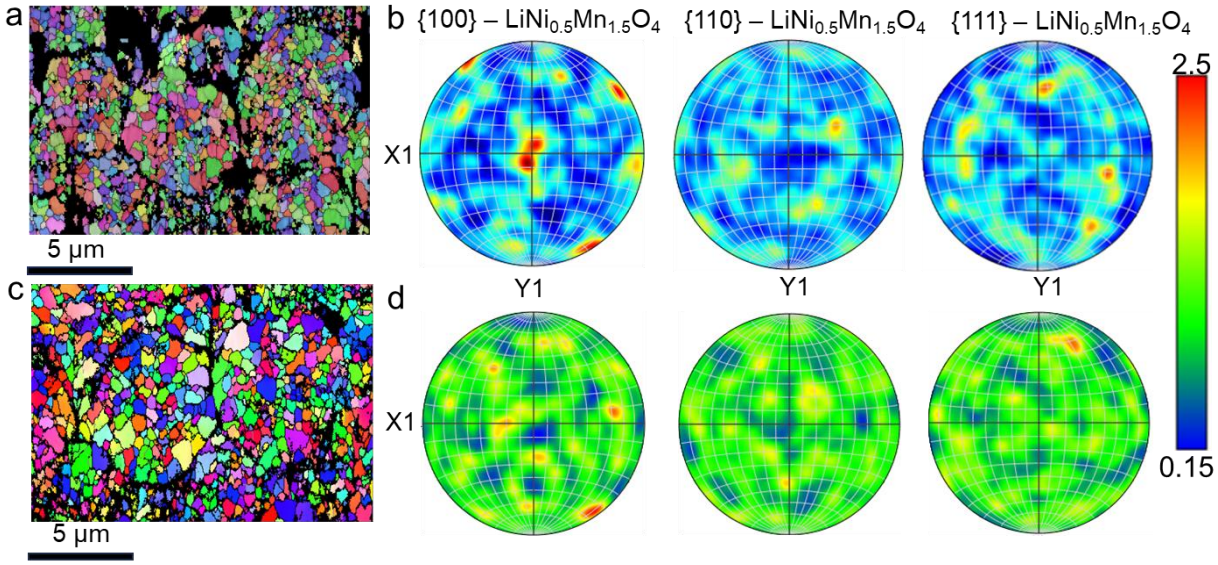

Figure 3-26 .Preferable orientation distribution of LNMO particles of interest. The selected area of (a) R-LNMO and (c) P-LNMO for EBSD statistical analysis after cleanup. The colored pole figures of (b) R-LNMO and (d) P-LNMO.

Furthermore, it has been observed that the electrochemical properties, especially the rate performance, are also influenced by the preferred crystallographic planes in spinel-type cathodes[125]. As a primary outcome of the annealing step, the recrystallization enables the growth of preferential crystallographic planes in regenerated samples[125]. A significant increase in average grain size is noted in regenerated cathodes (0.45 µm), compared to the pristine sample (0.35 µm),

indicating crystal regrowth following the annealing step (**Figure 3-27**). In the Inverse Pole Figures (IPF) mapping (**Figure 3-24g, h**), unlike the predominantly <001>-oriented grains observed in pristine samples, preferred <111>-oriented grains appear in regenerated cathodes. Additionally, from X-ray diffraction pattern (XRD), an enhancement of the relative peak intensity between the (111) peak and the (311) peak in regenerated samples (**Figure 3-28**). Preferred {111} facet facilitates the efficiency for intragranular Li^+ diffusion[126, 127]. Therefore, the defect control step, combined with twin boundaries and preferred crystalline facets, results in distinct rate performance, facilitating rapid Li^+ diffusion.

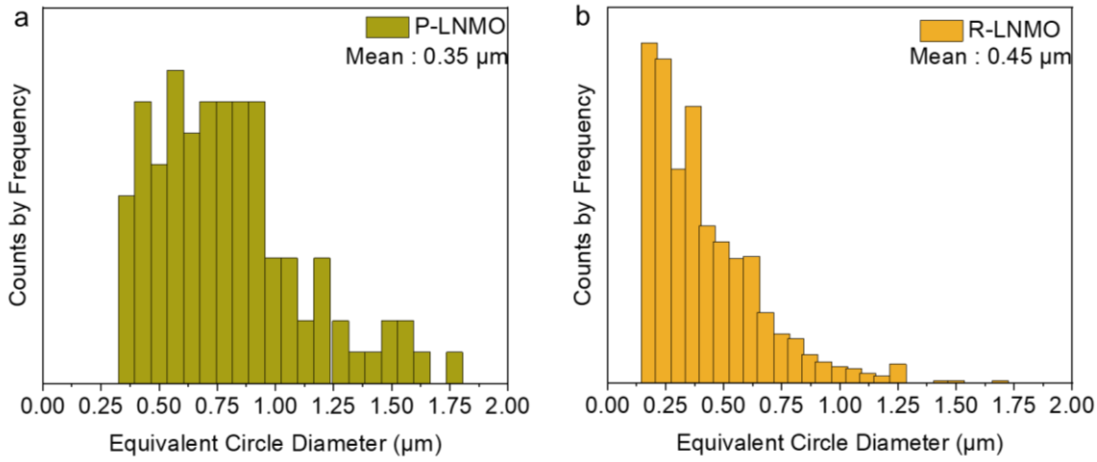

Figure 3-27 Grain size distribution of LNMO particles of interest. The size distribution of equivalent circle diameter of grains in (a) P-LNMO and (b) R-LNMO.

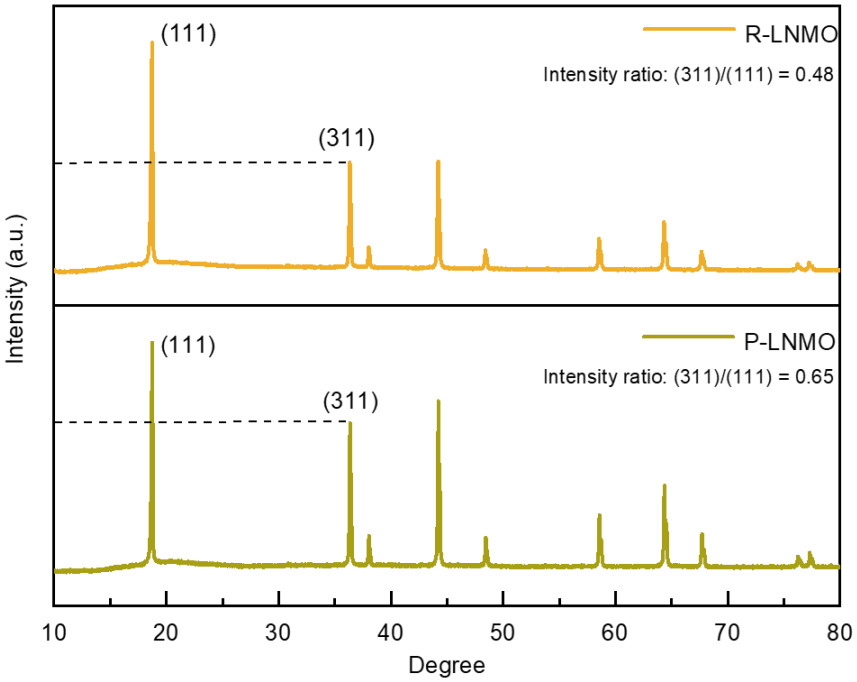

Figure 3-28 Preferable orientation investigation of LNMO particles of interest. The X-ray diffraction pattern of P-LNMO and R-LNMO.

3.2.3 Conclusion

In summary, our study comprehensively investigated the mechanisms of rejuvenation for high-voltage spinel-type cathodes by systematic control and tuning of composition and structural defects. Through advanced characterization methods, we illustrated the existence of Li/Mn disordering during the relithiation step, which contributes to the failure of restoring electrochemical performance. In addition to mitigating Li/Mn disordering, the induction of twin boundaries and preferred grain regrowth, identified through STEM and EBSD techniques, effectively promotes inter-granular lithium-ion diffusion in a defect engineering step via controlled short annealing. Significantly, the resulting regenerated LNMO demonstrates a substantial enhancement in its rate performance without sacrificing energy density at low rates, retaining 97.4% capacity after 100 cycles and 87.96 % after 200 cycles at C/3. This effective direct recycling method, by leveraging defect control, not only provides a systematic understanding of the healing

mechanism in spinel structures but also integrate defect engineering into the cathode design of primary synthesis, thereby enhancing the sustainability of next-generation LIBs.

3.2.4 Acknowledgements

Chapter 3, in full, is a reprint of the material “Understanding and Controlling Structural Defects and Disordering in $LiNi_{0.5}Mn_{1.5}O_4$ Cathodes for Direct Recycling” as it appears in ACS nano Hongpeng Gao, Bing Han, Duc Tran, Luqi Zhang, Zishuo Zhao, Yu-ting Chen, Wei Tang, Mingjie Xu, Junlin Wu, Xiaolu Yu, Varun Gupta, Maura Appleberry, Haodong Liu, Yijie Yin, Weiliang Yao, Mingqian Li, Weikang Li, Linqin Mu, Ying Shirley Meng, Zheng Chen, 2024. The dissertation author was the primary investigator and author of this paper.

Chapter 4 Direct Upcycling of Spent Low Nickel Cathodes to Nickle-Rich NCMs: from Polycrystals to Single-Crystals

4.1 Introduction

Rapid growth in lithium-ion battery (LIB) production has served the rising demand for portable electronics, electric vehicles (EVs), and grid energy storage systems[128]. Since the 2010s, an expeditious growth of EVs has been accompanied by tumbling prices and enormous enthusiasm for LIBs[129]. As these EVs inevitably reach their end of life (EOL), a large number of spent LIBs would be generated after their service life of up to 8-10 years[9]. For these EOL batteries from the primary applications with 80% of their original capacity, one potential solution is to reuse them in less demanding applications, such as utility and backup power storage devices, where they can extend their lifespan[130-132]. Nonetheless, this approach only postpones the eventual recycling of LIBs. It remains a critical and pressing issue to recycle all EOL LIBs.

Hydrometallurgical and pyrometallurgical processes have been adopted in the state-of-the-art LIB recycling industry. Involving intensive energy consumption and caustic processes, such as high-temperature smelting, acid leaching, and chemical precipitation, are inevitably associated with heavy CO_2 emission and other waste generation. On the other hand, the emerging direct recycling technology has attracted rising attention due to the minimum energy consumption and maximum potential profit compared with traditional hydrometallurgical and pyrometallurgical recycling methods[95, 100, 133, 134]. Extensive efforts have been devoted to healing the structure and composition defects of cathode active materials from spent LIBs, including solid-state sintering[135], hydrothermal treatment[13, 93, 134], ionothermal[136], redox mediation[137], and molten eutectic salt relithiation[31] followed by a short annealing process. While solid-state sintering by mixing all precursors in a stoichiometric ratio seems to be a simple strategy, determining the amount of supplementary Li source is challenging for the mixed waste streams with spent LIBs with a wide

range of state of health (SOH). By comparison, some self-saturated relithiation strategies have demonstrated high effectiveness in direct recycling without considering the SOH variation[31, 95, 100, 101, 138].

However, with the growing demands in high energy density LIBs, improving the performance of spent cathode active materials beyond the original pristine materials via recycling processes remains challenging as a critical milestone in the next-generation battery recycling[139]. In addition, single-crystal $LiNi_xCo_yMn_{1-x-y}O_2$ (NCM) cathodes have attracted increasing attention due to their superior structural stability compared with conventional polycrystalline particles[140]. As the accumulation of lattice strain and lattice distortion are susceptible in the polycrystalline particles due to the grain boundary evolution,[141] an effective direct approach to eliminate grain boundary fracture is to convert polycrystalline into single-crystal domains, delivering superior kinetics and rate capability with significant integrity improvement with optimized size and morphology control[142]. Recently, a molten salt method based on LiOH-Li_2SO_4 salt mixture has been demonstrated to upgrade polycrystalline NCM 111[143] and NCM 532[144] into single-crystal NCM 622. This concept has also been illustrated to convert spent polycrystal $LiNi_{0.88}Co_{0.095}Al_{0.025}O_2$ (NCA) into regenerated single-crystal with same composition by LiOH-Na_2SO_4 eutectic molten salt system[145]. Moreover, a reciprocal ternary molten salt system of $LiNO_3$-NaCl is developed for upcycling spent NCM 111 into NCM 622[146]. At the same time, producing high-performance nickel-rich cathodes (Ni > 80%) has garnered significant attention due to their high energy output. In this regard, upgrading spent NCM 111 into single-crystal NCM 811 (or even higher Ni) is being considered as one of the ultimate solutions to avoid the multi-step high-temperature calcination process by using excess lithium salt or a molten-salt flux method[147]. However, upcycling low- nickel cathodes to NCM811 remains a difficult task.

Herein, we report an efficient method to upgrade polycrystalline delithiated NCM 111 (D-NCM 111) into single-crystal NCM 811 with LiOH as a single supplementary source of lithium. The universality of this simple method was further demonstrated in synthesizing single-crystal NCM 433 and 622 by tuning the precursor ratios. We found that the Ostwald ripening phenomenon, occurring during flux growth of oxides when merging D-NCM with Ni precursor, played a dominant role in determining particle morphology. Various characterization methods were applied to examine the uniformity of Ni valence and distribution within the single-crystal particle. These upcycled single-crystal NMC showed outstanding electrochemical performance compared with their polycrystalline counterparts. Particularly, the resulting upcycled NCM 811 exhibited a significant improvement of its rate capability with superior cycling stability, surpassing the performance of the original polycrystalline NCM 811. This effective direct upcycling method with limited Li salt, avoiding excess molten salt flux, significantly reduces the overall cost as well as simplifying the recycling process, which provides a feasible pathway to scalable direct upcycling.

4.2 Direct Upcycling of Spent $LiNi_{0.33}Co_{0.33}Mn_{0.33}O_2$ Cathodes to Nickle-Rich NCMs Using Lean Precursors: from Polycrystals to Single-Crystals

4.2.1 Experimental

4.2.1.1 Materials

Chemically delithiated NCM111 with ~10% of Li loss, denoted as "D-NCM111", was made by the Materials Engineering Research Facility (MERF) at Argonne National Laboratory. Briefly, pristine NCM111 (provided by Toda America Inc.) was reacted with an aqueous solution of potassium persulfate to leach Li out. Afterwards, the leached material was washed by water, then acetonitrile, and finally dried under vacuum at the ambient condition. This delithiated NCM111 was utilized as our starting material for additive screening and was manufactured at 1

kg per batch size. $Ni(OH)_2$ were also provided by the Materials Engineering Research Facility (MERF) at Argonne National Laboratory

4.2.1.2 Direct upcycling of cathode materials

10g of D-NCM 111 and certain amounts of nickel precursor (calculated based on the end product) were mixed in 15 ml of acetone by the PQ-N04 planetary ball milling (Across International) at 600 rpm for 12h. The mixture was collected after drying overnight in a vacuum oven.

1g of ball milled mixture was pelleted with 1.1x molar ratio (based on stoichiometry in final product, $Li_{1.1}Ni_xCo_yMn_zO_2$ for compensating the Li loss during sintering) of LiOH. For sintering, the pellet was held at 480 ℃ for 3 h with a ramping rate of 5 ℃/min and then held at a certain temperature for 10h, 12h, and 15h with a ramping rate of 10 ℃/min under pure oxygen flow. The optimal condition for upcycling NCM 811 is sintering the pellet under 850℃ for 12h.

4.2.1.3 Materials Characterization

The chemical composition of NCM powders was evaluated by inductively coupled plasma mass spectrometry (ICP–MS, Thermo Scientific, iCAP RQ model). Their crystal structures were examined by X-ray powder diffraction (XRD) employing a Bruker D2 Phaser (Cu Kα radiation, λ=1.5406 Å). The morphology of the NCM powders was observed by FEI Apreo LoVac scanning electron microscope (SEM) with X-Max 80 EDS detector. The particle size distribution was analyzed with Nano Measurer software. The size distribution is counted by Nanomeasurer 1.2. Since the irregular shape of single-crystals we consider the greatest diameter(the length of the line which connects the two farthest boundary points) as the diameter of particles.

Brunauer-Emmett-Teller (BET) surface area analysis was conducted using an Autosorb IQ gas adsorption analyzer (Anton Parr) following the multiple points BET method, with the

adsorption–desorption isotherms of nitrogen. Samples were degassed at 300 °C for 6 hours to remove the residual molecules before characterization.

The thermogravimetric analysis (TGA) and differential scanning calorimetry (DSC) curve of upcycling process were collected in alumina pans by A Instruments™ Discovery SDT 650™ simultaneous DSC/TGA in UC San Diego Materials Research Science and Engineering Center (UCSD MRSEC).

Time-of-flight (TOF) powder neutron diffraction was measured at the VULCAN instrument at the Spallation Neutron Sources (SNS), Oak Ridge National Laboratory (ORNL). The diffraction pattern was measured at the detector banks at $2\theta = \pm 90°$, equipped with 5 mm receiving collimators. Neutron powder diffraction patterns were collected in the high-intensity mode ($\Delta d/d$ ~0.45%) for a duration of 2 h under the nominal 1.4 MW SNS operation and then processed using VDRIVE software. Rietveld refinement against the neutron diffraction was performed using General Structure Analysis System (GSAS) software with the EXPGUI interface[46, 47].

X-ray photoelectron spectroscopic (XPS) measurement was conducted with an AXIS Supra by Kratos Analytical with an Al Ka anode source working at 15 kV and 10^{-8} Torr chamber pressure. The spectra data were processed by CasaXPS software. All spectra were calibrated with the hydrocarbon C 1s peak at 284.6 eV. The cross-section images of upcycled NCM experiments were performed using a FEI scios dual beam focused ion beam (FIB). Aberration corrected scanning transmission electron microscopy (AC-STEM) and energy-dispersive X-ray spectroscopy (EDS) were conducted using a JEOL JEM-ARM 300F at 300 kV.

Spectroscopic transmission X-ray microscopy (TXM) was performed at the 6-2c beamline at the Stanford Synchrotron Radiation Light source (SSRL). 8.95 keV X-rays were utilized to characterize the particle morphology. The NCM particles were placed in a quartz tube and sealed

with epoxy in an Ar-filled glovebox. The tomography data were taken over an angular range of 180°. The field of view of each tile was 16 μm, consisting of 1024 × 1024 pixels, with a pixel size of 28.7 nm. The images were then processed in the TXM-Wizard software suite, with reference correction, energy average, image alignment, and 2D X-ray Absorption Near-Edge Structure (2D XANES) analysis.[148] The edge energy maps saved by TXM-Wizard were exported into 64-bit .raw files using MATLAB for visualization.

4.2.1.4 Electrochemical characterization

Pristine NCM 111, NCM 433, NCM 622, and NCM 811 (noted as T-NCM 111, T-NCM 433, T-NCM 622 and T-NCM 811) were obtained from Canrd Ltd, China. The active materials were mixed with polyvinylidene difluoride (PVDF) and Super P65 in NMP at a mass ratio of 8:1:1 to make electrode slurries. Then the formed slurries were cast on an aluminum foil using a doctor blade and dried in a vacuum at 120 °C for 6 h. The electrodes were cut and compressed by rolling. The areal mass loading of electrodes was around 6 mg/cm^2. Coin cells were assembled with a Li metal disc (thickness 1.1 mm) as the counter electrode, 1.2 M $LiPF_6$ in EC/EMC = 3:7 as the electrolyte, and a tri-layer membrane (Celgard 2325) as the separator. Galvanostatic charge-discharge was carried out using a Neware battery testing system in the potential range of 3.0-4.3 V at different rates for 100 cycles after C/10 in the first 3 activation cycles.

4.2.2 Results and discussions

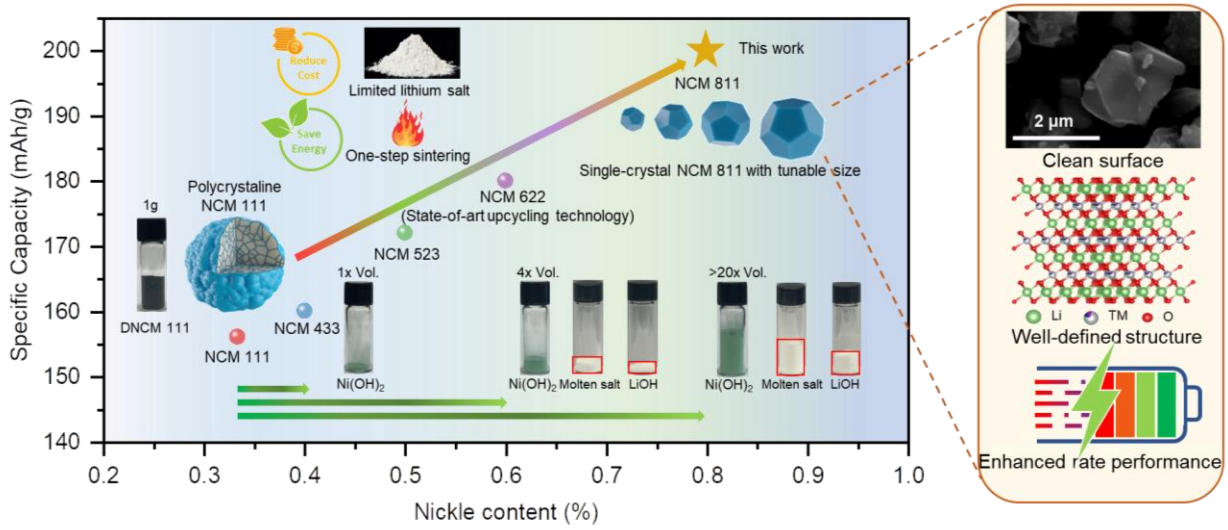

Figure 4-1 Schematic illustration of the direct upcycling method. The spent (delithiated) polycrystalline NCM particles (e.g., D-NCM111) are mixed with Ni-containing precursors (e.g., $Ni(OH)_2$) by ball milling to form a homogenous mixture, which is subject to relithiation with limited amount of LiOH (by the sintering process) to obtain single-crystal NCM particles with clean surface (no lithium salt residuals), well-defined structure and enhanced rate performance. The amount of molten salt is based on the state-of-the art method by Ma et al.'s work[143]

It is a growing consensus that increasing the nickel content is a direct way to boost the specific capacity of the NCM cathodes, which can also be applied to recycling/upcycling areas. In **Figure 4-1**, we show an efficient and versatile method to upgrade the polycrystalline D-NCM 111 to higher nickel NCM with single-crystal morphology control using limited Li supplementary source. The SEM images of D-NCM 111 and $Ni(OH)_2$ precursor are shown in **Figure 4-2a-b**. The morphology evolution reveals the transformation of polycrystalline particles to single-crystal particles. To achieve such a transformation, the D-NCM 111 was first pulverized into primary grains via ball milling with $Ni(OH)_2$ precursor, facilitating the extra Ni to diffuse into the NCM bulk phase. The homogenous precursor (**Figure 4-2c**) was then subject to a relithiation sintering step with 10% molar excess LiOH (to compensate for Li loss during sintering step). The TGA-DSC analysis (**Figure 4-3**) illustrated the compositional evolution during the sintering process. A temperature hold at 480 ℃ for 3 h is applied to form a uniform lithium hydroxide solution with

D-NCM and decomposed $Ni(OH)_2$ precursor. Following by a long-term sintering at high temperature, the fully-lithiated single-crystal NCM 811 was obtained with no significant lithium salt residual on the surface. Similar methods can be applied to synthesize NCM 433 and 622 with good control of composition (**Table 4-1**) and phase purity (**Figure S4-5**). The corresponding samples under the optimal conditions are denoted as "U-NCM 433", "U-NCM 622", and "U-NCM 811", respectively.

Compared with single-crystal NCM 622 obtained using excess amount of molten salt flux of Li mixture reported in recent works[143, 144, 146], our lean LiOH approach enabled a better control of homogeneity as it is challenging to upgrade into single-crystal NCM 811 from the same starting material, D-NCM 111 with large excess of Li salt, which also involves a large amount of transition metal diffusion between metal precursors and the existing NCM host. As shown in **Figure 4-1**, more than 20x or 4x of the volume of $Ni(OH)_2$ is required to reach the compositional formula for final NCM811 product compared with NCM 433 or NCM 622 upcycling. More importantly, instead of using a large amount of mixed lithium salts to form the molten salt system, our direct upgrading process utilizes a minimum amount of single lithium salt (LiOH) to compensate the lithium loss in spent NCM and to react with newly added Ni precursor to form the desired Ni-rich NCM single- crystals with high uniformity and tunable particle sizes. Our work demonstrated such a simple yet efficient method to upgrade NCM 111 into single-crystal NCM 811 with high elemental integrity and superior electrochemical performance without any excess molten salt flux, which is critical for low-cost and scalable upcycling. Particularly, in large scale operation this lean salt upcycling process will significantly reduce the water and energy usage for washing and reclaiming the extra Li.

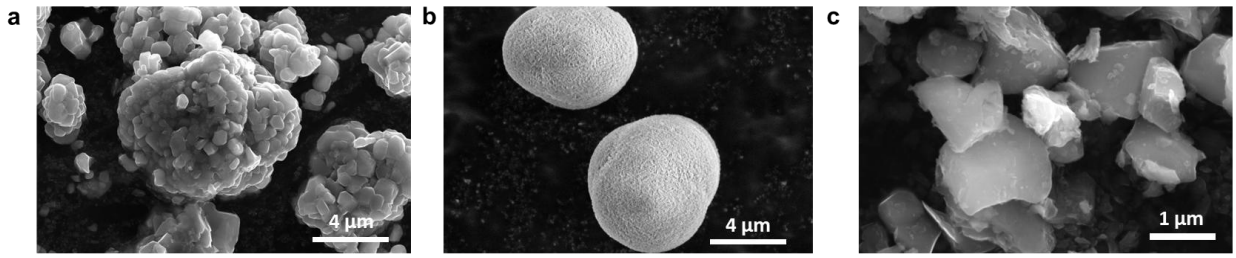

Figure 4-2 SEM image of D-NCM 111, Ni(OH)2 and mixture after ball milling.

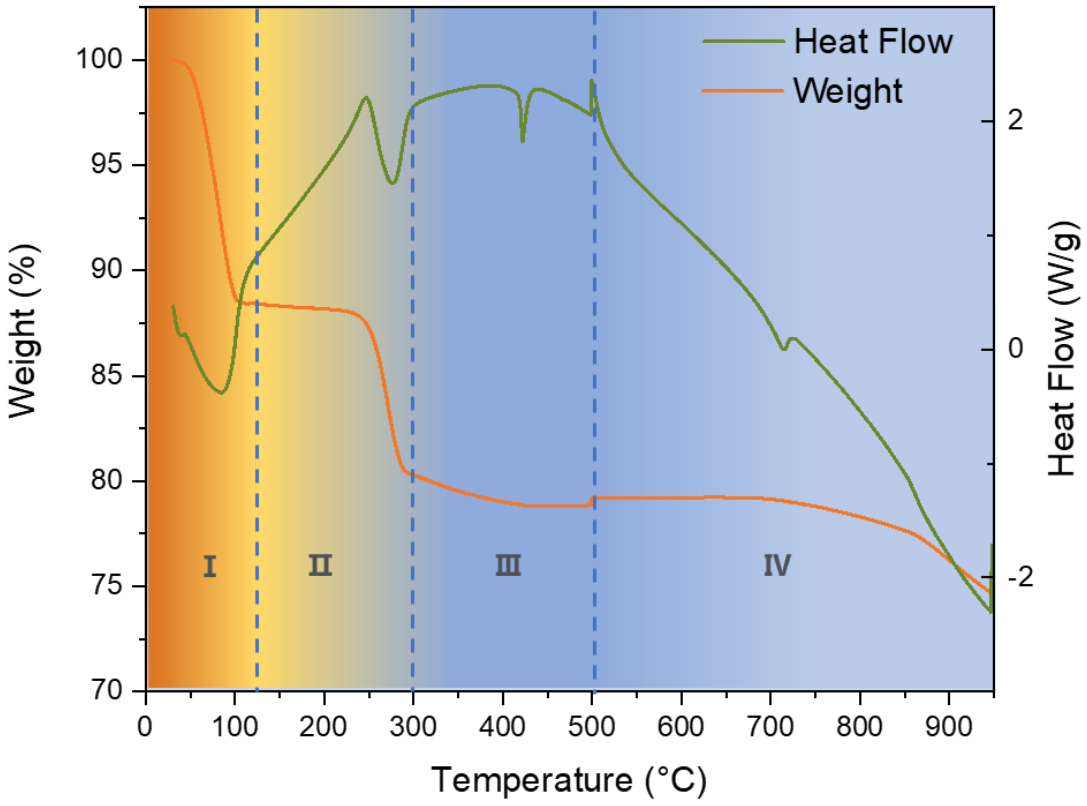

Figure 4-3 The thermogravimetric analysis (TGA) and differential scanning calorimetry (DSC) measurement during the upcycling process. Zone I : $LiOH.H_2O$ lost H_2O to form LiOH. Zone II : $Ni(OH)_2$ melts and decomposes into NiO_x. Zone III : LiOH starts to melt. NiO_x and D-NCM merge into LiOH solution. Zone IV: DNCM starts to decompose and reacts with NiO_x.

Table 4-1 ICP result of pristine NCM particles, precursor mixtures and upcycled NCM particles.

Sample	Li	Ni	Co	Mn
D-NCM 111	0.901	0.334	0.335	0.332
T-NCM 433	1.006	0.401	0.294	0.305
U-NCM 433	1.025	0.377	0.309	0.314
D-NCM 111+ $Ni(OH)_2$(622)	0.597	0.594	0.200	0.206
T-NCM 622	1.04	0.612	0.189	0.200
U-NCM 622	1.061	0.599	0.202	0.207
D-NCM 111+$Ni(OH)_2$(811)	0.284	0.802	0.096	0.102
T-NCM 811	1.022	0.801	0.096	0.103
U-NCM 811	1.064	0.801	0.097	0.102

The ability to control the size of the upcycled particles has been investigated by tunning the sintering conditions. This process has revealed the occurrence of the well-known Ostwald ripening phenomenon, which is caused by variations in the solubility of smaller and larger particles in the surrounding medium. It affects the diffusion of Ni into D-NCM 111, merging in the mixture of $Ni(OH)_2$ and LiOH. By extending the sintering time from 10h to 15h at 900℃, the obvious growing trend of primary particle sizes has been observed in "U-NCM 811-900-10h", "U-NCM 811-900-12h" and "U-NCM 811-900-15h" with the D50 size of 1.8, 2.1, and 2.5 μm, respectively (**Figure 4-4**). Additionally, the smallest (1.6 μm) and largest (4.9 μm) D50 sizes are obtained for U-NCM 811-850-10h and U-NCM 811-925-15h. The morphology on temperature dependence can be ascribed to the higher solubility and mobility of the reactive components, allowing Ni diffusion and lithiation at higher temperature[149]. These manners of crystal growth have been observed in the

flux growth of oxides, suggesting that the crystal size increases with the reaction time and holding temperature[150, 151]. Thus, through the optimization of sintering duration and temperature, we were able to exert control over the morphology of the upcycled NCM 811 material. The conversion of particles and their morphology change was thus featured as the Ostwald ripening phenomenon, which occurs during the flux growth of oxides when D-NCM particles merge and grow at the expense of the Ni precursor via dissolution and precipitation.

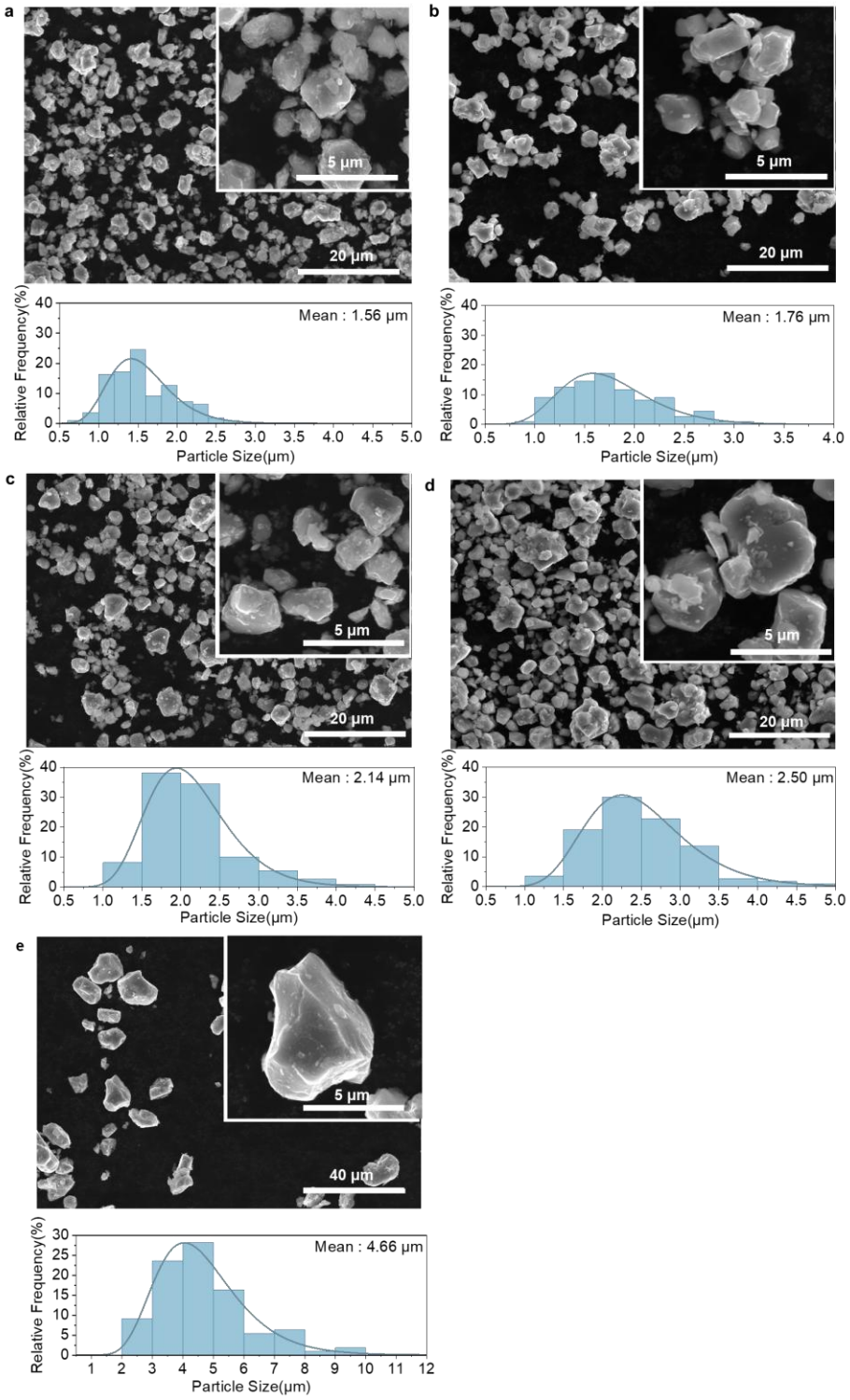

Figure 4-4 The scanning electron microscopic (SEM) images and size distributions of (a) U-NCM 811 -850-10h, (b) U-NCM 811-900-10h, (c) U-NCM 811-900-12h, (d) U-NCM 811-900-15h and (e) U-NCM 811-925-15h.

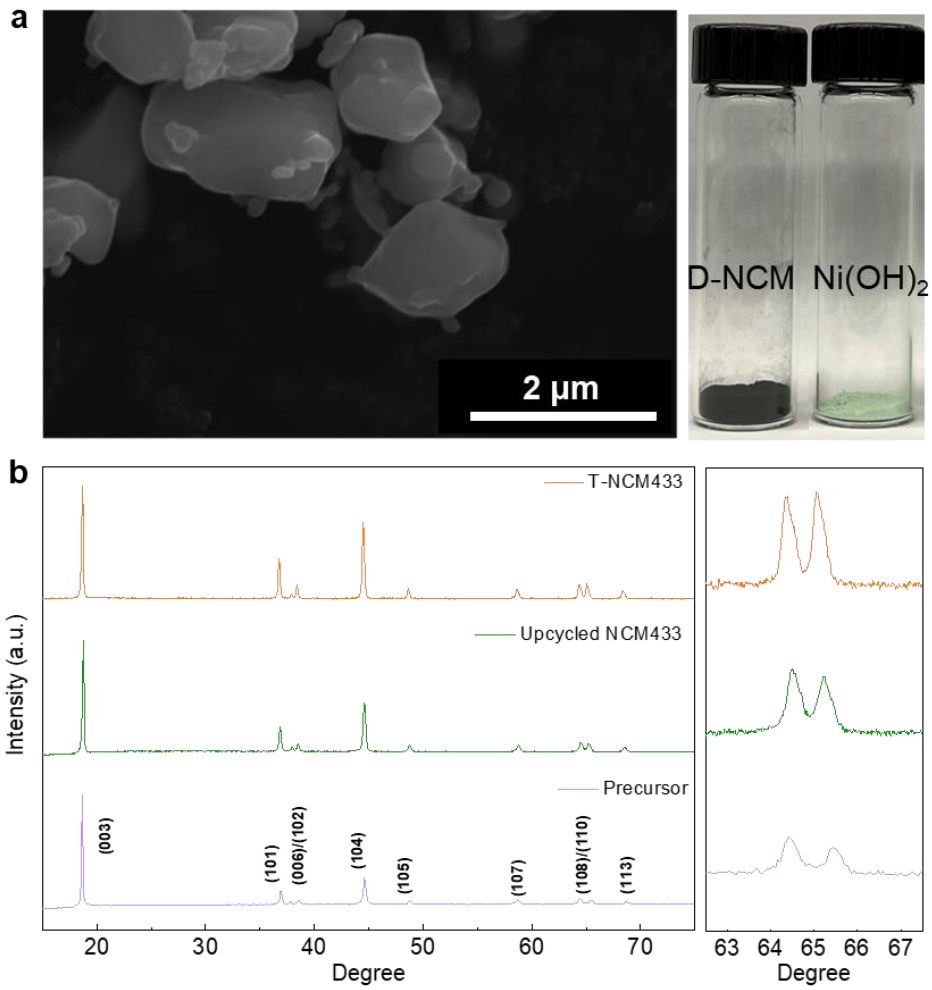

Figure 4-5 (a) The scanning electron microscopic (SEM) images of upcycled NCM 433. (b) The XRD patterns of pristine, upcycled NCM 433 and the precursors with enlargement of the regions in the range of 63.0-66.0°.

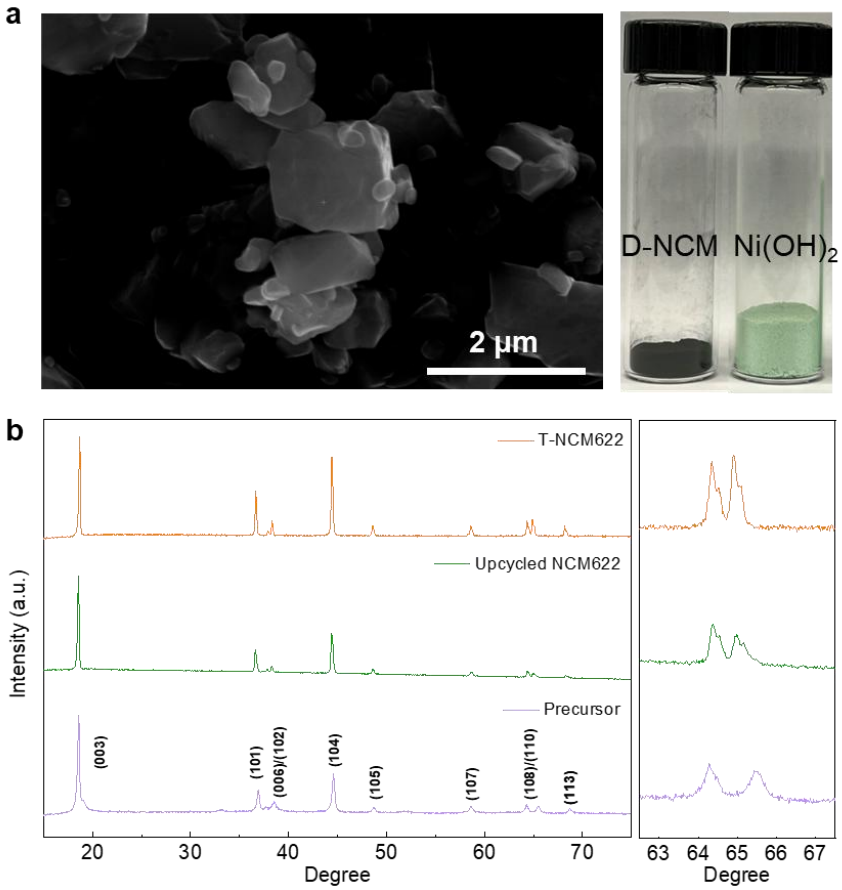

Figure 4-6 (a) The scanning electron microscopic (SEM) images of upcycled NCM 622. (b) The XRD patterns of pristine, upcycled NCM 622 and the precursors with enlargement of the regions in the range of 63.0-66.0°.

With the aforementioned direct upcycling method, the Ni-rich NCM single-crystals are obtained with desired compositions, confirmed by inductively coupled plasma mass spectrometry (ICP-MS) (**Table 4-1**). Note that the 10% Li-deficient D-NCM 111 ($Li_{0.901}Ni_{0.334}Co_{0.335}Mn_{0.331}O_2$) was converted into fully-lithiated NCM primary particles ($Li_{1.025}Ni_{0.377}Co_{0.309}Mn_{0.314}O_2$, $Li_{1.061}Ni_{0.599}Co_{0.202}Mn_{0.207}O_2$, and $Li_{1.064}Ni_{0.801}Co_{0.097}Mn_{0.102}O_2$) in the form of single-crystal particles. According to the Brunauer-Emmett-Teller (BET) analysis (**Table 4-2**), the U-NCM 811 shows a relatively higher surface area (1.74 m^2/g) than that of polycrystalline T-NCM 811(1.20 m^2/g). To illustrate the effectiveness of our developed synthesis method, SEM images and XRD

patterns of U-NCM 811 with optimized synthesis condition are shown in **Figure 4-7a and 2b.** Meanwhile, **Figure 4-5, 4-6** illustrates the XRD patterns of other upcycled cathode samples, including both NCM 433 and NCM 622. Rietveld refinement was performed on all the XRD patterns using the GSAS software with EXPGUI as the graphic user interface (**Table 4-3**). The standard pattern of a hexagonal α-$NaFeO_2$ type structure with the *R-3m* space group was validated in all samples without detectable phase impurities. The peak positions are well matched in all regenerated samples and the virgin polycrystalline NCM sample (T-NCM 433, T-NCM 622, and T-NCM 811), indicating that the pure high Ni phase was successfully constructed. Moreover, the separation of (108)/(110) peaks became narrower when the Ni content increased in NCM, indicating the smaller *c*/*a* ratio in a hexagonal lattice[152]. The regenerated samples maintain the same peak separation with T-NCM433, T-NCM622 and T-NCM811 while the precursor samples have larger distances. The refinement results show that the *c*-axis lattice parameter (14.257 **Å** in T- NCM 111, 14.248 **Å** in U-NCM 433, 14.198 **Å** in U-NCM 622, 14.179 **Å** in U-NCM 811) of the NCM cathodes decreases, while the *a*-axis parameter and lattice volume increase with the increase in the Ni content in the structure of the cathodes (2.859 **Å** in T-NCM 111, 2.867 **Å** in U-NCM 433, 2.871 **Å** in U-NCM 622, 2.874 **Å** in U-NCM 811) (**Table 4-2**)[153]. This can be attributed to the increased proportion of Ni^{3+} ions and the simultaneous decrease in the concentration of Mn^{4+} ions[154]. Furthermore, the peak intensity ratio of *I*(003)/ *I*(104) was above 1.85 in single-crystal samples compared to 1.44 in the pristine polycrystalline particles, which indicates the highly ordered lattice structure and lower Li/Ni mixing in single-crystal particles[155].

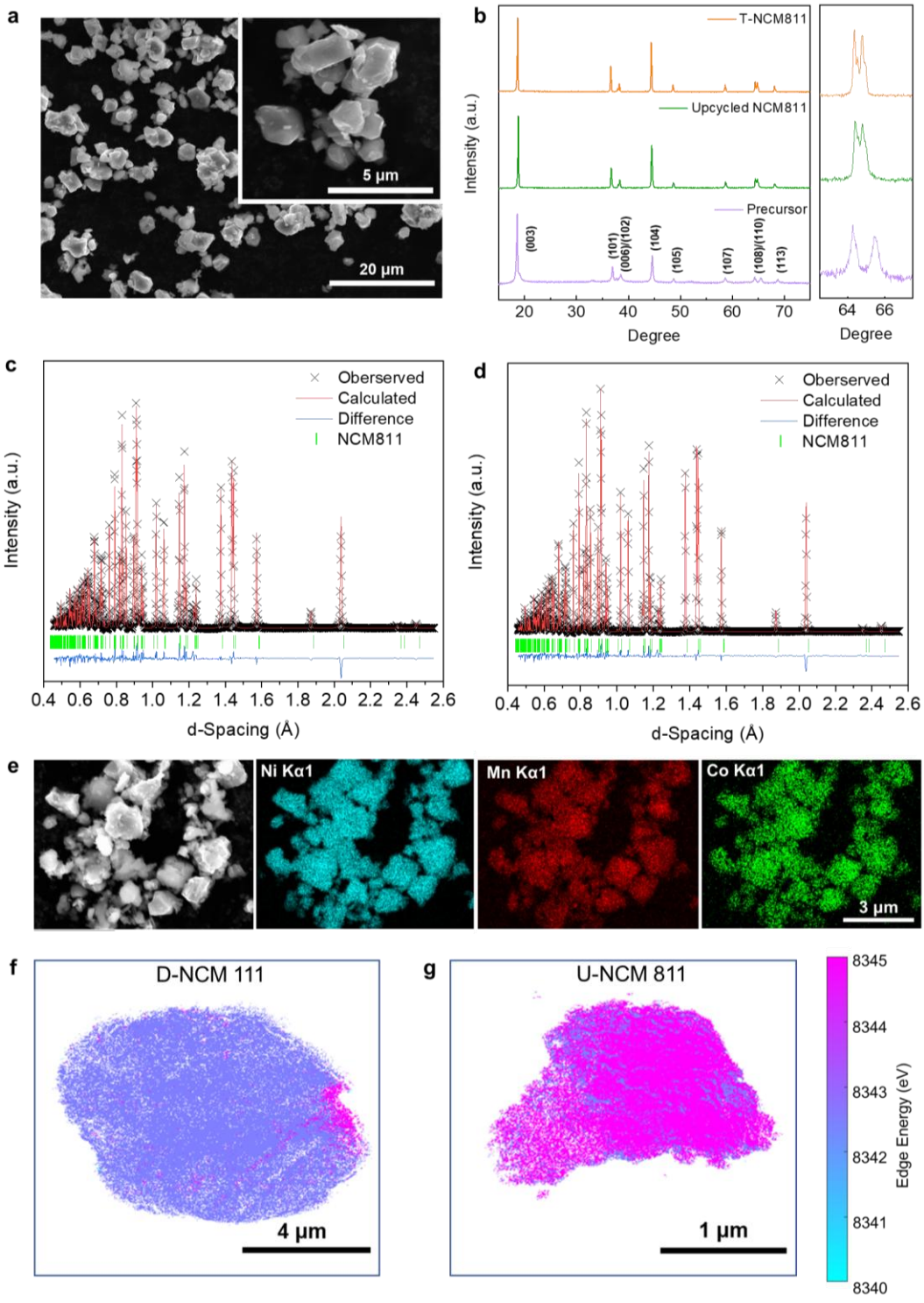

Figure 4-7 The phase determination and bulk information of nickel distribution of upcycled NCM 811. (a)The SEM images and size distribution of U-NCM 811 synthesized at optimized condition. (b)The XRD pattern of U-NCM 811, T-NCM 811 and precursors. The neutron diffraction patterns of (c) U-NCM 811 and (d) T-NCM 811. (e)The SEM-EDS image of U-NCM 811. The 2D XANES mapping image of Ni in (f) U-NCM 811 and (g) D-NCM 111.

Table 4-2 Brunauer-Emmett-Teller (BET) surface area analysis of pristine polycrystal NCM 811 and upcycled NCM 811.

Sample	Surface Area (m^2/g)
T-NCM 811(poly)	1.20
U-NCM 811	1.74

Table 4-3 XRD refinement results of upcycled NCM particles

Sample	a/Å	c/Å	(003)/(104)	R_{wp}/%	R/%
T-NCM 111	2.859	14.257	1.443	3.93	2.05
T-NCM 433	2.867	14.248	1.456	4.37	3.02
U-NCM 433	2.867	14.244	1.861	3.39	2.63
T-NCM 622	2.8712	14.225	1.427	3.44	3.12
U-NCM 622	2.8710	14.198	1.770	5.45	3.15
T-NCM 811	2.8760	14.218	1.485	3.45	3.09
U-NCM 811	2.8735	14.179	1.657	4.45	3.58

To further quantify the occupancy of Li sites and the percentage of Li/Ni anti-site defects in the lattice, neutron diffraction was conducted on the T-NCM 811 and U-NCM 811(**Figure 4-7a** and **4-7b**). Both samples demonstrate the O3 type layered α-$NaFeO_2$ structure, which consists of a closely packed oxygen array occupying the 6c sites. Li and transition metals (Ni, Co and Mn) occupy the octahedral sites along the (111) plane, named as 3a and 3b sites[156]. Typically, the Li/Ni anti-sites defects are composed of Li^+ and Ni^{2+} due to their closer radius (0.76 Å for Li^+, 0.69 Å for Ni^{2+})[157]. According to the Rietveld refinement results listed in **Table 4-2**, the upcycled NCM

811 contains less oxygen loss and less Ni^{2+} compared with pristine NCM 811 due to the highly ordered structure inhibiting the oxygen release. Hence, the lower Li/Ni mixing (3.54%) is observed in U-NCM 811 compared with 3.97% in T-NCM 811.

To confirm the uniformity of transition metal distribution in the U-NCM 811 sample, SEM-EDS was performed, and the related mappings are shown in **Figure 4-7e**. It is apparent that Ni, Co, and Mn are uniformly distributed along with the whole single-crystal particles. Similarly, the elemental distribution in upcycled NCM 433 and NCM 622 was also confirmed by SEM-EDS in **Figure 4-8** and **Figure 4-9**, respectively, showing uniform composition. Moreover, a 3D tomography by transmission X-ray microscopy (TXM) and 2D X-ray Absorption Near-Edge Structure (XANES) mapping with the resolution of 28.7 nm per pixel were performed for a detailed investigation on Ni valence distribution to reveal the element uniformity with good resolution. **Figure 4-10** demonstrate the volume renderings of a primary particle from U-NCM 811 and D-NCM 111. The spherical D-NCM111 particle with secondary structure is > 5 μm in diameter, while the single-crystal U-NCM 811 is ~ 1.8 μm with an anomalous shape. The 2D XANES mapping illustrates that the near-edge energy of Ni shifts to higher energy with good uniformity after the upcycling process (**Figure 4-7f-g**). Therefore, a well-defined bulk structure characterized by a highly uniform Ni distribution was achieved through this simple sintering method with limited lithium source, resulting in upcycled single-crystal NCM 811 products.

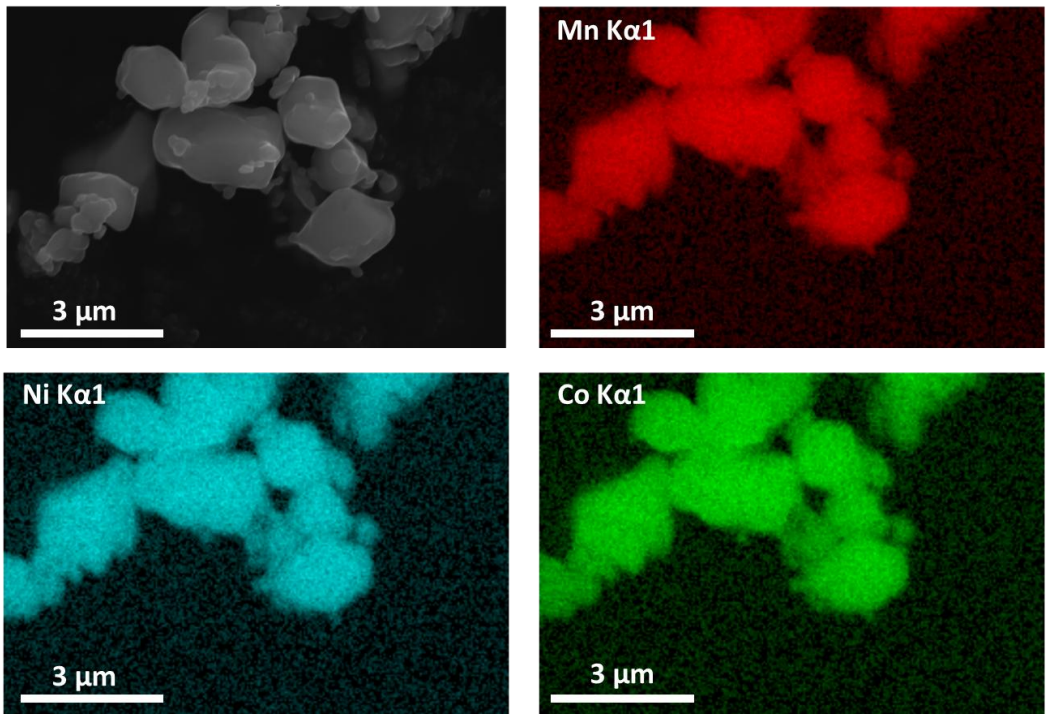

Figure 4-8 SEM-EDS mapping of U-NCM 433.

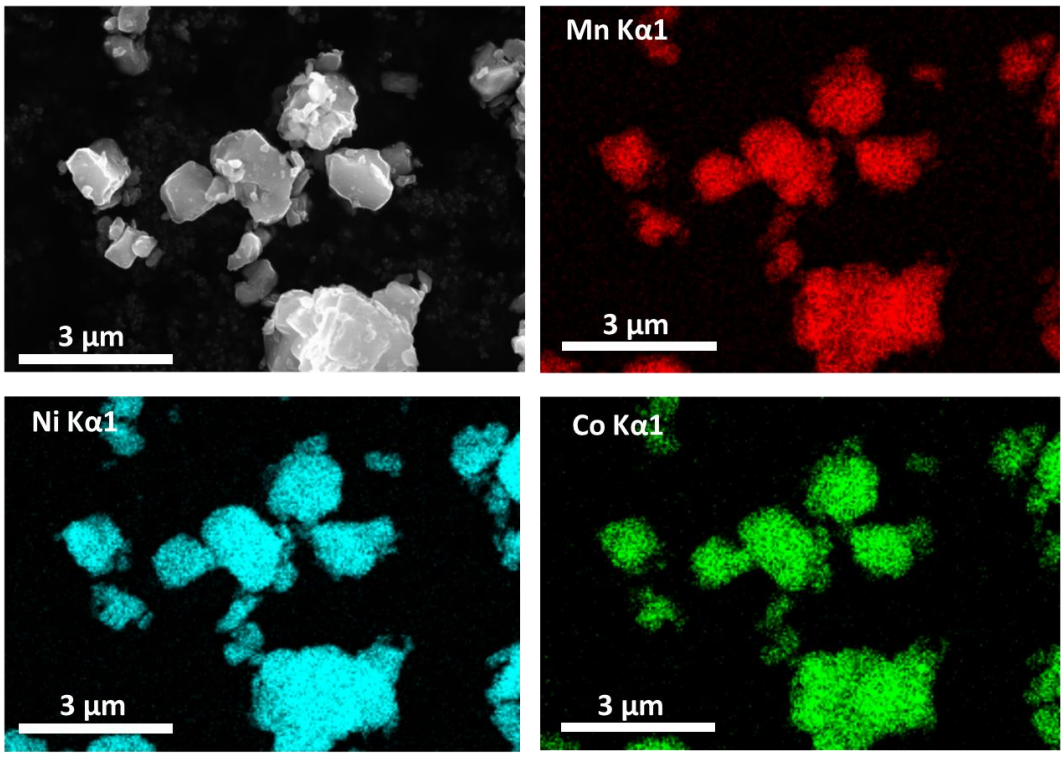

Figure 4-9 SEM-EDS mapping of U-NCM 622.

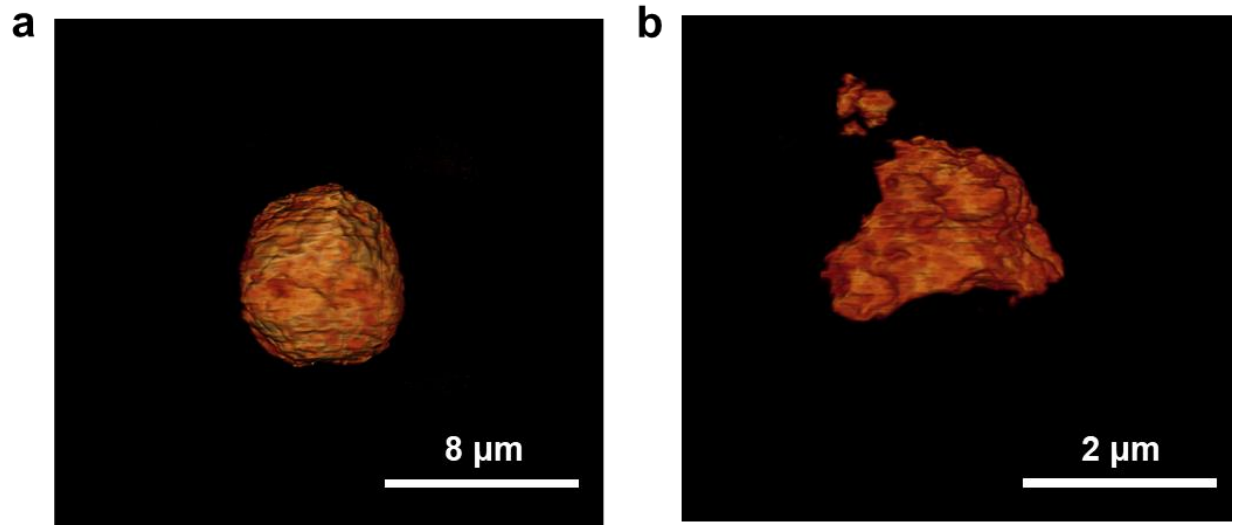

Figure 4-10 The screenshot of the 3D morphology of (a) D-NCM 111 and (b) U-NCM 811.

To investigate the valence distribution of transition metals from the upcycled cathode material, XPS was performed on the upcycled NCM 811 and D-NCM 111. The fitted Ni $2p_{3/2}$ spectra in **Figure 4-11a** illustrates an unneglectable amount of Ni^{3+} observed in D-NCM 111 due to a significant lithium deficiency in D-NCM 111. **Figure 4-11b** reveals a higher Ni^{3+}/Ni^{2+} ratio in upcycled NCM 811 in a fully-lithiated status, suggesting that the average valence of Ni increases when its content increases from 33% in D-NCM 111 to 80% in U-NCM 811. The XPS results are consistent with the observation from 2D XANES mapping.

To further understand the microstructure of upcycled materials, the FIB lamella of the U-NCM 811 was prepared and examined by STEM. **Figure 4-11c** shows the cross-sectional view of U-NCM 811 without any cavities, cracks, and clear grain boundaries. The high-resolution high-angle annular dark-field (HAADF)-STEM images with fast Fourier transform (FFT) pattern again confirm the pure phase of α-$NaFeO_2$-type layered structures (**Figure 4-11d**). EDS mapping illustrates the uniform local distribution of Ni, Mn and Co at tens of nanometer scale (**Figure 4-11e**). The linear scanning validates the distribution of Ni, Mn and Co with exact 8:1:1 ratio with high uniformity in the grain of interest (**Figure 4-11f**).

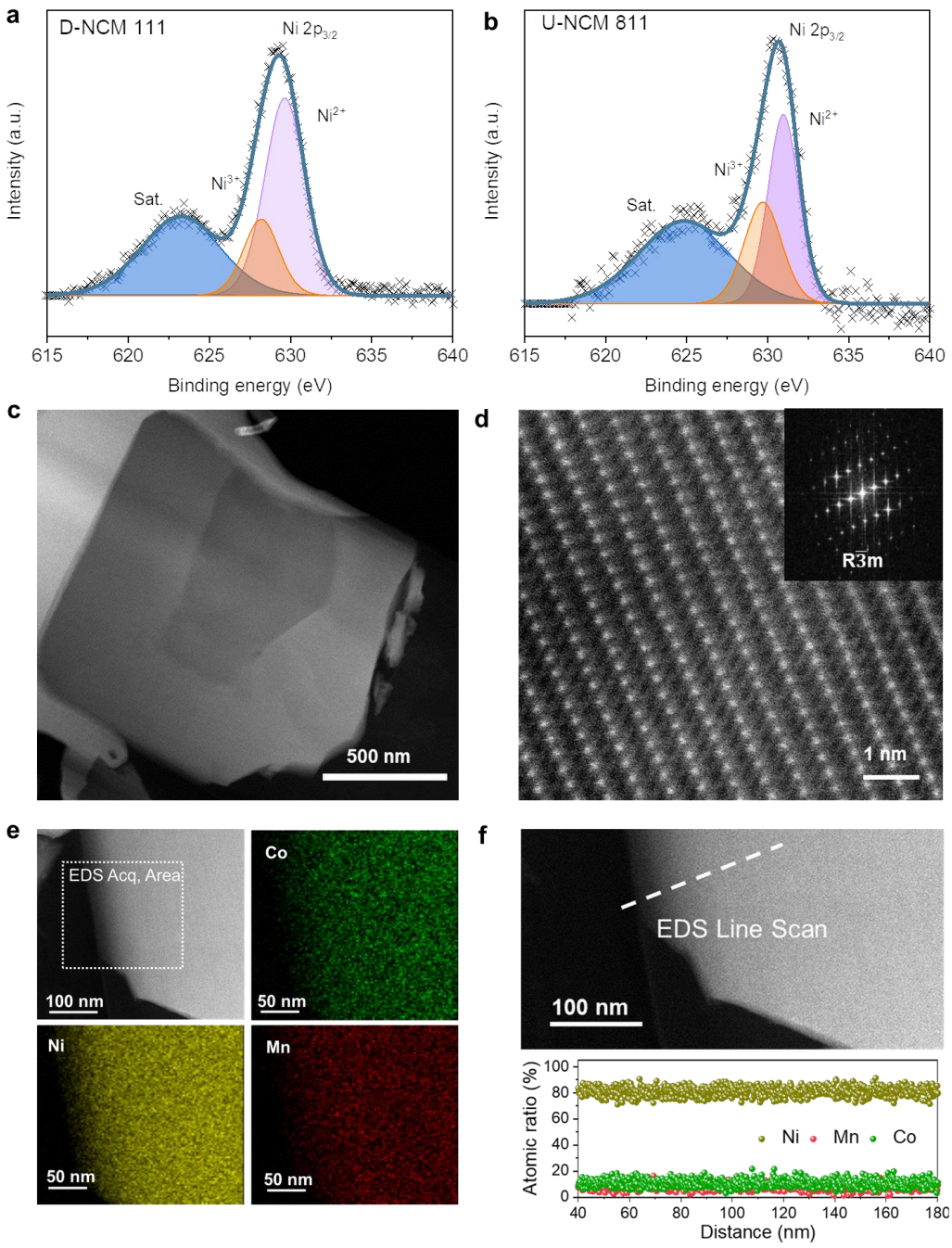

Figure 4-11 Microstructure and valence uniformity analysis of upcycled NCM 811. The XPS spectra of (a) D-NCM 111 and (b)U-NCM 811. (c) The cross-section image of U-NCM 811. (d) HAADF-STEM image of upcycled NCM 811 with the inserted image of the FFT pattern. (e)The TEM-EDS mapping of Ni, Co and Mn. (f) The EDS linear scanning with inserted elemental distribution intensity.

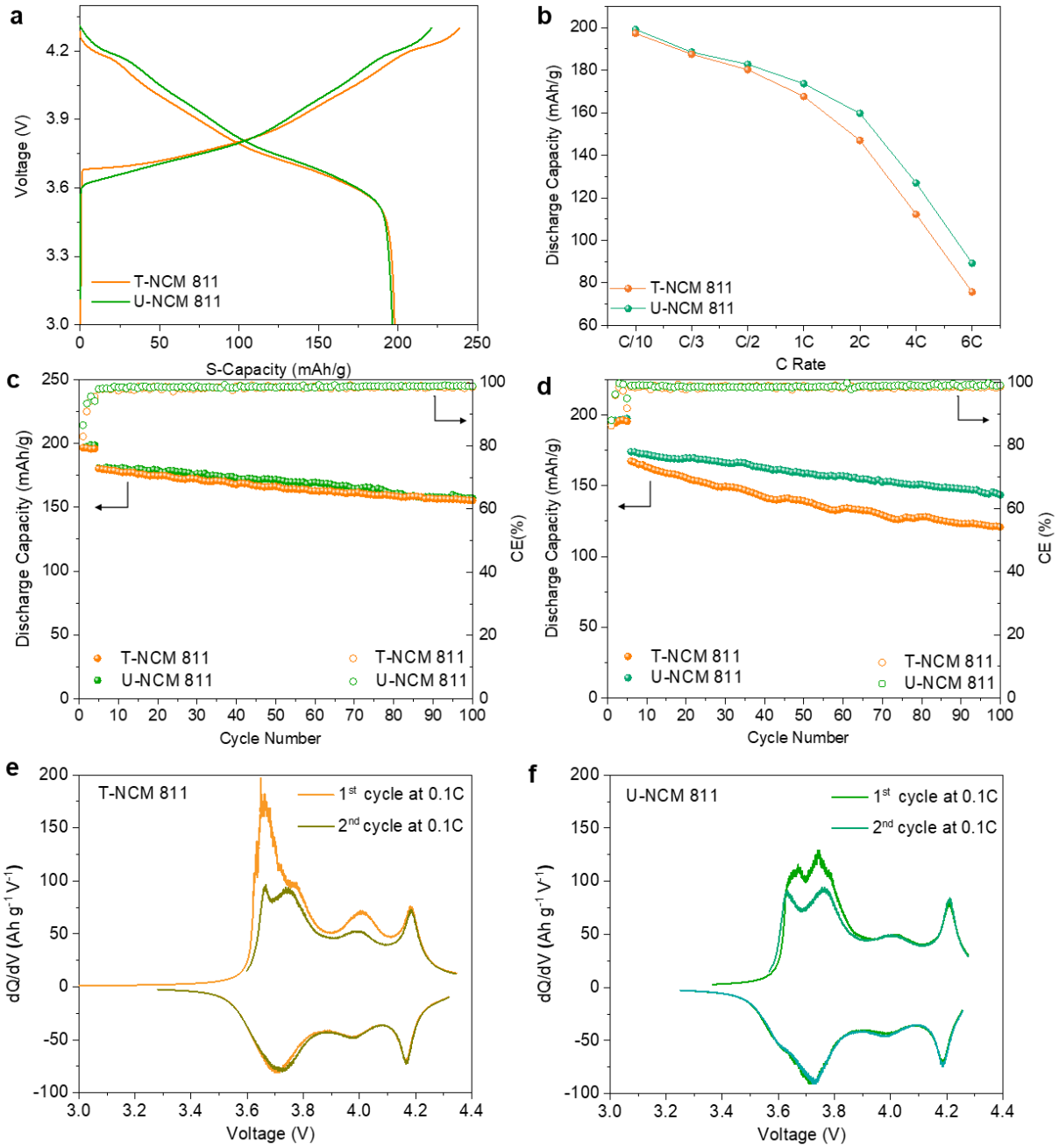

Figure 4-12 The electrochemical performance evaluation of upcycled materials. (a)Voltage profile at 0.1C and (b)The rate performance of T-NCM 811 and U-NCM 811. Cycling performance of T-NCM 811 and U-NCM 811 at (c)C/3 and (d)1C cycling. The dQ/dV plots of (e) U-NCM 811 and (f) T-NCM 811 at the first two activation cycles.

The electrochemical performance of the pristine and upcycled NMC811 cells was evaluated by half cells at the potential between 2.8 and 4.3 V (versus Li/Li^+). The U-NCM 811 exhibits a similar specific discharge capacity at 1st C/10 cycle (~198mAh/g) and similar retention under C/3 cycling (**Figure 4-12a-c**) compared with the pristine sample. Moreover, **Figure 4-12b** illustrates the superior rate performance of U-NCM 811 compared with controlled sample. The 1C/1C cycling data reveals the significant improvement of structural durability in upcycled NCM 811, ascribing to the single-crystal structural integrity. The U-NCM 811 shows 82.6% capacity retention after 100 cycles at 1C/1C cycling compared to only 72.2% retention in the pristine polycrystal sample (**Figure 4-12d**). To elaborate the difference between U-NCM 811 and T-NCM 811, the *d*Q/*d*V curves of the materials of interests are plotted in **Figure 4-12e** and **4-12f**. As shown the *d*Q/*d*V curve of the first two activation cycles, more irreversible capacity appears at ~3.8V in upcycled single-crystal NCM while a significant irreversible capacity is observed at ~4.1V in the pristine polycrystaline NCM. The extra charging capacity at low state of charge (SOC) may be ascribed to the H1-M-H2 transition behavior in the single-crystal NCM 811, similar to that of $LiNiO_2$, triggered by the rearrangement of Li/vacancy ordering[158]. A sluggish redox kinetics at low SOC governed by ionic transport at low SOC in single-crystals is also confirmed by a recent study[159]. Generally, the *d*Q/*d*V feature could show the H1-M-H2 transition existing in the first activation cycle at slow rate. The smooth transition between H1 to H2 with M phase significantly reduces the strains and mechanical crack on the grain boundaries raised by the coexistence of H1 and H2 phase[160]. It could be one of the important factors leading to the high stability of upcycled single-crystal particles at a high rate. On the hand, without significant H1-M-H2 phase transition in lower Ni NCMs such as NCM 622, the difference of rate performance in upcycled NCM 622 and pristine sample is not as significant as that in NCM 811, which is only 88.1% vs 81.0% after

100 cycles at 1C/1C (**Figure S9**). Both pristine and upcycled NCM 622 cathodes show similar dQ/dV at ~4.1V (**Figure S10**), which demonstrates the said phenomenon could not be observed in lower Ni NCMs.

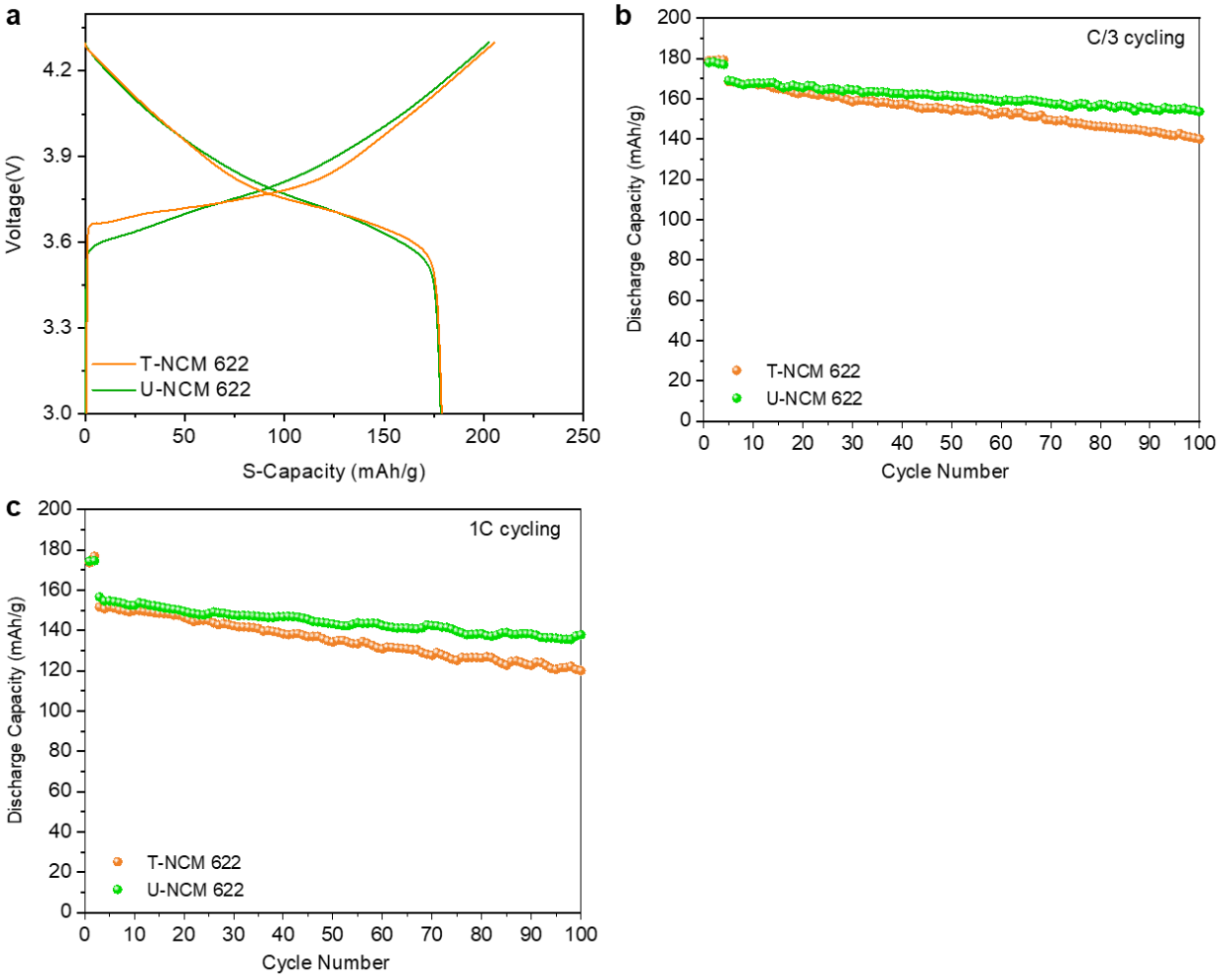

Figure 4-13 (a)Voltage profile and cycling stability of T-NCM 622 and U-NCM 622 at (b) C/3 and (c) 1C

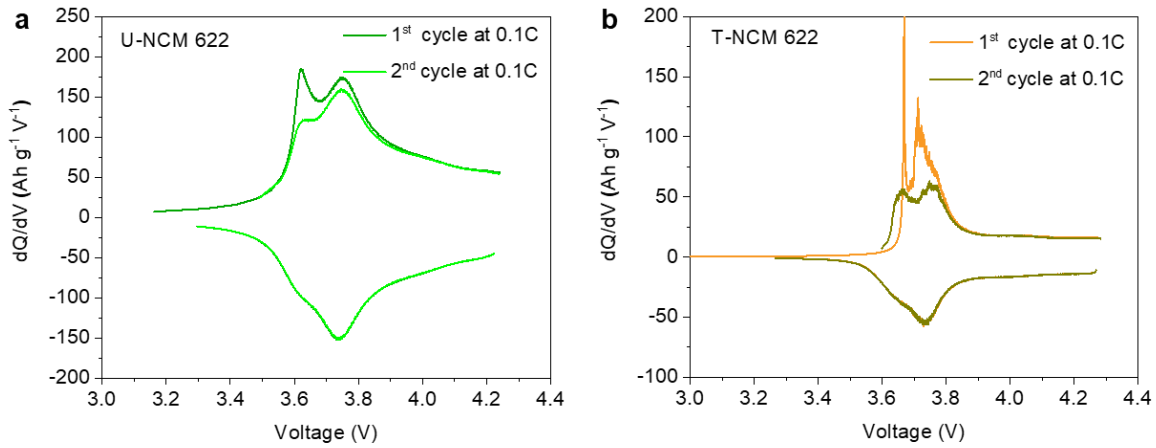

Figure 4-14 The dQ/dV plots of (a) U-NCM 622 and (b) T-NCM 622 at the first two activation cycles.

4.2.3 Conclusion

In summary, we successfully demonstrated an effective strategy for direct upcycling cathodes with minimized lithium source. Our approach involves converting spent polycrystalline NCM 111 into single-crystal high Ni NCM particles with desired Ni content and crystal size. We have also revealed a mechanism controlling the growth of NCM single-crystals, supported by a thorough investigation of the size distribution and improved Ni content in the upcycled single-crystal NCM. By leveraging this straightforward process, the desired composition and high phase purity were achieved in the upcycled single-crystal particles, leading to superior rate performance and improved cycling stability compared to the virgin polycrystalline cathodes. This study paves the way for a cost-effective and scalable upcycling approach for spent LIB materials, accommodating the diverse chemistries used in today's NCM cells.

4.2.4 Acknowledgements

Chapter 4, in full, is a reprint of the material “Direct Upcycling of Spent $LiNi_{0.33}Co_{0.33}Mn_{0.33}O_2$ Cathodes to Nickle-Rich NCMs Using Lean Precursors: from Polycrystals to Single-Crystals” as it appears in ACS Energy Letters Hongpeng Gao, Qizhang Yan, Duc Tran,

Xiaolu Yu, Haodong Liu, Mingqian Li, Weikang Li, Junlin Wu, Wei Tang, Varun Gupta, Jian Luo, Zheng Chen, 2023. The dissertation author was the primary investigator and author of this paper.

Chapter 5 Enhanced Electrolyte Transport and Kinetics in Fast-Charging Li-Ion Batteries

5.1 Introduction

The widespread adoption of lithium-ion battery (LIB) powered electric vehicles (EVs) is a vital step in the transition to a future based on sustainable energy sources[76].Though substantial progress has been made in extending the driving range of EVs due to advancements in LIB energy density, battery charging times lag far behind standard refueling periods for gas-powered automobiles. To address this, the US Department of Energy has set an ambitious extreme fast-charge (XFC) goal to achieve charging times of 15 minutes or less without a significant reduction in energy density or cycle life of the cell[161]. To achieve and exceed this benchmark, various limiting kinetic processes within high-energy LIBs must be optimized and understood. In principle, the kinetic limitations of LIB operation are considered to be diffusion of Li^+ within the bulk of the electrode materials, migration of Li^+ through the solid-electrolyte-interphase (SEI), diffusion of Li^+ through the electrolyte bulk, and charge-transfer at the electrode interphase[162, 163].

Though there is a deep history in the literature on improving the performance retention of battery electrode materials at high rate of 4 C or above, achieving adequate energy density and cycle stability in concert with the aforementioned charging times remains an immense challenge. Though alternative electrode materials designed for high-rate cycling exist, none have projected energy densities comparable to graphite anodes and transition-metal oxide cathodes[164, 165]. However, maintaining the electrode materials and loadings required for EV – level energy density results in extreme cyclability and safety tradeoffs for high-rate cycling. Cathode materials have been shown to face reduced capacity retention at high rates due to insufficient kinetics associated with micron-scale particles, placing undue strain on the electrode composite[161]. In this regard, previous works have found that despite significant structural changes and surface reorganization

as a result of high degrees of Li^+ loss, these losses in NMC cathodes are relatively recoverable[166-168]. Hence, the limiting electrode for the retention of energy and cycle-life is generally understood to be the anode[169-171]. Specifically, the proximity of the LiC_6 redox potential to Li/Li^+ has been shown to lead to Li metal plating, which leads to rapid cell failure, and causes immense safety concerns due to internal shorting from dendritic growth[167, 170, 171]. To mitigate these issues, researchers have demonstrated a variety of electrode design methods, including patterning of graphite anode architectures[172-174] and increasing of active surface area either by modification of the graphite itself or the inclusion of high-area carbons within the composite[175, 176]. Though they may be a promising route forward in some form, these strategies generally result in greater void space within the electrodes, increasing the minimum allowable electrolyte loading, giving rise to the reduced total energy density at scale[177, 178]. Though rational design of the charging protocol is also a vital direction, rapid storage kinetics is still necessary[179]. In this regard, a number of strategies exist for electrode optimization, but many phenomena at the electrode/electrolyte interphase remains to be fully discovered and addressed.

Design of the battery electrolyte has been demonstrated to have a transformational effect on the performance retention of LIBs under XFC conditions. Generally, improving the bulk ionic conductivity and transference number has been considered as a crucial strategy, where Colclasure et al. has demonstrated a correlation between Li^+ depletion at the interphase to the induction of Li plating[180, 181]. These effects are therefore exacerbated in practical cells with increased electrode loadings and non-negligible effects from alignment and porosity[181, 182]. Additionally, the inclusion of additives known to form low-impedance SEI components have been a focus of development[183-185]. In this regard, electrolyte composed of low-viscosity solvents which offer rapid Li^+ diffusion, e.g. methyl acetate (MA) have shown great promise for energy density retention at high rates[185-

[189]. Moreover, work from Du et al. has demonstrated that variations in salt chemistry may also produce such improvements[188]. However, the electrochemical stability of these unorthodox solvents tend to yield reduced cycle life compared to conventional carbonate systems, and raise concerns associated with gas generation during cycling[186]. In addition to the SEI and bulk transport, recent evidence suggests that the solvation structure of Li^+ within the electrolyte dictates the desolvation-related charge-transfer impedance at the interphase[190-194]. In this regard, electrolytes which improve performance at reduced temperatures, where Li^+ desolvation dictates overall kinetics, may prove to be a valuable design metric. Hence, discovery of a battery electrolyte with rapid Li+ transport, facile charge transfer, low-impedance interphases, and exceptional electrochemical stability is vital to enable 4 C or above charging and understanding the processes of interest at the electrolyte/electrode interphase under kinetic strain.

Herein, we present an analysis of the rate-induced anode failure of $LiNi_{0.6}Mn_{0.2}Co_{0.2}$ (NMC 622) || graphite full pouch cells employing conventional carbonate electrolytes when run under XFC conditions. We demonstrate clear evidence that the graphite anode in cells employing conventional electrolytes undergo severe capacity decay due to loss of Li through Li plating, dislocation of isolated graphite, and exfoliation-driven interstitial SEI formation due to insufficient charge-transfer kinetics. Further, we comprehensively address each of these failures with proper selection, design and application of a carboxylate ester-based electrolyte. This optimized electrolyte, 1 M lithium hexafluorophosphate ($LiPF_6$) methyl propionate (MP) + 10 % fluoroethylene carbonate (FEC) (M9F1) enabled the retention of 82.5 % cell energy density when charged at 4 C (15 min) compared to only 73.4 % for cells employing the conventional 1.2 M $LiPF_6$ in 3:7 ethylene carbonate (EC)/ethyl methyl carbonate (EMC) (Gen 2) blend. Moreover, cells employing M9F1 were found to demonstrate 88.2 % and 77.9 % capacity retention after 500

and 1000 cycles, respectively, compared to only 54.1 % and 12.4 % in Gen 2. The ability of M9F1 to circumvent the aforementioned failure conditions was found to be a result of improved ionic conductivity, high transference number, a favorable solvation structure allowing facile charge transfer, and the formation of a thin SEI of favorable composition (**Figure 5-1**). This work unambiguously presents the compounding failure modes of LIBs under XFC protocols while demonstrating the transformational effect of electrolyte composition on such processes and the resulting performance.

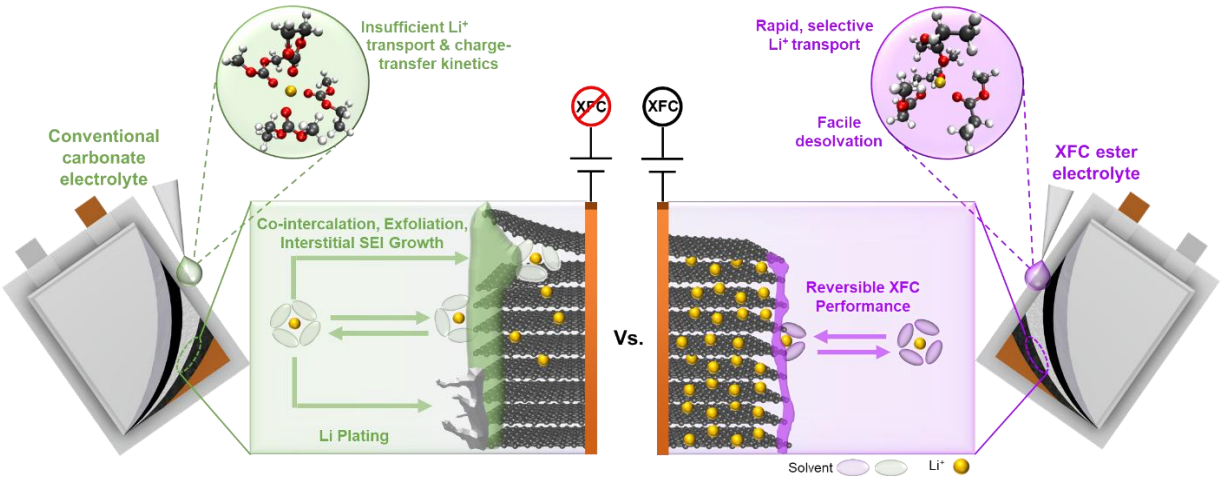

Figure 5-1 Impact of electrolyte chemistry on the typical failure modes of XFC lithium-ion batteries.

5.2 Enhanced Electrolyte Transport and Kinetics Mitigate Graphite Exfoliation and Li Plating in Fast-Charging Li-Ion Batteries

5.2.1. Experimental

5.2.1.1 Materials

LP40 (1.0 M LiPF6 in EC/DMC=50/50 (v/v)), methyl propionate (MP, 99%), methyl acetate (MA, anhydrous 99.5%) and methyl butyrate (MB, 99%) were purchased from Sigma. Gen 2 (1.2 M $LiPF_6$ in EC/EMC 3 : 7 w/w) and lithium hexafluorophosphate ($LiPF_6$) were purchased from Gotion and used as received. The Fluoroethylene carbonate (FEC, 98.0^{+}%) was purchased

from TCI America. MP, MA MB and FEC were soaked in molecular sieve (10 Angstrom, Sigma) over night before using.

5.2.1.2 Coin cell preparation

The cathode composition is $LiNi_{0.6}Co_{0.2}Mn_{0.2}O_2$ (Canrd Ltd.)/PVDF (*Kynar*® HSV 1800)/carbon black (Super-P) at 90:5:5 wt.% ratio. The areal capacity is 2.7 mAh cm^{-2}. The anode composition is graphite (Carnad Ltd.) / (*Kynar*® HSV 1800)/carbon black (Super-P) at 90:5:5 wt.% ratio. The anode areal capacity is 3 mAh cm^{-2}. The slurries of cathode and anode materials was casted on aluminum and copper foils, respectively. Both cathode and anode electrodes were transfer into vacuum oven for drying overnight at 120 °C and 80 °C, respectively. CR-2032 type coin cells were assembled with prepared cathodes and anodes (N/P ratio = 1.1) with a tri-layer membrane (Celgard 2325) as the separator soaked with 80 μL of electrolyte.

5.2.1.3 Electrochemical testing

All electrochemical data provided in this work were produced by CR2032 coin cells and heat-sealed multilayer pouch cells assembled in an Ar-filled glovebox kept at <0.5 ppm O_2 and <0.1 ppm H_2O. The NCM622||graphite dry pouch cells were made by Carnad Ltd. The dry pouch cells (Carnad Ltd) were filled with 1mL of electrolyte (4.7g Ah^{-1}) and sealed by vacuum sealer machine (MTI Corp.). The low-temperature data points were obtained from these cells inside a SolidCold C4-76A chamber for −40 °C testing. All potentiostatic tests were carried out on a Biologic VSP-300 potentiostat.

The NC622||graphite cells (CR-2032 type) were utilized for investigating the optimized MP/FEC ratio in for fast charging purposes. The coin cells were galvanostatically activated from 2.8V to 4.3 V at 0.1C (1C = 180 mAh g^{-1}) for 5 cycles before testing. The coulombic efficiency and specific capacity were analyzed at the first cycles of 4C/0.1C mode. Battery cyclers (Neware BTS-4000) were used for electrochemical cycling.

Pouch cells were galvanostatically activated from 2.8V to 4.3 V at 23mA (0.1C) for 5 cycles before testing. Both constant current (CC) with a charging voltage cutoff of 4.3 V and constant current- constant voltage (CC-CV) charging protocol with a charging time cutoff (15min for 4C and 10min for 6C) were operated for testing the capacity retention in designed electrolytes. For 15min/10min fast charging, the activated pouch cells were charged at a CC mode until reaching an upper voltage cutoff 4.3V and then held the potential until the total time (CC+CV) reached 15min/10min. The discharging rate was set at C/3 with a voltage cutoff of 2.7V. The galvanostatic testing was done on an Arbin LBT-10V5A system.

For low-temperature rate-capability test, the pouch cells were galvanostatically charged to 4.3V under room temperature, and then discharged to 2.8 V by different rate after switching the temperature to -40 °C. Cells are soaking for at least 2 hours to reach the target temperature. The galvanostatic testing of pouch cells was done on an Arbin LBT-10V5A system.EIS tests of NC622||graphite pouch cells were performed on a Biologic VSP-300 potentiostat with a 10 mV perturbation in the frequency range of 1 MHz to 100 mHz.

The transference numbers of all the electrolytes were measured by a potentiostatic polarization technique on a Biologic VSP-300 potentiostat. A Li||Li CR2032 coin cell with five Celgard 2325 separators filled by designed electrolyte was applied 5mV for 2h to obtain the initial current I_0. When the cation concentration is uniform and the current corresponds to both the cations and anions, the steady state current I_{ss}, is only attributed to the cations. The cell impedance before and after the polarization was obtained EIS spectra. Thus, the transference number was then calculated using the following equation:

$$t_+ = \frac{I_{SS}(\Delta V - I_0 R_0)}{I_0(\Delta V - I_{SS} R_{ss})}$$

5.2.1.4 Electrolytic thermal stability measurements

The thermogravimetric analysis (TGA) and differential scanning calorimetry (DSC) curve of electrolyte were tested in sealed aluminum pans by A Instruments™ Discovery SDT 650™ simultaneous DSC/TGA in UC San Diego Materials Research Science and Engineering Center (UCSD MRSEC).

5.2.1.5 Electrolytic conductivity measurements

The ionic conductivity of the electrolytes was measured by a customized stainless-steel two-electrode cells. Two polished stainless-steel (SS 316L) were spaced symmetrically as electrodes. The cell constant was calibrated from 0.447 to 80 mS cm^{-1} by using OAKTON standard conductivity solution. The data for ionic conductivities was measured by LabView Software. An ESPEC BTX-475 temperature chamber was utilized for testing data point at temperature from 60 °C to −60 °C. To maintain the cell at a set temperature, a 45 minutes intervals was applied during measurement. The ionic conductivities were calculated using the following equation: $\sigma_i = L / (A \times R)$, where L and A are the length and area of internal space between the electrodes, respectively, and R is the solution resistance.

$$\sigma = \frac{L}{A \times R}$$

5.2.1.6 Cell gassing test

Cell gassing tests were performed with NCM622||Gr pouch cells (cell capacity ~250 mAh). The evolution of gas volume during XFC cycling was measured via the Arrhenius method according to Dahn *et al*[195]. As shown in **Figure 5-2**, cells were weighed while submerged in deionized water (18MΩ cm) before and after the experiment. The volume of generated gas is

directly proportional to the difference in weight of the pouch cell while submerged in water. The volume of the gas generated after cycling was calculated by the following equation:

$$Volume\ of\ gas\ generation = \left(\frac{Weight\ of\ the\ cell\ in\ water\ before\ cycling}{} - \frac{Weight\ of\ the\ cell\ in\ water\ after\ cycling}{}\right)/Density\ of\ water$$

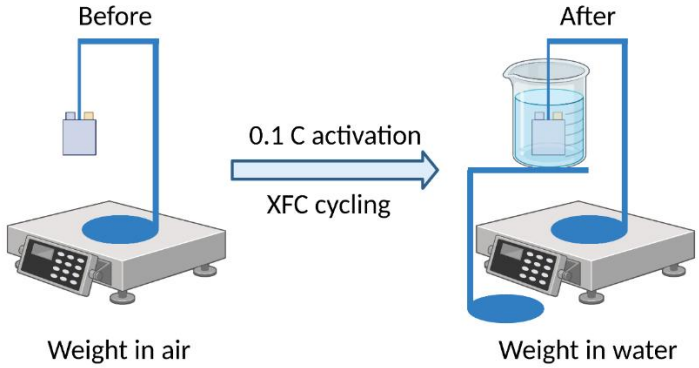

Figure 5-2 Scheme of cell gassing measurement.

5.2.1.7 Materials Characterization

The electrode cross-section experiments were performed using a FEI Scios DualBeam FIB/SEM. Cryo stage was used to prevent ion beam damage on the Li metal on the graphite electrodes. During ion beam milling, the cryo-stage temperature was maintained at around -180 °C. Cryo-TEM study was conducted using a JEOL 2800 TEM at 200 kV.

AC-STEM and EDX experiment was conducted using a JEOL JEM-ARM 300F at 300 kV. To prevent electron beam damage on the SEI, Gatan 626 cooling holder was used to maintain the sample temperature to about -170 °C during the TEM session. To fabricate the lamella samples, a

dual-beam focused ion beam FIB/SEM FEI Scios was used to lift-out the lamella from the cycled electrodes. Sample transfer in/out the FIB/SEM was performed using an air-free quick-loader (FEI) under vacuum. The sample transfer in/out the TEM was performed using an Ar-purged glove bag. The sample preparation and transfer were performed with minimum contact with ambient air. The detailed procedure was illustrated in Fig.S19.

XPS was performed using an AXIS Supra XPS from Kratos Analytical using a monochromatized Al Ka radiation under 10-9 Torr chamber pressure. The sample transfer was performed using the nitrogen filled glovebox directly attached to the XPS. For the depth profile experiment, a 5 keV Ar1000+ ion cluster was used to etch the electrode for 30 s. All spectra were analyzed using CasaXPS software.

Raman (Renishaw inVia/Bruker Innova) was performed with 532 nm illumination, provided by a Modu-Laser 50 mW Ar+ ion laser. The samples were prepared by placing the electrode onto a coverslip and sealed with Kapton tape in glovebox.

All X-ray diffraction (XRD) samples were prepared by placing the electrode onto a coverslip and sealed with Kapton tape in glovebox. Their crystal structures were examined by X-ray powder diffraction (XRD) employing a Rigaku Miniflex (Cu Kα radiation, λ=1.5406 Å) from scanning rate of 2 deg/min.

5.2.1.8 Neutron Diffraction mapping

The time-of-flight (TOF) powder neutron diffraction data were collected on VULCAN beamline at the Spallation Neutron Sources (SNS) of Oak Ridge National Lab (ORNL). The pouch cell was exposed to the neutron beam. An incident beam (5mm*5mm) of 0.7 to 3.5 Å bandwidth, allowing 0.5~2.5 Å d-space in the diffracted pattern of the ±90° 2q detector banks, was selected using the double-disk choppers at 30 Hz speed. High intensity mode was employed with Δd/d

~0.4%. Powder neutron diffraction data were collected in high intensity mode for a duration of 0.5 h and processed using VDRIVE software. Full pattern Rietveld refinement was performed using GSAS software, with EXPGUI interface.

5.2.1.9 Titration-gas chromatography analysis

The TGC experiments are performed using a Shimadzu GC-2010 Plus Tracera equipped with a barrier ionization discharge (BID) detector. The Split temperature was kept at 200 °C with a split ratio of 2.5 (split vent flow: 20.58 $ml \cdot min^{-1}$, column gas flow: 8.22 $ml \cdot min^{-1}$, purge flow: 0.5 $ml \cdot min^{-1}$). Column temperature (RT-Msieve 5A, 0.53 mm) was kept at 40 °C, and the BID detector was held at 235 °C. Helium (99.9999%) was used as the carrier gas, and the BID detector gas flow rate was 50 $ml \cdot min^{-1}$. The electrode sample was put in a septum sealed glass vial, and after injecting the 0.5 mL H_2SO_4 solution, the sample gases were injected into the machine via a 50 μL Gastight Hamilton syringe. The detailed quantification of lithium loss is described in **Figure. 5-3**.

a

Electrolyte system	Gen2	M9F1
Reversible capacity at 1st 4C cycle (mAh)	183.62	205.13
Total capacity density (mAh/cm^2)	2.09	2.33
Irreversible capacity LiC_x/Li^0 after 1000th 4C cycle (mAh/cm^2)	1.31	0.44
Reversible capacity after 1000th 4C cycle (mAh)	25.32	159.75
Reversible capacity after 1000th 4C cycle (mAh/cm^2)	0.29	1.82

b

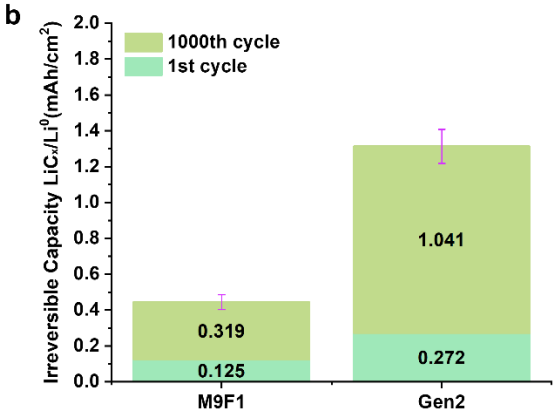

Figure 5-3 Quantification of lithium loss in cells after 1000 XFC cycles in the electrolytes of interest. a) The calculation results of TGC analysis. b) The irreversible capacity loss after 1000 XFC cycles in Gen2 and M9F1.

5.2.1.10 Computational methods

Standard MD simulations

Classical, fixed-charge Molecular Dynamics (MD) simulations were performed in LAMMPS using the General Amber forcefield for solvents and Li^+ with the anion described with OPLS-AA potentials and charges of Kumar et al[196]. Liquid simulation boxes were constructed from random distributions of the molecules, with 38 $LiPF_6$, 171 EC, and 257 EMC molecules for Gen 2 and 40 $LiPF_6$, 55 FEC, and 374 MP molecules for M9F1. In all cases the charges of the Li^+ and PF_6^- molecules were scaled to the high-frequency dielectric properties of the solvents present

in the system according to the method employed by Park *et al.*[197] which is 0.73 for M9F1 and 0.72 for Gen 2. Periodic boundary conditions were applied in all directions.

For each system, an initial energy minimization at 0 K (energy and force tolerances of 10-4) was performed to obtain the ground-state structure. After this, the system was slowly heated from 0 K to room temperature at constant volume over 0.01 ns using a Langevin thermostat, with a damping parameter of 100 ps. The system was then subjected to 5 cycles of quench-annealing dynamics in order to eliminate the persistence of any meta-stable states, where the temperature was slowly cycled between 298 K and 894 K with a ramp period 0.025 ns followed by 0.1 ns of dynamics at either temperature extreme. All 5 anneal cycles thus take 1.25 ns total. After annealing, the system was equilibrated in the constant temperature (Table S1), constant pressure (1bar) (NpT ensemble) for 1.5 ns. We resolved stresses in the system isotropically using the Andersen barostat (pressure relaxation constant of 1 ps). Finally, we performed 10 ns of constant volume, constant temperature (NVT) production dynamics. Visualized simulation boxes were generated in VMD.

MD Metadynamics simulations

MD simulation boxes after equilibration (Standard MD section) were used as initial configuration for the free energy sampling with the metadynamics protocol. This protocol was applied in a 2-D fashion with respect to Li^+/EMC or Li^+/MP distance (defined by center-of-mass) and coordination number based on the following definition of CN:

$$\sum_{i=1}^{N} \frac{1-\left(\frac{r_i}{r_0}\right)^p}{1-\left(\frac{r_i}{r_0}\right)^q}$$

where p=6 and q=12. r_i is the distance between Li^+ and the i-th coordinating atom. In this case only the solvent carbonyl oxygen was considered as a coordinating species, consistent with

observations from the RDF analysis. r_0 is the cut-off radius that defines atoms as inside or outside of the first solvation sphere, where *i* runs over the range that includes all possible coordinating atoms. The applied cut-off radius was 3.25 Angstroms The simulations were carried out using the Colvars module in LAMMPS. In **Table 5-1** we summarize the parameters of the metadynamics free energy sampling for various simulations: height of the Gaussian hills (kcal/mol), frequency of hill creation (steps), width of hills in Å for electrode distance or unitless for CN, and simulation time in ns. The free energy profiles shown in this work were averaged over the last 100 ns using Python and set to the same maximum free energy value for comparisson. 2-D profiles were generated in gnuplot.

Table 5-1 Metadynamics parameters for each simulation of interest.

Simulation	**Hill Height (kCal mol^{-1})**	**Hill Width (kCal mol^{-1})**	**Hill Creation Freq. (fs)**	**Simul. Time (ns)**
Gen 2 **2-D, 298 K** Li^+/EMC distance based on center-of-mass (1-10 Å) Li^+/solvent CN based on carbonyl oxygen of EMC **or** EC (1.5 – 6.0)	0.02	0.05	200	~ 400
M9F1 **2-D, 298 K** Li^+/MP distance based on center-of-mass (1-10 Å) Li^+/solvent CN based on carbonyl oxygen or MP **or** FEC (1.5 – 6.0)	0.02	0.05	200	~ 400

Quantum Chemistry Calculations

Quantum chemistry simulations were performed using the Q-Chem 5.1 quantum chemistry package. Ionization potential and electron affinity simulations (Figure S2) involved a geometry

optimization step at the M06-HF//6-31+G(d,p) level of theory followed by single point energy measurement in neutral, oxidized, and reduced states at the M06-HF//6-311++G** level of theory. Solvent removal simulations (Figure S8) involved a geometry optimization step at the B3LYP//6-31+G(d,p) level of theory where binding energy was calculated as follows:

$$\Delta E = \left(E_{Li^+(MP)_3} + E_{MP}\right) - E_{Li^+(MP)_4}$$

$$or$$

$$\Delta E = \left(E_{Li^+(EMC)_2(EC)} + E_{EMC}\right) - E_{Li^+(EMC)_3(EC)}$$

5.2.2 Results and discussions

5.2.2.1. Electrolyte Impact in Extreme Fast Charging LIBs

Carboxylate ester systems have been shown to improve the energy retention of cells at reduced temperature due to their beneficial physicochemical properties[186, 187, 194, 198]. We have applied similar MP/FEC electrolytes for improving low-temperature performance retention, establishing a clear correlation between systems designed for low-temperature and those designed for high-rate is a useful endeavor[199, 200]. Additionally, the well-understood, inherently kinetic temperature scaling relationships of this system makes it an ideal platform to investigate improvement strategies for the failure modes associated with long-term XFC cycling. However, the long-term cycling performance of cells utilizing such solvents requires consideration of their electrochemical stability and kinetic benefits. To evaluate the impact of ester selection, the long-term stability of 250 mAh NMC 622 || graphite pouches (**Figure 5-4**) was assessed by comparing methyl acetate (MA), MP, and methyl butyrate (MB) with a 10% FEC additive. This FEC additive has been previously demonstrated as the minimum amount required for stable graphite cycling[186, 199]. As shown in **Figure 5-5**, MA/FEC and MB/FEC were found to be less desirable for XFC applications, resulting in capacity retentions of 55.3% and 80.3% after 500 cycles. Instead, we find that the M9F1 system exhibited optimal characteristics, retaining 88.2% capacity under the same

conditions. We hypothesize that this optimum is a product of a balance between electrochemical stability and viscosity, where MP shows an improved reductivity compared to MA (**Figure 5-6**), at a reduced molecular size relative to MB. The MP/FEC ratio of 9:1 was also found to be optimal in terms of discharge capacity retention during a 4 C charge (**Figure 5-7**).

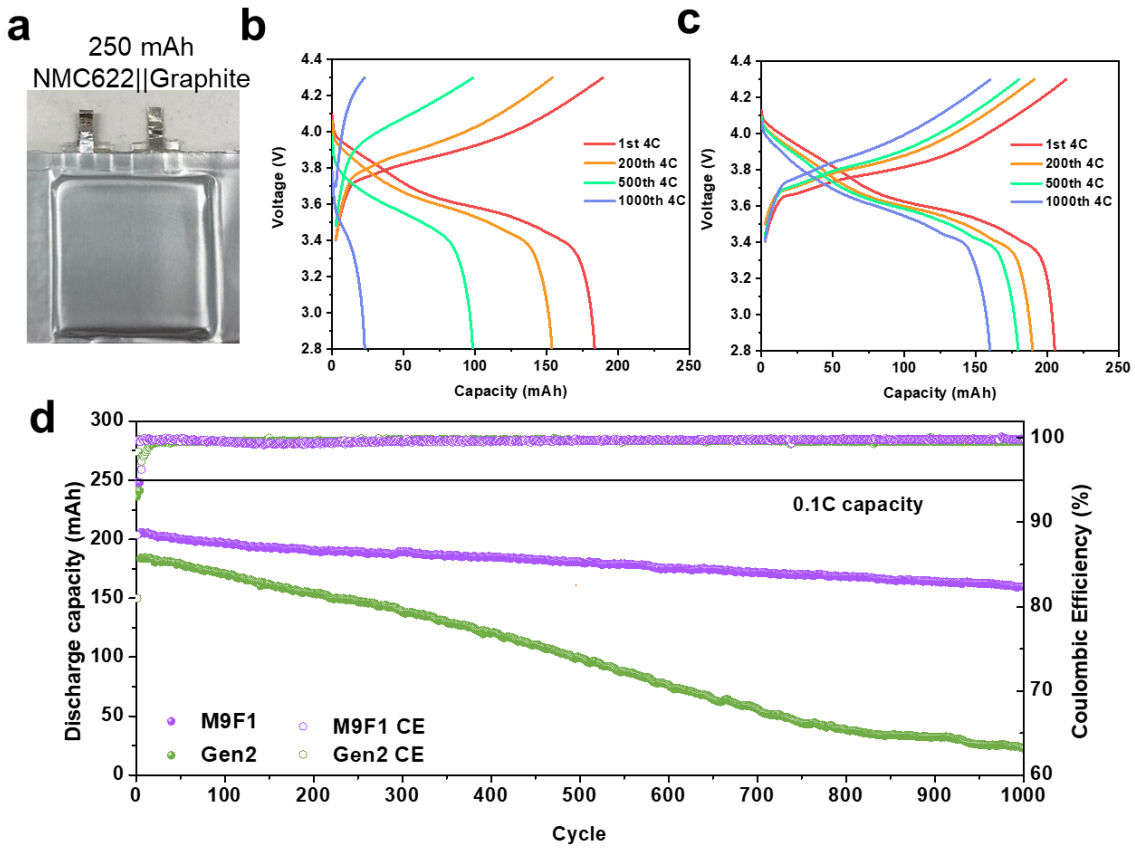

Figure 5-4 Dependence of XFC Performance on Electrolyte in Pouch Cells. a) Photograph of 250 mAh NMC 622||graphite pouch cells applied in this work. b) Cycling performance of pouch cells in electrolytes of interest. Voltage profiles over 4 C constant current cycling duration in c) Gen 2, and d) M9F1 electrolytes.

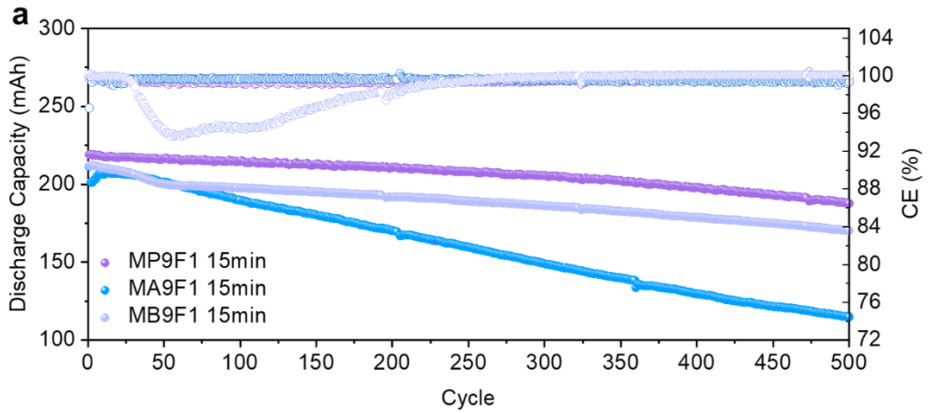

b

Electrolyte	t_+
LP40	0.34
Gen 2	0.35
M9F1	0.46
MA9F1	0.48
MB9F1	0.44

Figure 5-5 Extended electrochemical performance in ester-based electrolytes of interest. a) The extended XFC cycling performance in MA9F1, MB9F1, and MP9F1. b) Summary of Li^+ transference numbers of carbonate and carboxylate ester electrolyte.

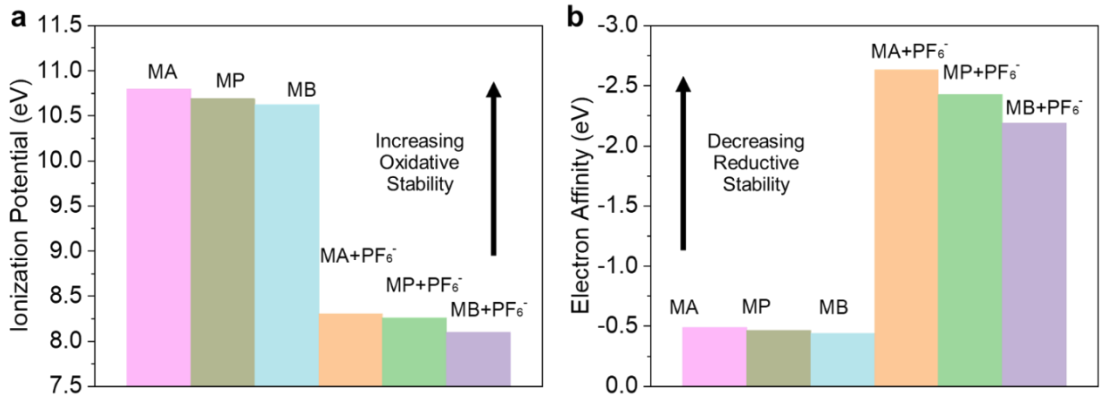

Figure 5-6 DFT calculation of ester solvents. a) Ionization potential of MA, MB, and MP with and without PF_6^-. b) Electron affinity of MA, MB, and MP with and without PF_6^-.

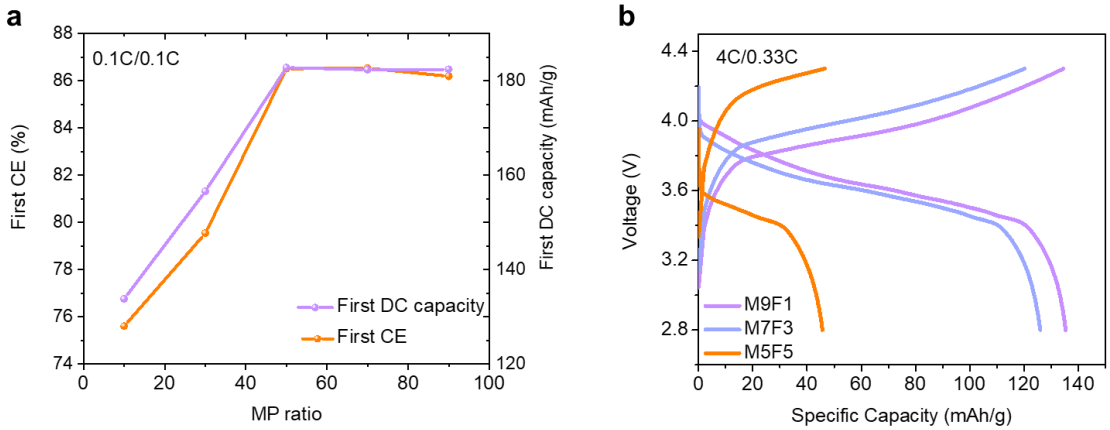

Figure 5-7 Investigation of composition optimization of MP/FEC system for XFC applications in homemade coin cells. a) The coulombic efficiency and discharge capacity of different MP ratios

in the MP/FEC system at the first 0.1C/0.1C activation cycle. b) Voltage profile at first 4C/0.33C cycle in each electrolyte.

To understand the performance advantages of M9F1 over a state-of-the-art carbonate system (Gen 2), pouch cells employing each electrolyte were constructed and subjected to a 4 C constant charging protocol and a C/3 discharge. Under such conditions, the cell employing Gen 2 exhibited 73.4% of its C/10 capacity in addition to a substantial and progressive increase in voltage polarization and a rapid decline in capacity to 54.1 % after 500 cycles (**Figure 5-4b, c**). In contrast, the M9F1 cell was found to retain 82.5% of C/10 energy and retains 88.2% and 77.9% of this capacity after 500 and 1000 cycles with minimal loss in output voltage over the cycling duration (**Figure 5-4b, d**). To ensure that M9F1 is also compatible with typical constant current-constant voltage (CC-CV) charging procedures, this protocol was also applied with a total charging time cutoff of 15 (4 C), 10 (6 C) and 6 (10 C) minutes. Under such conditions, M9F1 cells achieved 86.95%, 85.53% and 84.43% discharge capacity of its C/10 capacity for only 15min, 10min, and 6min charging, respectively (**Figure 5-8**). In addition, those M9F1 cells obtained a capacity retention of 85.9% and 71.8% after 500 cycles of 4C and 6C fast charging, respectively (**Figure 5-9**)[161]. To our knowledge, such cycling stabilities under 6C fast-charging conditions have only been produced by a specialized carbonate-phosphate-nitrile blend on the order of 50 repeated cycles[189]. Additionally, the improved XFC performance of M9F1 does not come at the expense of stability at typical rates, exhibiting stable long-term cycling at C/3 (**Figure 5-10**). Though such an improvement in XFC performance as a result of electrolyte design is valuable, understanding the physiochemical properties required for said improvement is vital for future progress.

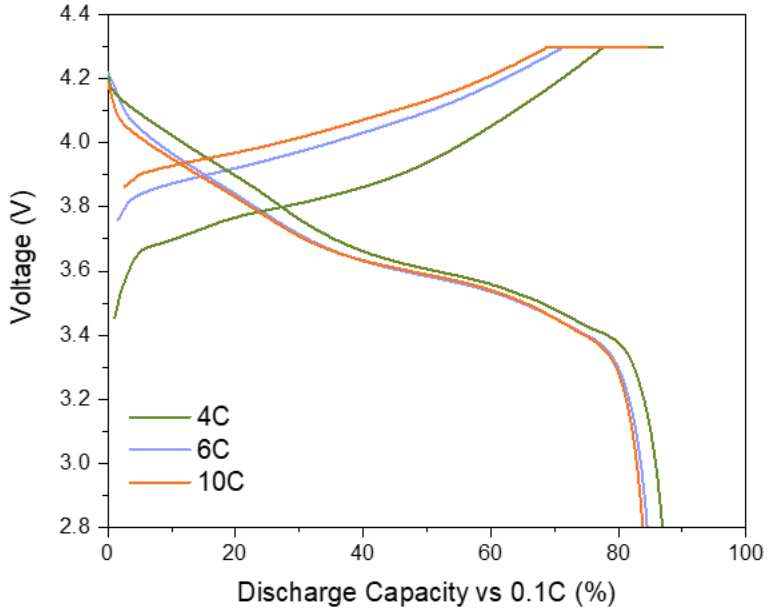

Figure 5-8 Rate performance of MP/FEC system. First cycle discharge capacity retention （vs. 0.1C discharge capacity) under 15min/10min/6min CCCV charging protocol in M9F1 electrolyte.

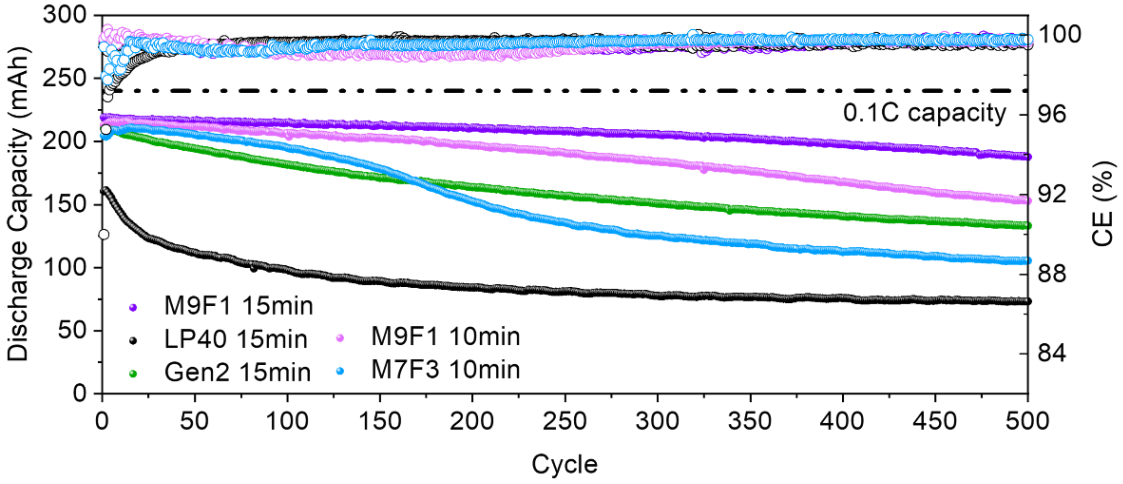

Figure 5-9 Dependence of extended XFC performance of pouch cells with different electrolytes. Cycling performance over 15min/10min CCCV charging protocol in M9F1, M7F3, Gen2, and LP40 electrolytes for 500 cycles.

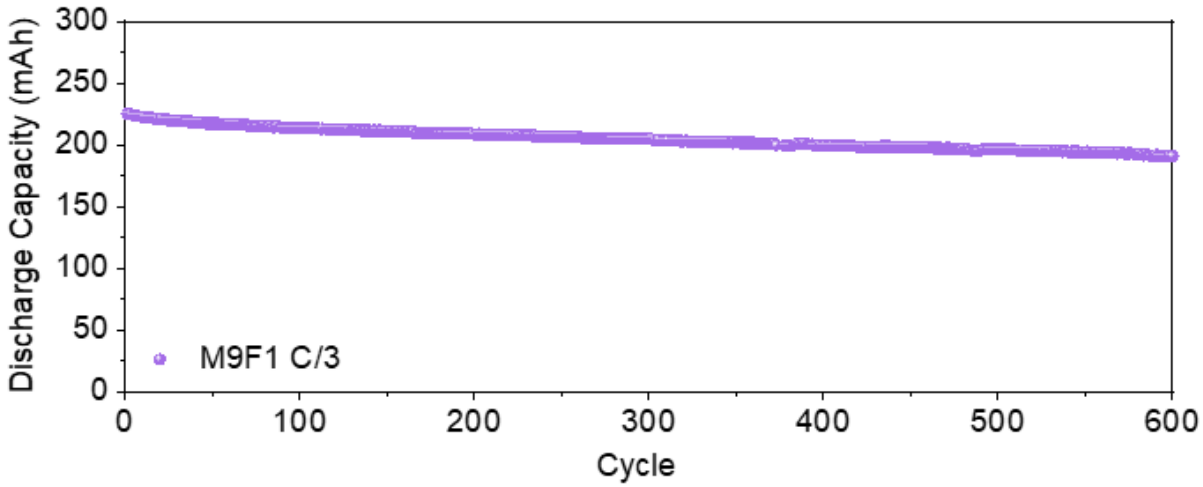

Figure 5-10 Cycling stability of pouch cells employing the M9F1 electrolyte under 0.33C/0.33C current density.

To provide a basis for the improvement in XFC performance and the following characterization of failure mode mitigation, we apply a series of experimental and computational characterization techniques to the electrolytes of interest. As shown in Figure 2a, the M9F1 system demonstrates an improved ionic conductivity of 12.1 mS cm^{-1} at room temperature compared to 8.25 mS cm^{-1} and 6.95 mS cm^{-1} for Gen2 and 1 M $LiPF_6$ in EC/diethyl carbonate (DEC) (1:1), (commonly referred to as LP40), respectively. Moreover, we find that M9F1 also exhibits enhanced retention of this conductivity at reduced temperatures, retaining 7.66 and 2.48 at -20 and -60 ^oC, respectively. The improved ionic conductivity of M9F1 does not come at the expense of Li^+ transport selectivity, where the t_{Li^+} of M9F1 was determined to be 0.46, compared to 0.35 and 0.34 in Gen 2 and LP40, respectively (**Figure 5-11b**). A similar simultaneous increase in ionic conductivity and t_{Li^+} was observed via the implementation of LiFSI, and is a rare but sought after electrolyte characteristic[188]. To further investigate the wide operation temperature window of MP/FEC electrolyte system, thermogravimetric analysis (TGA) and differential scanning calorimetry (DSC) are conducted among Gen 2, M9F1 and M7F3(**Figure 5-12**). Even though the M9F1 behaves an obvious volatile property compared with Gen 2 due to its ester- based solvent,

the thermal stability has been significant improved by blending with carbonate (FEC) in. Even under 45 °C cycling, M9F1 still shows a good capacity retention of 90.7% after 100 cycles, which is comparable to Gen 2 electrolyte (**Figure 5-13**) and with other ester systems. Though such rapid, selective Li^+ transport in the bulk electrolyte is known to be crucial for improved high-rate performance, factors impacting charge-transfer at the interphase are also crucial to consider.

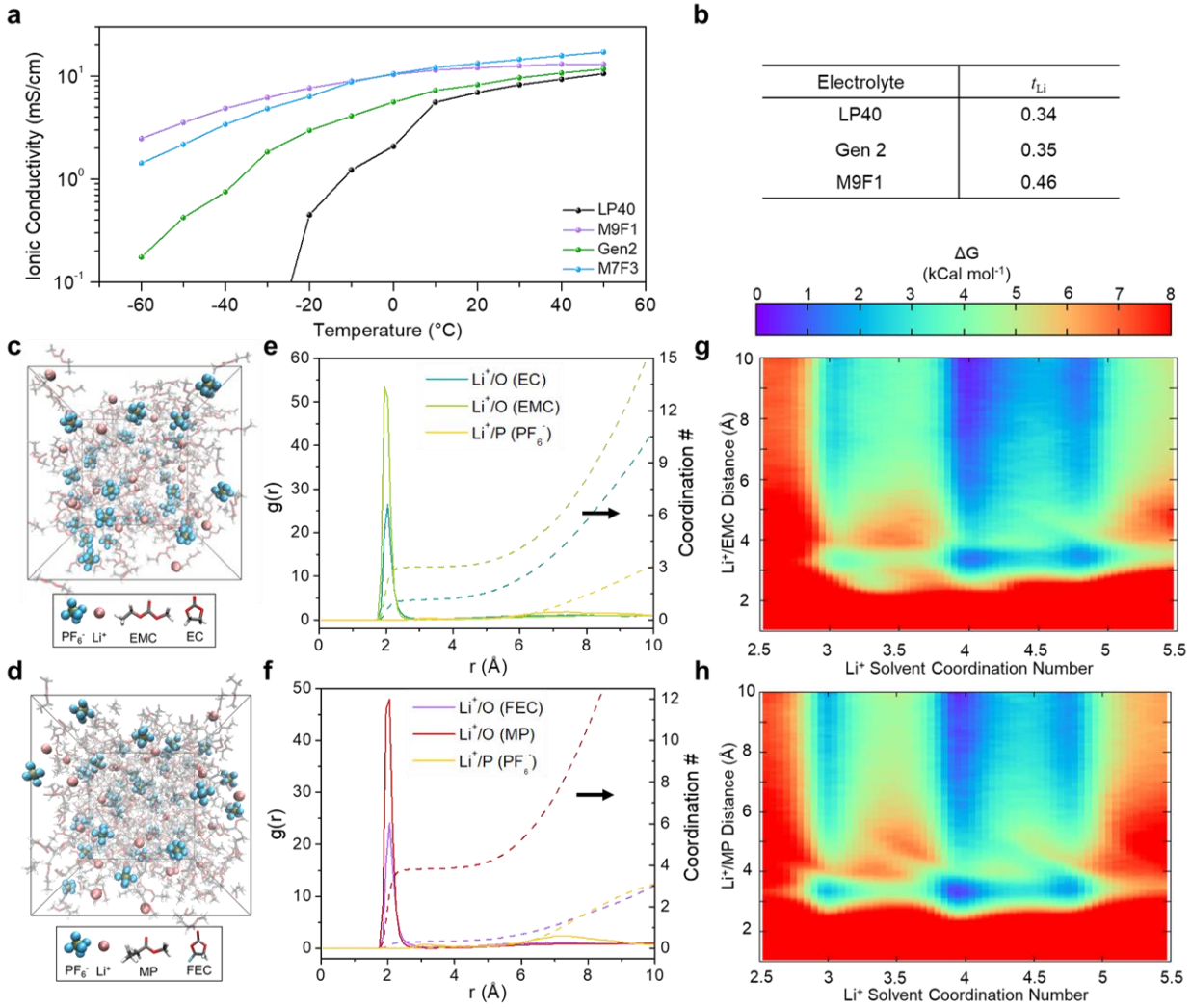

Figure 5-11 Experimental and Simulated Electrolyte Properties. Measured a) ionic conductivity, and b) Li+ transference numbers of carbonate and carboxylate ester electrolyte of interest. Snapshots of MD simulations involving c) Gen 2, and d) M9F1 electrolytes. Calculated rdf and coordination numbers with respect to Li+ extracted from MD of e) Gen 2, and f) M9F1. 2-D free energy profiles with respect to Li+/solvent coordination number and g) Li+/EMC distance in Gen 2, h) Li+/MP distance in M9F1.

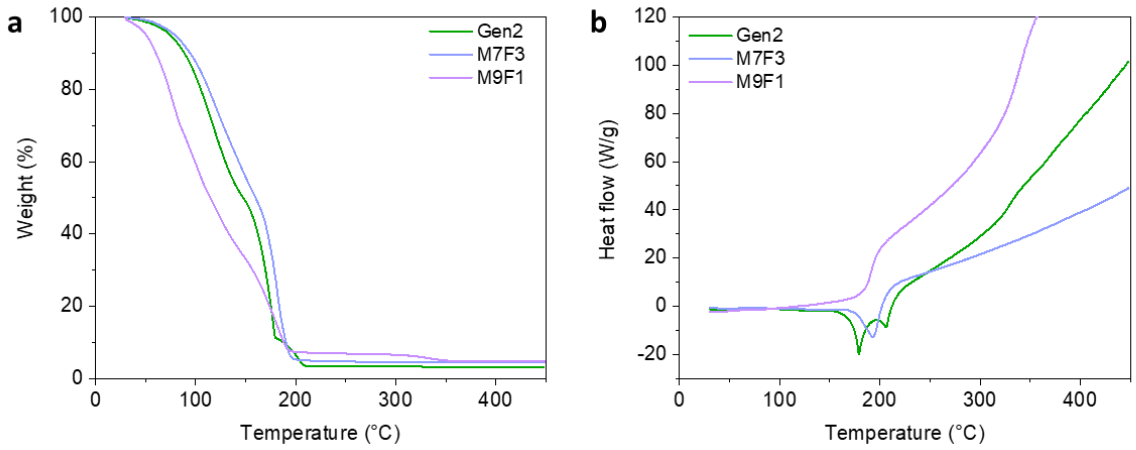

Figure 5-12 Investigation of thermal stability of MP/FEC system and Gen2 electrolyte. a) The thermogravimetric analysis (TGA) curve of Gen2, M9F1 and M7F3. b) The differential scanning calorimetry (DSC) curve of Gen2, M9F1 and M7F3.

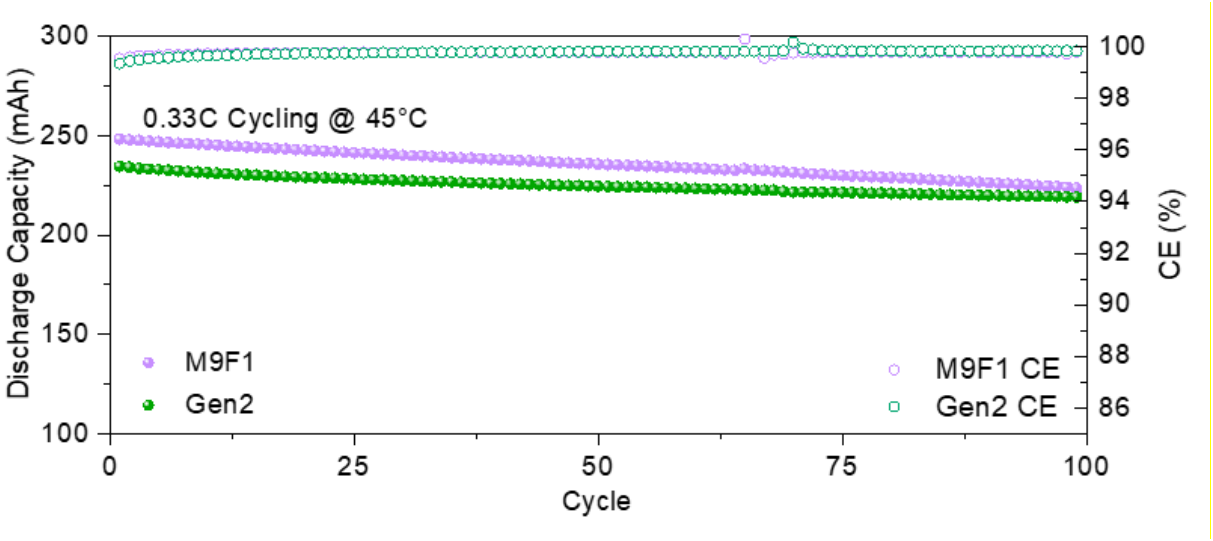

Figure 5-13 Cycling stability of MPFEC system in wide operation window. Cycling performance under 0.33C CCCV charging protocol in M9F1 and Gen2 at 45 °C.

There is growing consensus that the Li^+ desolvation portion of the charge-transfer process at the electrode is highly influential in electrochemical kinetics, and is fundamentally defined by the solvation structure of Li^+ in the electrolyte[170, 191, 194]. To gain a more precise understanding of the underlying structure and behavior of these electrolytes at an atomic level, molecular dynamics (MD) simulations of the systems of interest were carried out in the manner outlined in materials

and methods (**Figure 5-11c, d**). After equilibration, the radial distribution functions (RDFs) with respect to Li^+ in M9F1 and Gen 2 were computed and shown in **Figure 5-11e** and **5-11f**. In terms of probability, it was found that EC and EMC were relatively comparable (**Figure 5-11e**), resulting in an average solvation structure of $[Li(EMC)_{3.1}(EC)_{1.0}]^+$ (not equimolar due to overall molecular prevalence in the 7:3 mixture). On the other hand, we find that the most probable coordinating species in M9F1 is MP, resulting in an average structure of $[Li(MP)_{3.8}(FEC)_{0.3}]^+$. For both systems, it was found that there was negligible pairing between Li^+ and PF_6^-, indicating that the improved transference number of M9F1 is not a result of ion-pairing. Rather, we hypothesize that the improved ionic conductivity and transference number in M9F1 is a direct result of the advantageous transport of MP itself, as shown by its improved diffusivity relative to EMC (**Figure 5-14**). Though the movement of MP appears to be facile relative to EMC, whether or not such behavior results in facile desolvation is still relatively uncertain.

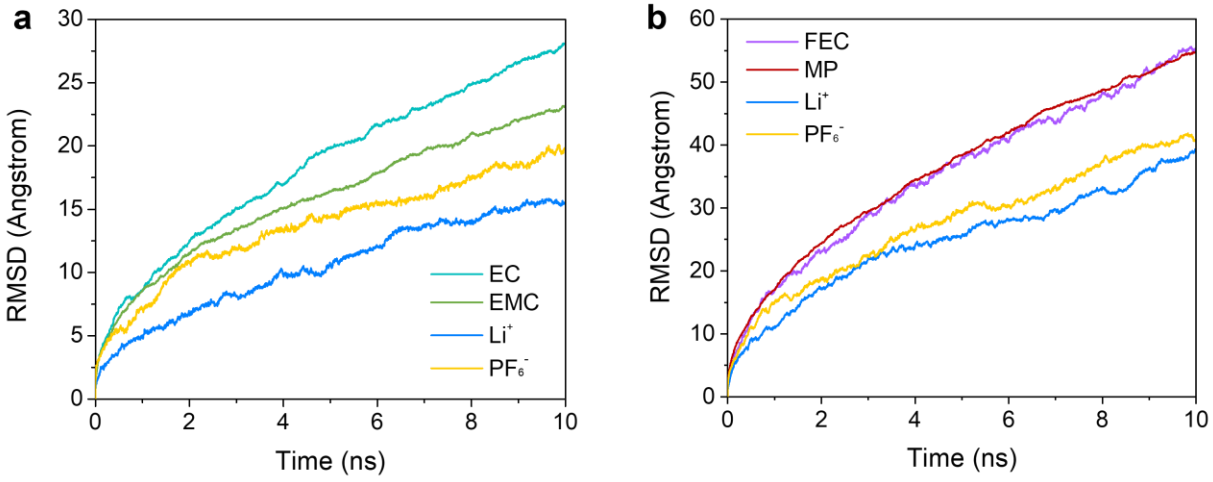

Figure 5-14 Root-mean-squared displacement of various electrolyte molecules during the duration of MD simulations in a) Gen 2, and b) M9F1 systems.

To answer this fundamental question, we apply a MD metadynamics free energy sampling technique which has been previously applied to understand the dynamic ion solvation behavior of Mg^{2+} and Li^{+} systems[201-204]. In doing so, we are able to explore multiple aspects of the electrolyte phase space, including states beyond what is thermally accessible through standard MD simulations. Though density functional theory (DFT) binding energy calculations are typically applied to understand this process, the above approach accounts for thermal motion and many body effects present in the electrolyte that would otherwise be ignored[205-207]. Specifically, we examine 2 dimensional free energy surfaces with respect to the coordination number of one Li^{+} and the distance between said Li^{+} and a coordinating solvent molecule (**Table 5-1**). We only consider removal of one coordinating solvent, which is generally considered to be the necessary step to induce electronic coupling between electrode and charge carrier, as the removal of all coordinating species typically produces activation barriers far too large to represent experimental measurements[170, 208]. It is important to note that this analysis is carried out in the bulk electrolyte without the inclusion of an explicit electrode to obtain an indication of desolvation energetics, where removal of one coordinating solvent molecule would otherwise be replaced by the electrode. While ideal, the inclusion of such an electrode would necessitate a 3-D free energy analysis, which is currently unfeasible.

When examining the 2-D free energy profiles shown in **Figures 5-11g** and **5-11h**, we consider a solvent removal pathway to be a reduction of coordination number (CN, *x*-axis) from the global minima of 4 to 3 with a simultaneous increase in the given EMC or MP distance. Note that this CN definition is strictly defined by cutoff distance (see Methods), in which the carbonyl oxygen of any solvent present in the system may contribute (MP, FEC, EMC, and EC). We take EMC/MP removal as the most probable removed species due to the increased dielectric of cyclic

carbonates as well as the higher average CN of these species shown in the RDF analysis **(Figure 5-11e, f**). As shown in **Figure 5-15**, this removal can proceed via 2 pathways, either by direct removal of the solvent (point A to C in **Fig. 5-15**), or by detachment of the carbonyl oxygen via solvent rotation followed by removal (point A to B to C in **Fig. 5-15**). When examining the profiles for Gen 2 (**Figure 5-11g**) and M9F1 (**Figure 5-11h**) from this perspective, it is clear that the M9F1 system displays a well-defined pathway (point A to C) for direct removal within the energy range of ~5 kCal mol^{-1}, whereas the Gen 2 system exceeds 7 kCal mol^{-1}. It is noteworthy that the removal of one such species is followed by the replacement of the coordination site by either a single-bonded oxygen or a PF_6^- (neither contribute to the defined CN), however the initial removal contributes largely to the energy penalty. While the energetics of this replacement may diverge slightly in the investigated systems, we find that the formation of the lower CN = 3 state in quantum chemistry simulations is significantly more facile in M9F1, which further indicates that MP removal from Li^+ in M9F1 faces a significantly lower barrier than EMC removal from Li^+ in Gen 2 (**Figure 5-16**). The facile desolvation behavior of M9F1 is also supported by the significant reduction of charge transfer impedance shown in **Figure 5-17**, and its substantially improved performance at -40 ^oC over Gen 2, where desolvation is known to define performance (**Figure 5-18**)[209, 210]. Despite the clear physiochemical advantages of M9F1, the effect of these properties on the LIB failure modes introduced by XFC conditions is necessary to fully understand the influence of electrolyte design on performance.

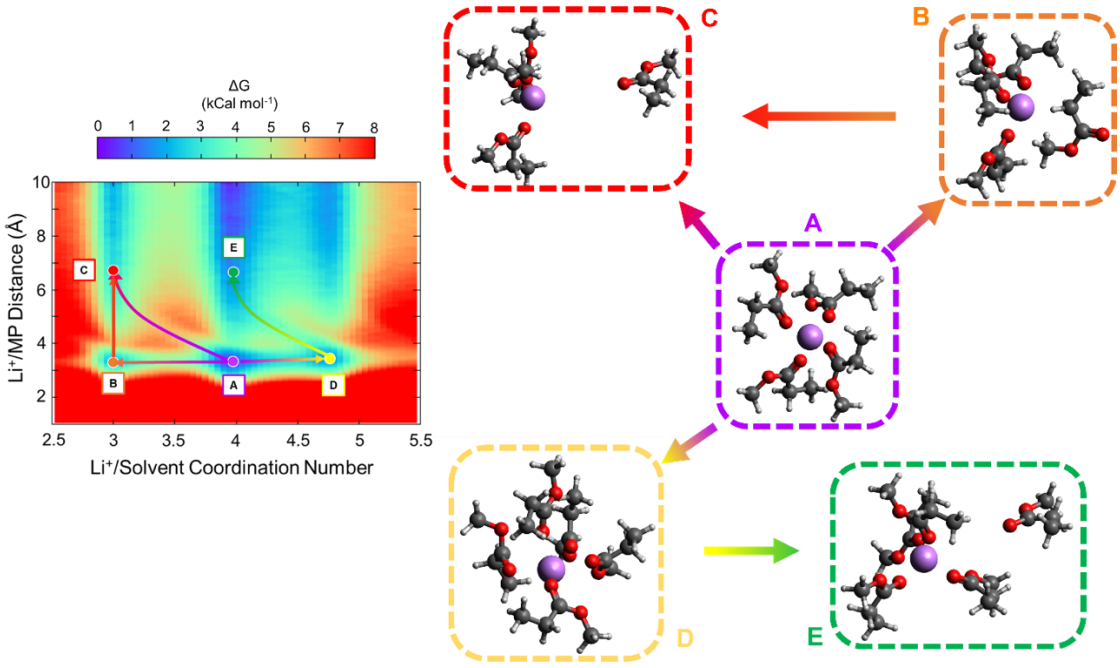

Figure 5-15 2-D Free energy surface breakdown for M9F1 with visualized molecular processes. Of the depicted processes, only A→B→C and A→C correspond to desolvation.

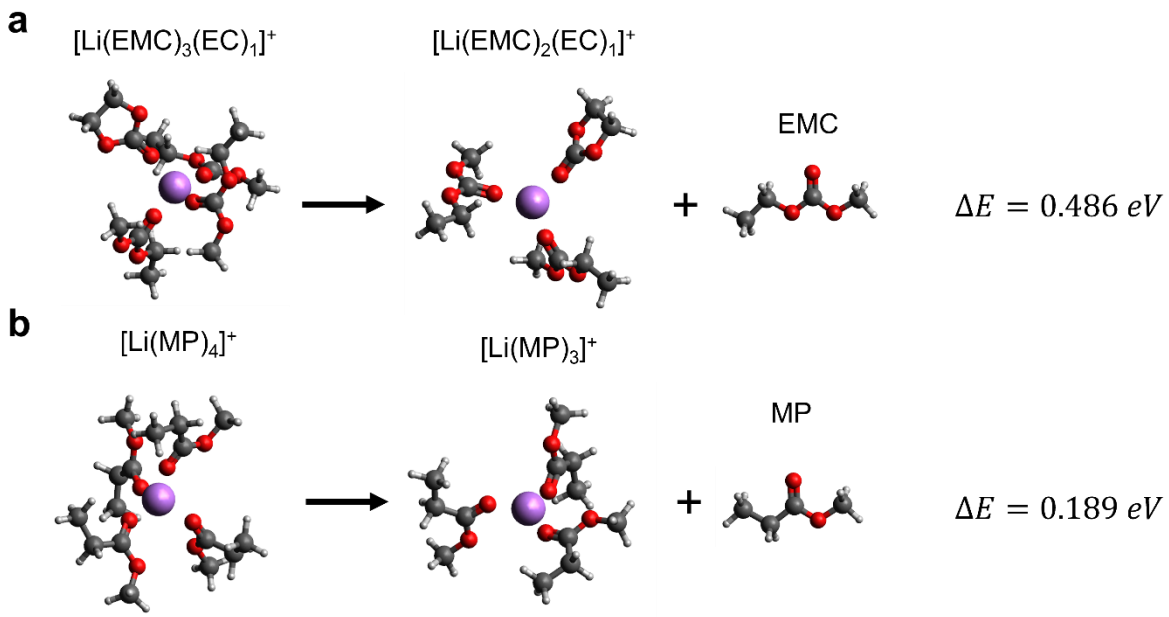

Figure 5-16 Binding energy of single component removal from average solvation shells found in a) Gen 2, and b) M9F1 electrolytes.

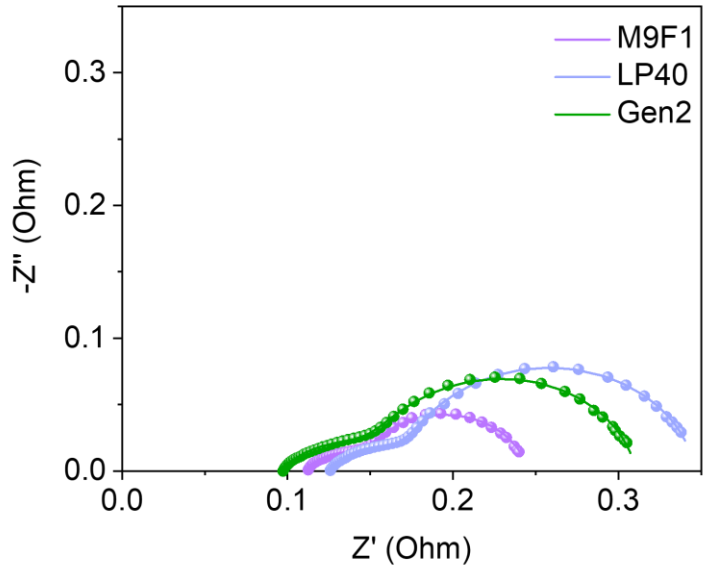

Figure 5-17 Dependence of charge transfer impedance on electrolytes in pouch cells. The EIS spectra after 20th XFC cycling at 50% SOC in pouch cells.

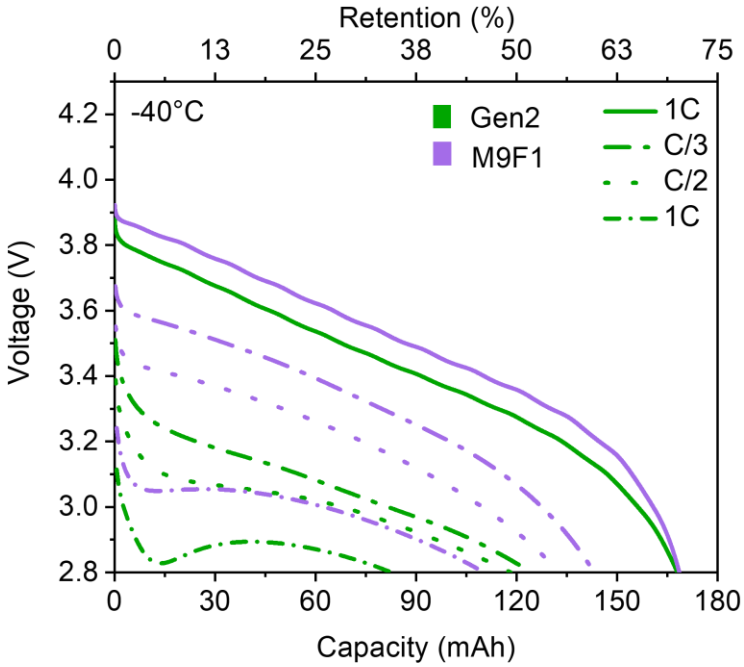

Figure 5-18 Dependence of low-temperature behavior on different electrolytes. Voltage profile of different discharge rates in Gen2 and M9F1 at -40 °C.

5.2.2.2. Identification and Mitigation of Active Li^+ Loss

To understand the origin of capacity loss in each cell, we conduct titration gas chromatography (TGC) analysis of graphite anodes in the discharged state after 1000 cycles in each electrolyte of interest. This technique allows for the differentiation between capacity lost to metallic Li and Li^+ in the SEI through quantification of H_2 produced after reaction of the ostensibly delithiated anode with a protic solvent (**Figure 5-20a**)[211, 212]. While TGC has been previously applied to quantify the amount of "dead" Li formed during Li metal cycling in various electrolytes, similar chromatography has been recently applied to graphite anodes cycled under fast-charge protocols, where reacted and unreacted in the SEI and the electrode, respectively can be differentiated[213, 214]. We apply TGC here to differentiate between Li lost to SEI formation, and remaining reactive Li, which may exist as dead Li^0, or LiC_x in each electrolyte of interest. It is crucial to note that the latter may be active or inactive, where active Li^+ would be trapped within the anode as a result of cathode degradation or increased anode polarization. When applied to the discharged graphite anodes harvested after 1000 XFC cycles in Gen 2 and M9F1, we find that 23 % of capacity loss after 1000 cycles in Gen 2 can be attributed to SEI growth, compared to only 3 % in M9F1. This 20 % difference between cells implies that SEI growth during cycling is continuous, and is likely a result of the growth of Li metal and/or the exfoliation of said graphite during XFC charge[161, 168]. This excessive capacity loss in Gen 2 clearly implies the formation of excessive reactive sites for decomposition during cycling, where the cell employing M9F1 produced only 0.17 mL of gas after 100 cycles compared to 0.66 mL in Gen 2 (**Figure 5-19**). Moreover, 63 % of the capacity loss after 1000 cycles in Gen 2 can be attributed to irreversible LiC_x or Li^0, compared to only 19 % in M9F1. The morphology evolution of cathodes reveals no significant changes after 1000 cycles fast cycling even at such a high amount of Li loss from NCM particles (**Figure 5-21**). Through monitoring the lattice parameters evolution from cathode side via neutron diffraction

mapping, we also find that this Li^+ loss is relatively uniform throughout the pouch cell (**Figure 5-22**). Such degradation is in agreement with the work from Liu et al, and is likely a result of loss in Li^+ inventory due to the aforementioned effects.[9] However, the origin of this excessive SEI growth and irreversible Li requires further characterization.

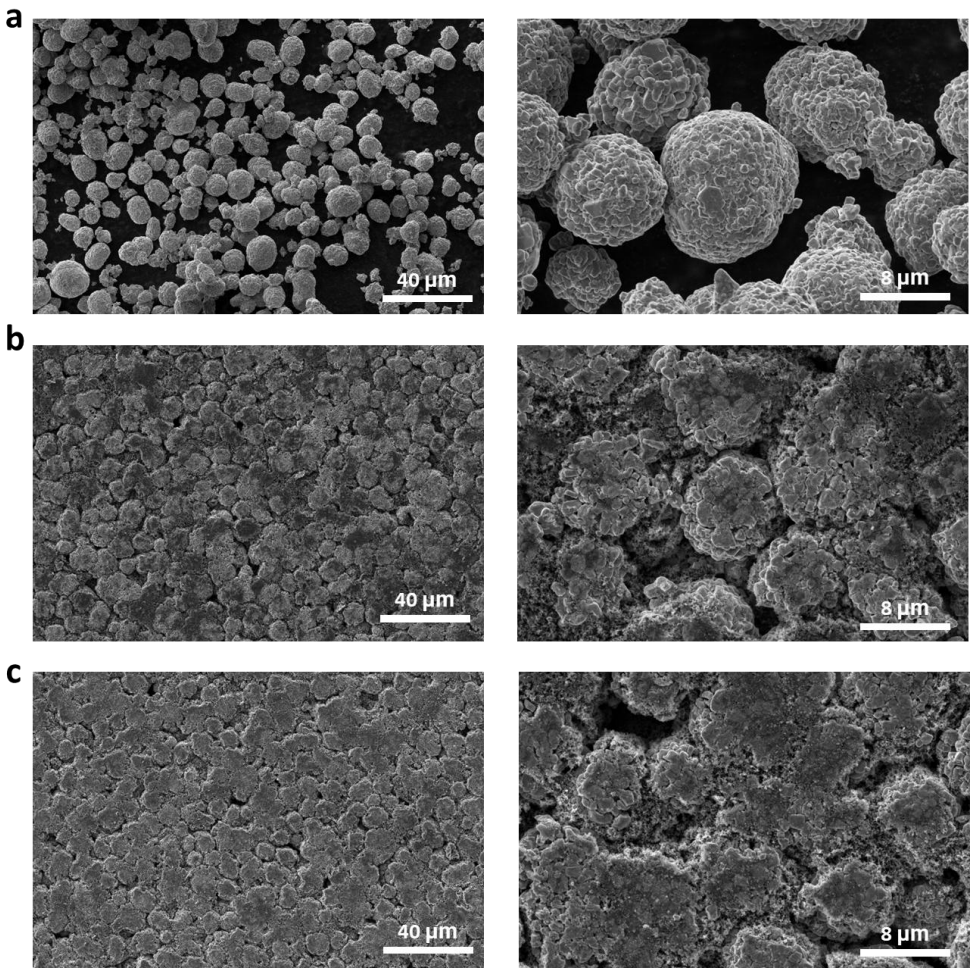

Figure 5-19 Morphology evolution after 1000 cycles in electrolyte of interest. The SEM image of (a) pristine NCM particles, (b) pristine cathode electrodes and (c) cycled cathode electrodes after 1000 cycles in M9F1.

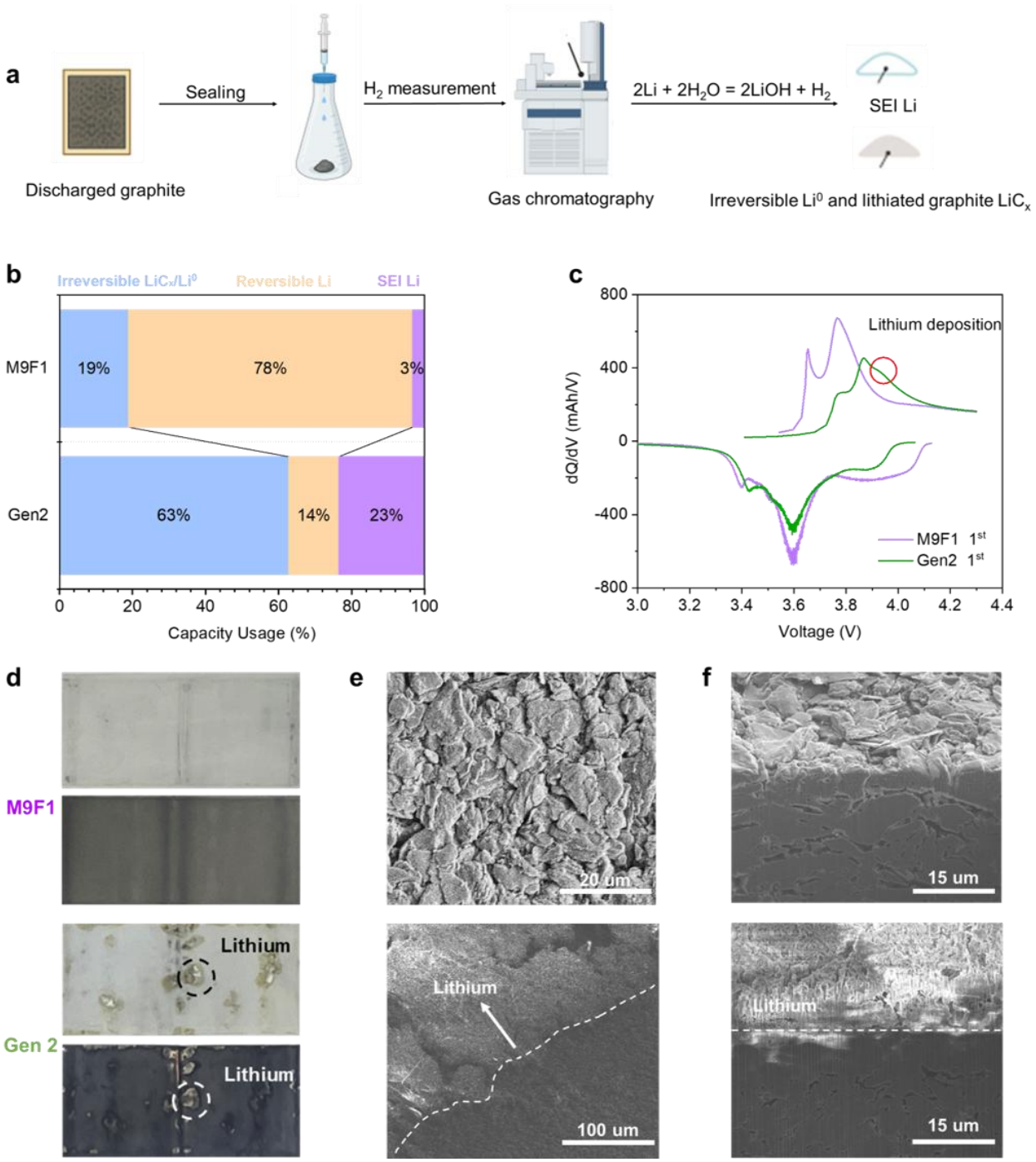

Figure 5-20 Quantification of capacity loss under XFC conditions and direct evidence of Li plating. a) Titration gas chromatography , and b) Quantification of Li loss in cells after 1000 XFC cycles. c) dQ/dV profile of 1st cycle of XFC cells in Gen 2 and M9F1 consisting of a 4 C charge and C/3 discharge. d) Optical photograph of separators and anodes harvested from pouch cells after 1000 cycles in Gen 2 and M9F1. SEM images of graphite anodes after cycling in Gen 2 and M9F1; e) top-view, and f) cross-section SEM image after FIB milling.

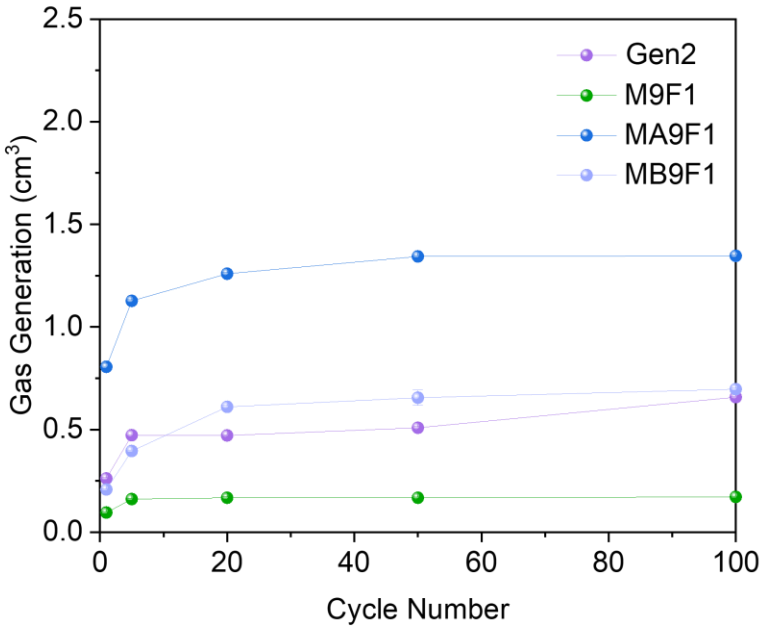

Figure 5-21 The evolution of gas volume under extreme charging condition employing electrolytes of interest. The gas generation measurement during 15min CCCV/0.33C cycling after 5 cycles 0.1C activation in Gen 2, M9F1, MA9F1, and MB9F1.

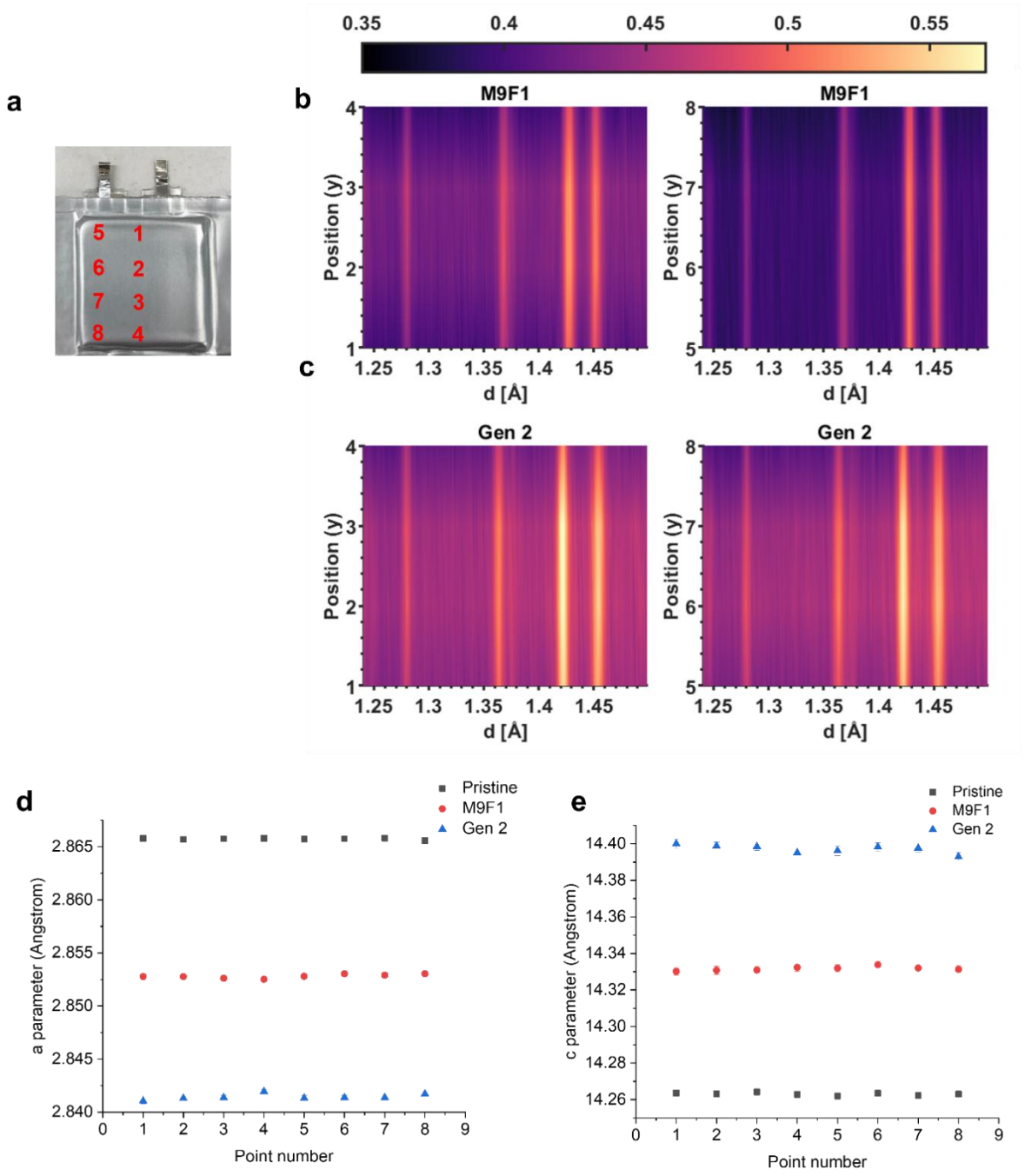

Figure 5-22 The detection of Li loss from cathodes in different electrolytes. a) The photography of scanning points for neuron beam. The neutron mapping across the whole pouch cell along with middle(left) and edge(right) in b) M9F1 c) Gen 2. The refinement neutron result of d) a parameter and e) c parameter of NMC cathodes for pristine cells, M9F1 cells, and Gen2 cells after 500 15min CCCV cycles.

To probe the existence of Li metal during XFC charge in Gen 2, we first compare the differential capacity/voltage (dQ/dV) profiles of cells employing the electrolytes of interest during

their first cycle. As shown in Figure 3c, the 4 C charging profile of Gen 2 exhibits substantially increased polarization compared with M9F1, with a third peak present at high voltage, implying the formation of another phase during charge. As this peak is clearly not visible in either the M9F1 XFC profile, or in either electrolyte at 0.1 C (**Figure 5-23**), it is highly probable that this peak represents Li plating as a result of excessive polarization[161, 169, 170]. When disassembled, metallic Li was also observed on both the anode surface and the separator of cells employing Gen 2, further confirming this conclusion (**Figure 5-20d**). In comparison, there was no visible Li^0 found on either the separator or anode of the cell employing M9F1, even when fully un-wound (**Figure 5-24**). When examined under SEM, plated Li^0 was also clearly observed on the surface of the graphite anode cycled in Gen 2, which was also found to be covered in a considerable SEI layer, given the poor conductivity of the material during imaging (**Figure 5-20e, f**). As a comparison, no metallic Li was observed on top or between the particles of the M9F1-cycled anode, which exhibited a morphology comparable to the pristine electrode (**Figure 5-20e, f, Figure 5-25**). It is also noteworthy that no plated Li was observed in the other carboxylate ester electrolytes of interest, whereas the LP40 system displayed Li growth far beyond that of Gen 2. Though the improved transport and charge-transfer behavior of the M9F1 system are likely highly influential in the mitigation of Li plating during XFC cycling, further characterization of the formed SEI is also necessary to determine compositional or thickness variance that may contribute to the disparate kinetics.

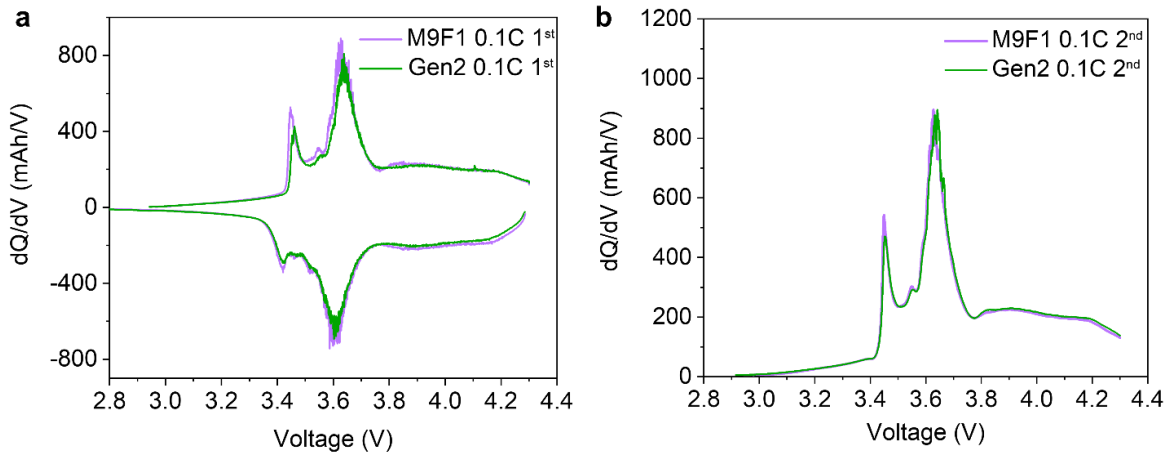

Figure 5-23 Electrochemical behavior at slow rate in different electrolytes. The dQ/dV curve of a) the 1st activation cycle and b) the following activation cycle at 0.1C in Gen2 and M9F1.

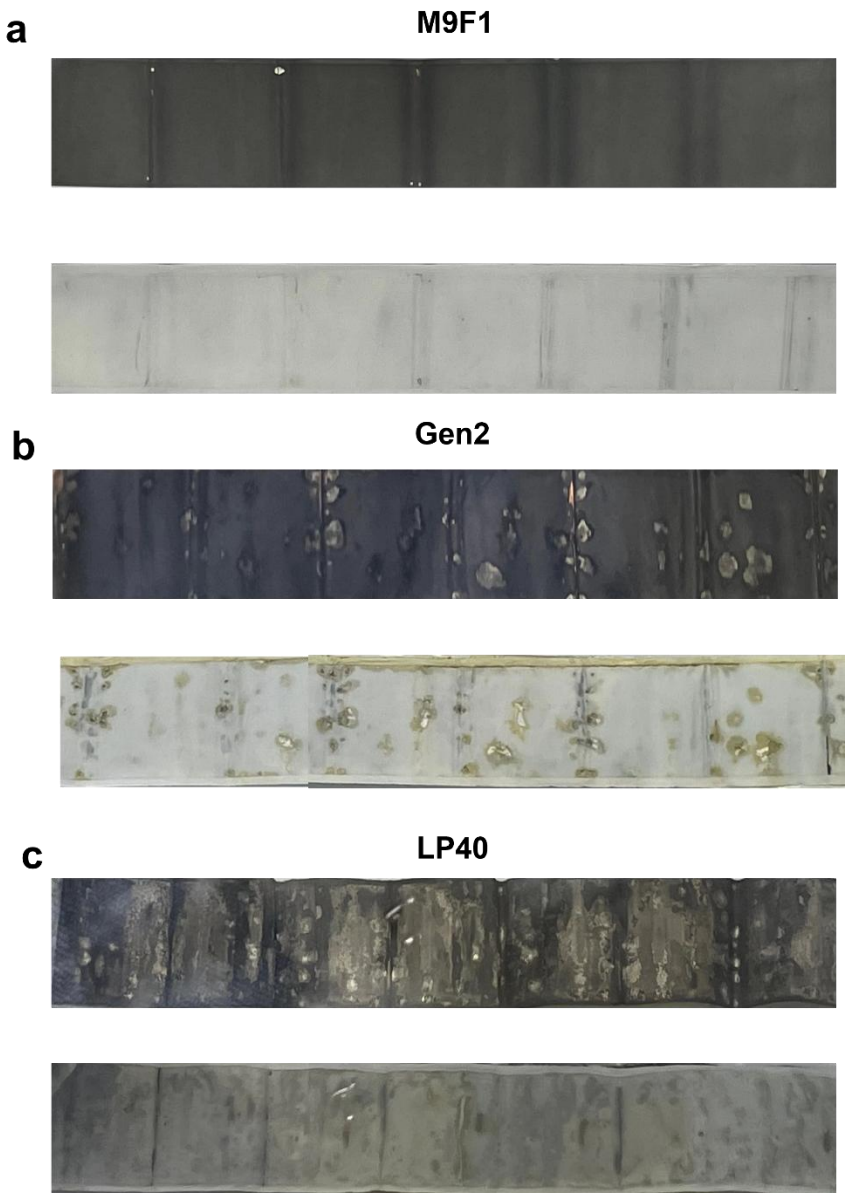

Figure 5-24 Large-area of anodes and separators harvested from pouch cells employing a) M9F1, b) Gen 2, and c) LP40 electrolytes. Exposed metal in a) is a result of electrode delamination during disassembly, not metallic Li.

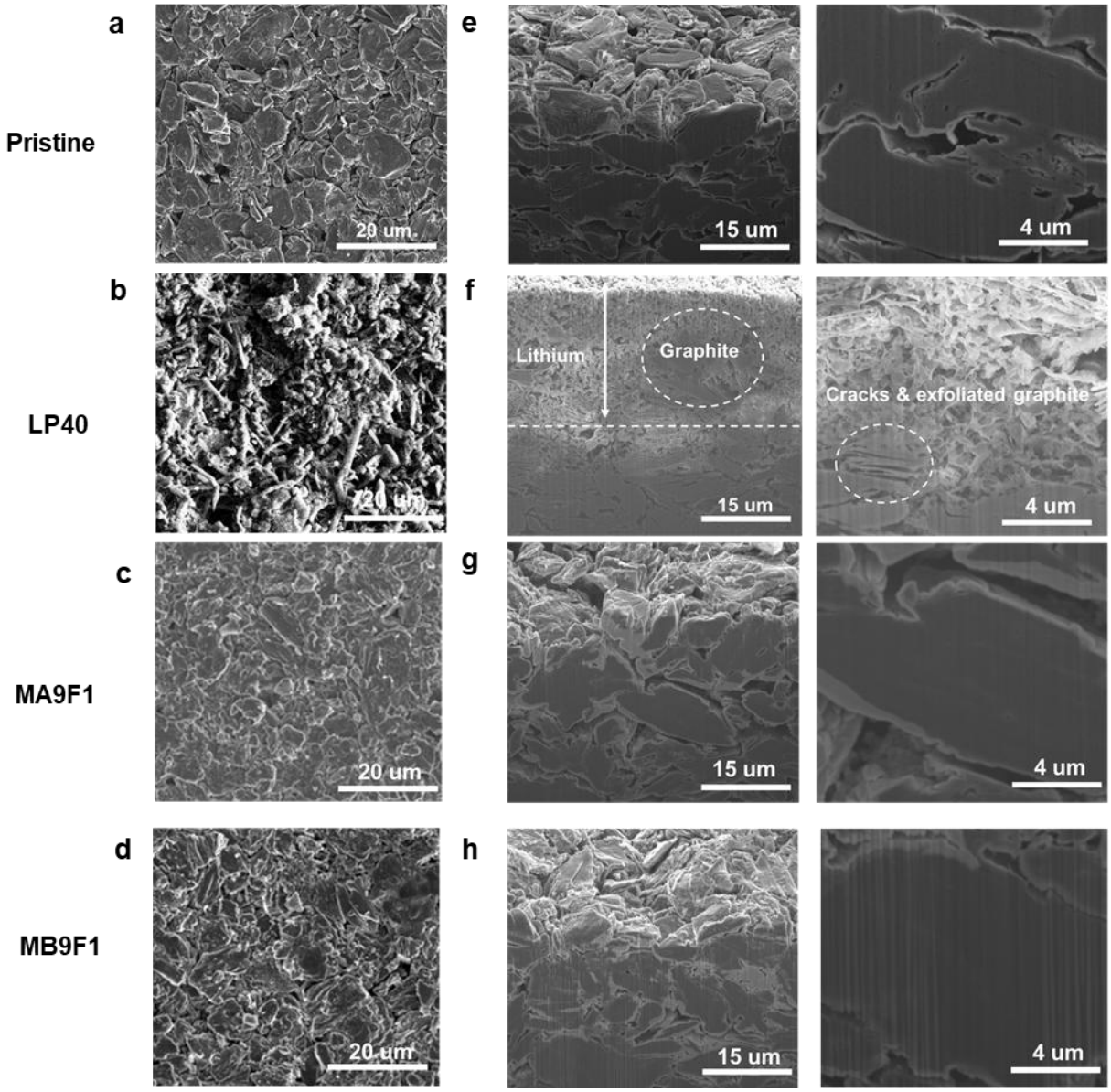

Figure 5-25 Extended direct evidence of Li plating under XFC condition. SEM photographs of graphite anodes in pristine pouch cells and the pouch cells after 500 15min CCCV cycling in LP40, MA9F1, and MB9F1; **a-d)** top-view, and **e-h)** cross-section after cryo-FIB milling.

5.2.2.3. Rate-Driven SEI Growth, Co-intercalation and Interstitial Decomposition

To determine any variation in SEI composition between cells employing Gen 2 and M9F1, we first examine its thickness via cryogenic transmission electron microscopy (cryo-TEM). This analysis revealed that the interphase formed after 1000 cycles in Gen 2 was ~20-30 nm thick, compared to M9F1, which was ~10-15 nm (**Figure 5-25a, b**). Further, X-ray photoelectron

spectroscopy (XPS) measurements also reveal significant compositional differences between the two systems. The compositional analysis of surface spectra from **Figure 5-27** & **5-28** are shown in **Figure 5-25c-e**. We find that in addition to the thickness differences, the SEI formed in M9F1demonstrated a substantially larger LiF/Li_xPF_y ratio, indicative of more effective passivation and aligned with Cryo-TEM results. Further, a substantially lower ratio of $ROCO_2Li/Li_2CO_3$ species are found in M9F1, which are generally believed to be sub-optimal for Li^+ migration through the SEI[165, 214]. Generally, we also find that the SEI formed in M9F1 contains more fluorine, and maintains a more homogenous composition than that formed in Gen 2 and LP 40 (**Figure 5-29**). However, we do notice a significant discrepancy in the XPS data, where LiC_x is observed in the Gen 2 surface spectra, which would not be expected given the larger thickness of its SEI relative to M9F1, and should in principle exceed the XPS sampling depth of ~10 nm. A closer examination of this finding reveals another source of capacity loss for the Gen 2 system which further highlights the importance of rapid charge-transfer for XFC applications.

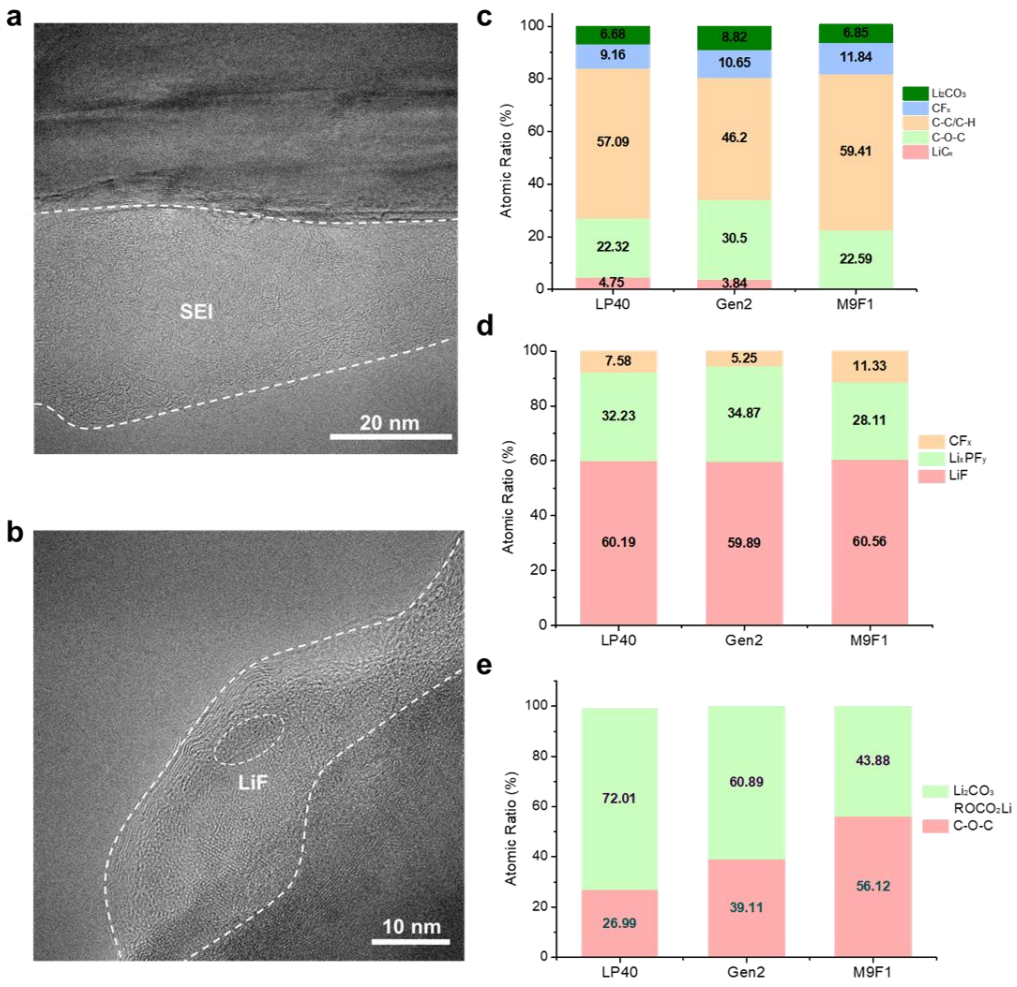

Figure 5-26 SEI Characterization of Anodes Cycled in Electrolytes of Interest. Cryo-TEM images of the graphite surface after 1000 cycles in a) Gen 2, and b) M9F1. XPS compositional analysis from c) C 1s, d) F 1s, and e) O1s spectra of anodes cycled in electrolytes of interest.

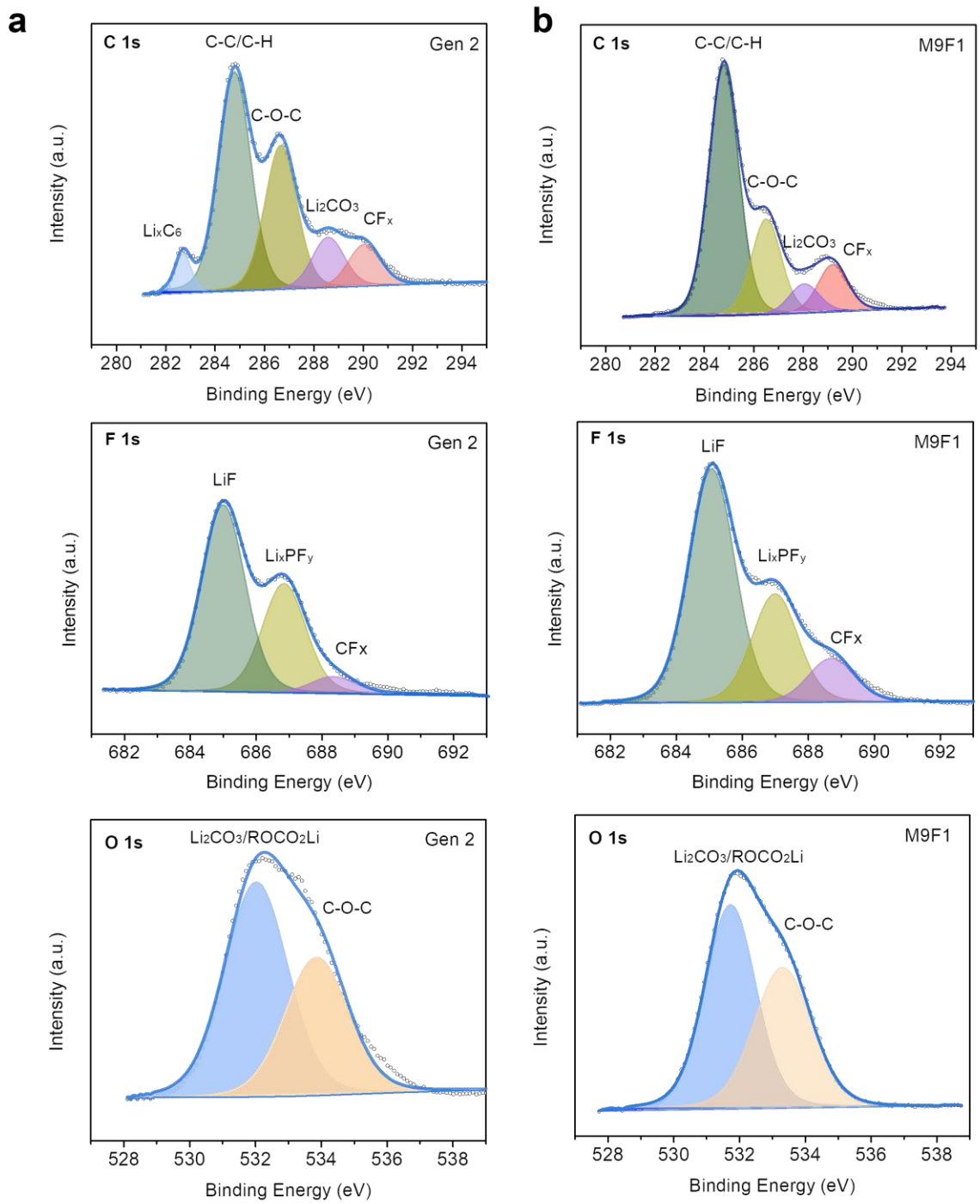

Figure 5-27 Extended SEI surface characterization of anode cycled in electrolytes of interest. Extended XPS fitting of C1s, F1s, and O1s regions of graphite anodes after 1000 cycles in a) Gen 2, and b) M9F1 without etching.

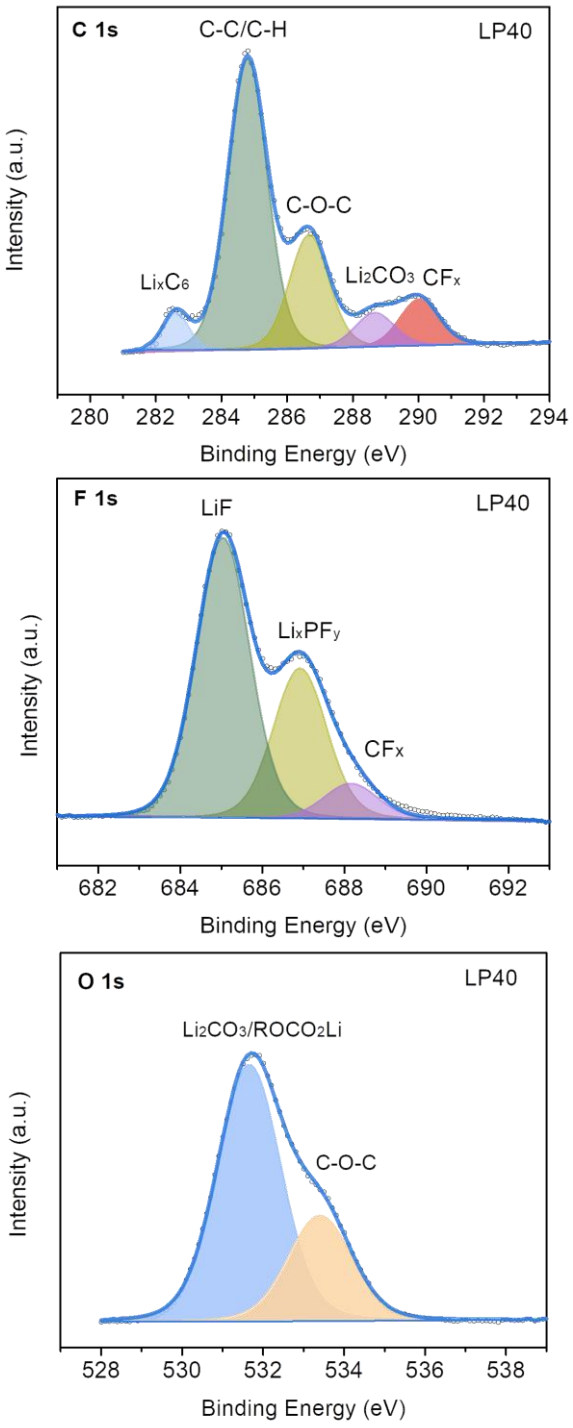

Figure 5-28 Extended SEI surface characterization of anode cycled in electrolytes of interest. Extended XPS fitting of C1s, F1s, and O1s regions of graphite anodes after 1000 cycles in LP40 without etching.

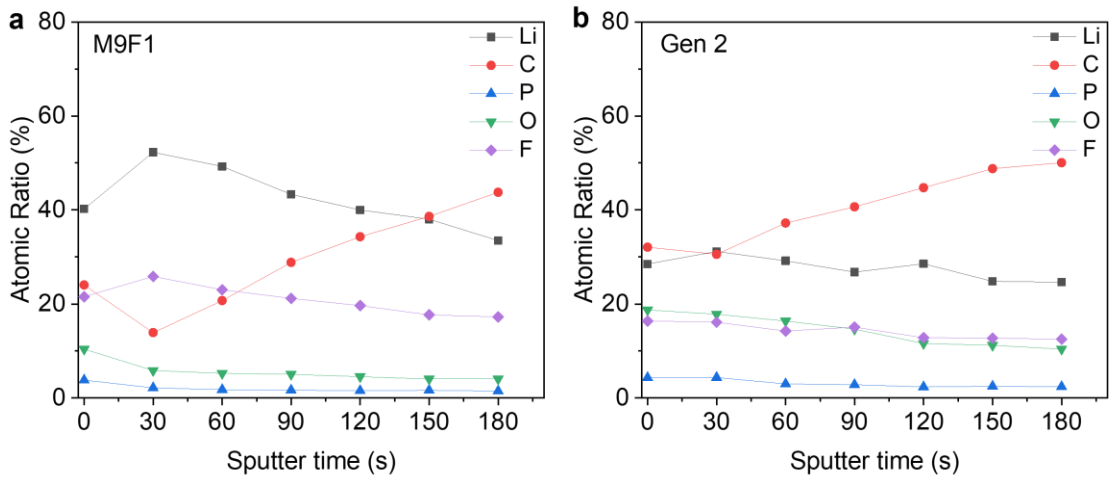

Figure 5-29 SEI composition analysis of anode cycled in electrolytes of interest. XPS quantitative element composition ratios of SEI interface with a various duration of Ar^+ sputtering after 1000 cycles in a) M9F1 and b) Gen2.

Throughout the history of LIB development, the mitigation of Li^+/solvent co-intercalation between graphene sheets has been a critical step towards the stabilization of long-term anode cycling[215, 216]. While the well-known transition from propylene carbonate (PC) to EC has effectively solved this issue under standard operating conditions due to the formation of a solvent-shedding SEI, the fact remains that the activation energy for Li^+/solvent co-intercalation has been measured to be roughly half that of intercalation including de-solvation[217]. For this reason, it has been proposed that high kinetic stress such as XFC charging may result in the co-intercalation of Li^+/solvent complexes, which would then further exfoliate the graphite layers, leading to poor cycling stability[161, 169, 170]. As the activation energy of de-solvation relative to co-intercalation at the interphase directly governs this phenomenon, we conclude that the improved de-solvation mechanics of M9F1 gave rise to an intrinsic advantage in this regard.

By conducting cryo-TEM investigations of the graphite anode cycled in Gen 2, multiple incidents of such exfoliation events were observed (**Figure 5-30a**). Further, it is clear that the co-intercalation of such complexes resulted in substantial SEI growth between graphene sheet,

effectively increasing the active area for electrolyte decomposition to a degree that we believe to be significant in the aforementioned SEI loss discrepancy. To further study the SEI penetration into the bulk of the graphite particles, focused ion beam (FIB) lamella of the cycled graphite powders was prepared and studied using cryogenic aberration corrected electron microscope (Cryo-AC-STEM). After cycling in Gen 2, the graphite showed nanometer-thick cracks penetrating into the bulk particles (**Figure 5-30b**). Energy-dispersive x-ray spectroscopy (EDS) mapping of the same region showed enrichment of O, F, and P signals within the crack, which further showcased the co-intercalation of the solvent and anions followed by interstitial decomposition between the graphene layers (**Figure 5-31**). Through further zooming in at the origin of the crack in **Figure 5-30e,** the bright field (BF) image also reveals that there is a significant *d*-spacing difference between graphite on the right side (~0.341 nm) and the left side (~0.335 nm), which implies that graphite within exfoliated regions may struggle to be fully delithiated. Evidence of such exfoliation was also observed in both Raman spectroscopy and X-ray diffraction of the cycled anodes, which reveals a substantially higher D/G ratio and *d*-spacing for the anode cycled in Gen 2 (**Figure 5-32**). We propose that the exfoliation of such lithiated graphite domains leads to the observation of LiC_x in the XPS spectra of the Gen 2 system at significantly more shallow sampling depths (**Figure 5-30d,e**).

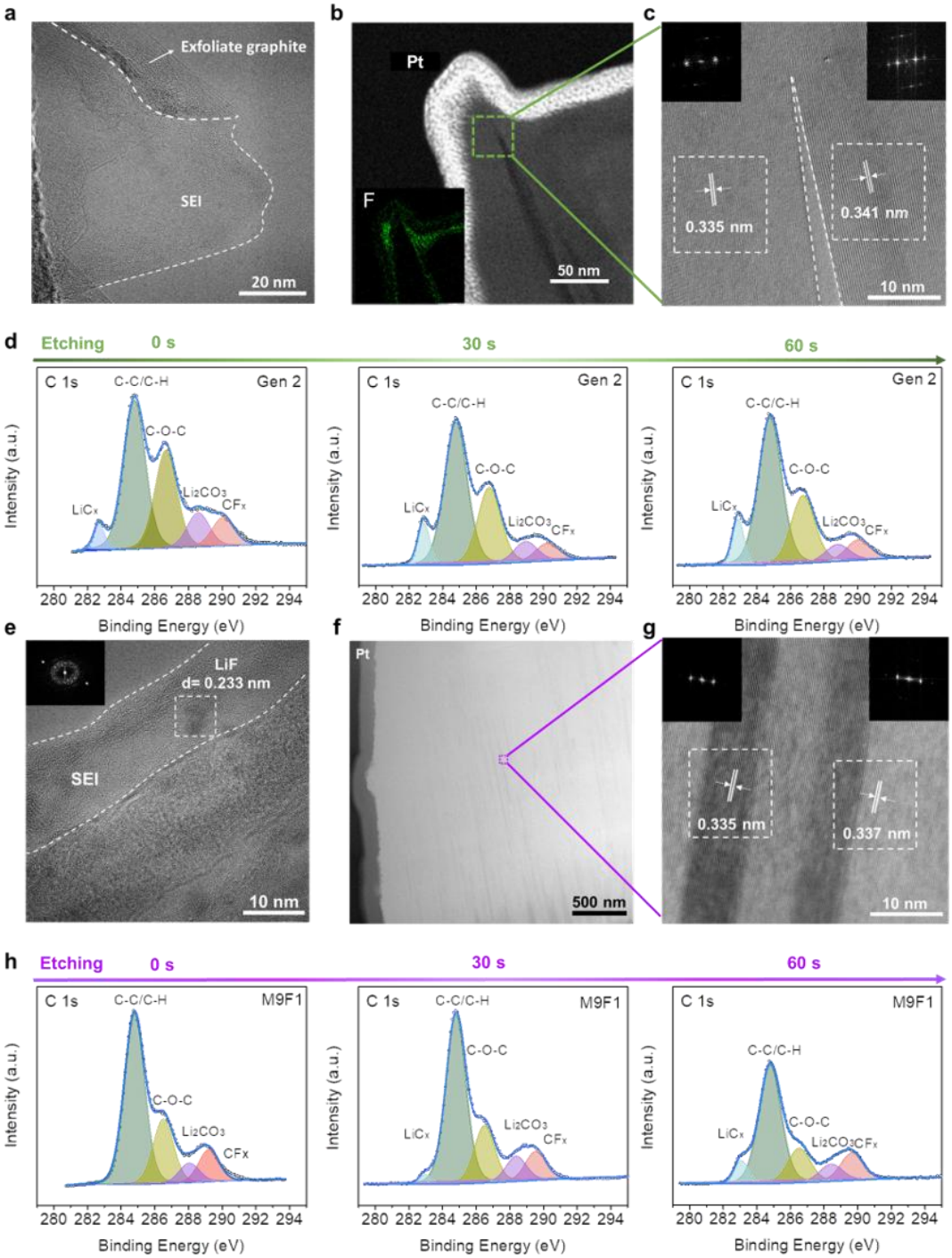

Figure 5-30 Evidence of Exfoliation and Interstitial SEI Formation in Graphite Cycled under XFC Conditions. Cryo-TEM images of graphite after 1000 XFC cycles in Gen 2. a) Cryo-TEM image of exfoliated graphite with interstitial SEI formation between graphene sheets. b,c) Cryo-STEM images of the cycled graphite FIB lamella with fluorine EDS inset. d) XPS C1s spectra of graphite cycled in Gen 2 at various stages of etching. Cryo-TEM images of graphite after 1000 XFC cycles in M9F1. e) Cryo-TEM image of graphite without the presence of exfoliation. f,g) Cryo-STEM images of the cycled graphite FIB lamella. h) XPS C1s spectra of graphite cycled in M9F1 at various stages of etching.

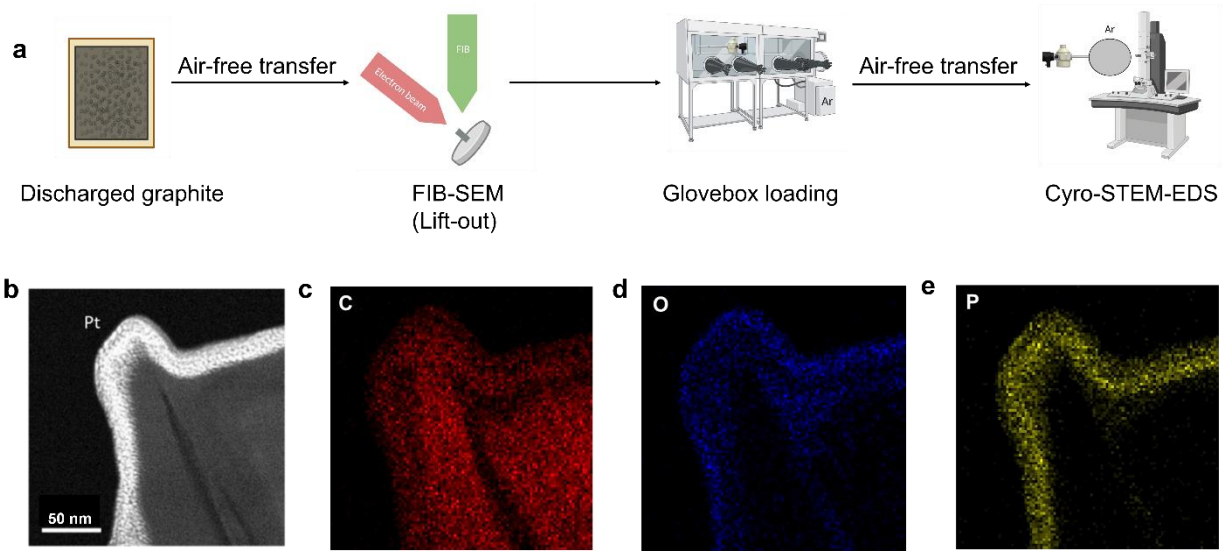

Figure 5-31 Extended evidence of exfoliation and interstitial SEI formation in graphite cycled under XFC conditions. a) The schematic of Cyro-STEM-EDS analysis. Cryo-STEM images of b) the cycled graphite FIB lamella with c) carbon, d) phosphorus and e) oxygen EDS signal.

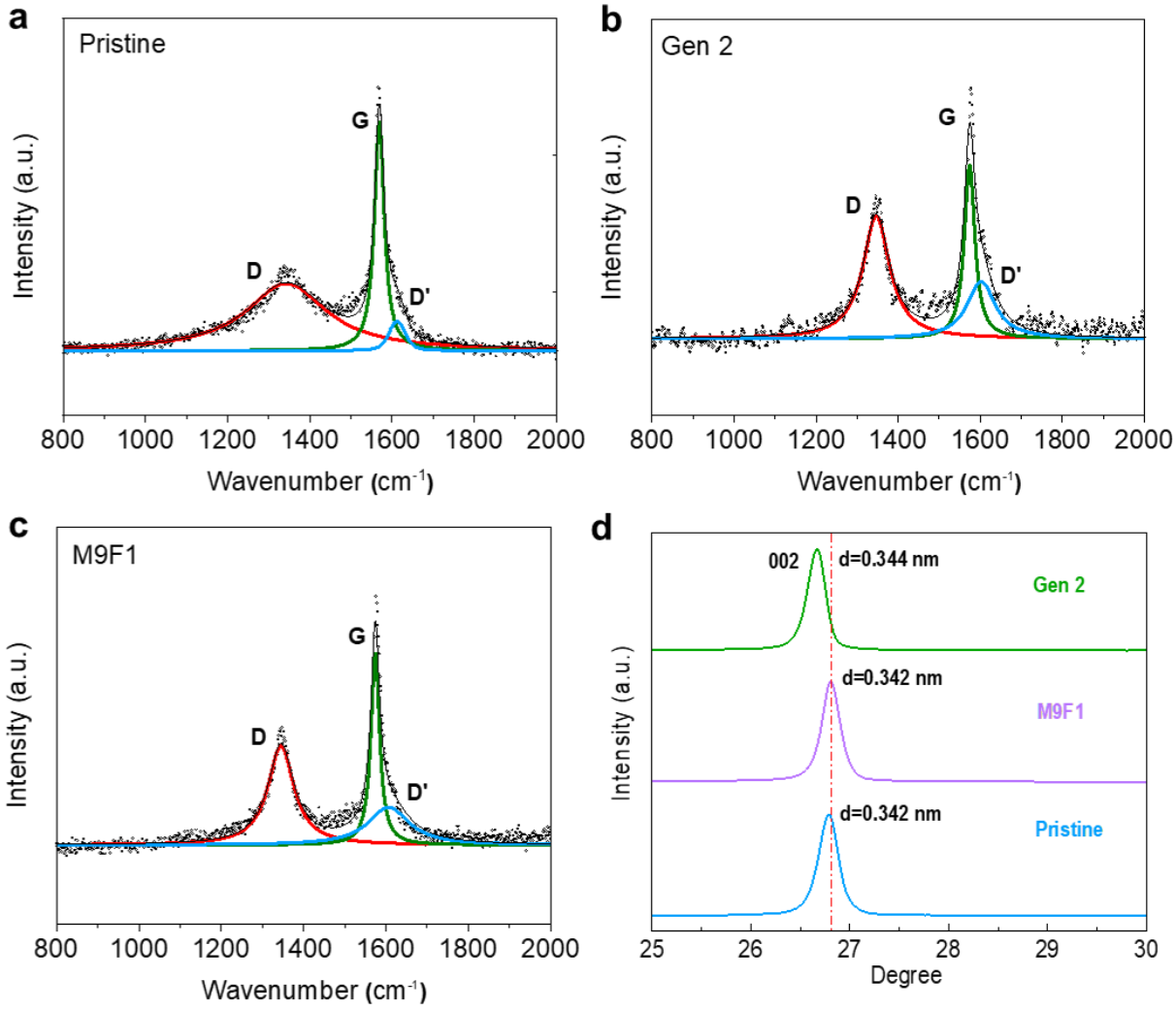

Figure 5-32 Evidence of exfoliation in graphite cycled under XFC conditions in the electrolyte of interest. The Raman spectra of a) the pristine anode and anodes cycled in b) Gen2 and c) M9F1 after 1000 cycles. d) The XRD pattern of the pristine anode and anodes in each electrolyte after 1000 cycles.

In comparison, no signs of significant graphite exfoliation or interstitial SEI growth was observed in the graphite cycled in M9F1, which demonstrated a uniform SEI consistent with the previously presented images (**Figure 5-30f, 4b**). Furthermore, FIB lamella of the cycled graphite in M9F1 indicated no signs of cracking or co-intercalation inside the bulk of the particles, as shown in the cross-section low-magnification high angle annular dark field (HAADF) image in **Figure 5-30g**. We also find that the *d*-spacing of graphite layers within the bulk are substantially more

homogenous than that of Gen 2, which were observed to be between 0.337 and 0.335 nm (**Figure 5-30h**). Additionally, XPS spectroscopy at various etching depths reveals an intuitive trend, where the outer SEI regions do not show detectable LiC_x species, the signal for which slowly increases as the bulk of the particle is reached during etching (**Figure 5-30i**). In addition to the mitigation of Li plating and increased cell polarization during cycling, the optimized physiochemical properties of M9F1 effectively resolves rate-induced co-intercalation, exfoliation, and interstitial SEI formation.

5.2.3 Conclusion

In this work, we make significant progress towards achieving commercially viable LIBs charged at 15 minutes or less through the comprehensive design of the battery electrolyte. Specifically, by employing M9F1, a carboxylate-ester-based system results in a substantial improvement in XFC performance, retaining 82.5% of C/10 energy when charged at 4 C compared to only 73.4 % in identical cells employing Gen 2. Crucially, cells employing M9F1 also demonstrated 88.2 % capacity retention after 500 cycles, compared to only 54.1 % in Gen 2. We find that this rapid capacity loss in Gen 2 is a result of a combination of Li plating, poor SEI characteristics, the co-intercalation of Li^+ /solvent complexes and excessive gassing, resulting in graphite exfoliation and interstitial SEI formation. On the other hand, the rapid, selective Li^+ transport, and facile Li^+ desolvation provided by the M9F1 system was found to successfully mitigate all of the aforementioned failure modes, and is responsible for the state-of-the-art performance. This work highlights the various electrolyte characteristics responsible for improved fast-charging performance while demonstrating the origin of benchmark-exceeding electrochemical behavior.

5.2.4 Acknowledgements

Chapter 5, in full, is a reprint of the material “Enhanced Electrolyte Transport and Kinetics Mitigate Graphite Exfoliation and Li Plating in Fast-Charging Li-Ion Batteries” as it appears in Advanced Energy Materials Hongpeng Gao, Qizhang Yan, John Holoubek, Yijie Yin, Wurigumula Bao, Haodong Liu, Artem Baskin, Mingqian Li, Guorui Cai, Weikang Li, Duc Tran, Ping Liu, Jian Luo, Ying Shirley Meng, Zheng Chen, 2023. The dissertation author was the primary investigator and author of this paper.

Chapter 6 Conclusion and outlook

This thesis focuses on addressing two critical challenges in lithium-ion batteries: sustainability and fast-charging performance limitations. To enhance both aspects, I propose innovative recycling and upcycling strategies for NCM and spinel-type cathodes, along with the development of ester-based electrolytes capable of enabling 6C/10C charging. Direct recycling technology has gained increasing attention due to its low energy consumption and high economic potential compared to traditional commercialized recycling methods. Through in-depth research on degradation mechanisms, direct recycling has been effectively applied to advanced cathode chemistries using various techniques. However, there is still significant room for improvement to further optimize sustainability and overcome performance limitations, ensuring both substantial environmental benefits and strong economic viability.

- To meet the growing demand for extended EV driving ranges, advanced cathode materials with high nickel content are expected to dominate the market due to their superior energy density and lower costs. However, recycling these high-Ni chemistries remains a major challenge, even within the research community. Developing a universal and efficient method for recycling all types of NCM cathodes will be a long-term yet crucial endeavor.
- As the development and adoption of next-generation cathode materials for EVs accelerate, improving the performance of spent LIB cathodes beyond their original pristine state remains a challenge. Strategies such as single-crystal structures, increased nickel content, and dopant incorporation are still in their early stages. Comprehensive and systematic research is needed to assess their feasibility for future LIB recycling efforts.
- Currently, direct recycling methods have only been demonstrated at the laboratory scale. Scaling up these processes may introduce inconsistencies in electrochemical performance,

posing challenges for commercialization. Further efforts are required to accelerate the industrial adoption of direct recycling and achieve the anticipated economic benefits.

- The slow charging speed of lithium-ion batteries (LIBs), particularly in electric vehicles (EVs), remains a significant hurdle to widespread adoption. Unlike internal combustion engine (ICE) vehicles that refuel within minutes, current LIBs require 30–60 minutes for a full charge. Meeting global fast-charging targets, such as the U.S. Department of Energy's 15-minute EV charging goal, demands that LIBs support high charging rates (≥4C) while maintaining long-term stability. However, fast charging accelerates battery degradation, leading to lithium plating (which increases the risk of short circuits and capacity loss), graphite exfoliation and SEI instability (reducing efficiency), and high interfacial resistance (causing excessive heat and electrolyte breakdown). To mitigate these challenges, electrolyte engineering is crucial in enhancing fast-charging performance. Innovations such as dual-ion ester-based electrolytes with high Li^+ transference numbers and SEI-stabilizing additives facilitate faster Li^+ diffusion to minimize polarization and lithium plating, improve charge transfer kinetics to extend battery lifespan, and enhance compatibility with cathodes, paving the way for sustainable high-performance LIBs.

By combining sustainability with cutting-edge performance improvements, this thesis contributes to the advancement of next-generation lithium-ion batteries, addressing the dual challenges of resource constraints and technological limitations in energy storage.

REFERENCES

1. Lv, W.; Wang, Z.; Cao, H.; Sun, Y.; Zhang, Y.; Sun, Z., A Critical Review and Analysis on the Recycling of Spent Lithium-Ion Batteries. *ACS Sustainable Chemistry & Engineering* **2018,** *6* (2), 1504-1521.

2. Singer, A.; Zhang, M.; Hy, S.; Cela, D.; Fang, C.; Wynn, T. A.; Qiu, B.; Xia, Y.; Liu, Z.; Ulvestad, A.; Hua, N.; Wingert, J.; Liu, H.; Sprung, M.; Zozulya, A. V.; Maxey, E.; Harder, R.; Meng, Y. S.; Shpyrko, O. G., Nucleation of dislocations and their dynamics in layered oxide cathode materials during battery charging. *Nature Energy* **2018,** *3* (8), 641-647.

3. Meshram, P.; Mishra, A.; Abhilash; Sahu, R., Environmental impact of spent lithium ion batteries and green recycling perspectives by organic acids - A review. *Chemosphere* **2020,** *242*, 125291.

4. Georgi-Maschler, T.; Friedrich, B.; Weyhe, R.; Heegn, H.; Rutz, M., Development of a recycling process for Li-ion batteries. *Journal of Power Sources* **2012,** *207*, 173-182.

5. Schmuch, R.; Wagner, R.; Hörpel, G.; Placke, T.; Winter, M., Performance and cost of materials for lithium-based rechargeable automotive batteries. *Nature Energy* **2018,** *3* (4), 267-278.

6. Ciez, R. E.; Whitacre, J. F., Examining different recycling processes for lithium-ion batteries. *Nature Sustainability* **2019,** *2* (2), 148-156.

7. Zheng, X.; Zhu, Z.; Lin, X.; Zhang, Y.; He, Y.; Cao, H.; Sun, Z., A Mini-Review on Metal Recycling from Spent Lithium Ion Batteries. *Engineering* **2018,** *4* (3), 361-370.

8. Gaines, L.; Richa, K.; Spangenberger, J., Key issues for Li-ion battery recycling. *MRS Energy & Sustainability* **2018,** *5*.

9. Chen, M.; Ma, X.; Chen, B.; Arsenault, R.; Karlson, P.; Simon, N.; Wang, Y., Recycling end-of-life electric vehicle lithium-ion batteries. *Joule* **2019,** *3* (11), 2622-2646.

10. Xu, P.; Tan, D. H.; Chen, Z., Emerging trends in sustainable battery chemistries. *Trends in Chemistry* **2021**.

11. Tan, D. H. S.; Xu, P.; Chen, Z., Enabling sustainable critical materials for battery storage through efficient recycling and improved design: A perspective. *MRS Energy & Sustainability* **2020,** *7*, E27.

12. Yang, Y.; Song, S.; Lei, S.; Sun, W.; Hou, H.; Jiang, F.; Ji, X.; Zhao, W.; Hu, Y., A process for combination of recycling lithium and regenerating graphite from spent lithium-ion battery. *Waste Management* **2019,** *85*, 529-537.

13. Shi, Y.; Chen, G.; Liu, F.; Yue, X.; Chen, Z., Resolving the Compositional and Structural Defects of Degraded LiNixCoyMnzO2 Particles to Directly Regenerate High-Performance Lithium-Ion Battery Cathodes. *ACS Energy Letters* **2018,** *3* (7), 1683-1692.

14. Sun, Q.; Li, X.; Zhang, H.; Song, D.; Shi, X.; Song, J.; Li, C.; Zhang, L., Resynthesizing LiFePO4/C materials from the recycled cathode via a green full-solid route. *Journal of Alloys and Compounds* **2020,** *818*, 153292.

15. Wang, Y.; Ma, L.; Xi, X.; Nie, Z.; Zhang, Y.; Wen, X.; Lyu, Z., Regeneration and characterization of LiNi0.8Co0.15Al0.05O2 cathode material from spent power lithium-ion batteries. *Waste Management* **2019,** *95*, 192-200.

16. Yang, T.; Lu, Y.; Li, L.; Ge, D.; Yang, H.; Leng, W.; Zhou, H.; Han, X.; Schmidt, N.; Ellis, M.; Li, Z., An Effective Relithiation Process for Recycling Lithium-Ion Battery Cathode Materials. *Advanced Sustainable Systems* **2020,** *4* (1), 1900088.

17. Or, T.; Gourley, S. W. D.; Kaliyappan, K.; Yu, A.; Chen, Z., Recycling of mixed cathode lithium-ion batteries for electric vehicles: Current status and future outlook. *Carbon Energy* **2020,** *2* (1), 6-43.

18. Natarajan, S.; Aravindan, V., Recycling Strategies for Spent Li-Ion Battery Mixed Cathodes. *ACS Energy Letters* **2018,** *3* (9), 2101-2103.

19. Bai, Y.; Muralidharan, N.; Sun, Y.-K.; Passerini, S.; Stanley Whittingham, M.; Belharouak, I., Energy and environmental aspects in recycling lithium-ion batteries: Concept of Battery Identity Global Passport. *Materials Today* **2020,** *41*, 304-315.

20. Placke, T.; Heckmann, A.; Schmuch, R.; Meister, P.; Beltrop, K.; Winter, M., Perspective on Performance, Cost, and Technical Challenges for Practical Dual-Ion Batteries. *Joule* **2018,** *2* (12), 2528-2550.

21. Etacheri, V.; Marom, R.; Elazari, R.; Salitra, G.; Aurbach, D., Challenges in the development of advanced Li-ion batteries: a review. *Energy & Environmental Science* **2011,** *4* (9), 3243-3262.

22. Blomgren, G. E., The Development and Future of Lithium Ion Batteries. *Journal of The Electrochemical Society* **2016,** *164* (1), A5019-A5025.

23. Zhang, Y.; Li, Y.; Tao, Y.; Ye, J.; Pan, A.; Li, X.; Liao, Q.; Wang, Z., Performance assessment of retired EV battery modules for echelon use. *Energy* **2020,** *193*, 116555.

24. Zhang, X.; Li, L.; Fan, E.; Xue, Q.; Bian, Y.; Wu, F.; Chen, R., Toward sustainable and systematic recycling of spent rechargeable batteries. *Chemical Society Reviews* **2018,** *47* (19), 7239-7302.

25. Li, L.; Dunn, J. B.; Zhang, X. X.; Gaines, L.; Chen, R. J.; Wu, F.; Amine, K., Recovery of metals from spent lithium-ion batteries with organic acids as leaching reagents and environmental assessment. *Journal of Power Sources* **2013,** *233*, 180-189.

26. Nie, H.; Xu, L.; Song, D.; Song, J.; Shi, X.; Wang, X.; Zhang, L.; Yuan, Z., LiCoO2: recycling from spent batteries and regeneration with solid state synthesis. *Green Chemistry* **2015,** *17* (2), 1276-1280.

27. Li, L.; Bian, Y.; Zhang, X.; Guan, Y.; Fan, E.; Wu, F.; Chen, R., Process for recycling mixed-cathode materials from spent lithium-ion batteries and kinetics of leaching. *Waste Management* **2018,** *71*, 362-371.

28. Yun, L.; Linh, D.; Shui, L.; Peng, X.; Garg, A.; LE, M. L. P.; Asghari, S.; Sandoval, J., Metallurgical and mechanical methods for recycling of lithium-ion battery pack for electric vehicles. *Resources, Conservation and Recycling* **2018,** *136*, 198-208.

29. Wang, S.; Wang, C.; Lai, F.; Yan, F.; Zhang, Z., Reduction-ammoniacal leaching to recycle lithium, cobalt, and nickel from spent lithium-ion batteries with a hydrothermal method: Effect of reductants and ammonium salts. *Waste Management* **2020,** *102*, 122-130.

30. Wang, T.; Luo, H.; Bai, Y.; Li, J.; Belharouak, I.; Dai, S., Direct Recycling of Spent NCM Cathodes through Ionothermal Lithiation. *Advanced Energy Materials* **2020,** *10* (30), 2001204.

31. Shi, Y.; Zhang, M.; Meng, Y. S.; Chen, Z., Ambient-Pressure Relithiation of Degraded LixNi0.5Co0.2Mn0.3O2 ($0 < x < 1$) via Eutectic Solutions for Direct Regeneration of Lithium-Ion Battery Cathodes. *Advanced Energy Materials* **2019,** *9* (20), 1900454.

32. Shi, Y.; Chen, G.; Chen, Z., Effective regeneration of LiCoO2 from spent lithium-ion batteries: a direct approach towards high-performance active particles. *Green Chemistry* **2018,** *20* (4), 851-862.

33. Li, J.; Lu, Y.; Yang, T.; Ge, D.; Wood, D. L.; Li, Z., Water-Based Electrode Manufacturing and Direct Recycling of Lithium-Ion Battery Electrodes—A Green and Sustainable Manufacturing System. *iScience* **2020,** *23* (5), 101081.

34. Wang, H.; Whitacre, J. F., Direct Recycling of Aged LiMn2O4 Cathode Materials used in Aqueous Lithium-ion Batteries: Processes and Sensitivities. *Energy Technology* **2018,** *6* (12), 2429-2437.

35. Li, X.; Zhang, J.; Song, D.; Song, J.; Zhang, L., Direct regeneration of recycled cathode material mixture from scrapped LiFePO4 batteries. *Journal of Power Sources* **2017,** *345*, 78-84.

36. Bertuol, D. A.; Machado, C. M.; Silva, M. L.; Calgaro, C. O.; Dotto, G. L.; Tanabe, E. H., Recovery of cobalt from spent lithium-ion batteries using supercritical carbon dioxide extraction. *Waste Management* **2016,** *51*, 245-251.

37. Wu, H. M.; Tu, J. P.; Yuan, Y. F.; Chen, X. T.; Xiang, J. Y.; Zhao, X. B.; Cao, G. S., One-step synthesis LiMn2O4 cathode by a hydrothermal method. *Journal of Power Sources* **2006,** *161* (2), 1260-1263.

38. Liu, Z.; Wang, W.-l.; Liu, X.; Wu, M.; Li, D.; Zeng, Z., Hydrothermal synthesis of nanostructured spinel lithium manganese oxide. *Journal of Solid State Chemistry* **2004,** *177* (4), 1585-1591.

39. Kim, D. K.; Muralidharan, P.; Lee, H.-W.; Ruffo, R.; Yang, Y.; Chan, C. K.; Peng, H.; Huggins, R. A.; Cui, Y., Spinel LiMn2O4 Nanorods as Lithium Ion Battery Cathodes. *Nano Letters* **2008,** *8* (11), 3948-3952.

40. Han, X.; Ouyang, M.; Lu, L.; Li, J., A comparative study of commercial lithium ion battery cycle life in electric vehicle: Capacity loss estimation. *Journal of Power Sources* **2014,** *268*, 658-669.

41. Zhan, C.; Lu, J.; Jeremy Kropf, A.; Wu, T.; Jansen, A. N.; Sun, Y.-K.; Qiu, X.; Amine, K., Mn(II) deposition on anodes and its effects on capacity fade in spinel lithium manganate–carbon systems. *Nature Communications* **2013,** *4* (1), 2437.

42. Chung, K. Y.; Kim , K.-B., Investigation of Structural Fatigue in Spinel Electrodes Using In Situ Laser Probe Beam Deflection Technique. *Journal of The Electrochemical Society* **2002,** *149* (1), A79-A85.

43. Chung, K. Y.; Kim, K.-B., Investigations into capacity fading as a result of a Jahn–Teller distortion in 4V LiMn2O4 thin film electrodes. *Electrochimica Acta* **2004,** *49* (20), 3327-3337.

44. An, K.; Skorpenske, H. D.; Stoica, A. D.; Ma, D.; Wang, X.-L.; Cakmak, E., First in situ lattice strains measurements under load at VULCAN. *Metallurgical and Materials Transactions A* **2011,** *42* (1), 95-99.

45. An, K.; Wang, X.; Stoica, A., Vulcan data reduction and interactive visualization software. *ORNL Report* **2012,** *621*.

46. Toby, B. H., EXPGUI, a graphical user interface for GSAS. *Journal of applied crystallography* **2001,** *34* (2), 210-213.

47. Larson, A.; Von Dreele, R. *General Structure Analysis System (GSAS)(Los Alamos National Laboratory, Los Alamos, NM)*; Technical Report LAUR 86-748: 2004.

48. Casey, P.; McCoy, A. P.; Bogan, J.; Byrne, C.; Walsh, L.; O'Connor, R.; Hughes, G., In Situ Investigations into the Mechanism of Oxygen Catalysis on Ruthenium/Manganese Surfaces and the Thermodynamic Stability of Ru/Mn-Based Copper Diffusion Barrier Layers. *The Journal of Physical Chemistry C* **2013,** *117* (31), 16136-16143.

49. Tang, D.; Sun, Y.; Yang, Z.; Ben, L.; Gu, L.; Huang, X., Surface Structure Evolution of LiMn2O4 Cathode Material upon Charge/Discharge. *Chemistry of Materials* **2014,** *26* (11), 3535-3543.

50. Dai, Q.; Spangenberger, J.; Ahmed, S.; Gaines, L.; Kelly, J. C.; Wang, M. *EverBatt: A Closed-loop Battery Recycling Cost and Environmental Impacts Model*; Argonne National Lab.(ANL), Argonne, IL (United States): 2019.

51. Adopted, I. J. I. G., Szwitzerland, Climate change 2014 synthesis report. **2014**, 1059-1072.

52. Appiah, W. A.; Park, J.; Byun, S.; Ryou, M.-H.; Lee, Y. M., A Mathematical Model for Cyclic Aging of Spinel LiMn2O4/Graphite Lithium-Ion Cells. *Journal of The Electrochemical Society* **2016,** *163* (13), A2757-A2767.

53. Yunjian, L.; Xinhai, L.; Huajun, G.; Zhixing, W.; Qiyang, H.; Wenjie, P.; Yong, Y., Electrochemical performance and capacity fading reason of LiMn2O4/graphite batteries stored at room temperature. *Journal of Power Sources* **2009,** *189* (1), 721-725.

54. Ryou, M.-H.; Han, G.-B.; Lee, Y. M.; Lee, J.-N.; Lee, D. J.; Yoon, Y. O.; Park, J.-K., Effect of fluoroethylene carbonate on high temperature capacity retention of LiMn2O4/graphite Li-ion cells. *Electrochimica Acta* **2010,** *55* (6), 2073-2077.

55. Hawley, W. B.; Parejiya, A.; Bai, Y.; Meyer, H. M.; Wood, D. L.; Li, J., Lithium and transition metal dissolution due to aqueous processing in lithium-ion battery cathode active materials. *Journal of Power Sources* **2020,** *466*, 228315.

56. Yuan, G.; Bai, J.; Doan, T. N. L.; Chen, P., Synthesis and electrochemical investigation of nanosized LiMn2O4 as cathode material for rechargeable hybrid aqueous batteries. *Materials Letters* **2014,** *137*, 311-314.

57. Massarotti, V.; Capsoni, D.; Bini, M.; Azzoni, C. B.; Paleari, A., Stoichiometry of Li2MnO3and LiMn2O4Coexisting Phases: XRD and EPR Characterization. *Journal of Solid State Chemistry* **1997,** *128* (1), 80-86.

58. Yang, X.; Tang, W.; Kanoh, H.; Ooi, K., Synthesis of lithium manganese oxide in different lithium-containing fluxes. *Journal of Materials Chemistry* **1999,** *9* (10), 2683-2690.

59. Kanamura, K.; Naito, H.; Yao, T.; Takehara, Z.-i., Structural change of the LiMn2O4 spinel structure induced by extraction of lithium. *Journal of Materials Chemistry* **1996,** *6* (1), 33-36.

60. Leifer, N.; Schipper, F.; Erickson, E. M.; Ghanty, C.; Talianker, M.; Grinblat, J.; Julien, C. M.; Markovsky, B.; Aurbach, D., Studies of Spinel-to-Layered Structural Transformations in LiMn2O4 Electrodes Charged to High Voltages. *The Journal of Physical Chemistry C* **2017,** *121* (17), 9120-9130.

61. Kamarulzaman, N.; Yusoff, R.; Kamarudin, N.; Shaari, N. H.; Abdul Aziz, N. A.; Bustam, M. A.; Blagojevic, N.; Elcombe, M.; Blackford, M.; Avdeev, M.; Arof, A. K., Investigation of cell parameters, microstructures and electrochemical behaviour of LiMn2O4 normal and nano powders. *Journal of Power Sources* **2009,** *188* (1), 274-280.

62. Hao, X.; Lin, X.; Lu, W.; Bartlett, B. M., Oxygen Vacancies Lead to Loss of Domain Order, Particle Fracture, and Rapid Capacity Fade in Lithium Manganospinel (LiMn2O4) Batteries. *ACS Applied Materials & Interfaces* **2014,** *6* (14), 10849-10857.

63. Putra, T. Y. S. P.; Yonemura, M.; Torii, S.; Ishigaki, T.; Kamiyama, T., Structure and electrochemical performance of the spinel-LiMn2O4 synthesized by mechanical alloying. *Solid State Ionics* **2014,** *262*, 83-87.

64. Sun, W.; Cao, F.; Liu, Y.; Zhao, X.; Liu, X.; Yuan, J., Nanoporous LiMn2O4 nanosheets with exposed {111} facets as cathodes for highly reversible lithium-ion batteries. *Journal of Materials Chemistry* **2012,** *22* (39), 20952-20957.

65. Kang, S.-H.; Goodenough, J. B.; Rabenberg , L. K., Nanocrystalline Lithium Manganese Oxide Spinel Cathode for Rechargeable Lithium Batteries. *Electrochemical and Solid-State Letters* **2001,** *4* (5), A49-A51.

66. Lee, S.; Oshima, Y.; Hosono, E.; Zhou, H.; Kim, K.; Chang, H. M.; Kanno, R.; Takayanagi, K., In Situ TEM Observation of Local Phase Transformation in a Rechargeable LiMn2O4 Nanowire Battery. *The Journal of Physical Chemistry C* **2013,** *117* (46), 24236-24241.

67. He, H.; Cong, H.; Sun, Y.; Zan, L.; Zhang, Y., Spinel-layered integrate structured nanorods with both high capacity and superior high-rate capability as cathode material for lithium-ion batteries. *Nano Research* **2017,** *10* (2), 556-569.

68. Nesbitt, H. W.; Banerjee, D., Interpretation of XPS Mn(2p) spectra of Mn oxyhydroxides and constraints on the mechanism of MnO 2 precipitation. *American Mineralogist* **1998,** *83* (3-4), 305-315.

69. Chen, Y.; Tian, Y.; Qiu, Y.; Liu, Z.; He, H.; Li, B.; Cao, H., Synthesis and superior cathode performance of sandwiched LiMn2O4@rGO nanocomposites for lithium-ion batteries. *Materials Today Advances* **2019,** *1*, 100001.

70. Hosono, E.; Kudo, T.; Honma, I.; Matsuda, H.; Zhou, H., Synthesis of Single Crystalline Spinel LiMn2O4 Nanowires for a Lithium Ion Battery with High Power Density. *Nano Letters* **2009,** *9* (3), 1045-1051.

71. Chen, K.-S.; Xu, R.; Luu, N. S.; Secor, E. B.; Hamamoto, K.; Li, Q.; Kim, S.; Sangwan, V. K.; Balla, I.; Guiney, L. M.; Seo, J.-W. T.; Yu, X.; Liu, W.; Wu, J.; Wolverton, C.; Dravid, V. P.; Barnett, S. A.; Lu, J.; Amine, K.; Hersam, M. C., Comprehensive Enhancement of Nanostructured Lithium-Ion Battery Cathode Materials via Conformal Graphene Dispersion. *Nano Letters* **2017,** *17* (4), 2539-2546.

72. Yu, L.; Qiu, X.; Xi, J.; Zhu, W.; Chen, L., Enhanced high-potential and elevated-temperature cycling stability of LiMn2O4 cathode by TiO2 modification for Li-ion battery. *Electrochimica Acta* **2006,** *51* (28), 6406-6411.

73. Cabana, J.; Valdés-Solís, T.; Palacín, M. R.; Oró-Solé, J.; Fuertes, A.; Marbán, G.; Fuertes, A. B., Enhanced high rate performance of LiMn2O4 spinel nanoparticles synthesized by a hard-template route. *Journal of Power Sources* **2007,** *166* (2), 492-498.

74. Ellingsen, L. A.-W.; Hung, C. R.; Strømman, A. H., Identifying key assumptions and differences in life cycle assessment studies of lithium-ion traction batteries with focus on greenhouse gas emissions. *Transportation Research Part D: Transport and Environment* **2017,** *55*, 82-90.

75. Winslow, K. M.; Laux, S. J.; Townsend, T. G., A review on the growing concern and potential management strategies of waste lithium-ion batteries. *Resources, Conservation and Recycling* **2018,** *129*, 263-277.

76. Chu, S.; Cui, Y.; Liu, N., The path towards sustainable energy. *Nature Materials* **2017,** *16* (1), 16-22.

77. Tran, M. K.; Rodrigues, M.-T. F.; Kato, K.; Babu, G.; Ajayan, P. M., Deep eutectic solvents for cathode recycling of Li-ion batteries. *Nature Energy* **2019,** *4* (4), 339-345.

78. Duffner, F.; Kronemeyer, N.; Tübke, J.; Leker, J.; Winter, M.; Schmuch, R., Post-lithium-ion battery cell production and its compatibility with lithium-ion cell production infrastructure. *Nature Energy* **2021,** *6* (2), 123-134.

79. Li, W.; Cho, Y.-G.; Yao, W.; Li, Y.; Cronk, A.; Shimizu, R.; Schroeder, M. A.; Fu, Y.; Zou, F.; Battaglia, V.; Manthiram, A.; Zhang, M.; Meng, Y. S., Enabling high areal capacity for Co-free high voltage spinel materials in next-generation Li-ion batteries. *Journal of Power Sources* **2020,** *473*, 228579.

80. Li, W.; Cheng, D.; Shimizu, R.; Li, Y.; Yao, W.; Raghavendran, G.; Zhang, M.; Meng, Y. S., Artificial cathode electrolyte interphase for improving high voltage cycling stability of thick electrode with Co-free 5 V spinel oxides. *Energy Storage Materials* **2022,** *49*, 77-84.

81. Yu, X., Releasing oxygen from the bulk. *Nature Energy* **2021,** *6* (6), 572-573.

82. Park, S. H.; Oh, S. W.; Kang, S. H.; Belharouak, I.; Amine, K.; Sun, Y. K., Comparative study of different crystallographic structure of LiNi0.5Mn1.5O4−δ cathodes with wide operation voltage (2.0–5.0V). *Electrochimica Acta* **2007,** *52* (25), 7226-7230.

83. Spence, S. L.; Xu, Z.; Sainio, S.; Nordlund, D.; Lin, F., Tuning the Morphology and Electronic Properties of Single-Crystal LiNi0.5Mn1.5O4−δ: Exploring the Influence of LiCl–KCl Molten Salt Flux Composition and Synthesis Temperature. *Inorganic Chemistry* **2020,** *59* (15), 10591-10603.

84. Yao, W.; Chouchane, M.; Li, W.; Bai, S.; Liu, Z.; Li, L.; Chen, A. X.; Sayahpour, B.; Shimizu, R.; Raghavendran, G.; Schroeder, M. A.; Chen, Y.-T.; Tan, D. H. S.; Sreenarayanan, B.; Waters, C. K.; Sichler, A.; Gould, B.; Kountz, D. J.; Lipomi, D. J.; Zhang, M.; Meng, Y. S., A 5 V-class cobalt-free battery cathode with high loading enabled by dry coating. *Energy & Environmental Science* **2023,** *16* (4), 1620-1630.

85. Jang, J.; Chen, Y.-T.; Deysher, G.; Cheng, D.; Ham, S.-Y.; Cronk, A.; Ridley, P.; Yang, H.; Sayahpour, B.; Han, B.; Li, W.; Yao, W.; Wu, E. A.; Doux, J.-M.; Nguyen, L. H. B.; Oh, J. A. S.; Tan, D. H. S.; Meng, Y. S., Enabling a Co-Free, High-Voltage LiNi0.5Mn1.5O4 Cathode in All-Solid-State Batteries with a Halide Electrolyte. *ACS Energy Letters* **2022,** *7* (8), 2531-2539.

86. Fehse, M.; Etxebarria, N.; Otaegui, L.; Cabello, M.; Martín-Fuentes, S.; Cabañero, M. A.; Monterrubio, I.; Elkjær, C. F.; Fabelo, O.; Enkubari, N. A.; López del Amo, J. M.; Casas-Cabanas, M.; Reynaud, M., Influence of Transition-Metal Order on the Reaction Mechanism of LNMO Cathode Spinel: An Operando X-ray Absorption Spectroscopy Study. *Chemistry of Materials* **2022,** *34* (14), 6529-6540.

87. He, J.; Melinte, G.; Darma, M. S. D.; Hua, W.; Das, C.; Schökel, A.; Etter, M.; Hansen, A. L.; Mereacre, L.; Geckle, U., Surface Structure Evolution and its Impact on the Electrochemical Performances of Aqueous‐Processed High‐Voltage Spinel LiNi0. 5Mn1. 5O4 Cathodes in Lithium‐Ion Batteries. *Advanced Functional Materials* **2022,** *32* (46), 2207937.

88. Xiao, J.; Chen, X.; Sushko, P. V.; Sushko, M. L.; Kovarik, L.; Feng, J.; Deng, Z.; Zheng, J.; Graff, G. L.; Nie, Z.; Choi, D.; Liu, J.; Zhang, J.-G.; Whittingham, M. S., High-Performance LiNi0.5Mn1.5O4 Spinel Controlled by Mn3+ Concentration and Site Disorder. *Advanced Materials* **2012,** *24* (16), 2109-2116.

89. Kim, J. W.; Kim, D. H.; Oh, D. Y.; Lee, H.; Kim, J. H.; Lee, J. H.; Jung, Y. S., Surface chemistry of LiNi0.5Mn1.5O4 particles coated by Al2O3 using atomic layer deposition for lithium-ion batteries. *Journal of Power Sources* **2015,** *274*, 1254-1262.

90. Piao, N.; Wang, P.-F.; Chen, L.; Deng, T.; Fan, X.; Wang, L.; He, X., Nonflammable all-fluorinated electrolytes enabling high-power and long-life LiNi0.5Mn1.5O4/Li4Ti5O12 lithium-ion batteries. *Nano Energy* **2023,** *105*, 108040.

91. Wang, R.; Chen, X.; Huang, Z.; Yang, J.; Liu, F.; Chu, M.; Liu, T.; Wang, C.; Zhu, W.; Li, S.; Li, S.; Zheng, J.; Chen, J.; He, L.; Jin, L.; Pan, F.; Xiao, Y., Twin boundary defect engineering improves lithium-ion diffusion for fast-charging spinel cathode materials. *Nature Communications* **2021,** *12* (1), 3085.

92. Gao, H.; Yan, Q.; Tran, D.; Yu, X.; Liu, H.; Li, M.; Li, W.; Wu, J.; Tang, W.; Gupta, V.; Luo, J.; Chen, Z., Upcycling of Spent LiNi0.33Co0.33Mn0.33O2 to Single-Crystal Ni-Rich Cathodes Using Lean Precursors. *ACS Energy Letters* **2023,** *8* (10), 4136-4144.

93. Yu, X.; Yu, S.; Yang, Z.; Gao, H.; Xu, P.; Cai, G.; Rose, S.; Brooks, C.; Liu, P.; Chen, Z., Achieving low-temperature hydrothermal relithiation by redox mediation for direct recycling of spent lithium-ion battery cathodes. *Energy Storage Materials* **2022,** *51*, 54-62.

94. Xu, P.; Yang, Z.; Yu, X.; Holoubek, J.; Gao, H.; Li, M.; Cai, G.; Bloom, I.; Liu, H.; Chen, Y.; An, K.; Pupek, K. Z.; Liu, P.; Chen, Z., Design and Optimization of the Direct Recycling of Spent Li-Ion Battery Cathode Materials. *ACS Sustainable Chemistry & Engineering* **2021,** *9* (12), 4543-4553.

95. Gao, H.; Yan, Q.; Xu, P.; Liu, H.; Li, M.; Liu, P.; Luo, J.; Chen, Z., Efficient Direct Recycling of Degraded LiMn2O4 Cathodes by One-Step Hydrothermal Relithiation. *ACS Applied Materials & Interfaces* **2020,** *12* (46), 51546-51554.

96. Qin, Z.; Zhang, Y.; Luo, W.; Zhang, T.; Wang, T.; Ni, L.; Wang, H.; Zhang, N.; Liu, X.; Zhou, J., A Universal Molten Salt Method for Direct Upcycling of Spent Ni‐rich Cathode towards Single‐crystalline Li‐rich Cathode. *Angewandte Chemie*

2023, e202218672.

97. Meng, X.; Hao, J.; Cao, H.; Lin, X.; Ning, P.; Zheng, X.; Chang, J.; Zhang, X.; Wang, B.; Sun, Z., Recycling of LiNi1/3Co1/3Mn1/3O2 cathode materials from spent lithium-ion batteries using mechanochemical activation and solid-state sintering. *Waste Management* **2019,** *84*, 54-63.

98. Wang, M.; Tan, Q.; Liu, L.; Li, J., Efficient separation of aluminum foil and cathode materials from spent lithium-ion batteries using a low-temperature molten salt. *ACS Sustainable Chemistry & Engineering* **2019,** *7* (9), 8287-8294.

99. Park, K.; Yu, J.; Coyle, J.; Dai, Q.; Frisco, S.; Zhou, M.; Burrell, A., Direct Cathode Recycling of End-Of-Life Li-Ion Batteries Enabled by Redox Mediation. *ACS Sustainable Chemistry & Engineering* **2021**.

100. Xu, P.; Dai, Q.; Gao, H.; Liu, H.; Zhang, M.; Li, M.; Chen, Y.; An, K.; Meng, Y. S.; Liu, P.; Li, Y.; Spangenberger, J. S.; Gaines, L.; Lu, J.; Chen, Z., Efficient Direct Recycling of Lithium-Ion Battery Cathodes by Targeted Healing. *Joule* **2020,** *4* (12), 2609-2626.

101. Shi, Y.; Chen, G.; Chen, Z., Effective regeneration of LiCoO 2 from spent lithium-ion batteries: a direct approach towards high-performance active particles. *Green Chemistry* **2018,** *20* (4), 851-862.

102. Lin, J.; Fan, E.; Zhang, X.; Li, Z.; Dai, Y.; Chen, R.; Wu, F.; Li, L., Sustainable Upcycling of Spent Lithium‐Ion Batteries Cathode Materials: Stabilization by In Situ Li/Mn Disorder. *Advanced Energy Materials* **2022,** *12* (26), 2201174.

103. Wan, T. H.; Saccoccio, M.; Chen, C.; Ciucci, F., Influence of the Discretization Methods on the Distribution of Relaxation Times Deconvolution: Implementing Radial Basis Functions with DRTtools. *Electrochimica Acta* **2015,** *184*, 483-499.

104. Wang, D.; Gao, C.; Zhou, X.; Peng, S.; Tang, M.; Wang, Y.; Huang, L.; Yang, W.; Gao, X., Enhancing reversibility of LiNi0. 5Mn1. 5O4 by regulating surface oxygen deficiency. *Carbon Energy* **2023**, e338.

105. Ding, H.; Wang, P.; Zhang, N.; Zhou, J.; Li, X.; Li, C.; Zhao, D.; Li, S., Improving electrochemical performances of LiNi0.5Mn1.5O4 by the strategy of oxygen vacancy doping. *Applied Materials Today* **2024,** *38*, 102248.

106. Jiang, H.; Zeng, C.; Zhu, W.; Luo, J.; Liu, Z.; Zhang, J.; Liu, R.; Xu, Y.; Chen, Y.; Hu, W., Boosting cycling stability by regulating surface oxygen vacancies of LNMO by rapid calcination. *Nano Research* **2024,** *17* (4), 2671-2677.

107. Sun, H.; Hu, A.; Spence, S.; Kuai, C.; Hou, D.; Mu, L.; Liu, J.; Li, L.; Sun, C.; Sainio, S., Tailoring disordered/ordered phases to revisit the degradation mechanism of high‐voltage LiNi0. 5Mn1. 5O4 spinel cathode materials. *Advanced Functional Materials* **2022,** *32* (21), 2112279.

108. Gao, C.; Liu, H.; Zhang, J.; Guo, Z.; Huang, H., Simplified crystal grain boundary engineering of solid electrolyte-infused LiNi0. 5Mn1. 5O4 cathodes for high cycling stability lithium-ion batteries. *Journal of Power Sources* **2023,** *582*, 233434.

109. Stüble, P.; Mereacre, V.; Geßwein, H.; Binder, J. R., On the Composition of LiNi0. 5Mn1. 5O4 Cathode Active Materials. *Advanced Energy Materials* **2023,** *13* (10), 2203778.

110. Zhu, X.; Schülli, T. U.; Yang, X.; Lin, T.; Hu, Y.; Cheng, N.; Fujii, H.; Ozawa, K.; Cowie, B.; Gu, Q.; Zhou, S.; Cheng, Z.; Du, Y.; Wang, L., Epitaxial growth of an atom-thin layer on a LiNi0.5Mn1.5O4 cathode for stable Li-ion battery cycling. *Nature Communications* **2022,** *13* (1), 1565.

111. Gupta, V.; Yu, X.; Gao, H.; Brooks, C.; Li, W.; Chen, Z., Scalable Direct Recycling of Cathode Black Mass from Spent Lithium‐Ion Batteries. *Advanced Energy Materials* **2023,** *13* (6), 2203093.

112. Kim, J.-H.; Myung, S.-T.; Yoon, C.; Kang, S.; Sun, Y.-K., Comparative study of LiNi0. 5Mn1. 5O4-δ and LiNi0. 5Mn1. 5O4 cathodes having two crystallographic structures: fd $\bar{3}$m and P 4332. *Chemistry of materials* **2004,** *16* (5), 906-914.

113. Choi, H. W.; Kim, S. J.; Rim, Y.-H.; Yang, Y. S., Effect of Lithium Deficiency on Lithium-Ion Battery Cathode LixNi0.5Mn1.5O4. *The Journal of Physical Chemistry C* **2015,** *119* (49), 27192-27199.

114. Pang, W. K.; Lu, C.-Z.; Liu, C.-E.; Peterson, V. K.; Lin, H.-F.; Liao, S.-C.; Chen, J.-M., Crystallographic origin of cycle decay of the high-voltage LiNi0.5Mn1.5O4 spinel lithium-ion battery electrode. *Physical Chemistry Chemical Physics* **2016,** *18* (26), 17183-17189.

115. Sushko, P. V.; Rosso, K. M.; Zhang, J. G.; Liu, J.; Sushko, M. L., Oxygen Vacancies and Ordering of d‐levels Control Voltage Suppression in Oxide Cathodes: the Case of Spinel LiNi0. 5Mn1. 5O4‐δ. *Advanced Functional Materials* **2013,** *23* (44), 5530-5535.

116. Lee, Y.; Shin, J.; Kang, H.; Lee, D.; Kim, T. H.; Kwon, Y. K.; Cho, E., Promoting the Reversible Oxygen Redox Reaction of Li‐Excess Layered Cathode Materials with Surface Vanadium Cation Doping. *Advanced Science* **2021,** *8* (6), 2003013.

117. Jo, M. R.; Kim, Y. I.; Kim, Y.; Chae, J. S.; Roh, K. C.; Yoon, W. S.; Kang, Y. M., Lithium‐Ion Transport through a Tailored Disordered Phase on the LiNi0. 5Mn1. 5O4 Surface for High‐Power Cathode Materials. *ChemSusChem* **2014,** *7* (8), 2248-2254.

118. Sun, H.; Hu, A.; Spence, S.; Kuai, C.; Hou, D.; Mu, L.; Liu, J.; Li, L.; Sun, C.; Sainio, S.; Nordlund, D.; Luo, W.; Huang, Y.; Lin, F., Tailoring Disordered/Ordered Phases to Revisit the Degradation Mechanism of High-Voltage LiNi0.5Mn1.5O4 Spinel Cathode Materials. *Advanced Functional Materials* **2022,** *32* (21), 2112279.

119. Gao, X.; Ikuhara, Y. H.; Fisher, C. A.; Moriwake, H.; Kuwabara, A.; Oki, H.; Kohama, K.; Yoshida, R.; Huang, R.; Ikuhara, Y., Structural distortion and compositional gradients adjacent to epitaxial LiMn2O4 thin film interfaces. *Advanced Materials Interfaces* **2014,** *1* (8), 1400143.

120. Shin, D. W.; Bridges, C. A.; Huq, A.; Paranthaman, M. P.; Manthiram, A., Role of Cation Ordering and Surface Segregation in High-Voltage Spinel LiMn1. 5Ni0. 5–x M x O4 (M= Cr, Fe, and Ga) Cathodes for Lithium-Ion Batteries. *Chemistry of Materials* **2012,** *24* (19), 3720-3731.

121. Aktekin, B.; Massel, F.; Ahmadi, M.; Valvo, M.; Hahlin, M.; Zipprich, W.; Marzano, F.; Duda, L.; Younesi, R.; Edström, K.; Brandell, D., How Mn/Ni Ordering Controls Electrochemical Performance in High-Voltage Spinel LiNi0.44Mn1.56O4 with Fixed Oxygen Content. *ACS Applied Energy Materials* **2020,** *3* (6), 6001-6013.

122. Lee, W.; Lee, S.; Lee, E.; Choi, M.; Thangavel, R.; Lee, Y.; Yoon, W.-S., Destabilization of the surface structure of Ni-rich layered materials by water-washing process. *Energy Storage Materials* **2022,** *44*, 441-451.

123. Priester, L., *Grain boundaries: from theory to engineering*. Springer Science & Business Media: 2012; Vol. 172.

124. Parajuli, P.; Mendoza‐Cruz, R.; Santiago, U.; Ponce, A.; Yacamán, M. J., The evolution of growth, crystal orientation, and grain boundaries disorientation distribution in gold thin films. *Crystal Research Technology* **2018,** *53* (8), 1800038.

125. Quinn, A.; Moutinho, H.; Usseglio-Viretta, F.; Verma, A.; Smith, K.; Keyser, M.; Finegan, D. P., Electron Backscatter Diffraction for Investigating Lithium-Ion Electrode Particle Architectures. *Cell Reports Physical Science* **2020,** *1* (8), 100137.

126. Jiang, C.; Tang, Z.; Wang, S.; Zhang, Z., A truncated octahedral spinel LiMn2O4 as high-performance cathode material for ultrafast and long-life lithium-ion batteries. *Journal of Power Sources* **2017,** *357*, 144-148.

127. Xu, C.; Li, J.; Feng, X.; Zhao, J.; Tang, C.; Ji, B.; Hu, J.; Cao, C.; Zhu, Y.; Butt, F. K., The improved performance of spinel LiMn2O4 cathode with micro-nanostructured sphere-interconnected-tube morphology and surface orientation at extreme conditions for lithium-ion batteries. *Electrochimica Acta* **2020,** *358*, 136901.

128. Gil-Alana, L. A.; Monge, M., Lithium: Production and estimated consumption. Evidence of persistence. *Resources Policy* **2019,** *60*, 198-202.

129. Fan, E.; Li, L.; Wang, Z.; Lin, J.; Huang, Y.; Yao, Y.; Chen, R.; Wu, F., Sustainable Recycling Technology for Li-Ion Batteries and Beyond: Challenges and Future Prospects. *Chemical Reviews* **2020,** *120* (14), 7020-7063.

130. Shahjalal, M.; Roy, P. K.; Shams, T.; Fly, A.; Chowdhury, J. I.; Ahmed, M. R.; Liu, K., A review on second-life of Li-ion batteries: prospects, challenges, and issues. *Energy* **2022,** *241*, 122881.

131. Abdelbaky, M.; Peeters, J. R.; Dewulf, W., On the influence of second use, future battery technologies, and battery lifetime on the maximum recycled content of future electric vehicle batteries in Europe. *Waste Management* **2021,** *125*, 1-9.

132. Geng, J.; Gao, S.; Sun, X.; Liu, Z.; Zhao, F.; Hao, H., Potential of electric vehicle batteries second use in energy storage systems: The case of China. *Energy* **2022,** *253*, 124159.

133. Harper, G.; Sommerville, R.; Kendrick, E.; Driscoll, L.; Slater, P.; Stolkin, R.; Walton, A.; Christensen, P.; Heidrich, O.; Lambert, S., Recycling lithium-ion batteries from electric vehicles. *Nature* **2019,** *575* (7781), 75-86.

134. Li, Y.; Zuba, M. J.; Bai, S.; Lebens-Higgins, Z. W.; Qiu, B.; Park, S.; Liu, Z.; Zhang, M.; Piper, L. F. J.; Meng, Y. S., Regeneration of degraded Li-rich layered oxide materials through heat treatment-induced transition metal reordering. *Energy Storage Materials* **2021,** *35*, 99-107.

135. Ma, T.; Guo, Z.; Shen, Z.; Wu, Q.; Li, Y.; Yang, G., Molten salt-assisted regeneration and characterization of submicron-sized LiNi0.5Co0.2Mn0.3O2 crystals from spent lithium ion batteries. *Journal of Alloys and Compounds* **2020,** *848*, 156591.

136. Yang, J.; Wang, W.; Yang, H.; Wang, D., One-pot compositional and structural regeneration of degraded LiCoO2 for directly reusing it as a high-performance lithium-ion battery cathode. *Green Chemistry* **2020,** *22* (19), 6489-6496.

137. Park, K.; Yu, J.; Coyle, J.; Dai, Q.; Frisco, S.; Zhou, M.; Burrell, A., Direct cathode recycling of end-of-life Li-ion batteries enabled by redox mediation. *ACS Sustainable Chemistry & Engineering* **2021,** *9* (24), 8214-8221.

138. Jing, Q.; Zhang, J.; Liu, Y.; Zhang, W.; Chen, Y.; Wang, C., Direct Regeneration of Spent LiFePO4 Cathode Material by a Green and Efficient One-Step Hydrothermal Method. *ACS Sustainable Chemistry & Engineering* **2020,** *8* (48), 17622-17628.

139. Zhang, R.; Meng, Z.; Ma, X.; Chen, M.; Chen, B.; Zheng, Y.; Yao, Z.; Vanaphuti, P.; Bong, S.; Yang, Z., Understanding fundamental effects of Cu impurity in different forms for recovered LiNi0. 6Co0. 2Mn0. 2O2 cathode materials. *Nano Energy* **2020,** *78*, 105214.

140. Zhang, F.; Lou, S.; Li, S.; Yu, Z.; Liu, Q.; Dai, A.; Cao, C.; Toney, M. F.; Ge, M.; Xiao, X.; Lee, W.-K.; Yao, Y.; Deng, J.; Liu, T.; Tang, Y.; Yin, G.; Lu, J.; Su, D.; Wang, J., Surface regulation enables high stability of single-crystal lithium-ion cathodes at high voltage. *Nature Communications* **2020,** *11* (1), 3050.

141. Qian, G.; Zhang, Y.; Li, L.; Zhang, R.; Xu, J.; Cheng, Z.; Xie, S.; Wang, H.; Rao, Q.; He, Y., Single-crystal nickel-rich layered-oxide battery cathode materials: synthesis, electrochemistry, and intra-granular fracture. *Energy Storage Materials* **2020,** *27*, 140-149.

142. Trevisanello, E.; Ruess, R.; Conforto, G.; Richter, F. H.; Janek, J., Polycrystalline and Single Crystalline NCM Cathode Materials—Quantifying Particle Cracking, Active Surface Area, and Lithium Diffusion. *Advanced Energy Materials* **2021,** *11* (18), 2003400.

143. Ma, X.; Hou, J.; Vanaphuti, P.; Yao, Z.; Fu, J.; Azhari, L.; Liu, Y.; Wang, Y., Direct upcycling of mixed Ni-lean polycrystals to single-crystal Ni-rich cathode materials. *Chem* **2022,** *8* (7), 1944-1955.

144. Qian, G.; Li, Z.; Wang, Y.; Xie, X.; He, Y.; Li, J.; Zhu, Y.; Xie, S.; Cheng, Z.; Che, H.; Shen, Y.; Chen, L.; Huang, X.; Pianetta, P.; Ma, Z.-F.; Liu, Y.; Li, L., Value-creating upcycling of retired electric vehicle battery cathodes. *Cell Reports Physical Science* **2022,** *3* (2), 100741.

145. Qin, Z.; Zhang, Y.; Luo, W.; Zhang, T.; Wang, T.; Ni, L.; Wang, H.; Zhang, N.; Liu, X.; Zhou, J., A Universal Molten Salt Method for Direct Upcycling of Spent Ni‐rich Cathode towards Single‐crystalline Li‐rich Cathode. *Angewandte Chemie* **2023**, e202218672.

146. Wang, T.; Luo, H.; Fan, J.; Thapaliya, B. P.; Bai, Y.; Belharouak, I.; Dai, S., Flux upcycling of spent NMC 111 to nickel-rich NMC cathodes in reciprocal ternary molten salts. *iScience* **2022,** *25* (2), 103801.

147. Yoon, M.; Dong, Y.; Huang, Y.; Wang, B.; Kim, J.; Park, J.-S.; Hwang, J.; Park, J.; Kang, S. J.; Cho, J., Eutectic salt-assisted planetary centrifugal deagglomeration for single-crystalline cathode synthesis. *Nature Energy* **2023**, 1-10.

148. Liu, Y.; Meirer, F.; Williams, P. A.; Wang, J.; Andrews, J. C.; Pianetta, P., TXM-Wizard: a program for advanced data collection and evaluation in full-field transmission X-ray microscopy. *Journal of Synchrotron Radiation* **2012,** *19* (2), 281-287.

149. Kimijima, T.; Zettsu, N.; Yubuta, K.; Hirata, K.; Kami, K.; Teshima, K., Molybdate flux growth of idiomorphic Li (Ni 1/3 Co 1/3 Mn 1/3) O 2 single crystals and characterization of their capabilities as cathode materials for lithium-ion batteries. *Journal of Materials Chemistry A* **2016,** *4* (19), 7289-7296.

150. Zhu, X.; Zhou, J.; Jiang, M.; Xie, J.; Liang, S.; Li, S.; Liu, Z.; Zhu, Y.; Zhu, J.; Liu, Z., Molten Salt Synthesis of Bismuth Ferrite Nano- and Microcrystals and their Structural Characterization. *Journal of the American Ceramic Society* **2014,** *97* (7), 2223-2232.

151. Park, J. H.; Lee, D. H.; Shin, H. S.; Lee, B. K., Transition of the Particle‐Growth Mechanism with Temperature Variation in the Molten‐Salt Method. *Journal of the American Ceramic Society* **1996,** *79* (4), 1130-1132.

152. Wang, J.; Zhang, Z.; He, W.; Wang, Z.; Weng, S.; Li, Q.; Wang, X.; Barg, S.; Chen, L.; Li, H.; Wu, F., Fast charge storage kinetics by surface engineering for Ni-rich layered oxide cathodes. *Journal of Materials Chemistry A* **2023,** *11* (19), 10239-10253.

153. Zhu, J.; Chen, G., Single-crystal based studies for correlating the properties and high-voltage performance of Li [Ni x Mn y Co 1− x− y] O 2 cathodes. *Journal of Materials Chemistry A* **2019,** *7* (10), 5463-5474.

154. Lee, K.-S.; Myung, S.-T.; Amine, K.; Yashiro, H.; Sun, Y.-K., Structural and Electrochemical Properties of Layered Li [Ni1− 2x Co x Mn x] O2 (x= 0.1–0.3) Positive Electrode Materials for Li-Ion Batteries. *Journal of The Electrochemical Society* **2007,** *154* (10), A971.

155. Kosova, N.; Devyatkina, E.; Kaichev, V., Optimization of Ni 2+/Ni 3+ ratio in layered Li(Ni,Mn,Co)O 2 cathodes for better electrochemistry. *Journal of Power Sources* **2007,** *174*, 965-969.

156. Tsebesebe, N.; Kgatwane, K.; Ledwaba, R.; Ngoepe, P., Investigating the Structural and Electronic Properties of LiMO 2 (M: Mn, Ni, Co) as Potential Cathode Materials: A DFT Study. *Journal of Physics: Conference Series* **2022,** *2298*, 012010.

157. Wang, C.; Wang, R.; Huang, Z.; Chu, M.; Ji, W.; Chen, Z.; Zhang, T.; Zhai, J.; Lu, H.; Deng, S.; Chen, J.; He, L.; Liang, T.; Wang, F.; Wang, J.; Deng, Y.; Cai, W.; Xiao, Y., Unveiling the migration behavior of lithium ions in NCM/Graphite full cell via in operando neutron diffraction. *Energy Storage Materials* **2022,** *44*, 1-9.

158. Chien, P. H.; Wu, X.; Song, B.; Yang, Z.; Waters, C. K.; Everett, M. S.; Lin, F.; Du, Z.; Liu, J., New insights into structural evolution of LiNiO2 revealed by operando neutron diffraction. *Batteries & Supercaps* **2021,** *4* (11), 1701-1707.

159. Ge, M.; Wi, S.; Liu, X.; Bai, J.; Ehrlich, S.; Lu, D.; Lee, W. K.; Chen, Z.; Wang, F., Kinetic Limitations in Single‐Crystal High‐Nickel Cathodes. *Angewandte Chemie International Edition* **2021,** *60* (32), 17350-17355.

160. Zhu, H.; Tang, Y.; Wiaderek, K. M.; Borkiewicz, O. J.; Ren, Y.; Zhang, J.; Ren, J.; Fan, L.; Li, C. C.; Li, D.; Wang, X.-L.; Liu, Q., Spontaneous Strain Buffer Enables Superior Cycling Stability in Single-Crystal Nickel-Rich NCM Cathode. *Nano Letters* **2021,** *21* (23), 9997-10005.

161. Ahmed, S.; Bloom, I.; Jansen, A. N.; Tanim, T.; Dufek, E. J.; Pesaran, A.; Burnham, A.; Carlson, R. B.; Dias, F.; Hardy, K.; Keyser, M.; Kreuzer, C.; Markel, A.; Meintz, A.; Michelbacher, C.; Mohanpurkar, M.; Nelson, P. A.; Robertson, D. C.; Scoffield, D.; Shirk, M.; Stephens, T.; Vijayagopal, R.; Zhang, J., Enabling fast charging – A battery technology gap assessment. *Journal of Power Sources* **2017,** *367*, 250-262.

162. Xu, K., "Charge-transfer" process at graphite/electrolyte interface and the solvation sheath structure of Li+ in nonaqueous electrolytes. *Journal of the electrochemical society* **2007,** *154* (3), A162.

163. Xu, K.; von Cresce, A.; Lee, U., Differentiating contributions to "ion transfer" barrier from interphasial resistance and Li+ desolvation at electrolyte/graphite interface. *Langmuir* **2010,** *26* (13), 11538-11543.

164. Babu, B.; Simon, P.; Balducci, A., Fast charging materials for high power applications. *Advanced Energy Materials* **2020,** *10* (29), 2001128.

165. Zhu, G. L.; Zhao, C. Z.; Huang, J. Q.; He, C.; Zhang, J.; Chen, S.; Xu, L.; Yuan, H.; Zhang, Q., Fast charging lithium batteries: recent progress and future prospects. *Small* **2019,** *15* (15), 1805389.

166. Tanim, T. R.; Weddle, P. J.; Yang, Z.; Colclasure, A. M.; Charalambous, H.; Finegan, D. P.; Lu, Y.; Preefer, M.; Kim, S.; Allen, J. M., Enabling extreme fast‐charging: challenges at the cathode and mitigation strategies. *Advanced Energy Materials* **2022,** *12* (46), 2202795.

167. Wu, X.; Bai, Y.; Li, Z.; Liu, J.; Zhao, K.; Du, Z., Effects of charging rates on LiNi0. 6Mn0. 2Co0. 2O2 (NMC622)/graphite Li-ion cells. *Journal of Energy Chemistry* **2021,** *56*, 121-126.

168. Liu, T.; Du, Z.; Wu, X.; Rahman, M. M.; Nordlund, D.; Zhao, K.; Schulz, M. D.; Lin, F.; Wood, D. L.; Belharouak, I., Bulk and surface structural changes in high nickel cathodes subjected to fast charging conditions. *Chemical Communications* **2020,** *56* (51), 6973-6976.

169. Liu, Y.; Zhu, Y.; Cui, Y., Challenges and opportunities towards fast-charging battery materials. *Nature Energy* **2019,** *4* (7), 540-550.

170. Cai, W.; Yao, Y.-X.; Zhu, G.-L.; Yan, C.; Jiang, L.-L.; He, C.; Huang, J.-Q.; Zhang, Q., A review on energy chemistry of fast-charging anodes. *Chemical society reviews* **2020,** *49* (12), 3806-3833.

171. Paul, P. P.; Thampy, V.; Cao, C.; Steinrück, H.-G.; Tanim, T. R.; Dunlop, A. R.; Dufek, E. J.; Trask, S. E.; Jansen, A. N.; Toney, M. F., Quantification of heterogeneous, irreversible lithium plating in extreme fast charging of lithium-ion batteries. *Energy & Environmental Science* **2021,** *14* (9), 4979-4988.

172. Billaud, J.; Bouville, F.; Magrini, T.; Villevieille, C.; Studart, A. R., Magnetically aligned graphite electrodes for high-rate performance Li-ion batteries. *Nature Energy* **2016,** *1* (8), 1-6.

173. Chen, K.-H.; Namkoong, M. J.; Goel, V.; Yang, C.; Kazemiabnavi, S.; Mortuza, S. M.; Kazyak, E.; Mazumder, J.; Thornton, K.; Sakamoto, J., Efficient fast-charging of lithium-ion batteries enabled by laser-patterned three-dimensional graphite anode architectures. *Journal of Power Sources* **2020,** *471*, 228475.

174. Kim, N.; Chae, S.; Ma, J.; Ko, M.; Cho, J., Fast-charging high-energy lithium-ion batteries via implantation of amorphous silicon nanolayer in edge-plane activated graphite anodes. *Nature communications* **2017,** *8* (1), 812.

175. Cheng, Q.; Yuge, R.; Nakahara, K.; Tamura, N.; Miyamoto, S., KOH etched graphite for fast chargeable lithium-ion batteries. *Journal of Power Sources* **2015,** *284*, 258-263.

176. Chen, K. H.; Goel, V.; Namkoong, M. J.; Wied, M.; Müller, S.; Wood, V.; Sakamoto, J.; Thornton, K.; Dasgupta, N. P., Enabling 6C fast charging of Li‐ion batteries with graphite/hard carbon hybrid anodes. *Advanced energy materials* **2021,** *11* (5), 2003336.

177. Betz, J.; Bieker, G.; Meister, P.; Placke, T.; Winter, M.; Schmuch, R., Theoretical versus practical energy: a plea for more transparency in the energy calculation of different rechargeable battery systems. *Advanced energy materials* **2019,** *9* (6), 1803170.

178. Liu, J.; Bao, Z.; Cui, Y.; Dufek, E. J.; Goodenough, J. B.; Khalifah, P.; Li, Q.; Liaw, B. Y.; Liu, P.; Manthiram, A., Pathways for practical high-energy long-cycling lithium metal batteries. *Nature Energy* **2019,** *4* (3), 180-186.

179. Dufek, E. J.; Abraham, D. P.; Bloom, I.; Chen, B.-R.; Chinnam, P. R.; Colclasure, A. M.; Gering, K. L.; Keyser, M.; Kim, S.; Mai, W., Developing extreme fast charge battery protocols–A review spanning materials to systems. *Journal of Power Sources* **2022,** *526*, 231129.

180. Colclasure, A. M.; Dunlop, A. R.; Trask, S. E.; Polzin, B. J.; Jansen, A. N.; Smith, K., Requirements for enabling extreme fast charging of high energy density Li-ion cells while avoiding lithium plating. *Journal of the electrochemical society* **2019,** *166* (8), A1412.

181. Colclasure, A. M.; Tanim, T. R.; Jansen, A. N.; Trask, S. E.; Dunlop, A. R.; Polzin, B. J.; Bloom, I.; Robertson, D.; Flores, L.; Evans, M., Electrode scale and electrolyte transport effects on extreme fast charging of lithium-ion cells. *Electrochimica Acta* **2020,** *337*, 135854.

182. Chinnam, P. R.; Colclasure, A. M.; Chen, B.-R.; Tanim, T. R.; Dufek, E. J.; Smith, K.; Evans, M. C.; Dunlop, A. R.; Trask, S. E.; Polzin, B. J., Fast-charging aging considerations: Incorporation and alignment of cell design and material degradation pathways. *ACS Applied Energy Materials* **2021,** *4* (9), 9133-9143.

183. Li, M.; Wang, C.; Chen, Z.; Xu, K.; Lu, J., New concepts in electrolytes. *Chemical reviews* **2020,** *120* (14), 6783-6819.

184. Liao, B.; Li, H.; Xu, M.; Xing, L.; Liao, Y.; Ren, X.; Fan, W.; Yu, L.; Xu, K.; Li, W., Designing low impedance interface films simultaneously on anode and cathode for high energy batteries. *Advanced energy materials* **2018,** *8* (22), 1800802.

185. Logan, E. R.; Dahn, J. R., Electrolyte design for fast-charging Li-ion batteries. *Trends in Chemistry* **2020,** *2* (4), 354-366.

186. Logan, E. R.; Hall, D. S.; Cormier, M. M. E.; Taskovic, T.; Bauer, M.; Hamam, I.; Hebecker, H.; Molino, L.; Dahn, J. R., Ester-based electrolytes for fast charging of energy dense lithium-ion batteries. *The Journal of Physical Chemistry C* **2020,** *124* (23), 12269-12280.

187. Smart, M. C.; Lucht, B. L.; Dalavi, S.; Krause, F. C.; Ratnakumar, B. V., The effect of additives upon the performance of MCMB/LiNixCo1− xO2 Li-ion cells containing methyl

butyrate-based wide operating temperature range electrolytes. *Journal of The Electrochemical Society* **2012,** *159* (6), A739.

188. Du, Z.; Wood Iii, D. L.; Belharouak, I., Enabling fast charging of high energy density Li-ion cells with high lithium ion transport electrolytes. *Electrochemistry communications* **2019,** *103*, 109-113.

189. Gao, N.; Kim, S.; Chinnam, P.; Dufek, E. J.; Colclasure, A. M.; Jansen, A.; Son, S.-B.; Bloom, I.; Dunlop, A.; Trask, S., Methodologies for design, characterization and testing of electrolytes that enable extreme fast charging of lithium-ion cells. *Energy storage materials* **2022,** *44*, 296-312.

190. Wu, X.; Liu, T.; Bai, Y.; Feng, X.; Rahman, M. M.; Sun, C.-J.; Lin, F.; Zhao, K.; Du, Z., Effects of solvent formulations in electrolytes on fast charging of Li-ion cells. *Electrochimica acta* **2020,** *353*, 136453.

191. Wen, B.; Deng, Z.; Tsai, P.-C.; Lebens-Higgins, Z. W.; Piper, L. F. J.; Ong, S. P.; Chiang, Y.-M., Ultrafast ion transport at a cathode–electrolyte interface and its strong dependence on salt solvation. *Nature Energy* **2020,** *5* (8), 578-586.

192. Huang, B.; Myint, K. H.; Wang, Y.; Zhang, Y.; Rao, R. R.; Sun, J.; Muy, S.; Katayama, Y.; Corchado Garcia, J.; Fraggedakis, D., Cation-dependent interfacial structures and kinetics for outer-sphere electron-transfer reactions. *The Journal of Physical Chemistry C* **2021,** *125* (8), 4397-4411.

193. Wang, Z.; Sun, Z.; Shi, Y.; Qi, F.; Gao, X.; Yang, H.; Cheng, H. M.; Li, F., Ion‐dipole chemistry drives rapid evolution of Li ions solvation sheath in low‐temperature Li batteries. *Advanced Energy Materials* **2021,** *11* (28), 2100935.

194. Cheng, H.; Sun, Q.; Li, L.; Zou, Y.; Wang, Y.; Cai, T.; Zhao, F.; Liu, G.; Ma, Z.; Wahyudi, W., Emerging era of electrolyte solvation structure and interfacial model in batteries. *ACS Energy Letters* **2022,** *7* (1), 490-513.

195. Petibon, R.; Harlow, J.; Le, D.; Dahn, J., The use of ethyl acetate and methyl propanoate in combination with vinylene carbonate as ethylene carbonate-free solvent blends for electrolytes in Li-ion batteries. *Electrochimica Acta* **2015,** *154*, 227-234.

196. Kumar, N.; Seminario, J. M., Lithium-Ion Model Behavior in an Ethylene Carbonate Electrolyte Using Molecular Dynamics. *The Journal of Physical Chemistry C* **2016,** *120* (30), 16322-16332.

197. Park, C.; Kanduč, M.; Chudoba, R.; Ronneburg, A.; Risse, S.; Ballauff, M.; Dzubiella, J., Molecular simulations of electrolyte structure and dynamics in lithium–sulfur battery solvents. *Journal of Power Sources* **2018,** *373,* 70-78.

198. Hou, S.; Ji, X.; Gaskell, K.; Wang, P.-f.; Wang, L.; Xu, J.; Sun, R.; Borodin, O.; Wang, C., Solvation sheath reorganization enables divalent metal batteries with fast interfacial charge transfer kinetics. *Science* **2021,** *374* (6564), 172-178.

199. Holoubek, J.; Yin, Y.; Li, M.; Yu, M.; Meng, Y. S.; Liu, P.; Chen, Z. J. A. C., Exploiting mechanistic solvation kinetics for dual‐graphite batteries with high power output at extremely low temperature. **2019,** *131* (52), 19068-19073.

200. Cho, Y.-G.; Li, M.; Holoubek, J.; Li, W.; Yin, Y.; Meng, Y. S.; Chen, Z., Enabling the low-temperature cycling of NMC|| graphite pouch cells with an ester-based electrolyte. *ACS Energy Letters* **2021,** *6* (5), 2016-2023.

201. Baskin, A.; Prendergast, D., "Ion Solvation Spectra": free energy analysis of solvation structures of multivalent cations in aprotic solvents. *The journal of physical chemistry letters* **2019,** *10* (17), 4920-4928.

202. Baskin, A.; Prendergast, D., Ion Solvation Engineering: How to Manipulate the Multiplicity of the Coordination Environment of Multivalent Ions. *The Journal of Physical Chemistry Letters* **2020,** *11* (21), 9336-9343.

203. Baskin, A.; Lawson, J. W.; Prendergast, D., Anion-Assisted Delivery of Multivalent Cations to Inert Electrodes. *The Journal of Physical Chemistry Letters* **2021,** *12* (18), 4347-4356.

204. Holoubek, J.; Baskin, A.; Lawson, J. W.; Khemchandani, H.; Pascal, T. A.; Liu, P.; Chen, Z., Predicting the Ion Desolvation Pathway of Lithium Electrolytes and Their Dependence on Chemistry and Temperature. *The Journal of Physical Chemistry Letters* **2022,** *13* (20), 4426-4433.

205. Holoubek, J.; Liu, H.; Wu, Z.; Yin, Y.; Xing, X.; Cai, G.; Yu, S.; Zhou, H.; Pascal, T. A.; Chen, Z.; Liu, P., Tailoring electrolyte solvation for Li metal batteries cycled at ultra-low temperature. *Nature Energy* **2021,** *6* (3), 303-313.

206. Okoshi, M.; Yamada, Y.; Yamada, A.; Nakai, H., Theoretical Analysis on De-Solvation of Lithium, Sodium, and Magnesium Cations to Organic Electrolyte Solvents. *Journal of The Electrochemical Society* **2013,** *160* (11), A2160.

207. Fan, X.; Ji, X.; Chen, L.; Chen, J.; Deng, T.; Han, F.; Yue, J.; Piao, N.; Wang, R.; Zhou, X.; Xiao, X.; Chen, L.; Wang, C., All-temperature batteries enabled by fluorinated electrolytes with non-polar solvents. *Nature Energy* **2019,** *4* (10), 882-890.

208. Pinto, L. M. C.; Spohr, E.; Quaino, P.; Santos, E.; Schmickler, W., Why Silver Deposition is so Fast: Solving the Enigma of Metal Deposition. *Angewandte Chemie International Edition* **2013,** *52* (30), 7883-7885.

209. Li, Q.; Lu, D.; Zheng, J.; Jiao, S.; Luo, L.; Wang, C.-M.; Xu, K.; Zhang, J.-G.; Xu, W., Li+-Desolvation Dictating Lithium-Ion Battery's Low-Temperature Performances. *ACS Applied Materials & Interfaces* **2017,** *9* (49), 42761-42768.

210. Zhang, S. S.; Xu, K.; Jow, T. R., The low temperature performance of Li-ion batteries. *Journal of Power Sources* **2003,** *115* (1), 137-140.

211. Fang, C.; Li, J.; Zhang, M.; Zhang, Y.; Yang, F.; Lee, J. Z.; Lee, M.-H.; Alvarado, J.; Schroeder, M. A.; Yang, Y.; Lu, B.; Williams, N.; Ceja, M.; Yang, L.; Cai, M.; Gu, J.; Xu, K.; Wang, X.; Meng, Y. S., Quantifying inactive lithium in lithium metal batteries. *Nature* **2019,** *572* (7770), 511-515.

212. Bao, W.; Fang, C.; Cheng, D.; Zhang, Y.; Lu, B.; Tan, D. H. S.; Shimizu, R.; Sreenarayanan, B.; Bai, S.; Li, W.; Zhang, M.; Meng, Y. S., Quantifying lithium loss in amorphous silicon thin-film anodes via titration-gas chromatography. *Cell Reports Physical Science* **2021,** *2* (10).

213. McShane, E. J.; Bergstrom, H. K.; Weddle, P. J.; Brown, D. E.; Colclasure, A. M.; McCloskey, B. D., Quantifying Graphite Solid-Electrolyte Interphase Chemistry and its Impact on Fast Charging. *ACS Energy Letters* **2022,** *7* (8), 2734-2744.

214. McShane, E. J.; Colclasure, A. M.; Brown, D. E.; Konz, Z. M.; Smith, K.; McCloskey, B. D., Quantification of Inactive Lithium and Solid–Electrolyte Interphase Species on Graphite Electrodes after Fast Charging. *ACS Energy Letters* **2020,** *5* (6), 2045-2051.

215. Winter, M.; Barnett, B.; Xu, K., Before Li Ion Batteries. *Chemical Reviews* **2018,** *118* (23), 11433-11456.

216. Liu, T.; Lin, L.; Bi, X.; Tian, L.; Yang, K.; Liu, J.; Li, M.; Chen, Z.; Lu, J.; Amine, K.; Xu, K.; Pan, F., In situ quantification of interphasial chemistry in Li-ion battery. *Nature Nanotechnology* **2019,** *14* (1), 50-56.

217. Abe, T.; Fukuda, H.; Iriyama, Y.; Ogumi, Z., Solvated Li-Ion Transfer at Interface Between Graphite and Electrolyte. *Journal of The Electrochemical Society* **2004,** *151* (8), A1120.